Broadband Coherent anti-Stokes Raman Spectroscopy for Single-Cell Imaging

By Ryan Muddiman

Department of Electronic Engineering

Maynooth University

For partial fulfilment of requirements for the degree of

Doctor of Philosophy

Supervised by

Prof. Bryan Hennelly

Head of department

Prof. Gerard Lacey

March 26, 2025

Contents

Acknowledgements

I would like to thank my parents and family for their enormous support throughout completing this thesis. Their constant interest and enquiry in to this work was a significant source of encouragement. I would also like to thank my partner Niamh for her unwavering support through the last four years, without which I know I would have been less able to manage this work. Finally, my supervisor Bryan Hennelly was a very inspiring mentor. Through working with him, I learned so much about optics and research in general. His patience and trust made completing this thesis an enjoyable experience.

Abstract

In the clinical context microscopy still plays a pivotal role in analysing cells with a range of downstream analyses available. The choice of which is usually dependent on the information required, such as the level of protein expression, genetic marker identification or cell population estimation. Many cell analyses are optical in nature, but use either bulk properties that are unspecific or where measurement is based on pre-labelling the sample. Alternatively, Raman spectro-microscopic approaches are highly attractive for cell diagnostics as they provide a molecular fingerprint of a cell that is very sensitive to the cell micro-environment, is label-free and can be non-destructive. There is however common understanding that the rate of signal generation is too low for use in high-throughput scenarios, such as for clinical screening and diagnosis. Broadband CARS (BCARS) is a spectroscopic technique that probes the same molecular vibrations as Raman spectroscopy using coherent excitation by employing focused ultrafast laser pulses. The resulting signal obtained can be orders of magnitude stronger than conventional Raman scattering because it is a nonlinear effect. In this thesis, BCARS is investigated as a tool for single cell imaging, with the ultimate goal of label-free single-cell classification and high-throughput imaging. Exogenous fluorochromes were not used in any of the samples studied in this thesis. In this work, single cell imaging consisted of preparing an adequate cell sample, acquiring a hyperspectral dataset, where each point in the image corresponds to a Broadband CARS spectrum, and finally, interpreting the molecular information. In order to reach this capability, a highly optimised BCARS opto-electronic system was constructed, consisting of a commercial ultrafast laser, a modified microscope and several optical elements. The microscope was rigorously tested on non-biological samples such as pure solvents and microplastics, which enabled the tuning of the optical parameters of the system such as its resolution. After system optimisation much work was done on developing a sample targeting procedure and an automated software program was developed to enable scanning of images. Finally, bespoke data analysis procedures were developed and implemented in several single-cell image studies that were of relevance to clinical diagnostics.

List of Tables

List of Figures

1. Introduction

Optical microscopy plays a crucial role in the biosciences, serving a range of functions such as the rapid assessment of a microorganism's confluence in culture, automated cell counting, and comprehensive diagnostic analysis by pathologists. In its basic form, optical microscopy provides information about a specimen's reflectivity and transmittance, which are directly related to material properties. When images are interpreted by a human observer, heuristics like hue, brightness, and shape are used to infer details about the sample. These contrast mechanisms are inherently bulk properties, and while they may vary at the microscope's resolution scale, such variations are often not sample-specific, limiting quantitative interpretation. Fluorescent markers (fluorochromes) can be artificially introduced prior to microscopy in order to enhance contrast. In such a case, a sample is pre-labelled with the marker and then viewed under excitation light, which highlights the presence and location of the marker, indicating where binding of the marker has occurred. Through understanding the chemical structure of the marker and its binding mechanisms, specific features in the sample, such as the DNA-binding affinity of 4',6-diamidino-2-phenylindole (DAPI), can be identified, which allows nuclear regions of cells to be highlighted. Fluorescence microscopy thus complements light microscopy by providing both qualitative and, in some cases, quantitative characterization of samples. Fluorescence microscopy has the fundamental limitation of sample perturbation, whereby the presence of the fluorochrome changes the biological function of the sample. This approach to cellular analysis is therefore subject to confounding by the method itself.

If scattered or transmitted light from a sample is collected and dispersed using a spectrograph, the potential to analyse molecular composition and conformation emerges, a process known as spectroscopy. There are many types of spectroscopy, typically distinguished by the properties of

the incident light used. In biological applications, light in the THz to PHz range is commonly used, corresponding to the infrared part of the electromagnetic spectrum. This frequency range coincides with the natural vibrational frequency of molecular bonds, and provides access to a molecules vibrational spectrum. There are two types of vibrational spectroscopy, (i) corresponding to absorption of the incident light, known as infrared spectroscopy, or (ii) scattering of the incident light, called Raman spectroscopy. When incident light couples to the electrons or dipoles in an oscillating bond, it can induce a shift in the vibrational energy of the bond and a corresponding shift in the light frequency, called the Raman shift. Measurement of this frequency shift gives direct access to the molecular bond oscillation frequency. In biological media, Raman spectroscopy can report the vibrational spectrum in a purely non-invasive manner, assuming photodamage is avoided. It therefore provides much richer contrast, as compared to light microscopy. Raman microscopy is a specific spectroscopy technique which uses a microscope to deliver and collect the light, and Raman images can be produced by scanning either the sample or the laser focus over an area. This is much more informative than single point measurements, as both spatial and spectral dimensions are measured. In a Raman image, chemical and physical properties provide the contrast. Since the resolution of Raman imaging is limited only by diffraction, it is well suited to imaging biological samples such as cells[2]. One of the most commonly cited downfalls of Raman imaging is the low probability of Raman scattering, which necessitates relatively long dwell times for the acquisition of images. This feature cannot typically be overcome by increased irradiance, because there is a point at which photodamage will inevitably occur. This can instead be mitigated by exploiting the nonlinear properties of matter. Through the use of high peak power lasers, coherent Raman scattering (CRS) becomes possible. In CRS, the incident lasers drive the vibrational energy shift, thus increasing the output light intensity by orders of magnitude compared to the linear Raman process. Coherent-anti Stokes Raman Scattering (CARS) is one such method, and it is the broadband version of CARS - BCARS which is the main focus of this thesis. In particular, the testing and development of BCARS as a tool to probe single biological cells was the major focus. BCARS provides access to the same molecular information as linear Raman spectroscopy, however, there is high directionality of the output beams, a gain corresponding to the driving of the vibrational transitions, and the output intensity depends on the product of three input intensities. As there is some ambiguity in the literature, the term BCARS in this thesis is reserved for the measurement

of the full Raman vibrational spectrum (fingerprint and high wavenumber regions) in a single shot. Some authors for example use BCARS to describe only the fingerprint region[3].

BCARS is a powerful technique for investigating complex biological matter, as it enables the recording of content-rich images of specimen, with scan times on the order of minutes for a 200 $\times$ 200 μm area at 0.6 μm lateral resolution[4]. Due to some of the above mentioned benefits of BCARS, it is beginning to be increasingly applied to functional biomedical applications, such as animal tissue imaging[5, 6] and pharmaceutical analysis[7, 8]. Previously, the application of BCARS for imaging isolated cells was demonstrated in concept, by Parekh[9]. However, while this work highlighted the potential for label-free cell imaging, the clinical application of the method was not explored and it has not been demonstrated to date. In particular, the ability for BCARS to perform a high-speed, label-free classification of eukaryotic cells of different origin has not been performed. Notably, classification of several different eukaryotic cells using spontaneous Raman spectroscopy has been reported[10, 11, 12], but the potential for BCARS to enable a much higher analysis throughput due to its signal intensity improvement was still unknown at the beginning of writing this thesis. This question was explored in chapter 8. The ability to differentiate and quantify various cell types based solely on chemical composition variations obtained from the Raman spectrum has the potential to eliminate the need for several analyte-specific processing methods used in clinical applications. This concept is however not yet clinically applied using spontaneous Raman spectroscopy due to several issues, not least of which is the speed limitation, where dwell times of tens of seconds per cell are typical[13].

The relevance of BCARS for cell imaging and analysis is largely due to the high specificity of the vibrational spectrum and the demonstrably high signal intensity obtained in biological media[4]. The current requirement for specialised sample preparation routines in medical laboratory tests is largely based on the varying sensitivity and specificity of the chemical and physical measurements used. For example, fluorescence flow cytometry is used to quantify the frequencies and polymorphisms of red blood group molecules and for classifying lymphocytic leukemia as originating from B or T cells[14] and while these methods are highly specific, they critically rely on pre-labelling of the cells. Fluorescence-free flow cytometry is also reasonably specific for distinguishing major white blood

cells using physical scatter metrics such as size and granularity, provided that no other cell types are present. The specificity arising from a molecular approach such as BCARS could, in theory, be much greater, compared to purely physical and or labelling mechanisms like those mentioned above, and the benefit of much greater imaging speeds could make redundant the numerous sample specific analyses that are ubiquitously applied in clinical laboratories. Most importantly however, as a purely spectroscopic technique, BCARS does not require sample-specific processing, provided the contrast obtained in the expected specimen is suitably high. Regardless of these potential benefits, advancement of diagnostic methods require extensive evidence of demonstrated suitability to basic tasks, along with an improvement in some operating characteristic, such as specificity, reliability or predictive value. In this work, the positive predictive value of the vibrational spectrum in cell classification was known *a priori* based on published spontaneous Raman spectroscopy studies[10, 11, 13, 15], but the optical engineering, data processing, and ultimate suitability of BCARS as a cell analysis method was not previously demonstrated. The major initial task of this thesis was to acquire spectroscopic images from eukaryotic cells using BCARS, at a level of spectral and spatial detail similar to spontaneous Raman imaging, and at a much faster rate.

Developments of BCARS applications involving single-cell imaging have been previously slow, especially compared to its other CRS counterpart - stimulated Raman scattering (SRS). SRS is a non-parametric third-order optical effect that results in a gain or loss in the input photon numbers due to vibrational transitions occurring. Due to this, signal is only present when a vibrational transition is probed and no non-resonant background is generated. Apart from the technical complexity of constructing the BCARS microscope, the signal from a cell is also extremely weak relative to other clinically relevant specimen, such as tissues, and single cells are also difficult to target, meaning the use of conventional analysis protocols designed for spontaneous Raman imaging usually do not suffice. For example, since BCARS is a third-order process, the scattered signal intensity is highly sensitive to the axial position of the sample, whereas for conventional Raman scattering, a measurable signal may be obtained even when the sample is slightly misaligned with respect to the focal plane of the laser. Secondly, as BCARS is a broadband multiphoton technique, the optimal signal is obtained when the input beams are focussed to the smallest possible volume, requiring considerations for optical aberrations present in the input beams. In this regard, we appear to be the

first to implement a deformable mirror in a BCARS microscope to optimize the focussing of the input beams. This approach is described in chapter 5.1.

BCARS is also known to have a major drawback termed the non-resonant background (NRB) which is related to the electronic polarization in the sample. The NRB in BCARS prevents direct analysis of the raw intensity measurement since the background corrupts the chemical dependence, and in some cases completely obscures the signal contrast. In this work, the raw fingerprint spectrum from a cell was largely indistinguishable from noise. To overcome this problem, many NRB suppression or correction methods have been devised[16, 17, 18, 19, 20]. This problem is absent in SRS, and is likely a major reason for the rapid advancement in this method over the last ten years. The lack of an NRB has afforded pixel dwell times of hundreds of microseconds[21]. However SRS has limitations which make BCARS the more attractive option for single-cell analysis. In particular, the broadband single-shot acquisition in SRS is not possible, since it requires lock-in signal measurement, thus only recording a single wavenumber at a time. Novel numerical methods to remove the NRB in BCARS are proposed in chapters 6 and 7 and an optical method to do so is explored in chapter 10.

Another highly applicable clinical problem of interest in this work was the rapid imaging of a routine cell sample for pathogen detection and this is the subject of chapter 9. This is a very common procedure performed in microbiology and pathology laboratories in hospitals, that aims to determine the state of infection in a patient suspected with a disease. The application of BCARS in this sense would be well suited to the task, as it can rapidly provide molecular contrast at the cellular level, while images can resolve spatial information such as size, concentration, morphology and site of adhesion of the pathogen within cells. This problem is somewhat less defined than the above problem of phenotyping multiple cells, as the minimum requirement is detection of an anomalous biological species within otherwise “normal” cell populations. While in the routine clinical diagnostic setting, it could be envisaged that a multivariate statistical model could be devised to distinguish known and common cell types based on the chemical contrast provided by its spectrum, in the case of pathogen detection it is unlikely that a reference database or model could be developed or trained to distinguish all existing pathogen likely to be encountered. Therefore, alternative approaches to

multivariate statistical classification were developed to apply BCARS as a rapid screening tool for cell analysis using purely unsupervised approaches.

1.1 Research questions

To summarise the main research questions explored in this thesis;

1. Can BCARS provide cell imaging capabilities beyond that obtained using standard cell analysis protocols, with the goal of distinguishing cell type at millisecond acquisition times?
2. To what extent can BCARS be used to provide automated high-throughput cell analysis, for screening of cells?
3. What are the optical requirements, measurement protocol, data processing steps and sample preparation procedures required in order to achieve the above?
4. Can the NRB be removed with sufficient accuracy to produce classifiable Raman-like spectra from a BCARS system.

1.2 Contributions

The remaining chapters of this thesis are noted below, with my contributions stated where applicable.

- Chapter 2 is a literature review covering the major previous works that are of relevance to this thesis.
- Chapter 3 describes the underlying physics theory of the BCARS process.
- Chapter 4 is devoted to describing the key methods both implemented and devised that were commonly used throughout all of the results chapters. The novel contribution in this chapter is the bespoke preprocessing pipeline developed for preparing single-cell hyperspectral BCARS images for analysis, such that they can be analysed using conventional methods.

- Chapter 5 presents the engineering considerations of the experimental optical system, its optimization and its characterisation. I was the sole student working on the BCARS platform development, and I performed all of the optical design and optimisation work.

- Chapter 6 is the first results chapter. This chapter describes the development of a novel deep-learning architecture for NRB removal in BCARS measurements, which was named VECTOR. My contribution to this work was in the conceptual design of the simulation of artificial BCARS data, which was required for training the network, and i was also involved in analysing the networks performance on the simulated data. The results of this chapter are published in the Journal of Raman spectroscopy[22].

- Chapter 7 is a results chapter based on an improved NRB removal approach using an identical network architecture to the one described in chapter 6, with a much improved BCARS simulation procedure and loss function. My contribution to these results were the development of a novel high-fidelity BCARS simulator that uses system-specific information from the laser spectra to mimic experimental BCARS data, such that the NRB removal could be tailored to a particular microscope system. I also performed all data analysis, recorded experimental BCARS spectra for evaluation, and recorded spontaneous Raman spectra to aid in a comparison. The results of this chapter are published in the Journal Analytical Methods[23].

- Chapter 8 is a results chapter based on multivariate statistical classification of blood cells using label-free BCARS imaging.This was the first experimental classification of two isolated cell lines, and a mixture of cells, using BCARS. In particular, for this chapter, I acquired the hyperspectral images of the cells and performed all statistical analysis. This work required significant input from collaborators in the Maynooth University Department of Biology, who provided the cell lines for imaging. At the time of writing a paper based on the work presented in this chapter has been accepted for publication in the Journal of Biophotonics, pending major revisions.

- Chapter 9 is a results chapter based on fungal pathogen identification using BCARS imaging. The results presented are the first demonstration of unsupervised pathogen detection in a cell

mixture using BCARS. For this work, I performed all BCARS imaging of the cell samples, data analysis of the images and recorded spontaneous Raman spectra of the fungal samples for verification of the method. The cells for this study were provided by the Maynooth University Department of Chemistry. At the time of writing we are considering submitting the results presented in this chapter to a journal, pending further experimental results.

- Chapter 10 is a results chapter based on a hybrid optical approach to NRB removal, known as spectral interferometric polarization CARS (SIPCARS). SIPCARS is a relatively new technique that has been previously been demonstrated for providing polarization resolved BCARS spectra that are free from NRB interference. My contribution was the first application of SIP-CARS to single cell imaging using a modification to the BCARS system. The samples were provided by the Maynooth University Department of Biology. For this chapter, I performed all BCARS image acquisitions, recorded spontaneous Raman spectra for comparison of the spectra, and analysed all the data.

2. Literature Review

2.1 Raman Scattering

The phenomenon of inelastic light scattering was first proposed by Smekal in 1923[24] and later observed by Raman and Krishnan in 1928[25], using sunlight as a light source and a telescope as the collector. Raman demonstrated that new light frequencies could be generated when incident light is scattered by a material. This effect, known as Raman scattering, arises from the random molecular vibrations of materials at temperatures above absolute zero. As a result, the scattered radiation is relatively weak, emitted randomly in time and direction, with only about 1 in every 10^7 incident photons undergoing Raman scattering. After this discovery, the development of photoelectric instruments allowed for the electronic recording of the scattered radiation, leading to the widespread use of Raman spectroscopy for studying materials. Modern advancements have significantly improved the efficiency of this scattering process, making Raman spectroscopy a powerful and widely-used technique for analysing vibrational modes and studying vibrational transitions in samples.

In 1946, Harrand and Lennuier first experimentally observed the phenomenon of Raman resonance enhancement[26]. They found that the Raman signal intensity increased in a dichloronitrobenzene solution when the excitation wavelength matched the electronic absorption band. Their findings also showed that only a few vibrational modes were enhanced, suggesting that only those modes coupled to the chromophoric group could experience enhancement. This discovery sparked intense research, as it introduced the potential for greater Raman selectivity and sensitivity. Resonance

occurs only when the excitation wavelength overlaps with an electronic absorption band[27], and the effect became known as resonance Raman scattering (RRS).

The concept of stimulating molecular transitions was first discussed by Townes and Schawlow in 1958[28]. This led to the demonstration of the first maser by Maiman in 1960[29], followed by the development of the Helium-Neon laser by Javan, Bennett, and Herriott in 1961[30]. The invention of the laser in the 1960s sparked significant interest in Raman scattering, as the laser's ability to focus many photons onto a small area greatly amplified the intensity of the effect. The laser's monochromatic nature also provided a narrow impulse response, which paved the way for modern Raman spectroscopy, enabling the study of a material's vibrational and rotational states. Due to their simplicity and available frequencies, the ruby maser and He-Ne laser became popular light sources for Raman spectroscopy. In 1961, Porto and Wood conducted the first laser-based Raman spectroscopy experiment[31]. Today, a wide range of tunable laser sources, including continuous-wave (CW) and pulsed dye lasers, as well as parametric oscillators, are available. These technological advancements have allowed in-depth exploration of the Raman effect across a broad frequency range, with increasingly powerful pulse sources.

Although lasers greatly enhanced Raman scattering, the effect remained spontaneous, as scattering occurs only when random transitions take place. However, shortly after the introduction of the laser, the phenomenon of stimulated Raman scattering (SRS) was discovered. SRS uses two optical beams to induce Raman transitions and is sensitive to the same molecular vibrations as spontaneous Raman scattering (SR), but with coherent scattered light due to the molecules' synchronized polarization. Within a year of the lasers invention, the intense pulses enabled the discovery of nonlinear optical effects, such as second-harmonic generation (SHG) in 1961[32] and third-harmonic generation (THG) in 1962[33].

In 1962, Woodbury and Ng observed laser lines near the output of their laser that were longer in wavelength than those produced by the ruby gain medium[34]. They attributed these new lines to Raman scattering, specifically the symmetric stretching vibration of the NO_2 group in nitrobenzene. Nitrobenzene, which was used in the laser cavity as a Kerr cell shutter to pulse the laser, facilitated this scattering. Recognizing the similarity to spontaneous Raman scattering

but noting that the emission was coherent and consistent in time, they named the phenomenon stimulated Raman scattering (SRS). The vibrational coherence in SRS significantly amplifies the signal, making detection easier due to the coherent nature of the radiation. The development of more efficient spectrographs, advanced detectors like Charge-Coupled Devices (CCDs) and photomultiplier tubes (PMTs), along with more powerful lasers, spurred a renewed interest in applying Raman spectroscopy to biochemical research during this period[35, 36].

In 1974, Fleischmann *et al.* observed a new type of enhanced Raman spectrum from pyridine adsorbed on roughened silver surfaces[37]. Initially, these spectra were not recognized as distinct from those produced by spontaneous Raman scattering. However, in 1977, Jeanmaire *et al.*[38] identified this as a new phenomenon, where the Raman signal was enhanced due to the surface structure and electronic properties of the sample. This effect was later termed surface-enhanced Raman spectroscopy (SERS). The exact mechanism of enhancement is still debated, but the two most widely accepted theories are the electromagnetic enhancement mechanism, which involves the amplification of radiation through localized surface plasmon resonances (LSPR)[39], and the charge-transfer mechanism, which arises from new coupled states between the sample and the substrate[40]. SERS can provide up to a 10^6-fold increase in signal intensity compared to normal Raman scattering[41]. SERS can be performed on colloidal solutions, but for solid samples, it typically involves applying a layer of nanoparticles to the surface. While this surface treatment is a limitation, the technique's ability to detect extremely low concentrations of molecules makes it highly valuable for applications such as biomarker detection[42] and forensic analysis.[43]

2.2 CARS

In 1965, at Ford Motor Company, Maker and Terhune provided a detailed description of a new Raman spectroscopy technique[44]. They investigated various nonlinear optical effects using a giant pulsed ruby laser, developing simplified models to describe an effect they termed "frequency mixing." In their setup, they used a 0.1 J output pulse focused on a sample, with anti-Stokes emission collected using a $NiSO_4$-$CoSO_4$ water filter to remove the source laser, and a grating monochromator

for wavelength discrimination and detection via a photomultiplier. This technique, now known as coherent anti-Stokes Raman spectroscopy (CARS), has become the most widely used nonlinear Raman scattering method.[45]

CARS occurs when a “pump” photon and a “Stokes” photon induce a coherent vibration in the sample at the frequency difference between them. A third ”probe” photon scatters off the excited state, gaining energy equal to the vibrational mode energy of the prepared state. Unlike spontaneous Raman scattering, CARS involves an active pump process, with the Stokes photon inducing a Stokes transition. In 1973, Régnier and Taran proposed applying CARS to gas flow analysis, particularly for measuring gas concentrations[46]. In 1975, Bjorklund demonstrated that under tight focusing conditions, the phase-matching requirement for CARS could be satisfied in a co-linear beam geometry, which would later prove crucial for CARS microscopy.[47]

A key advantage of CARS is that the measured radiation is at a higher frequency than the excitation frequency, effectively eliminating background fluorescence. In 1974, Begley *et al.* emphasized the advantages of CARS over spontaneous Raman scattering, noting its five-orders-of-magnitude higher conversion efficiency and its suitability for studying biological compounds where fluorescence interference is problematic[48]. In 1977, Tolles *et al.* published a comprehensive review of the CARS effect, covering the fundamental theory, signal generation conditions, and the mechanism of the non-resonant background (NRB)[49]. By the early 1980s, two separate books detailed the numerous applications of CARS, particularly in the study of flames, jets, and combustion engines.[50, 51]

Spontaneous and coherent Raman spectroscopy were soon coupled with microscopy with the ability to now target microscopic regions within a sample or to create vibrational images of samples. Coherent Raman scattering (CRS) which encompasses all Raman effects that produce a coherent beam, are the most suited for vibrational microscopy since they exploit the nonlinear dependence of the samples response and can generate signal at much higher intensities. In 1982, Duncan and colleagues developed a CARS instrument that used spatial scanning for chemical imaging, the first iteration of the CARS microscope[52]. In 1987, Bloembergen published a detailed review of stimulated Raman scattering spectroscopy, including CARS[53] and in 1990, Puppels demonstrated

a method of high resolution spontaneous Raman microspectroscopy of biological samples[54]. This setup allowed the recording of a Raman spectrum from a confocally filtered region within single cells at a resolution of $\sim 6 - 7$ cm^{-1}. The exposure time per spectrum however was on the order of minutes, resulting in an extremely slow sample speed.

A major advancement in the field of coherent Raman microscopy was made by Zumbusch *et al.* in 1999 when they used a CARS microscope to create three-dimensional images of live cells[55]. Most importantly, this was the first use of CARS microscopy in the co-linear beam configuration, the most common setup used today due to its simplicity, as opposed to the BOX-CARS configuration, which required angle tuning of the input beams. Using two femtosecond pulses from a Ti:Sapphire regenerative amplifier at 855 nm centre wavelength, coupled co-linearly in to an optical microscope and focused using an oil-immersion objective, they then raster scanned the sample using a 10 ms acquisition time while collecting the anti-Stokes emission using photon counting equipment. Zumbusch also stated the use of the near-infrared excitation has an advantage over visible laser sources in CARS as it avoids any two-photon electronic resonance.

Once the fundamental concept was demonstrated and a reliable method of CARS spectroscopy was established, there began some research on dealing with the non-resonant background inherent to the process. In 2001, Cheng *et al.* reported on a scheme for suppressing the non-resonant background signal using an epi-detection configuration, calling it epi-detected CARS (E-CARS), where the anti-Stokes radiation is collected in the backwards direction rather than the conventional forward direction.[56, 57] The E-CARS method utilizes the suppression of the solvent NRB signals in the backward direction due to destructive interference, effectively enhancing the measured resonant signal.

In the same year, Cheng *et al.* also published a technique using selective polarization to suppress the non-resonant background, calling it Polarization CARS (P-CARS)[20]. This technique was applied to unstained cells based on the contrast of the protein amide I band. A common name for the standard unpolarised and forward collected CARS configuration was then noted, namely F-CARS, to prevent confusion to the other types. In P-CARS, the difference in depolarization of the resonant versus the non-resonant susceptibility is used to selectively block radiation that is purely

non-resonant using linear polarisers.

In 2002, Cheng developed a laser scanning CARS microscope tailored for biological samples. The system used a pair of galvanometer mirrors to control the scanning of the beams in the x-y plane. The depth scanning was achieved by moving the water objective with a stepping motor. The pump and probe pulses were both transform-limited 5 ps pulses from a Ti:Sapphire source and were tunable in wavelength. The detection used photomultiplier tubes (PMT) and therefore could measure only one Raman shift at a time. Cheng also gave a very detailed description of the theoretical beam propagation of the CARS radiation based on a Green's function method.[58]

In-vivo imaging using CARS at the video-rate was then achieved by Evans *et al.* in 2005[59]. Evans used the E-CARS configuration to image real time chemical diffusion in the skin of mice. The laser used was a Neodymium Vanadate laser which produced a 7 ps Stokes pulse, and used a portion of the Stokes beam with an OPO for the pump beam. By selectively tuning the beams to excite the CH_2 stretch mode, the imaging of lipid rich structures in the mice was possible. The use of a 1.2 NA objective provided high resolution in the axial (1.5 μm) and lateral (0.3 μm) directions.

2.3 Broadband CARS

The phase matching condition for efficient mixing of the pump, Stokes and probe photon in a medium is an essential requirement for CARS, without which, there is no appreciable buildup of the anti-Stokes radiation. This is detailed in chapter 3. As stated above, the CARS microscopy literature has been concerned with two main geometries for achieving phase matching; BOX-CARS and tight-focussing. These two methods both give the necessary beam geometries of the input pulses to satisfy the requirement for signal generation that is not limited by the coherence length of the medium. The BOX-CARS geometry involves a crossed-triple-beam technique using two lenses of equal focal distance and directing the three input beams at specific angles relative to each other. The tight-focussing geometry is much simpler and obtains phase matching by using the fact that high NA lenses produce a large continuum of exit rays that may mix to produce the four-wave mixing. In modern CARS microscopy, the tight-focussing regime is ubiquitous as it can be incorporated in to

life science microscopes with ease.

The first report of optical multiplexing in CARS microspectroscopy was in 2002 by Cheng *et al.*[60] In their setup, a picosecond pump and femtosecond Stokes beam were used. The Stokes pulse had a broad spectral width (160 cm^{-1}), corresponding to a transform-limited pulse of 91 fs duration. The pump was centred at 713 nm and had a spectral width of 2.9 cm^{-1}. The excited spectral region covered was from 2750-3050 cm^{-1}. The multiplex nature of this setup allowed several Raman modes to be probed by the CARS process, and was thus termed multiplex CARS (M-CARS). The tight-focusing condition was fulfilled using a high numerical aperture objective lens in the microscope. Their setup also utilized P-CARS for non-resonant background suppression and to determine the depolarization ratios of Raman bands. The effect of spectral chirp was also evaluated theoretically, since their use of an ultrashort pulse for the Stokes would have introduced chirp due to the dispersive optics in the setup. In the same year, Cheng[61] used two transform-limited 5 ps infrared beams to demonstrate live cell metabolism, however this setup used single-frequency tunable CARS, rather than bCARS. The setup incorporated two galvanometer mirrors for spatial scanning and detected both the forward and epi-CARS signals simultaneously. Since the SF-CARS does not require a spectrometer, the signal was detected using multiple bandpass filters and a photomultiplier tube. Thus, only a single Raman band was detected at any one time. Cheng reported an acquisition time of 10 s for a CARS image of 512 $\times$ 512 pixels, and showed that CARS imaging can be coupled with differential interference contrast and fluorescence microscopy for improved contrast imaging.

In 2007 Pestov *et al.*[62] studied methods in optimizing the shape of the input laser pulses for multiplex CARS, with an emphasis on biological sample identification. This work demonstrated efficient ultrafast broadband excitation using transform-limited femtosecond Stokes pulses and a narrowband pulse that was several hundred femtoseconds long. Various samples were identified through spectroscopic investigation of the recorded Raman bands. The samples included *B. subtilis* and sodium dipicolinate powder. It was shown experimentally that the probe temporal properties affect the NRB contribution greatly. When the probe pulse has zero delay with respect to the Stokes pulse, the NRB to resonant signal strength was inversely proportional to the probe spectral width. Therefore it is attractive to use ultrashort Stokes pulses to enhance the coherence generation width,

but longer probe pulses in order to suppress the NRB. It was also noted that the NRB signal strength is largest for zero delay, and that a combination of tailoring the temporal duration and temporal delay of the probe pulse to the Raman linewidths of interest should yield optimal NRB suppression overall.

2.4 BCARS for Biomedical Applications

During the development of CARS as a technique to study biological matter, the methods became established in the field. This consisted of lasers coupled in to a conventional high numerical aperture microscope objective (tight-focussing) to focus the beams and this was found to be more practical than the BOX-CARS approach to phase matching. Coupled with either a miniaturised galvanometric scanning system or digitally controlled stage which allowed imaging of biological media allowed adoption of CARS imaging as a biological microscopy. The main advantages of CARS microscopy over other modalities were its inherent chemical selectivity due to the Raman effect, high relative intensities compared to spontaneous Raman scattering, depth selectivity due to it being a third -order optical effect and its capability for fluorescence free signals. However, at this point the main drawbacks to CARS microscopy were the NRB and its effect on the interpretability of spectra.

In 2009 a review of CARS microspectroscopy for biological imaging was published by Krafft *et al.*[63]. This review was heavily focused on the application of CARS to cells and tissues and briefly describes the key principles of the method. This review mentioned that implementations of CARS at the time of publishing was prohibited by cost and complexity arising from the required spatial and temporal overlap of the three input pulses for four-wave mixing to occur. These concerns were often cited as CARS became more common, and CARS was typically compared to spontaneous Raman spectroscopy, which was much less complex to implement. However the benefit of drastically increased Raman signals was seen as a worthwhile cause to develop CARS for biomedical applications.

A broadband CARS microscope was presented by Camp *et al.* in 2014[4] and this paper can be considered seminal in the context of this thesis. A key part of this thesis consisted of replicating the

performance and extending the capability of the system. In that work, chemical images of murine liver and pancreatic tissue were created from broadband CARS spectra using a motorized sample stage for spatial data acquisition. The BCARS system comprised of a narrowband probe at 770 nm and a broadband Stokes which spanned from approximately 900 nm to 1350 nm. The images were generated from false-color transformed spectra using typically one Raman band for biochemical contrast. Remarkably, the bandwidth recorded for each spectrum was 470 cm^{-1} to 3,800 cm^{-1}. In this work, the NRB had been removed using an implementation of the Kramers-Kronig relations and a phase correction procedure based on an assumption of a spectrally flat NRB. This seminal work demonstrated that highly interpretable Raman spectra were obtainable from BCARS measurements of biological tissues when spectral denoising methods were used prior to NRB removal. The emphasis on the requirement for spectral denoising was noted, since NRB removal methods are mathematical transforms that are highly dependent on the input noise. This is explicated in chapter 4.

Voronine *et al.*[64] in 2018 published a review article on surface-enhanced CARS using the femtosecond adaptive spectroscopic technique (FAST). This review focused on biophotonics applications of this approach. FAST CARS is a technique for optimally controlling the input laser pulses to suppress the non-resonant background in the anti-Stokes signal using probe pulses that maximally prevent NRB generation from the temporal properties of the pulse. This approach is in effect a temporal suppresion of the NRB, using pulse shaping rather than a pulse delay.

A critical review of coherent Raman microscopy for clinical and biological studies was published in 2015 by Schie *et al.*[65] Their findings indicate most research in to biological studies with CARS has been focused on the high-wavenumber region. This is mainly due to the relatively stronger Raman response from these vibrations compared to the weaker fingerprint region due in part to the much larger local concentration of CH_2 vibrational modes. The biological applications of CARS studied were mainly lipid droplet research and histopathologic tissue imaging. Lipid droplets (LD) are a popular target for CARS since they have a high scattering cross-section and tissue imaging benefits from the 3-D sectioning capabilities of CARS. LDs in particular are cellular organelles that act as storage vesicles, protect cells from lipotoxicity and are a source for membrane lipid

biosynthesis, protein storage and metabolism. CARS enables the sizing, quantification and imaging of LDs within cells that contain them. The other main application, tissue imaging showed examples of single-frequency CARS combined with second-harmonic generation images to visualize cells and the extracellular matrix for disease detection.

A review of broadband coherent Raman techniques was published by Polli *et al.* in 2018[66]. This review focused mainly on BCARS and SRS in the context of biological imaging. This review also collated the many novel variants of coherent Raman imaging such as time-stretch SRS, which converts a broadband signal in to a long duration signal, such that it can be captured by a high frequency analog to digital converter. In the review, a table summarized the main coherent Raman imaging modalities, of which BCARS was one. Importantly, SRS was identified as a modality that was not expected to incur revolutionary changes due to it being at the shot noise limit, but stated it is likely to benefit from increased source bandwidth from new optical parametric oscillator technologies. It was noted that CARS can be expected to benefit from enhanced multichannel detectors with lower noise, providing higher speed and contrast, and that the demonstrated ability of BCARS for tissue imaging[4] was inspiring for the future.

The demonstration of a novel imaging technique using a spectral interferometry method applied to BCARS measurements was demonstrated by Littleton *et al.*[67, 68] This work used selective polarization shaping of the input beams to probe different components of the third-order susceptibility tensor, such that the measured signal was free from the NRB. This work, unlike previous attempts to optically remove the NRB was stated to not have the drawback of reduced resonant intensity, demonstrating major potential for bioimaging. This method also was almost fully optical, requiring only a subtraction of two simultaneously recorded and orthogonal spectra. Since interference signals such as fluorescence were common mode in each measurement direction, they cancelled in the difference spectrum.

In this chapter we examined the key prior contributions in the development of coherent Raman microscopy for biological imaging, with an emphasis on CARS and BCARS, which are central to this thesis. In particular, the BCARS system proposed by Camp *et al.*, capable of recording Raman-like spectra from a wide band covering both the fingerprint and CH bands, is relevant to this

work. In the next chapter, we introduce the background theory behind BCARS imaging and in the later chapters we demonstrate the application of BCARS for single cell imaging.

3. Theory

3.1 Incoherent Light Scattering

Light interacts with matter by absorption or scattering. Absorption requires the energy of the incident photon to correspond to the energy gap between two states within an atom or molecule. Scattering can occur regardless of whether the photon corresponds to an energy level gap in the matter. When light interacts with matter, it causes electrons to polarize due to the electric field and the electrons increase in energy. The polarized state is a "complex" between the light and electrons during which it is typically assumed the atomic nuclei do not have time to move. The complex is typically called a virtual state, since it is not an eigenfunction of any operator and therefore cannot be observed. The energy of this virtual state is dependent on the incident photon energy and the amount of polarization induced is related to the electronic properties of the atom or molecule involved[69]. Two types of optical scattering occur at low incident electric field strengths ($< 10^8$ V/m). The most common type is known as Rayleigh scattering and occurs when the excited state relaxes without any movement of the atomic nuclei. This process is elastic since there is no change in energy between the initial and final state of the atom or molecule. The other type of scattering is called Raman scattering, a much rarer event which involves approximately one photon typically in every 10^6-10^8[70] incident photons. Raman scattering occurs if the polarizability changes due to a vibration or rotation. Since the nuclei are much heavier than the electrons, there will be a change in the energy of the molecule to a higher or lower energy depending on whether the initial state is the ground state or an excited state.

Light may also be completely absorbed by a material. In this case, higher energy electronic states become populated. When these states release energy in the form of non-radiative transitions, energy is dissipated in the form of heat. In radiative transitions the light is re-emitted and called luminescence. Luminescence can be spontaneous, meaning it occurs in the absence of incident radiation or stimulated by radiation. Spontaneous emission in which the upper and lower spin quantum number is unchanged is known as fluorescence, and the emission is characteristically lower in energy than the initial absorbed light. Fluorescence occurs when an excited electron drops back down to a lower energy state (usually the ground state) without a change in spin. This process is fast, typically occurring within nanoseconds. Another form of emission can occur when the spin quantum number changes, known as phosphorescence. These processes are shown diagrammatically in figure 3.1. In the figure, the potential energy curve of a molecular bond is shown for three different states. The stationary point is the equilibrium bond length R_0, which may change according to the states energy. The form of the potential is given here as a Morse potential, which describes an anharmonic potential and approximates real data quite well.

3.1.1 Maxwell's equations in matter

The interaction of light and matter is described by Maxwell's equations which are the fundamental equations of electromagnetism. Maxwell's equations apply to all media which are at rest with respect to the coordinate system being used to describe them and also apply to linear and nonlinear media. The linear equations in SI units will be described first and then expanded upon to derive the nonlinear wave equation. As a starting point the equations for isotropic media are given as[71]

$$\nabla \cdot \mathbf{D} = \rho_{\mathrm{f}} \tag{3.1}$$

$$\nabla \cdot \mathbf{B} = 0 \tag{3.2}$$

$$\nabla \times \mathbf{E} = -\frac{\partial \mathbf{B}}{\partial t} \tag{3.3}$$

$$\nabla \times \mathbf{H} = \frac{\partial \mathbf{D}}{\partial t} + \mathbf{J}_{\mathrm{f}} \tag{3.4}$$

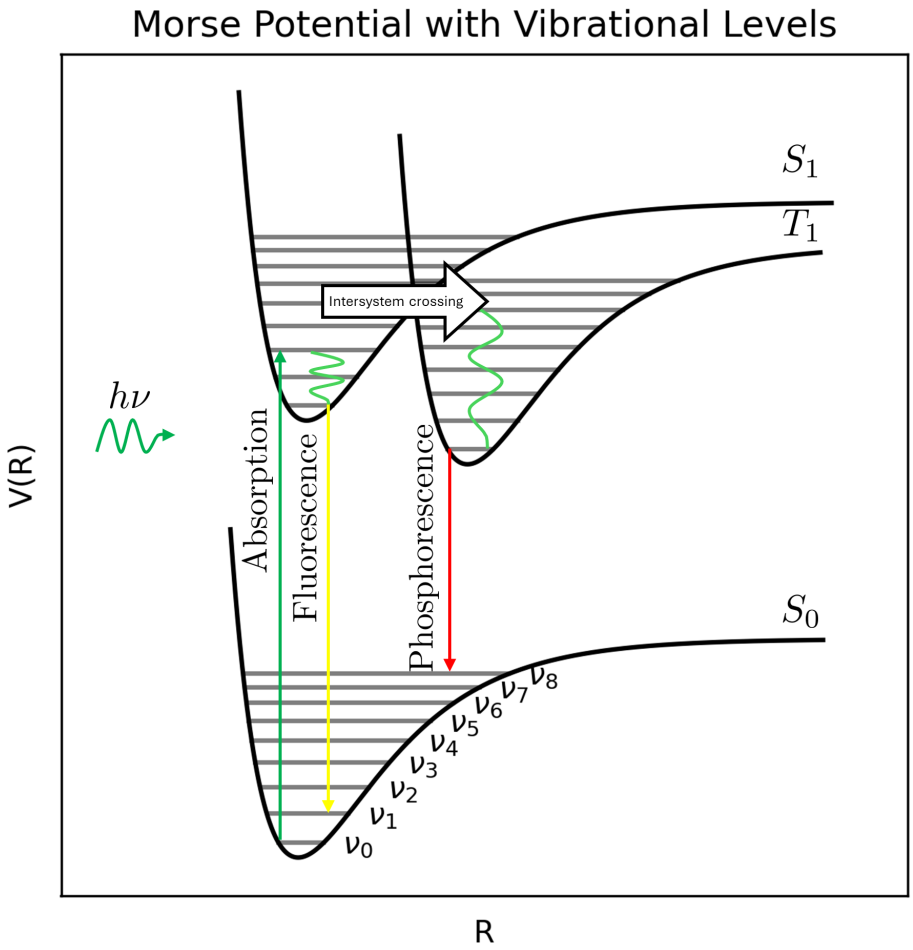

Figure 3.1: Jablonski diagram of the Morse long-range potential of three electronic states, the ground state S_0, 1st excited state S_1 and an excited triplet state T_1.

where $\mathbf{D}$ is the electric displacement, $\mathbf{B}$ is the magnetic flux density, $\mathbf{H}$ is the magnetic field, ρ_f is the free charge density and $\mathbf{J}_\mathrm{f}$ is the free current density. The displacement is related to the electric field $\mathbf{E}$ through

$$\mathbf{D} = \epsilon_0 \mathbf{E} + \mathbf{P} \tag{3.5}$$

where ϵ_0 is the electric permittivity of free space and $\mathbf{P}$ is the electric polarization. Substituting this in to equation 3.4

$$\nabla \times \mathbf{H} = \epsilon_0 \frac{\partial \mathbf{E}}{\partial t} + \frac{\partial \mathbf{P}}{\partial t} + \mathbf{J_f} \tag{3.6}$$

Equation 3.4 can be written in terms of $\mathbf{B}$, using the fact that $\mathbf{B} = \mu_0(\mathbf{H} + \mathbf{M})$, where μ_0 is the magnetic permeability and $\mathbf{M}$ is the magnetic polarization (magnetization) in the material. The total

current density can be expressed as a sum of free, bound and polarization current as follows,

$$\mathbf{J} = \mathbf{J_f} + \mathbf{J_b} + \mathbf{J_p} = \mathbf{J_f} + \nabla \times \mathbf{M} + \frac{\partial \mathbf{P}}{\partial t} \tag{3.7}$$

therefore,

$$\nabla \times \mathbf{B} = \mu_0 \epsilon_0 \frac{\partial \mathbf{E}}{\partial t} + \mu_0 \mathbf{J} \tag{3.8}$$

Taking the time derivative,

$$\nabla \times \frac{\partial \mathbf{B}}{\partial t} = \mu_0 \epsilon_0 \frac{\partial^2 \mathbf{E}}{\partial t^2} + \mu_0 \frac{\partial \mathbf{J}}{\partial t} \tag{3.9}$$

substituting equation 3.3 for $\frac{\partial \mathbf{B}}{\partial t}$,

$$-\nabla \times \nabla \times \mathbf{E} = \mu_0 \epsilon_0 \frac{\partial^2 \mathbf{E}}{\partial t^2} + \mu_0 \frac{\partial \mathbf{J}}{\partial t} \tag{3.10}$$

finally, the vector identity $\nabla \times \nabla \times \mathbf{E} = \nabla \cdot (\nabla \cdot \mathbf{E}) - \nabla^2 \mathbf{E}$ is used, and in a typical solid there are no free charges, so $\nabla \cdot \mathbf{E} = \rho_\mathrm{f} = 0$

$$\nabla^2 \mathbf{E} = \mu_0 \epsilon_0 \frac{\partial^2 \mathbf{E}}{\partial t^2} + \mu_0 \frac{\partial \mathbf{J}}{\partial t} \tag{3.11}$$

the above is the general wave equation for electromagnetic waves. In a polarizable medium, there is an induced polarization due to the electric field, which, under typical conditions is a linear response,

$$\mathbf{P} = \chi \epsilon_0 \mathbf{E} \tag{3.12}$$

where χ is known as the electrical susceptibility. We give χ as a scalar here, denoting an isotropic medium. However, in an anisotropic medium the value of χ depends on the components of $\mathbf{E}$, and is described as a tensor.

Using the fact that a changing polarization results in a current (equation 3.7),

$$\frac{\partial \mathbf{J}}{\partial t} = \chi \epsilon_0 \frac{\partial^2 \mathbf{E}}{\partial t^2} \tag{3.13}$$

Therefore, the wave equation can be written as

$$\nabla^2 \mathbf{E} = \mu_0 \epsilon_0 (1 + \chi) \frac{\partial^2 \mathbf{E}}{\partial t^2} \tag{3.14}$$

the permittivity of the medium is written as

$$\epsilon = \epsilon_0 (1 + \chi) \tag{3.15}$$

and the index of refraction as

$$n = \sqrt{1 + \chi} \tag{3.16}$$

which then gives

$$\nabla^2 \mathbf{E} = \frac{n^2}{c^2} \frac{\partial^2 \mathbf{E}}{\partial t^2} \tag{3.17}$$

here $c = 1/\sqrt{\mu_0 \epsilon_0}$ is the speed of light.

3.1.2 Spontaneous Raman Scattering

As previously discussed, Maxwell's equations describe how electromagnetic waves, such as light, interact with materials, inducing currents and causing polarization in the material. This polarization gives rise to various scattering processes, including Raman scattering, where the oscillating electric field of light interacts with the vibrational modes of molecules. The scattered light undergoes a frequency shift based on these vibrations, leading to either Stokes or anti-Stokes shifts in the scattered light.

The spontaneous Raman effect involves the spontaneous change in the vibrational energy ΔE_v within the ground electronic state of an electron in a molecule during the scattering of a photon at frequency ω, which causes the photon to change in frequency. If the frequency is greater than the incident light, it is termed anti-Stokes Raman scattering ($\omega + \frac{\Delta E}{\hbar}$), whereas if the frequency is lower, it is termed Stokes Raman scattering ($\omega - \frac{\Delta E}{\hbar}$)[72]. All molecules possess intrinsic vibrations, and depending on selection rules governed by the symmetry of the mode, they can undergo Raman scattering. The difference in the frequency of the light before and after scattering is equal to the

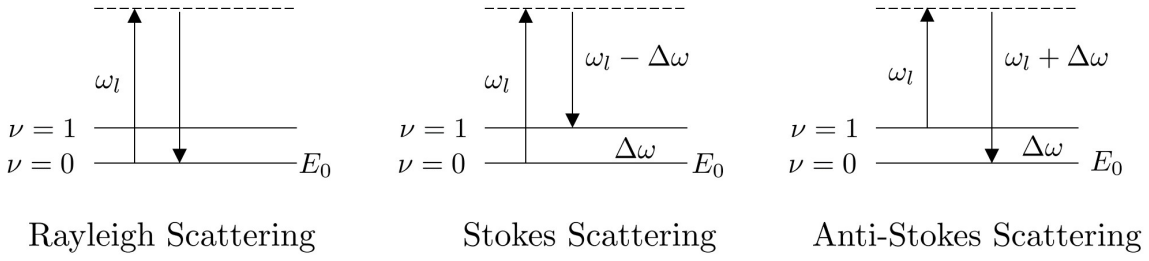

Figure 3.2: Diagram of the Rayleigh scattering, Raman Stokes scattering and Raman Anti-Stokes scattering effects.

difference in frequency between the two energy levels. Stokes shifted light is decreased in frequency and Anti-stokes shifted light is increased in frequency equal to Ω. A Raman spectrum is a histogram that describes the intensity of the light as a function of the frequency shift between the incident and scattered radiation. Since there is a net exchange of energy between the incident light and the molecule, Raman scattering is an inelastic scattering process.

When the incident light is scattered and the frequency remains the same, it is termed Rayleigh scattering. This is also a spontaneous effect as the relaxation of the molecule occurs in the absence of a driving field. A diagram of the two spontaneous Raman effects and the Rayleigh scattering effect is shown in figure 3.2 below. In the diagram, unbroken horizontal lines indicate discrete eigenstates of the molecule, whereas broken horizontal lines indicate virtual quantum states. These light scattering processes are called spontaneous because the matter fluctuations responsible for them are due to thermal or quantum effects that are not correlated with the input photon.

When a photon is absorbed by a molecule, energy is conserved and the photon energy is converted in to the energy required to change the quantum state of the electron. In inelastic scattering however, such as Raman scattering, the photon field loses or gains energy to the molecule. An upward pointing arrow in the below diagram indicates photon annihilation, while a downward arrow indicates photon creation. The change in the quantum state is due to "stimulated transitions" from the vacuum fluctuations which is explained by the quantum nature of radiation[73]. The observed Raman and Rayleigh intensities are directly proportional to the irradiance of the incident light and thus are termed linear scattering. Most molecules at rest and at room temperature are likely to be in the ground state. Therefore the majority of Raman scattering will be Stokes scattering, since

this is involves a net increase of energy in the atom from the ground state. The relative intensities of Stokes to anti-Stokes scattering is dependent on the number of molecules in the ground and excited vibrational levels respectively. These can be determined from the Boltzmann equation,

$$\frac{N_n}{N_m} = \frac{g_n}{g_m}\exp\left[\frac{-(E_n - E_m)}{kT}\right] \tag{3.18}$$

where N_n and N_m are the number of molecules in the excited (n) and ground (m) vibrational levels, g is the degeneracy of each level, $E_n - E_m$ is the difference in energy between each level, k is Boltzmann's constant and T is the temperature.

In any molecule, the total energy consists of translational, vibrational and rotational energy. Translational energy can be described by three orthogonal vectors and so has three degrees of freedom. The same is true for rotational energy. In a linear molecule, such as carbon monoxide however, there are only two rotational degrees of freedom, rotation perpendicular to the molecular axis, since rotation around the molecular bond does not change the mass distribution. Thus all molecules have three translational and three rotational degrees of freedom except for linear molecules which have only two rotational degrees of freedom. N atoms requires $3N$ coordinates to specify their position, however, in the molecule frame where only relative displacement is meaningful, three of the translational coordinates are redundant. There are also two angles needed to specify the rotation of a linear molecule in space, and three for a nonlinear molecule. Thus, the total number of vibrations expected will be $3N-6$ for all non-linear molecules and $3N-5$ for linear molecules. Not all vibrational modes are Raman active, meaning they do not all lead to a change in the molecules polarizability. Only vibrational modes that induce a change in the polarizability of the molecule can be observed through Raman spectroscopy.

As introduced in the section 3.1.1, the incident electromagnetic field interacts with the molecule and induces a polarization. This is a direct consequence of the electric field perturbing the electron, resulting in an induced dipole moment. A classical description of Rayleigh scattering and spontaneous Raman scattering in a diatomic molecule is as follows. We recall that the interaction between the electric field and the molecule leads to the induction of a dipole moment, which results in Rayleigh or Raman scattering. In Rayleigh scattering, the induced polarization leads to an elastic

interaction where the frequency of the scattered light remains unchanged, while in Raman scattering, the polarizability of the molecule changes due to vibrational motion, resulting in inelastic scattering and a shift in frequency.

An incident electric field $E(t)$ induces microscopic dipole moments $\mu(t)$ by perturbing the charge density of the electrons in the medium.

$$\mu(t) = -er(t) \tag{3.19}$$

where e is the electron charge and $r(t)$ is the separation. The macroscopic polarization due to the $\mu(t)$ is given as,

$$\mathbf{P}(t) = N\mu(t) \tag{3.20}$$

where N is the total number of induced moments per unit volume. The electronic polarizability $\alpha(t)$ of a diatomic molecule depends on the intra-molecular distance Q. This distance varies with time as

$$Q(t) = Q_0 \cos(\Omega_R t) \tag{3.21}$$

where Q_0 is the amplitude of the vibration and Ω_R is the vibrational frequency of the transition. A Taylor expansion of α about the initial value gives[74]

$$\alpha(t) = \alpha_0 + \left(\frac{\partial \alpha}{\partial Q}\right)_0 Q(t) \tag{3.22}$$

An incident monochromatic plane wave is given as

$$E(t) = E_0 \cos(\omega t) \tag{3.23}$$

which induces a macroscopic polarization in the molecule that, in the linear regime (low incident field intensity), can be stated as[75],

$$\mathbf{P}(t) = \epsilon_0 \chi^{(1)} E(t) \tag{3.24}$$

where $\chi^{(1)}$ is the linear electric susceptibility tensor, which in an isotropic medium can be represented

as a scalar. While the polarizability describes the molecular response to the electric field at the microscopic level, the electric susceptibility is a macroscopic property that reflects how an entire material responds to an applied electric field by becoming polarized.

The induced dipole moment is related to the electric field by the electronic polarizability,

$$\mu(t) = \alpha(t)E(t) \tag{3.25}$$

Substituting equation 3.25 and equation 3.22 in to equation 3.20,

$$\begin{aligned}\mathbf{P}(t) &= N\left[\alpha_0 + \left(\frac{\partial\alpha}{\partial Q}\right)_0 Q_0\cos(\Omega_R t)\right]E_0\cos(\omega t) \\ &= N\alpha_0 E_0\cos(\omega t) \\ &+ \frac{N(\frac{\partial\alpha}{\partial Q})_0 E_0 Q_0}{2}\cos[(\omega-\Omega)t] \\ &+ \frac{N(\frac{\partial\alpha}{\partial Q})_0 E_0 Q_0}{2}\cos[(\omega+\Omega)t]\end{aligned} \tag{3.26}$$

The term with the elastic component including ω represents Rayleigh scattering, while the $\omega \pm \Omega$ terms represent anti-Stokes and Stokes scattering respectively. The gross selection rule for a Raman transition is the molecule must have an anisotropic polarizability. There must therefore be a change in the shape or orientation of the electronic distribution during the transition for a particular mode to be Raman-active. The intensity of the spontaneous Raman scattering signal is given by[70]

$$I_{\text{Raman}} \propto Kl\alpha^2\omega_0^4 \tag{3.27}$$

where K consists of constants such as the speed of light, l is the incident laser power, α is the molecular polarizability, and ω_0 is the incident laser frequency. The polarizability is calculated using quantum mechanics according to the Kramers-Heisenberg-Dirac (KHD) expression as a sum over all states in the molecule[76]

$$(\alpha_{\rho\sigma})_{if} = \frac{1}{\hbar}\sum_n\left[\frac{\langle i|\mu_\rho|n|i|\mu_\rho|n\rangle\langle n|\mu_\sigma|f|n|\mu_\sigma|f\rangle}{\omega_0+\omega_{nf}+i\Gamma_n} - \frac{\langle i|\mu_\sigma|n|i|\mu_\sigma|n\rangle\langle n|\mu_\rho|f|n|\mu_\rho|f\rangle}{\omega_0-\omega_{ni}-i\Gamma_n}\right] \tag{3.28}$$

where ρ and σ denote the Cartesian components (x, y, z) of the rank two polarizability tensor in

the molecule frame, μ is the dipole operator, i, f and n denote the initial, final and an excited intermediate state, and Γ is the linewidth of a state. Each integral in the numerator, $\langle i|\mu|n|i|\mu|n\rangle$ for example, describes the mixing of state i with the result of operating on state n with μ. A mixture of states describes the distorted electron configuration due to the light-matter complex. The KHD expression gives the total polarizability by summing over all possible intermediate states that the molecule can temporarily occupy during the scattering process. This summation accounts for the fact that the interaction between light and matter is not limited to a single vibrational state but involves the contribution of multiple electronic and vibrational states.

It is helpful to describe the relation between the incident intensity and scattered intensity in the Raman effect. The Raman literature employs the following relation to describe the strength of the Raman scattering of a material[77]

$$dP_{\text{Raman}} = n \cdot d\sigma \cdot I \tag{3.29}$$

where dP_{Raman} is the rate of energy scattered into the Stokes frequency, $d\sigma$ is the differential Raman cross section of the mode and I is the incident intensity of the pump beam. The differential Raman cross section describes the probability that a photon is scattered into a solid angle $d\Omega$ with a specific frequency shift. This probability is proportional to the third power of the scattered frequency and is influenced by the polarizability changes of the molecule during the Raman transition. The units of σ are typically given in cm^2. The cross section and the polarizability are finally related by the equation[76]

$$\frac{d\sigma_{if}}{d\Omega} = \frac{\omega_{\text{S}}^3 \omega_0}{c^4} \left| \hat{e_s} \cdot \alpha_{if} \cdot \hat{e_0} \right| \tag{3.30}$$

where ω_{S} is the frequency of the scattered radiation and $\hat{e_s}$ and $\hat{e_0}$ are unit vectors describing the polarization directions of the scattered and incident radiation respectively. The dot product between these vectors and the polarizability tensor accounts for how the molecular response to the incident light depends on the alignment of the electric field and molecular vibrations.

An important distinction between Raman and Rayleigh scattering is that the latter is in phase with the incident radiation whereas the former depends on the phase of the molecular oscillation

which can be arbitrary. Because Raman scattering involves arbitrary phase shifts due to molecular vibrations, the scattered light is incoherent. This incoherence means that the scattered light from different molecules does not constructively interfere, leading to a much weaker overall intensity compared to Rayleigh scattering, which is phase-coherent.

3.1.3 Resonance Raman Scattering

The field of resonance Raman scattering is concerned with the coupling of vibrational and electronic states of the molecule, so called vibronic states. Vibronic states arise when electronic excitations are coupled with vibrational modes. This simultaneous interaction between the electronic and vibrational states creates resonance conditions that lead to significantly enhanced Raman scattering intensities. In Resonance Raman scattering, the chromophore (the molecular group responsible for absorbing light at specific wavelengths) determines the resonance condition. When the laser wavelength matches the electronic transition of the chromophore, the interaction between the light and the molecule is greatly amplified. In this case, the Raman intensity can be enhanced due to an increase in the transition polarizability α. Typical enhancement factors can be on the order of 10^5-10^6 times that compared to non-resonant Raman scattering[76]. Aside from the intensity increases provided by Resonance Raman, there is also high selectivity in the measurement, since only the chromophore group will be enhanced. In Resonance Raman scattering, fluorescence can sometimes interfere with the Raman signal, as both processes involve the absorption of light. Techniques such as time-gated detection or focusing on the anti-Stokes Raman signal can help mitigate the effects of fluorescence interference. When $\omega_0 \approx \omega_{ni}$, the denominator of the second part of equation 3.28 reduces to $-i\Gamma$, and thus this whole term becomes large. The second part dominates the equation and non-resonant states become relatively weak. Thus, the sum can be dropped in equation 3.28 for resonant conditions. The energy level diagram for resonance Raman scattering is shown in figure 3.3.

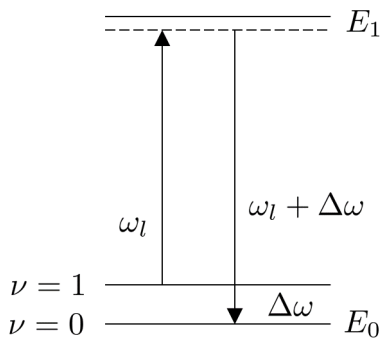

Figure 3.3: Energy diagram of resonance Raman scattering.

3.2 Nonlinear optics

3.2.1 Nonlinear polarization

The light scattering phenomena described until this point are rather weak processes. The cross section per unit volume for Raman scattering is approximately 10^{-6} cm^{-1}, resulting in 1 part per million photons undergoing Raman scattering within 1 cm of a scattering medium. This physical limitation however can be overcome using radiation that has extremely high peak power, such as that from pulsed sources. Nonlinear optical processes may occur in a non-linear optical medium as a result of multiple high-intensity incident fields on a material[50]. Under such illumination, the nonlinear response of matter becomes important as the electrons no longer oscillate harmonically. Nonlinear effects such as four-wave mixing (FWM) and stimulated Raman scattering (SRS) are such examples that will be described. In these coherent scattering events, the emitted radiation has a high directionality and therefore almost all of the generated light can be detected with high efficiency.

When high intensity fields are incident on a sample, equation 3.24 no longer holds since the electrons may be polarized with a nonlinear dependence on **E**. Therefore, a nonlinear polarization is introduced

$$\mathbf{P}_{\mathrm{NL}} = \mathbf{P}^{(2)} + \mathbf{P}^{(3)} + \mathbf{P}^{(4)} ... \tag{3.31}$$

where $\mathbf{P}^{(n)}$ is the n^{th}-order nonlinear polarization term. The total polarization in a material can

therefore be generalized, including the linear ($\mathbf{P}_{\mathrm{L}}$) and nonlinear ($\mathbf{P}_{\mathrm{NL}}$) terms. $\mathbf{P}_{\mathrm{L}}$ controls linear optical responses such as propagation, reflection and refraction, while $\mathbf{P}_{\mathrm{NL}}$ controls multi-wave responses. In a lossless and dispersionless medium the polarization is given as[76]

$$\mathbf{P}(t) = \epsilon_0[\chi^{(1)}\mathbf{E}(t) + \chi^{(2)}\mathbf{E}^2(t) + \chi^{(3)}\mathbf{E}^3(t) + ...] \tag{3.32}$$

$$= \mathbf{P}_{\mathrm{L}} + \mathbf{P}_{\mathrm{NL}}^{(2)} + \mathbf{P}_{\mathrm{NL}}^{(3)} + ... \tag{3.33}$$

The quantities $\chi^{(2)}$, $\chi^{(3)}$ etc. are the second and third-order etc. optical susceptibilities. The second-order susceptibility $\chi^{(2)}$ gives rise to phenomena like second-harmonic generation (SHG), where two photons are combined to produce a photon at twice the frequency of the original light. The third-order susceptibility $\chi^{(3)}$ is responsible for effects like third-harmonic generation and the Kerr effect, where the refractive index of the material depends on the intensity of the light. The above expansion is valid only when it converges i.e. when successive terms monotonically decrease. Due to the fact that the polarization can be induced in a direction different from the electric field, χ^n is an $n+1$ rank tensor.

From Maxwell's equations in matter[73], when the polarization varies in time, there is a polarization current density.

$$\frac{\partial \mathbf{P}}{\partial t} = \mathbf{J}_p \tag{3.34}$$

resulting in a source term for electromagnetic radiation. The polarization current density describes the movement of bound charges in response to a changing electric field. This movement effectively acts as a source for generating electromagnetic waves in nonlinear optical processes The nonlinear polarization is thus central to the description of nonlinear optical effects since a time-dependent polarization may create new sources of radiation within the medium. In order to highlight this effect, we take equation 3.11 and rearrange such that sources are on the right-hand side

$$\nabla^2\mathbf{E} - \mu_0\epsilon_0\frac{\partial^2\mathbf{E}}{\partial t^2} = \mu_0\frac{\partial \mathbf{J}}{\partial t} \tag{3.35}$$

then using equation 3.34 and substituting the speed of light for the vacuum constants

$$\nabla^2\mathbf{E} - \frac{1}{c^2}\frac{\partial^2\mathbf{E}}{\partial t^2} = \frac{1}{\epsilon_0 c^2}\frac{\partial^2\mathbf{P}}{\partial t^2} \tag{3.36}$$

This is the most general form of the wave equation in nonlinear optics, where $\mathbf{P}$ can have terms that depend on $\mathbf{E}$ nonlinearly.

Non-linear optical effects can be categorised into parametric and non-parametric effects. In parametric effects, such as four-wave mixing or second-harmonic generation, the materials quantum state remains unchanged. These processes involve energy and momentum conservation within the optical field. In contrast, non-parametric effects, such as Raman scattering, involve changes in the material's quantum state, often leading to the emission of new frequencies due to inelastic scattering. For example, the second-order susceptibility leads to effects like second-harmonic generation, where two photons are combined to form one photon with twice the frequency. Similarly, third-order processes can result in effects such as the Kerr effect, where the refractive index of the material becomes dependent on the light intensity. Parametric nonlinear effects are often described as instantaneous because the material response to the optical field occurs on a timescale much shorter than the light interaction time. However the response happens on the order of femtoseconds to picoseconds. An important aspect of parametric processes is phase matching, where the phase velocities of the interacting waves must align for the nonlinear process to build up coherently. Without phase matching, the efficiency of processes like second-harmonic generation or four-wave mixing is significantly reduced.

An illustrative example expression for the polarization will be given for second harmonic generation (SHG) as it is the lowest order nonlinearity. If a time-varying field $E(t) = Ee^{-i\omega t} + \text{c.c.}$ is incident on a material for which $\chi^{(2)}$ is non-zero, a second order nonlinear polarization will be produced, in addition to the linear polarization. The nonlinear polarization is given as

$$\mathbf{P}^{(2)}(t) = 2\epsilon_0\chi^{(2)}EE^* + (\epsilon_0\chi^{(2)}E^2e^{-i2\omega t} + \text{c.c.}) \tag{3.37}$$

In the above equation, there are two terms at differing frequencies, one at zero frequency which produces an effect called optical rectification and a term at the frequency 2ω, responsible for radiation at the second harmonic of the input frequencies. In SHG, two photons of frequency ω are destroyed and a photon at frequency 2ω is created in a single process.

3.2.2 The complex susceptibility

χ is in general a complex quantity describing the response of a charge to an electromagnetic field. According to equation 3.32, knowledge of χ allows calculation of the polarization due to incident electric fields on a system. The harmonic approximation is typically used as a starting point to describe the response. The harmonic approximation is used because, for small displacements, the restoring force on the charged particle is proportional to the displacement, following Hooke's law. This allows us to model the system as a simple harmonic oscillator, which provides a good approximation for many physical systems under weak-field conditions. In this approximation, a system is composed of charged harmonic oscillators of mass m and charge q, and its equation of motion is described as follows

$$m\ddot{x} = qE_0e^{-i\omega t} - m\Gamma\dot{x} - m\omega_0^2 x \tag{3.38}$$

where the three terms on the right correspond to the driving force from the electric field, the damping force, which is proportional to the velocity of the charge $\dot{x}$, and the restoring force $F = -Kx$. The natural frequency of the oscillator is given as $\omega_0 = \sqrt{\frac{K}{m}}$, where K is the spring constant. Γ is a term related to the energy lost in the system, usually due to friction or resistance in the material. Physically, it corresponds to how quickly the system returns to equilibrium after being disturbed, and it directly influences the linewidth of the resonance.

The solution to this differential equation is a sinusoid of the form

$$x(t) = x_0e^{-i(\omega t+\delta)} \tag{3.39}$$

where x_0 is the amplitude and δ is the phase difference between the oscillator and driving force.

Substitution of x in to equation 3.38 results in

$$x_0 = \frac{qE_0}{m} \frac{1}{\sqrt{(\omega_0^2 - \omega^2)^2 + \Gamma^2\omega^2}} \tag{3.40}$$

$$\tan(\delta) = -\frac{\Gamma\omega}{\omega_0^2 - \omega^2} \tag{3.41}$$

The polarization P is the dipole moment μ per unit volume

$$P = qx\frac{N}{V} \tag{3.42}$$

where N is the number of oscillators and V is the volume. Substitution of equation 3.39 in to 3.42 leads to

$$P = q\left(\frac{qE_0}{m} \frac{e^{-i(\omega t+\delta)}}{\sqrt{(\omega_0^2 - \omega^2)^2 + \Gamma^2\omega^2}}\right)\frac{N}{V} \tag{3.43}$$

Utilising equation 3.24, the susceptibility can be restated as

$$\chi = \frac{q^2N}{\epsilon_0 mV} \frac{e^{-i\delta}}{\sqrt{(\omega_0^2 - \omega^2)^2 + \Gamma^2\omega^2}} \tag{3.44}$$

or without the trigonometric functions it can be recast as

$$\chi = C\frac{(\omega_0^2 - \omega^2) + i\Gamma\omega}{(\omega_0^2 - \omega^2)^2 + \Gamma^2\omega^2} \tag{3.45}$$

where $C = \frac{q^2N}{\epsilon_0 mV}$. A simplification can be made here by noting the denominator is the magnitude-squared of the numerator. Whence, denoting the numerator as z,

$$\chi = C\frac{z}{|z|^2} = C\frac{z}{zz^*} = C\frac{1}{z^*} \tag{3.46}$$

therefore the susceptibility can be expressed as

$$\chi = \frac{C}{(\omega_0^2 - \omega^2) - i\Gamma\omega} \tag{3.47}$$

One final simplification is made to χ. Close to a resonance, $|\omega - \omega_0| \ll \omega_0$, then we have

$$\chi = \frac{C}{(\omega_0 - \omega)(\omega_0 + \omega) - i\Gamma\omega} \tag{3.48}$$

$$\tag{3.49}$$

$$\approx \left(\frac{C}{2\omega_0}\right) \frac{1}{\omega_0 - \omega - i\Gamma/2} \tag{3.50}$$

which is known as the resonance approximation. The Lorentzian shape of the susceptibility indicates that the material's response is strongest when the driving frequency is close to the material's natural resonance frequency. The full width at half maximum (FWHM) of the Lorentzian curve is related to the damping rate Γ, determining how sharply peaked the resonance is, and how much energy is absorbed. χ can have a real part corresponding to the in-phase component of polarization, and an imaginary part which corresponds to a polarization that is 90°out of phase with the driving field. A complex susceptibility implies a complex wavevector of the electric field, according to equation 3.17. If χ has an imaginary part, then the wavevector includes an imaginary term, resulting in solutions of the form

$$\mathbf{E} = E_0 e^{i(k_{\text{real}}x - \omega t)} e^{(-k_{\text{imag}}x)} \tag{3.51}$$

where the wavevector is

$$k = k_{\text{real}} + ik_{\text{imag}} \tag{3.52}$$

From the above equations, if a wave is propagating in a material with a non-zero imaginary part of the susceptibility, the wave will decay. The real part of the wavevector corresponds to the propagation of the wave, determining its wavelength and phase velocity. The imaginary part causes the amplitude of the wave to decay exponentially as it travels through the material, which corresponds to absorption.

3.2.3 Coherent anti-Stokes Raman scattering

High intensity radiation from two laser pulses at a pump frequency ω_{p} and Stokes frequency ω_{S} can drive molecular oscillations within a medium at the frequency difference $\omega_{\text{p}} - \omega_{\text{S}}$. As a result of the nonlinear polarization of the medium, a coherent beam can be generated at frequency

$\omega_{as} = \omega_p - \omega_S + \omega_{pr}$ where ω_{pr} is the frequency of a third probe pulse[49]. When the frequency difference is equal to a vibrational frequency of the molecule Ω, the anti-Stokes signal is greatly enhanced. This four-wave mixing process is known as Coherent Anti-Stokes Raman Scattering (CARS). CARS has proven to be a useful spectroscopy that permits highly sensitive chemical information to be obtained, as it generates a coherent signal and thus gives much greater signal intensities compared to spontaneous Raman spectroscopy. CARS has on the order of a 10^4 times greater signal intensity compared to spontaneous Raman scattering[78].

For the CARS process to occur, three photons at frequencies ω_p, ω_S and ω_{pr} must all be incident on the molecule within the coherence time of the virtual level. Dispersion of the refractive index also places a phase-matching condition on the three photons in order for appreciable build up of the anti-Stokes signal to occur. One way to satisfy the phase-matching condition is to use co-linear laser beams with a high numerical aperture lens to ensure a multitude of wave-vectors are generated at the focus. Another way to ensure phase-matching is to angle the beams relative to each other, which ensures very small focal volumes, however the phase matching is difficult to optimize[70]. A great advantage of CARS is the fact that it is an anti-Stokes process, which means that the signal is of a higher frequency than the incident beam, resulting in a fluorescence-free measurement. This makes CARS ideal for studying complex media that otherwise would have very congested spontaneous Raman spectra due to fluorescence. There is however a major disadvantage to CARS which is an appreciable background signal that perturbs the chemical information. There are multiple ways of removing this background signal and they will be described in detail in chapter 4.4.2.

The conversion of the three incident photons into the anti-Stokes photon ω_{as} in the medium is a result of the non-linear properties of the material, specifically, the third-order non-linearity which is described by $\chi^{(3)}$. The third-order nonlinear polarization is given as

$$\mathbf{P}^{(3)}(\omega, k) = \chi^{(3)}(\omega, \omega_p, -\omega_S, \omega_{pr}) E_p(\omega_p, k_p) E_S^*(\omega_S, k_S) E_{pr}(\omega_{pr}, k_{pr}) \tag{3.53}$$

where k_p and ω_p represent the wave-vector and frequency of the pump beam, k_s and ω_S represent the wave-vector and frequency of the Stokes beam, k_{pr} and ω_{pr} represent the wave-vector and frequency of the probe beam. The momentum conservation is described in figure 3.4. The dual requirements

of energy and momentum conservation are critical for optimizing the CARS signal and enhancing the techniques effectiveness in spectroscopic applications.

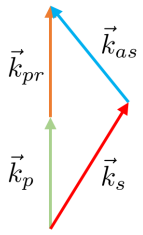

Figure 3.4: Momentum conservation condition in CARS.

The spectrum of ω_{as} contains information on the presence of the molecular vibrational modes, the frequency of which can be found from

$$\Omega = \omega_{as} - \omega_{pr} \tag{3.54}$$

The energy diagram of the CARS process is shown in figure 3.5. Solid lines represent eigenstates of the molecule and dashed lines represent purely virtual states of the light-matter interaction. As seen in the energy-level diagram, the initial and final state is the ground vibrational state. This results in no net energy transfer to the molecule, and the photon field energy is constant.

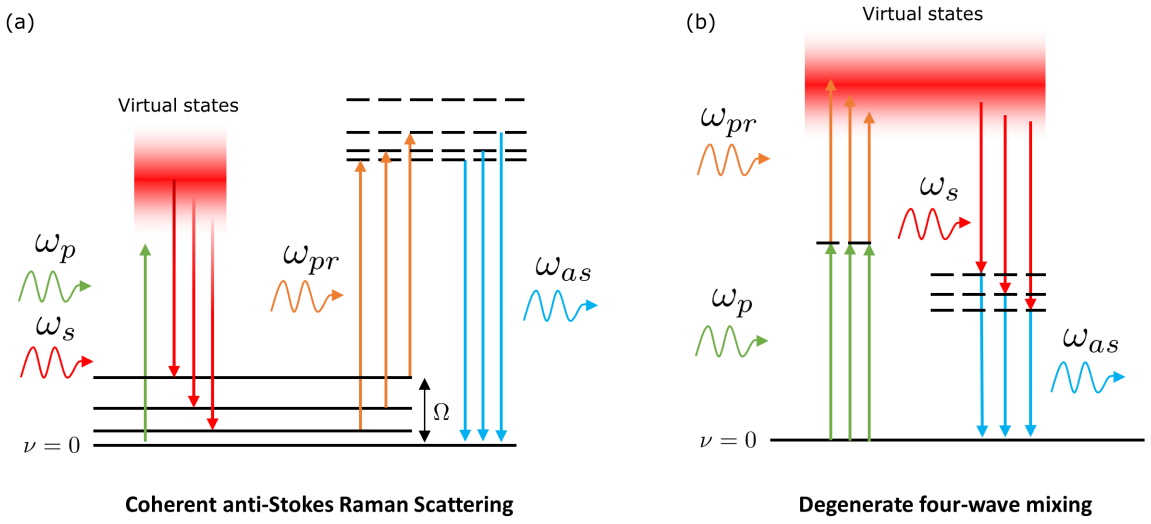

Figure 3.5: (a) Energy diagram of the Coherent Anti-Stokes Raman Scattering effect, (b) energy diagram of the degenerate four-wave mixing effect responsible for the NRB. (Solid horizontal lines denote eigenstates and dashed lines indicate virtual states).

A theoretical description of the CARS signal is as follows[79]. Incident radiation at frequency ω_1 and ω_2 can generate a time-varying force $F(t)$ on a molecular vibrational mode at the difference frequency $\Omega = \omega_1 - \omega_2$,

$$F(t) = \epsilon_0 \left(\frac{\partial \alpha}{\partial Q}\right)_0 \left[A_1 A_2^* e^{-i\Omega t} + \text{c.c.}\right] \tag{3.55}$$

where A_n is the amplitude of field n including the propagation term, $\dfrac{\partial \alpha}{\partial q}$ is the second term in the Taylor expansion of the polarizability from equation 3.22 and c.c. means complex conjugate. This force induces an oscillation of the bond and creates a polarization of the form

$$\mathbf{P}(t) = \epsilon_0 N \left[\alpha_0 + \left(\frac{\partial \alpha}{\partial Q}\right)_0 Q(t)\right] \left[\mathbf{E}_1(t) + \mathbf{E}_2(t)\right] \tag{3.56}$$

$Q(t)$ is again the intra-molecular distance. Terms proportional to a_0 correspond to linear polarization $\mathbf{P}_\text{L}$ and terms proportional to $\dfrac{\partial \alpha}{\partial Q}$ correspond to nonlinear polarization $\mathbf{P}_\text{NL}$. Expanding the brackets,

$$\mathbf{P}(t) = \underbrace{\epsilon_0 N \alpha_0 \mathbf{E}_1(t) + \epsilon_0 N \alpha_0 \mathbf{E}_2(t)}_{\mathbf{P}_\text{L}} + \underbrace{\epsilon_0 N \left(\frac{\partial \alpha}{\partial Q}\right)_0 Q(t)\mathbf{E}_1(t) + \epsilon_0 N \left(\frac{\partial \alpha}{\partial Q}\right)_0 Q(t)\mathbf{E}_2(t)}_{\mathbf{P}_\text{NL}} \tag{3.57}$$

Substituting plane wave expressions for $\mathbf{E}(t) = Ae^{-i(\omega t)} + \text{c.c.}$ and $Q(t) = Q_0(\omega)e^{-i(\Omega t)} + \text{c.c.}$,

$$\begin{aligned}\mathbf{P}_\text{NL}(t) = \epsilon_0 N \left(\frac{\partial \alpha}{\partial Q}\right)_0 \big[&Q_0(\omega) A_1 e^{-i(\omega_1+\Omega)t} + Q_0(\omega) A_2 e^{-i(\omega_2+\Omega)t} + \\ &Q_0(\omega)^* A_1 e^{-i(\omega_1-\Omega)t} + Q_0(\omega)^* A_2 e^{-i(\omega_2-\Omega)t} + \text{c.c.}\big]\end{aligned} \tag{3.58}$$

there is thus four terms that contribute to the nonlinear polarization. The first term oscillates at $\omega_1 + (\omega_1 - \omega_2) = 2\omega_1 - \omega_2$ and is known as the anti-Stokes component, corresponding to coherent anti-Stokes Raman scattering (CARS). The term oscillating at $\omega_2 - (\omega_1 - \omega_2) = 2\omega_2 - \omega_1$ is known as the Stokes component, corresponding to coherent Stokes Raman scattering (CSRS). The other two terms in equation 3.58 oscillate at the input frequencies ω_1 and ω_2 and do not correspond to a shift in energy of the light. These latter two terms correspond to nonlinear processes known as stimulated Raman loss (SRL) and stimulated Raman gain (SRG) respectively. All four nonlinear

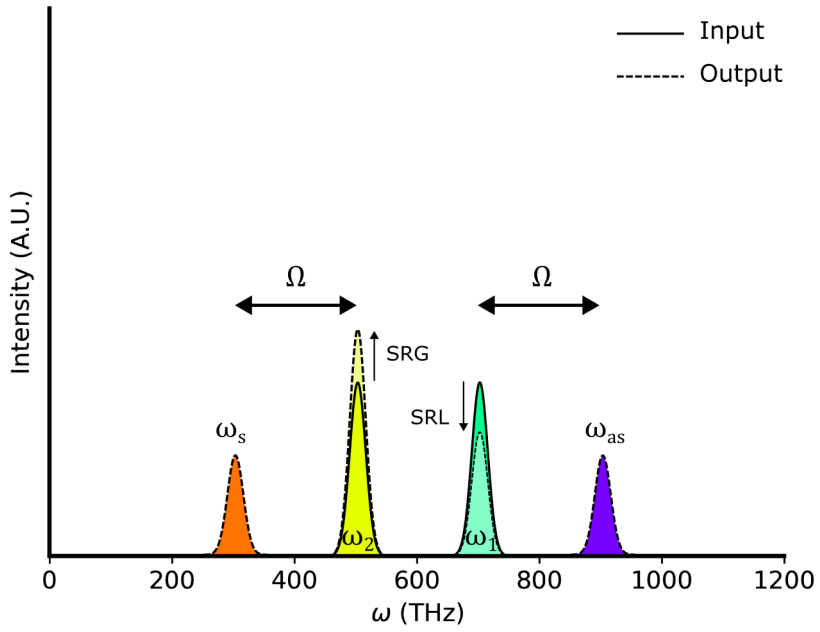

Figure 3.6: Frequency components generated due to the Third-order nonlinear susceptibility.

polarization components are shown in figure 3.6. The amplitude of the vibration as a function of frequency $Q(\omega)$ is given by

$$Q(\omega) = \frac{(\epsilon_0/m)(\partial\alpha/\partial q)_0 A_1 A_2^*}{\omega_0^2 - \Omega - i\Omega\Gamma} \tag{3.59}$$

The polarization at the anti-Stokes frequency is given as

$$P(\omega_{\text{as}}) = \frac{N\epsilon_0^2}{m}\left(\frac{\partial\alpha}{\partial Q}\right)_0 \frac{1}{\omega_0^2 - \Omega^2 - i\Omega\Gamma} A_1^2 A_2^* \tag{3.60}$$

we now define the third-order nonlinear susceptibility as

$$\chi^{(3)}(\omega_{\text{as}}) = \frac{(N\epsilon_0/3m)(\partial\alpha/\partial Q)_0^2}{\omega_0 - (\omega_1 - \omega_{\text{as}})^2 - i(\omega_1 - \omega_{\text{as}})\Gamma} \tag{3.61}$$

The intensity of radiation is given as the magnitude-squared of the polarization, thus using equation 3.60, the intensity of the CARS field can be expressed as

$$I_{\text{as}} \propto \left|\chi^{(3)}\right|^2 I_1^2 I_2 \tag{3.62}$$

where $I_n = |E_n|^2$ is the intensity of field n.

From here on we denote E_1 and E_2 as the pump and Stokes fields respectively, with amplitudes A_{p} and A_{S}. The spatial evolution of the anti-Stokes wave in an isotropic medium as a function of position z is given by[80]

$$\frac{\partial A_{\mathrm{as}}(z)}{\partial z} = \frac{i3\omega_{\mathrm{as}}}{2nc}\chi^{(3)}(\omega_{as})^{(3)}A_{\mathrm{p}}^2 A_{\mathrm{S}}^* e^{i\Delta kz} \tag{3.63}$$

where A_{as} is the anti-Stokes amplitude and the wavevector mismatch Δk is defined as

$$\Delta k = (2k_{\mathrm{p}} - k_{\mathrm{S}} - k_{as}) \cdot \hat{z} \tag{3.64}$$

The Anti-Stokes field at $z = l$ is thus given by,

$$A_{as}(L) = \int_0^L \frac{\partial A_{\mathrm{as}}}{\partial z} = \frac{i3\omega_{\mathrm{as}}}{2nc}\chi(\omega_{\mathrm{as}})L \cdot \mathrm{sinc}\left(\frac{\Delta kl}{2}\right)e^{i\frac{\Delta kL}{2}}A_{\mathrm{p}}^2 A_{\mathrm{S}}^* \tag{3.65}$$

The anti-Stokes intensity is thus,

$$I_{\mathrm{as}}(L) \propto |\chi(\omega_{\mathrm{as}})|^2 L^2 \mathrm{sinc}^2\left(\frac{\Delta kL}{2}\right) I_{\mathrm{p}}^2 I_{\mathrm{S}} \tag{3.66}$$

there is a restriction that effectively $\Delta kL \ll 2\pi$ must be true for I_{as} to be non-zero. Figure 3.7 (a) shows the intensity from the anti-Stokes field as a function of the wavevector mismatch. The sinc function results in nodes where the intensity vanishes at integer values of $\frac{\Delta kL}{2\pi}$, where L is the interaction length. Figure 3.7 (b) shows the effect of the coherence length, defined as

$$L_c = \frac{\pi}{\Delta k} \tag{3.67}$$

when $L = L_c$, the intensity is maximized. The total anti-Stokes field generated within the medium is the coherent summation of the fields along the direction of incidence. Therefore, at every point along the z direction, this field must be in phase with the induced polarization.

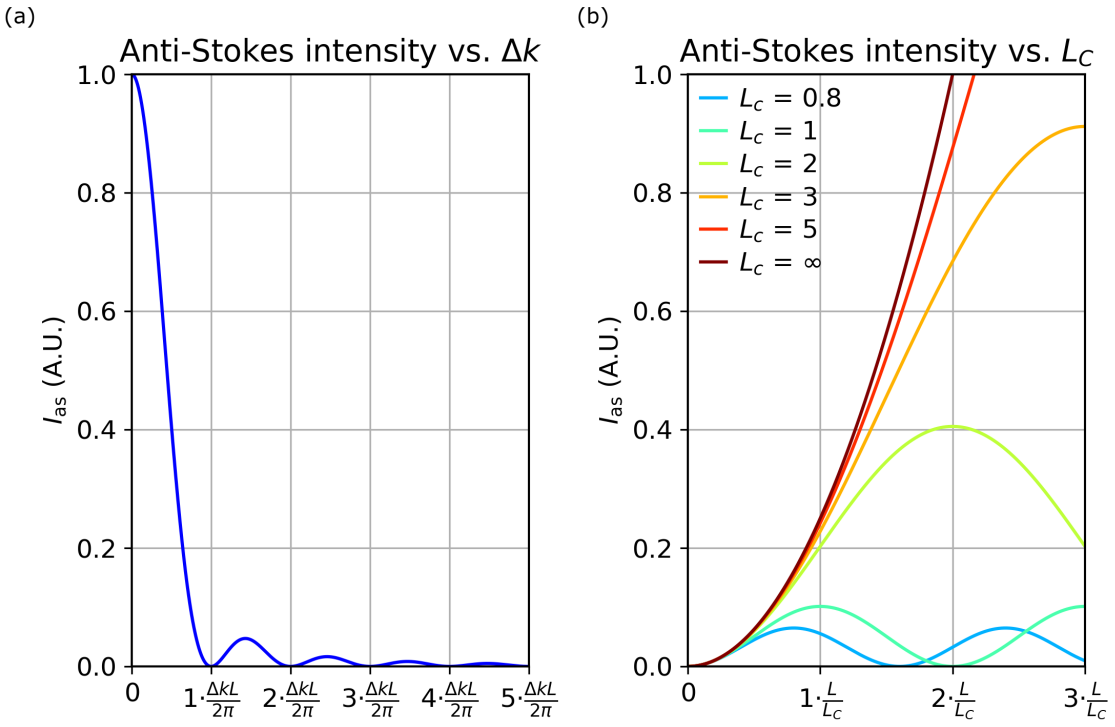

Figure 3.7: (a) Intensity of the anti-Stokes field vs. the wavevector mismatch for constant interaction length L. (b) Curve of anti-Stokes intensity versus L for various coherence lengths L_c.

The third-order susceptibility can be separated in to two parts,

$$\chi^{(3)} = \chi_{\mathrm{R}}^{(3)} + \chi_{\mathrm{NR}}^{(3)} \tag{3.68}$$

where $\chi_{\mathrm{R}}^{(3)}$ is the resonant part and $\chi_{\mathrm{NR}}^{(3)}$ is the non-resonant part that is due to virtual transitions. In general, the non-resonant term is frequency independent[50] and a real number[81]. From here, the superscript denoting the third-order of the nonlinear susceptibility will be dropped for brevity. The CARS signal depends upon $|\chi|^2$

$$I_{\mathrm{as}} \propto |\chi|^2 = |\chi_{\mathrm{R}} + \chi_{\mathrm{NR}}|^2 \tag{3.69}$$

the resonant part is a complex quantity, where the real part represents the normal refractive index and the imaginary part represents the absorption. Restating the above equation using the fact that

the squared norm is the product of the conjugate pair,

$$|\chi|^2 = \chi\bar{\chi} = (\chi_{\mathrm{R}} + \chi_{\mathrm{NR}})(\bar{\chi_{\mathrm{R}}} + \bar{\chi_{\mathrm{NR}}}) \tag{3.70}$$

$$|\chi|^2 = |\chi_{\mathrm{R}}|^2 + \chi_{\mathrm{R}}\bar{\chi_{\mathrm{NR}}} + \chi_{\mathrm{NR}}\bar{\chi_{\mathrm{R}}} + |\chi_{\mathrm{NR}}|^2 \tag{3.71}$$

since the non-resonant component of the susceptibility is purely real,

$$|\chi|^2 = |\chi_{\mathrm{R}}|^2 + |\chi_{\mathrm{NR}}|^2 + \chi_{\mathrm{NR}}(\chi_{\mathrm{R}} + \bar{\chi_{\mathrm{R}}}) \tag{3.72}$$

This can be simplified as

$$|\chi|^2 = |\chi_{\mathrm{R}}|^2 + |\chi_{\mathrm{NR}}|^2 + 2\chi_{\mathrm{NR}}\,\mathrm{Re}[\chi_{\mathrm{R}}] \tag{3.73}$$

The susceptibility for a single resonance with $\chi^{(3)}_{\mathrm{NR}} = 0$ is shown in figure 3.8. It can be seen that $\mathrm{Im}\left(\chi^{(3)}\right)$ and $\left|\chi^{(3)}\right|^2$ exhibit a Lorentzian lineshape, while $\mathrm{Re}\left(\chi\right)$ exhibits a dispersive lineshape with vanishing value at resonance. The magnitude-squared value, obtained from equation 3.69 has a maximum at resonance, and from equation 3.61 is proportional to the square of the number of oscillators (molecules) at ω.

In figure 3.9, the same resonance is plotted as in figure 3.8, but now including a nonzero value of χ_{NR}. Since $\chi^{(3)}_{\mathrm{NR}}$ is assumed purely real and constant, $\mathrm{Re}(\chi^{(3)})$ may become nonzero everywhere, depending on the value of $\chi^{(3)}_{\mathrm{NR}}$. Through the cross-term in equation 3.73, the dispersive lineshape of the real part of $\chi^{(3)}$ is imprinted on the intensity, leading to dispersive measured lineshapes. This has major implications for spectroscopy since the maximum of the intensity no longer coincides with the resonance frequency. The cross-term also introduces a polynomial dependence on molecular density

$$I_{\mathrm{as}} \propto \left|\chi^{(3)}\right|^2 \propto N^2 + N\chi^{(3)}_{\mathrm{NR}} + \left(\chi^{(3)}_{\mathrm{NR}}\right)^2 \tag{3.74}$$

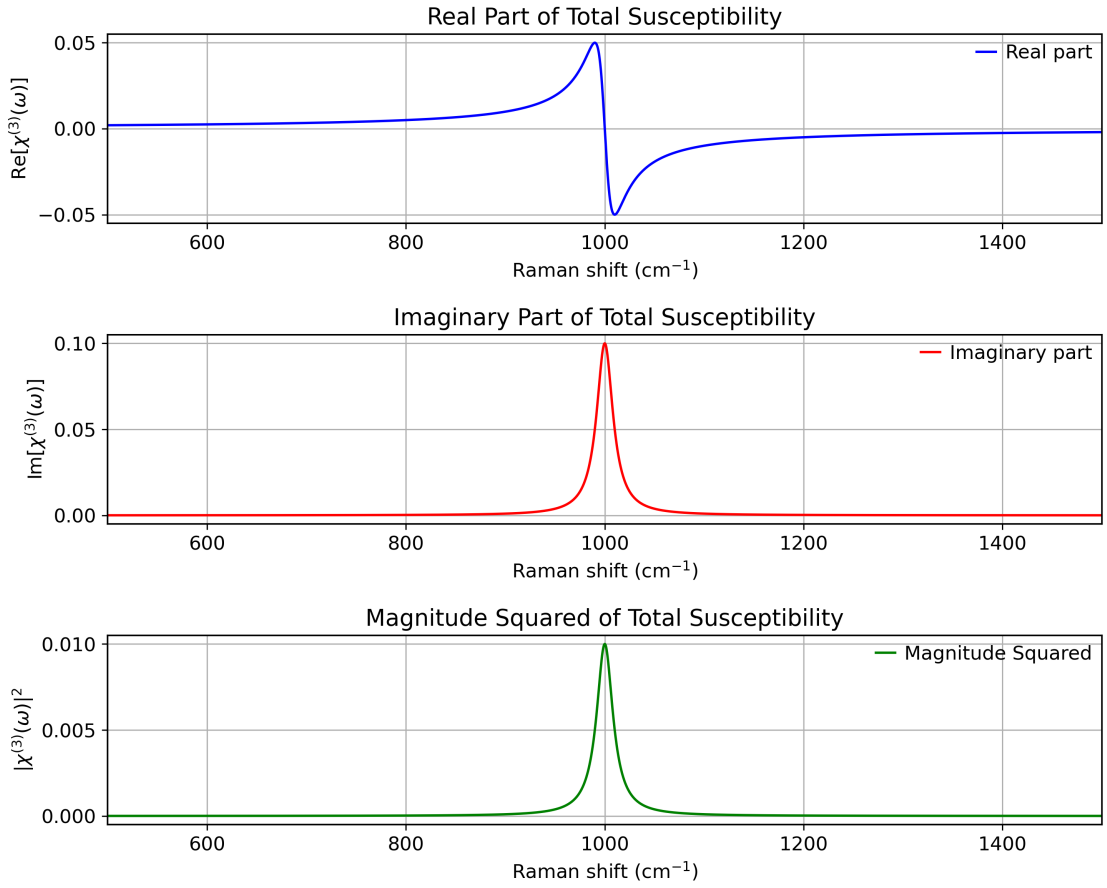

Figure 3.8: Diagram of the real part, imaginary part and magnitude-squared of the Raman susceptibility for a single resonance at $\Omega = 1000$ cm^{-1}, $\Gamma = 10$ cm^{-1}, $A = 1$, $\chi_{\text{NR}} = 0$.

3.2.4 Stimulated Raman Scattering

The stimulated Raman scattering (SRS) effect involves the driving of a molecular vibration into resonance by two fields, and subsequent Raman scattering. It is thus very similar to CARS. The main difference between SRS and CARS is that the induced nonlinear polarization $\mathbf{P}_{\text{NL}}$ occurs at the same frequency as one of the input fields. This polarization interferes with the two input fields and causes a reduction in the pump field intensity known as stimulated Raman loss (SRL) and an increase in the Stokes field intensity called stimulated Raman gain (SRG). The energy diagram for SRS is shown below. In SRS the detected field is proportional to the imaginary part of the third-order molecular susceptibility[79].

$$S(\Omega) \propto \pm 2\text{Im}[\chi^{(3)}(\omega)] \tag{3.75}$$

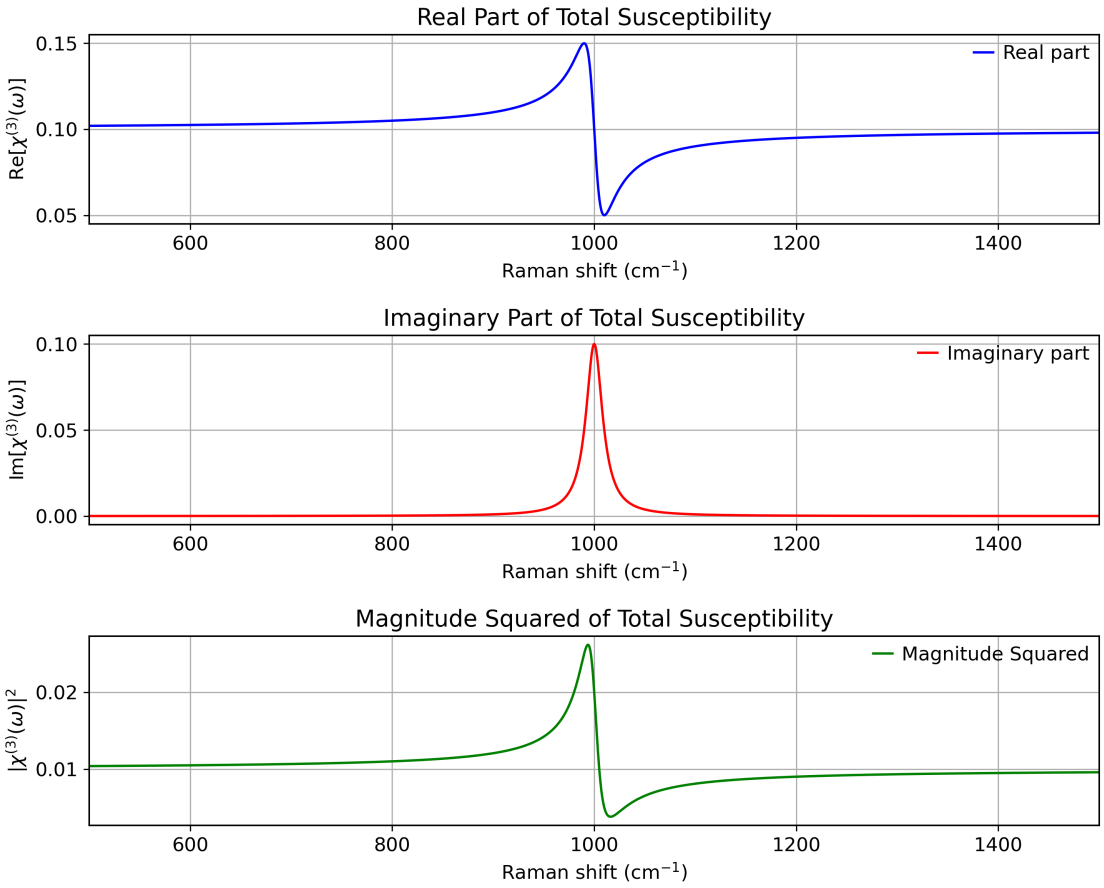

Figure 3.9: Diagram of the real part, imaginary part and magnitude-squared of the Raman susceptibility for a single resonance at $\Omega = 1000$ cm^{-1}, $\Gamma = 10$ cm^{-1}, $A = 1$, $\chi_{\text{NR}} = 0.1$.

SRS being a nonlinear technique is advantageous over spontaneous Raman scattering for spectroscopy mainly because the effect is multiple orders of magnitude greater in intensity, as is also true for CARS. It however does not have a non-resonant background since it is a non-parametric effect. This is a great advantage over CARS, as the intensity measurement is not spectrally distorted. There are several advantages of BCARS over SRS however, the main being that simultaneous acquisition of the whole vibrational spectrum is only possible with BCARS. This is because SRS requires lock-in detection to detect the signal. Thus, broadband spectroscopy where very low dwell times are necessary is more suited to BCARS.

The main differences between BCARS and SRS are described below in table 3.1.

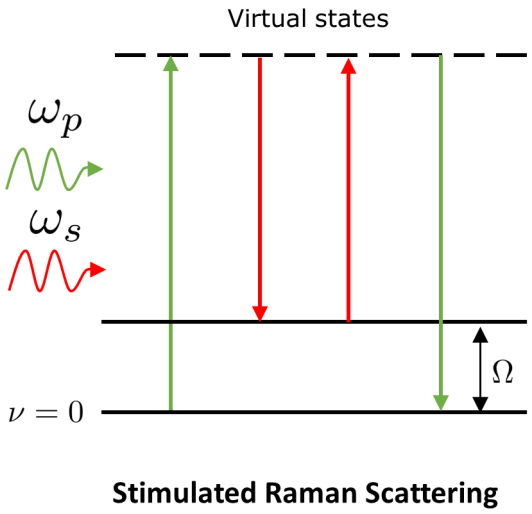

Figure 3.10: Energy diagram of stimulated Raman scattering (SRS).

Feature	BCARS	SRS
Measurement	anti-Stokes emission	Stimulated loss/gain
Spectral Range	Broadband	Narrowband
Background Interference	Non-resonant background	None
Concentration scaling	Variable	Linear

Table 3.1: Comparison of BCARS and SRS techniques.

3.3 Dispersion

Since nonlinear spectroscopy requires high-intensity electric fields, its application requires the use of ultrashort pulses and therefore necessitates a careful consideration of dispersion of the optical media used. This is because the efficient propagation of ultrafast pulses is highly dependent on dispersion. In this section, the main elements of dispersion are described.

Any linear optical element (LOE) such as a mirror, prism or grating transforms an incident field spectrum $E_{in}(\omega)$ as follows[82]

$$E(\omega) = H(\omega)E_{in}(\omega) \tag{3.76}$$

where the complex optical transfer function $H(\Omega)$ is given by

$$H(\omega) = R(\omega)e^{-i\varphi(\omega)} \tag{3.77}$$

$R(\omega)$ is a real amplitude response (Modulation transfer function) that essentially acts as a frequency filter and $\varphi(\Omega)$ is a spectral phase response (Phase transfer function) which acts as a spectral phase delay on the incoming field. The output field in the time-domain is thus given by the Fourier transform

$$E(t) = \mathscr{F}^{-1}[H(\omega)E_{in}(\omega)] = \frac{1}{2\pi}R\int_{-\infty}^{+\infty} E_{in}(\omega)e^{-i\varphi(\omega)}e^{i\omega t}d\omega \tag{3.78}$$

where $R(\omega)$ is typically assumed to be constant over the spectrum and thus the phase transfer function is typically of most interest. A Taylor expansion of $\varphi(\omega)$ about the signal carrier frequency ω_l yields

$$\varphi(\omega) = \sum_{n=0}^{\infty} b_n(\omega - \omega_l)^n \tag{3.79}$$

where b_n are the series coefficients given by

$$b_n = \frac{1}{n!}\frac{d^n\varphi}{d\omega^n}\bigg|_{\omega_l} \tag{3.80}$$

The output field can thus be stated as

$$E(t) = \frac{1}{2\pi}Re^{-ib_0}e^{i\omega_l t}\int_{-\infty}^{+\infty} E_{in}(\omega) \times \exp\Big(-i\sum_{n=2}^{+\infty} b_n(\omega-\omega_l)^n\Big)e^{i(\omega-\omega_l)(t-b_1)}d\omega \tag{3.81}$$

b_0 is a constant phase delay and so doesn't affect the spectral envelope. b_1 is equal to

$$b_1 = \frac{d\varphi}{d\Omega}\bigg|_{\omega_l} = z\frac{dk}{d\omega}\bigg|_{\omega_l} = \frac{z}{\nu_g} \tag{3.82}$$

which is simply a constant group delay τ_g which also does not change the envelope of the pulse. Therefore only the $n > 1$ Taylor coefficients transform the input field spectrally. The b_2 term is equivalent to the group velocity dispersion (GVD).

$$b_2 = \frac{1}{2}\frac{d^2\varphi}{d\Omega^2}\bigg|_{\omega_l} = z \cdot \text{GVD} \tag{3.83}$$

If the input field is described as a modulus and phase $E_{in}(\omega) = |E_{in}(\omega)|e^{i\Phi_{in}(\omega)}$, the output spectral

phase from an LOE for a given input can be stated using 1.2 as

$$\Phi(\omega) = \Phi_{in}(\omega) - \sum_{n=0}^{+\infty} b_n(\omega - \omega_l)^n \tag{3.84}$$

and if one is only concerned with the envelope of the phase changing i.e. observing in reference frame with $v = \left(\frac{dk}{d\omega}\right)^{-1}$, then the lower bound of summation becomes $n = 2$.

A series of LOEs is represented by the total optical transfer function

$$H(\omega) = \prod_{j=1}^{m} H_j(\omega) = \left(\prod_{j=1}^{m} R_j(\omega)\right) \cdot \exp\left[-i \sum_{j=1}^{m} \varphi_j(\omega)\right] \tag{3.85}$$

Subsequently, by a suitable choice of elements, one can reach a zero-phase response so that the action of several LOEs manifests only in terms of the amplitude response. In particular, the quadratic phase response of an element (e.g., dispersive glass path) leading to pulse broadening can be compensated with an element having an equal phase response of opposite sign (e.g. a prism pair) which automatically would recompress the pulse to its original duration. It should also be noted that mirrors can introduce GVD in to fs optical pulses (Chirped mirrors).

3.3.1 Group velocity dispersion in prisms

A prism tilts a pulse-front such that

$$\Delta\Phi = \varphi = 2\pi \frac{P_l}{\lambda} \tag{3.86}$$

Where P_l is the frequency dependent optical path length. The phase transfer function for an angular dispersive element (such as a prism) can thus be defined as follows

$$\varphi(\omega) = \frac{\omega}{c} P_l(\omega) \tag{3.87}$$

From equation 3.87 it can be deduced that,

$$\frac{d^2\varphi(\omega)}{d\omega^2} = \frac{1}{c}\left(2\frac{dP_l(\omega)}{d\omega} + \omega\frac{d^2P_l(\omega)}{d\omega^2}\right) \tag{3.88}$$

Using the chain-rule for differentiation it is known that

$$\frac{d}{d\omega} = -\frac{\lambda^2}{2\pi c}\frac{d}{d\lambda} \tag{3.89}$$

$$\frac{d^2}{d\omega^2} = \frac{\lambda^2}{(2\pi c)^2}\left(\lambda^2\frac{d^2}{d\lambda^2} + 2\lambda\frac{d}{d\lambda}\right) \tag{3.90}$$

therefore,

$$\frac{d^2\varphi}{d\omega^2} = \frac{\lambda^2}{(2\pi c)^2}\left(\lambda^2\frac{d^2\varphi}{d\lambda^2} + 2\lambda\frac{d\varphi}{d\lambda}\right) \tag{3.91}$$

In order to obtain the group delay dispersion (GDD), we consider only terms $d^n/d\lambda^n$ of order $n = 2$, resulting in the following definition

$$\text{GDD} = \frac{\lambda^3}{2\pi c^2}\frac{d^2P_l(\omega)}{d\lambda^2} \tag{3.92}$$

The sign convention typically used is that positive GDD corresponds to $\frac{d^2\varphi}{d\Omega^2} > 0$.

3.3.2 GVD control using prism pairs

A common setup for GVD control using two identical equilateral prisms is shown in figure 3.11. The phase change from the pair is a combination of the phase change from the path through the glass L_g of refractive index n (both prisms) and the path through air between the prisms from B to C and after the second prism D to E.

$$\varphi = \frac{\omega}{c}\left(nL_g + \overline{BC} + \overline{DE}\right) \tag{3.93}$$

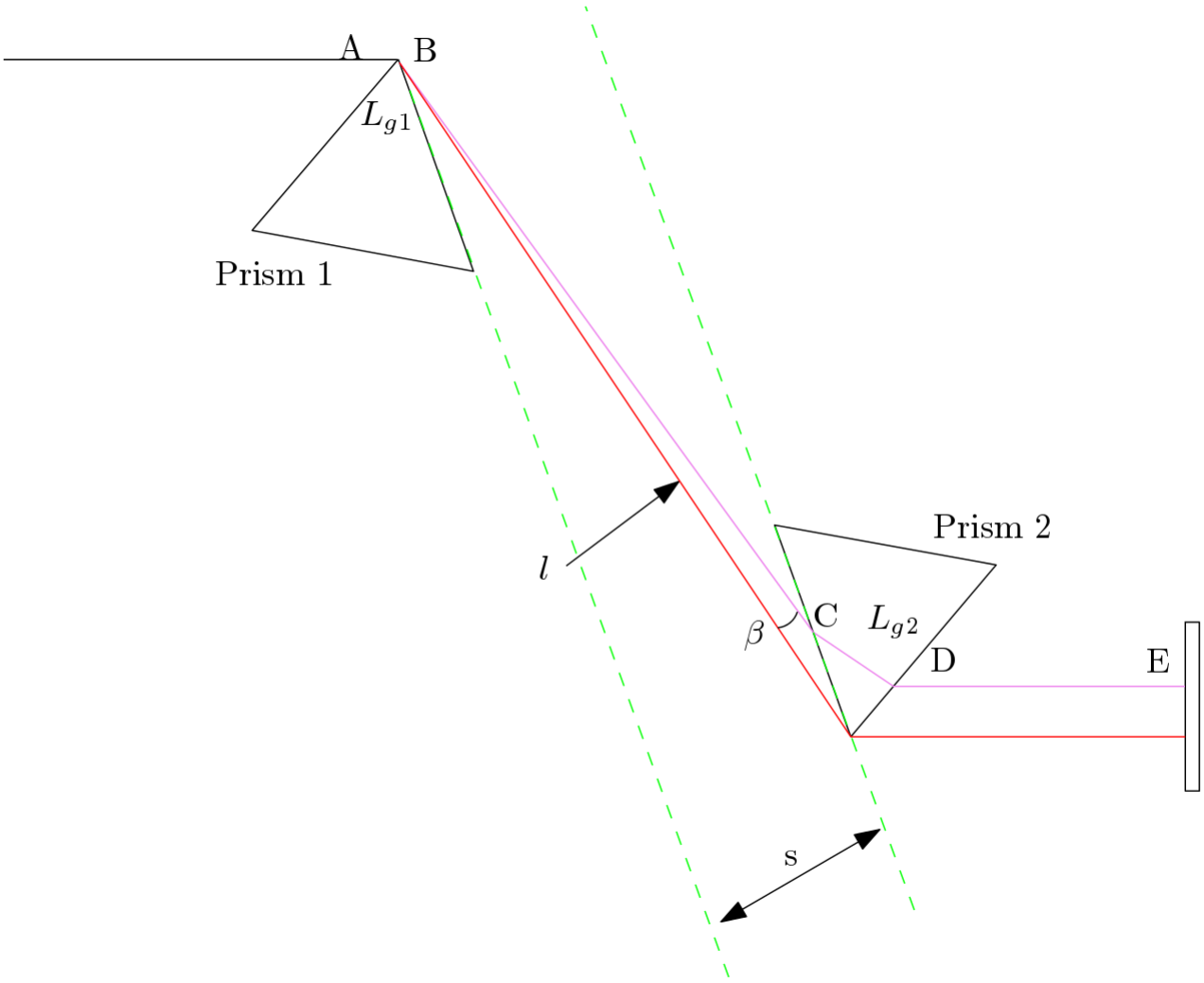

Figure 3.11: Sketch of the prism pair pulse compressor. Bold letters denote points of the rays. l is the distance between the two prism apices and s is the face to face distance between the prisms.

Where the term in brackets is dependent on wavelength. The second derivative of the phase leads to

$$\left.\frac{d^2\varphi}{d\omega^2}\right|_{\omega_l} = \frac{L_g}{c}\left[2\left.\frac{dn}{d\omega}\right|_{\omega_l} + \omega_l \left.\frac{d^2n}{d\Omega^2}\right|_{\omega_l}\right] - \frac{\omega_l}{c}\left(\frac{s}{cos\beta}\right)\left(\left.\frac{d\beta}{d\omega}\right|_{\omega_l}\right)^2 - \frac{n\omega_l}{c}L_g\left(\left.\frac{d\theta}{d\omega}\right|_{\omega_l}\right)^2 \tag{3.94}$$

Where θ and β are the entrance refraction angle of prism 1 and prism 2 respectively. For a symmetric beam path through the prisms and at Brewster angle incidence the equation becomes

$$\left.\frac{d^2\varphi}{d\omega^2}\right|_{\omega_l} = \frac{L_g}{c}\left[2\left.\frac{dn}{d\omega}\right|_{\omega_l} + \omega_l \left.\frac{d^2n}{d\omega^2}\right|_{\omega_l}\right] - \frac{\omega}{c}\left(4L + \frac{L_g}{n^3}\right)\left(\left.\frac{dn}{d\omega}\right|_{\omega_l}\right)^2 \tag{3.95}$$

The equation can be further modified as demonstrated by Fork *et al.*[83]

$$\left.\frac{d^2\varphi}{d\Omega^2}\right|_{\omega_l} = \frac{\lambda^3}{2\pi c^2}\left[4l\left\{\left[\frac{d^2n}{d\lambda^2}+\left(2n-\frac{1}{n^3}\right)\left(\frac{dn}{d\lambda}\right)^2\right]sin\beta-2\left(\frac{dn}{d\lambda}\right)^2 cos\beta\right\}+4\left(\frac{d^2n}{d\lambda^2}\right)\left(2D_{1/e^2}\right)\right] \tag{3.96}$$

where D_{1/e^2} is the beam diameter at 1/e^2 intensity. In a prism compressor, each ray of a plane-wave beam experiences identical optical paths[84]. As shown in figure 3.11, prism 1 disperses the beam and prism 2 collimates the beam so each outgoing ray is parallel again. Mirror (E) is typically used to redirect the beam back through the two prisms so that the output beam is spatially identical to the input. A beam-splitter or pick-off mirror at plane A can then redirect the output beam.

3.4 Ultrafast pulse characterisation

Ultrashort optical pulses that are generated using mode-locking require specialised methods to characterise them fully because modern optical detectors are not responsive to their extremely short durations. Ultrashort is commonly understood to mean pulses with a duration of the order of femtoseconds. As these pulses are electromagnetic wave packets, they are fully described by the electric field in space and time. In the area of laser spectroscopy, the space-dependent electric field is often not determined, because most often either the temporal nature of the field is enough to investigate the process, or the spatial dependence can be approximated by predictable functions. In using optical pulse diagnostic methods, careful consideration must be given to the possibility of its influence on the pulses intensity or phase and so knowledge of the exact optical transfer function is a great advantage because applying the inverse of this function to the output of any diagnostic result would yield the form of the pulse prior to passing through the measurement device. A full characterisation of a transform-limited pulse would be knowledge of its duration and electric field intensity spectrum in time. For transform-limited pulses, knowledge of the spectral phase or temporal phase is not required because the phase is constant. If a pulse was known to be monochromatic and predictable in its temporal shape, it could even be characterised solely based on its duration. A more useful characterisation for general complex pulses would be the time-frequency spectrum i.e. the electric field amplitude and phase as a function of both frequency

and time. Although frequency and time functions can be converted for intensity, there exists trivial ambiguities for phase when using the Fourier transform. Such ambiguities are the absolute phase shift, translation shift and time-reversal[85]. There has been many published methods to determine the time-frequency spectrum (spectrogram) or temporal intensity of ultrafast optical pulses and these will be discussed in this section. The methods vary in their complexity and level of information they provide about the pulse in question. A full review of ultrafast optical pulse characterisation techniques has already been published[86], however the main methods will be discussed briefly, with a focus on the primary method used in this work. There are three distinct types of characterisation method; simple, referenced complete, and self-referenced complete. The simple method typically allows one to determine the amplitude envelope of the pulse but not the electric field $E(t)$. Either of the two referenced methods use either a known or unknown reference pulse for electric field reconstruction. Self-referenced methods use the unknown pulse itself as a reference.

The full description of an ultrashort pulse is given by E(x, y, z, t) where the spatial dependence is almost always neglected. Practically, the electric field can be retrieved in either the time or frequency domain, where the trivial ambiguities of the Fourier transform are avoided. Time-ambiguity can be solved using intensity autocorrelation, which reveals a pulses intensity envelope over time. The translation shift and absolute phase shift ambiguities are not important in pulse characterization, because a they do not represent any information within the pulse itself, and they can be neglected in measurements.

The goal of pulse characterization is to determine $E(t)$. The four dimensional function of space and time is typically simplified to a function of only time, where the spatial dependence is ignored. In practical terms, the electric field of a pulse is almost always given in the following form of a complex amplitude,

$$E(t) = \sqrt{I(t)}\exp[-i\phi(t)] \tag{3.97}$$

where $I(t)$ is the temporal intensity and ϕ is the temporal phase. The complex conjugate term of this expression is required for completeness but is often omitted for simplicity. The pulse can also

be described by the electric field in the frequency domain $\tilde{E}(\omega)$, through the Fourier transform as,

$$\tilde{E}(\omega) = \sqrt{S(\omega)}\exp[-i\varphi(\omega)] \tag{3.98}$$

3.4.1 Intensity autocorrelation

Intensity autocorrelation is a simple method for determining the duration of a pulse only. The principal idea is that a test pulse is split in to two beams and then they are spatially overlapped in a nonlinear optical medium. The two input beams can be removed from the output signal using optical filters or a dispersive element such as a grating or prism, leaving only the signal generated from the nonlinear optical process, which is typically second-harmonic generation (SHG) or sum-frequency generation (SFG). The intensity of this generated light is recorded using a slowly responding detector as a function of the relative delay between the two pulses. This is usually achieved using a simple delay line. Since the non-linear medium emits light only when the two pulses are overlapping in space, the intensity as a function of delay allows a measurement of the pulse duration to be determined[87]. The pulse duration of the non-linear signal however is not exactly the duration of the test pulse, but is slightly longer due to the interaction. The measured intensity from the non-linear medium in a three-photon process such as SHG is given by

$$A(\tau) = \int_{-\infty}^{\infty} I(t)I(t-\tau)dt \tag{3.99}$$

A diagram of the intensity autocorrelator is shown in figure 3.12.

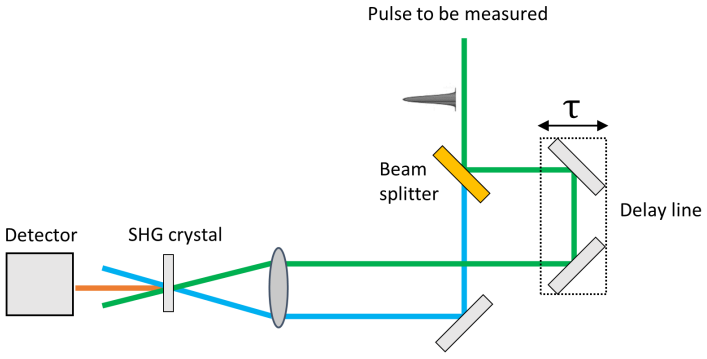

Figure 3.12: Diagram of an intensity autocorrelator.

3.4.2 Spectral interferometry

Spectral interferometry allows the full electric field of a pulse to be determined so long as another reference pulse is fully defined. The process involves first recording the spectrum of the test pulse to be characterised. This step fully determines the spectral amplitude $A(\omega)$. Then both pulses are combined and the resulting spectrum recorded. Superposition of the two fields will create visible fringes in the spectrum. These fringes are a measure of the coherence and can essentially be demodulated in to the unknown phase since the 'modulating' reference beam is fully known. The spectral phase $\varphi(\omega)$ can therefore also be fully determined non-iteratively.

3.4.3 Frequency-Resolved Optical Gating

Frequency-Resolved Optical Gating (FROG) is similar to intensity autocorrelation, however the spectrum of the crossed beams is detected instead of just the intensity. In effect, it is a spectrally-resolved autocorrelation[87]. FROG has been cited as the most reliable and practical method of spectrogram generation for unknown ultrafast pulses[88]. In FROG, the reference beam does not have to be known. The FROG signal is a convolution of the unknown pulse and the reference gate pulse $g(t)$. Conversion from the spectrogram of the FROG signal in to the electric field spectrum of the test pulse is a common 2-D inverse problem that can be solved iteratively. The recorded 2-dimensional spectrogram $S(\omega, \tau)$ is given by

$$S(\omega, \tau) \propto \left| \int_{-\infty}^{\infty} E(t) g(t - \tau) e^{-i\omega t} dt \right|^2 \tag{3.100}$$

Figure 3.13 shows a typical FROG setup.

3.4.4 Cross-Correlation Frequency-Resolved Optical Gating

The primary method of pulse characterisation used in this work is a variant of FROG called cross-correlation FROG (XFROG), which uses a well characterised reference beam as the gate, instead

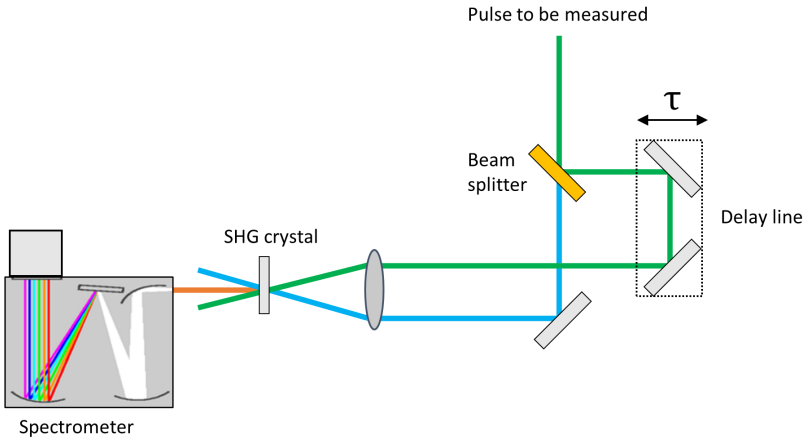

Figure 3.13: Diagram of a Frequency Resolved Optical Gating setup.

of a copy of the test beam[89]. Since the spectrum of the output is being measured, the gate pulse $g(t)$ does not need to be short in time. The XFROG spectrogram can be converted to the electric field of the test pulse using direct analytical methods. A diagram of the typical XFROG setup is shown in figure 3.14. A non-iterative method of retrieving the amplitude and phase of an unknown

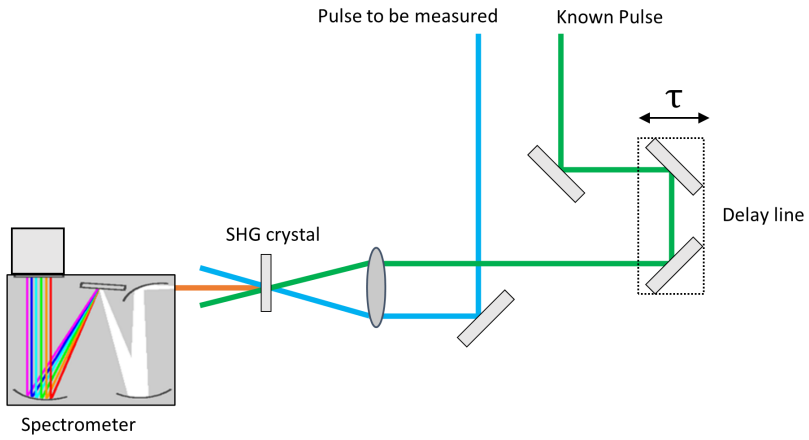

Figure 3.14: Diagram of a Cross-Correlation Frequency Resolved Optical Gating setup.

pulse using a flat-top gate pulse as the reference in an XFROG arrangement has been shown to be an efficient pulse characterisation technique by Selm *et al.*[90]. This method uses a reference gate pulse which is assumed to have a flat-top amplitude profile. The shape of the gate pulse is the important factor, rather than its duration, and in this paper it was actually three orders of magnitude longer than the test pulse.

Selm *et al.*[90] characterised an ultrafast broadband super-continuum pulse spanning from 900 nm to 1800 nm. This broadband pulse was generated using a highly non-linear fiber (HNF). The gate pulse used was a 3 ps pulse centred at 775 nm with a FWHM of 0.6 nm. The process outlined by Selm for obtaining the XFROG spectrogram was to record the spectrum $S(\omega)$ from the output signal after the non-linear medium, while varying the linear delay τ between the gate pulse and continuum pulse. The 2-D spectrogram $S(\omega, \tau)$ is thus generated sequentially resulting in a recorded signal which is approximately equal to the width of the larger of the two pulses (3 ps) along the delay dimension. The spectral width of S should be at least the width of the larger of the unknown or gate pulse i.e. the spectral measurement should be as broadband as possible to measure the full support of the XFROG intensity. The spectral amplitude of the test pulse as well as the group delay and thus phase was directly calculated from the spectrogram recorded using cross-correlation along the ω dimension of S with itself at a reference wavelength. Then using the Fourier transform, $E(t)$ was determined computationally.

The method described by Selm allowed for a simple extraction of the group delay as a function of the frequency of a supercontinuum pulse. The electric field of the test pulse is then directly reconstructed from the XFROG spectrogram. This method is ideal because it does not rely on iterative reconstruction methods to determine the electric field from the spectrogram, which are often difficult to error-check in both their validity and accuracy. An application of this method of pulse characterisation to multi-photon microscopes was highlighted by the authors, due to the fact that these setups almost always include a gate-like pulse which can be used as the known reference pulse. In this work the XFROG retrieval method gave expected results for the shape of the broadband beam and these are shown in section 5.2.

4. Background methods in BCARS

4.1 Introduction

In the previous chapter, the fundamental theoretical concepts underlying BCARS were introduced. In this chapter, the key methods developed in practice which are relevant throughout the rest of the thesis are described. Naturally, we begin with the measured response, in the form of the BCARS spectrum. The response is modelled using estimates of the laser and other parameters, which will serve as the basis for optimising the data processing workflow in subsequent sections.

4.2 Sample response

The intrinsically weak non-linear polarizability necessitates the use of pulsed laser sources to achieve a CARS scattering signal. CARS is typically further specified as either "single-frequency" CARS (SF-CARS) or "broadband" CARS (BCARS). The distinction being the use of a monochromatic source for resonance selectivity ($\omega_{\mathrm{p}} - \omega_{\mathrm{S}}$) in SF-CARS or a broadband Stokes source for addressing multiple resonances simultaneously[91] in BCARS. The basic concept of broadband CARS is to excite multiple coherent states at several frequencies using the spectrally broad Stokes pulse. This allows the fingerprint region of the Raman spectrum to be probed simultaneously by the probe wave packet and thus the generation of a spectrum of anti-Stokes radiation that can be collected in a multiplex manner. This is achieved using ultrashort pulses in the IR region and a spectrometer capable of detecting the full anti-Stokes Raman spectrum. The use of a broadband Stokes pulse is

thus the major difference between BCARS and SF-CARS.

To avoid confusion, we employ different nomenclature for the labelling of the photon types (probe, Stokes, pump) and for the laser sources, because BCARS employs two distinct photon mixing processes. In typical BCARS setups, there are only two laser sources used, and therefore one laser source provides two different photons for the FWM process, depending on the mixing configuration. The two sources used will be termed the narrowband and the broadband source. In BCARS, the use of a broadband Stokes beam permits the four-wave mixing of two different Stokes photons to generate the coherent Raman state, with the probe photon then scattering to produce anti-Stokes radiation. This results in two separate mechanisms of action, known as the "two-colour" and "three-colour" mechanism[4]. The two-colour process, which is a degenerate case where $\omega_{\mathrm{p}} = \omega_{\mathrm{pr}}$, uses the narrowband source for the pump and probe photons. The three-colour mechanism uses the narrowband purely for probing and the pump and Stokes photons both originate from the broadband source. The intensity spectrum of the CARS signal for the two-colour mechanism is given as a correlation between the Stokes spectrum and the pump spectrum, convolved with the probe spectrum. In the three-colour mechanism, the intensity spectrum is given by an auto-correlation of the Stokes spectrum, convolved with the probe spectrum. The frequency-domain CARS signal is given in equation 4.1,

$$I_{\mathrm{as}}(\omega) = \left| \left\{ \chi^{(3)} \left[E_s(\omega) \star E_p(\omega) \right] \right\} * E_{pr}(\omega) \right|^2 \tag{4.1}$$

where the $\star$ symbol denotes the cross-correlation operator and the $*$ symbol denotes the convolution operator. In the degenerate two-colour case where $E_p = E_{pr}$, the resultant CARS signal is given as the auto-correlation of the broadband source, convolved with the probe pulse. Since the three-colour mechanism involves an auto-correlation of a broad spectral signal, it has the greatest spectral range. Inspection of equation 4.1 shows that the vibrational frequency range probed is dependent only on the product $E_s(\omega) \star E_p(\omega)$, which we denote as the excitation profile $S(\omega)$. The wavelength of the anti-Stokes light however is dependent on E_{pr}. Since the probe is convolved with the excitation profile, the ultimate resolution obtainable is determined by the probe laser line-width. The spectral range of the BCARS signal using simulated laser and material parameters is shown in figure 4.1. In (a) a simulated Raman spectrum is shown, generated from a sum of Lorentzian functions ($\chi^{(3)}_{\mathrm{Res}}$ in equation 3.68). (b) shows a simulated NRB spectrum ($\chi^{(3)}_{\mathrm{NR}}$ in equation 3.68), using a Gaussian

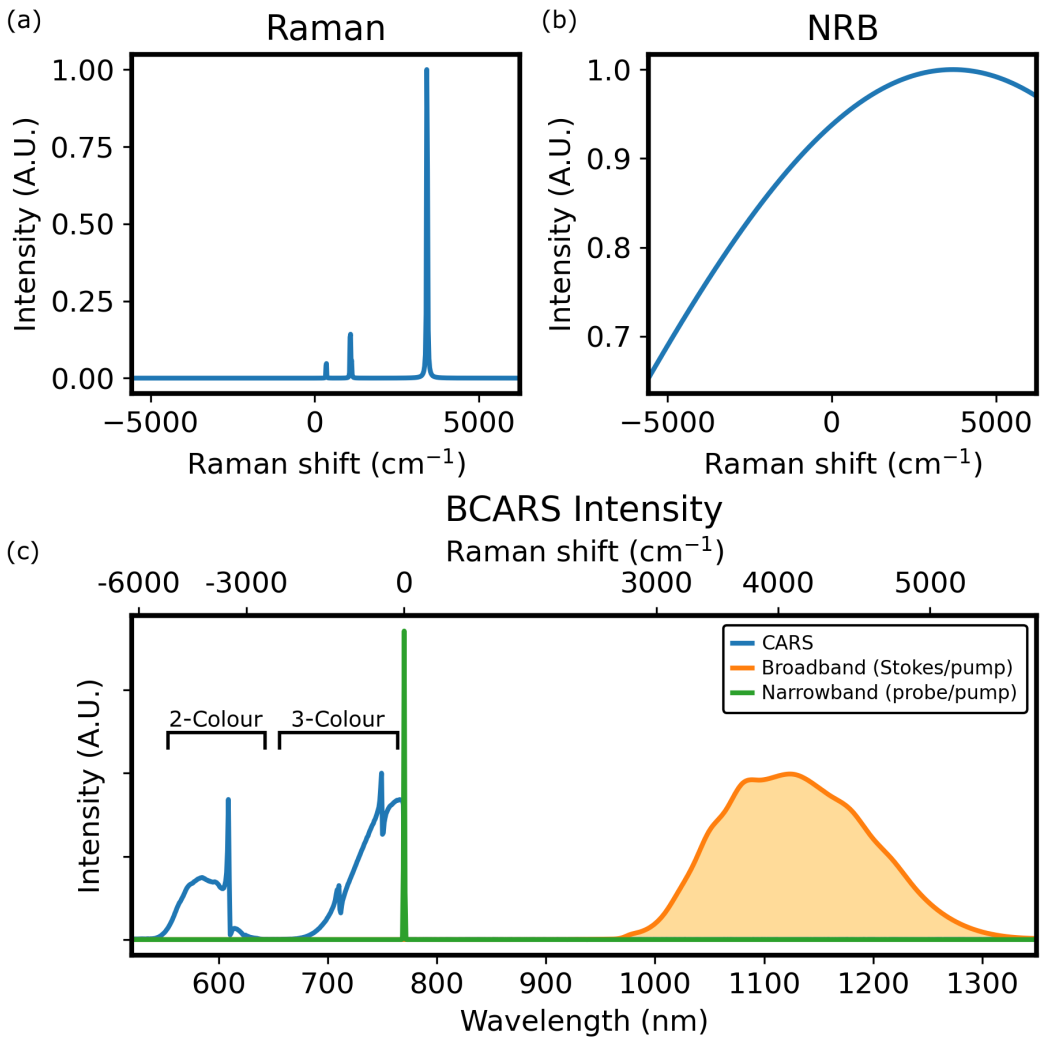

Figure 4.1: (a) Simulated Raman spectrum (Im$[\chi^{(3)}]$), (b) simulated NRB spectrum ($\chi^{(3)}_{\mathrm{NR}}$), (c) Input and output spectra from the BCARS FWM process using Raman and NRB information from (a) and (b).

function. In (c), the simulated laser spectrum from the narrowband and broadband sources used in this work is shown, along with the output BCARS anti-Stokes spectrum, according to equation 4.1.

From figure 4.1 (c) it can be seen the anti-Stokes signal contains two regions of nonzero four-wave mixing (FWM) signal intensity. The region centred on $\omega_{\mathrm{S}} - \omega_{\mathrm{S}} + \omega_{\mathrm{pr}}$ is the three-colour region as mentioned above, and coincides with a Raman shift from 0 cm^{-1} to approximately 2000 cm^{-1}. The region centred on $2\omega_{\mathrm{p}} - \omega_{\mathrm{S}}$ is the two-colour region and coincides with approximately 2800 cm^{-1} to 4000 cm^{-1}. There is also a region of no signal between the three and two-colour region, which, due to the centre frequency and separation of the narrowband and broadband source, does not result in any FWM response. This region serendipitously coincides with the so-called “silent” region of the

Raman spectrum. The resonances in the Raman spectrum in (a) are clearly seen in (C), however they are distorted in shape due to the NRB and reflected about the probe frequency. Also notable is the fact that FWM generates anti-Stokes signal far from any resonance. The laser excitation spectrum is effectively reproduced as an upper sideband channel offset from the narrowband source due to the NRB.

4.3 Noise

In laser spectroscopy experiments, noise will be present due to a wide array of sources and it is often a limiting factor in the scalability of a technique. The speed or throughput of a microscopy technique is intricately liked with the ratio of the signal strength to the noise level, the signal-to-noise ratio (SNR). The fundamental limit on the noise in a measurement involving light is due to the quantized nature of photons. This so-called shot-noise limit can be increased by increasing the irradiance, however there becomes a point where additional light may damage the sample of interest. There is thus a balance between SNR and sample damage that must be reconciled for BCARS.

The SNR of the measured anti-Stokes signal in BCARS can be given as[92]

$$\text{SNR} \propto \frac{n_{\text{as}}}{\sqrt{\sigma_{\text{shot}}^2 + \sigma_{\text{dark}}^2 + \sigma_{\text{read}}^2}} \tag{4.2}$$

where n_{as} is the number of signal anti-Stokes photoelectrons generated, σ_{shot} is the standard deviation of the signal due to shot noise, σ_{dark} is the standard deviation of the dark signal, and σ_{read} is the standard deviation of the readout process from the detector. In addition to these sources of noise there is also potentially background noise, due to photons arising from Rayleigh or spontaneous scattering and other luminescence processes, however modern detection setups can provide adequate rejection of these photons using long focal lengths and high performance spectral filters[93]. Another potential form of noise is flicker noise due to laser variations. This however is also suppressed in multichannel detectors. The number of useful photoelectrons detected is given as

$$n_{\text{as}} = Q_{\text{e}} G(\chi^{(3)}_{\text{signal}}) I_{\text{p}}^2 I_{\text{pr}} \tag{4.3}$$

where $\chi^{(3)}_{\text{signal}}$ is equal to equation 3.73 with the $\left|\chi^{(3)}_{\text{NR}}\right|^2$ term omitted since it is considered purely noise. Q_{e} is the quantum efficiency of the detector and G is the gain of the detector. All terms in equation 4.3 except for G are frequency dependent. Through substitution of equation 3.73, n_{as} can be given as

$$n_{\text{as}} = Q_{\text{e}}G(|\chi_{\text{R}}|^2 + 2\chi_{\text{NR}}\,\text{Re}[\chi_{\text{R}}])I_{\text{p}}^2 I_{\text{S}} \tag{4.4}$$

The denominator in equation 4.2 will now be determined. σ_{shot} is related to the finite number of photons from the non-resonant contribution, which is given as

$$\sigma_{\text{shot}} = \sqrt{|\chi^{(3)}_{\text{NR}}|^2 I_{\text{p}}^2 I_{\text{pr}}} = |\chi^{(3)}_{\text{NR}}| I_{\text{p}} \sqrt{I_{\text{pr}}} \tag{4.5}$$

here, we assumed the shot noise of the nonresonant background is much larger than the resonant signal, the so-called background shot-noise limited scenario[93]. The dark current standard deviation σ_{dark} is due to the thermal generation of electrons in the photo-active material of the detector and this is given by

$$\sigma_{\text{dark}} = \sqrt{\Phi t} \tag{4.6}$$

where Φ is the rate of dark signal generation (in $e^-\text{s}^{-1}$) and t is the integration time of the acquisition. In this work, the detector used had a $\Phi = 0.003\,e^- s^{-1}$ at maximum cooling (-100°C) and $\Phi = 0.1\,e^- s^{-1}$ while air-cooled (-80°C). The final term in the denominator of equation 4.2 is related to read noise from the detector. σ_{read} is the standard deviation of the resulting count value of a pixel from the conversion of electrons in that pixel. σ_{read} does not depend on the magnitude of the signal and is in units of e^-. The detector used had a typical read noise of 12 e^-. Therefore, when optimal cooling of the detector is used, such that dark noise and read noise are negligible compared to the shot noise, the SNR can be given as

$$\text{SNR} \propto \frac{Q_{\text{e}}G(|\chi_{\text{R}}|^2 + 2\chi_{\text{NR}}\,\text{Re}[\chi_{\text{R}}])I_{\text{p}}^2 I_{\text{S}}}{|\chi^{(3)}_{\text{NR}}| I_{\text{p}} \sqrt{I_{\text{pr}}}} \tag{4.7}$$

A simplification can be made in the limit of dilute concentrations of the sample, i.e. when $|\chi_{\text{R}}|^2 \ll |\chi_{\text{NR}}|^2$, and therefore $|\chi_{\text{R}}|^2 \ll 2\chi_{\text{NR}}\text{Re}[\chi_{\text{R}}]$, in which case the SNR can be stated

as

$$\text{SNR} \propto \frac{Q_e G(2\chi_{NR}\,\text{Re}[\chi_R])I_p^2 I_{pr}}{|\chi^{(3)}_{NR}|I_p\sqrt{I_{pr}}} \propto 2\text{Re}[\chi_R]I_p\sqrt{I_{pr}} \tag{4.8}$$

It is interesting to note that this form of the SNR is identical to that for SRS, in the shot-noise limited case[94]. Thus, in theory, CARS and SRS have the same detection limit. The real part of χ_R is proportional to the number of scatterers. An approach for characterising the relative detection limit is to formulate a common equation for SNR in both SR and CARS. Here we define the Raman absorbance[95], $\Lambda = n\frac{\sigma}{A}(\frac{\omega_p}{\omega_S})$, where n is the number of molecules in the focus, A is the area irradiated σ is the cross section of the molecule and ω_S and ω_p are the frequencies of the Stokes and pump photons respectively. The SNR of SR can then be stated as

$$\text{SNR}_{\text{Raman}} = \eta\Lambda N_P \tag{4.9}$$

where η is the SR collection efficiency and N_P is the incident photons passing through the sample in the dwell time. The SNR of CARS can also be reformulated as

$$\text{SNR}_{\text{CARS}} = E\Lambda\sqrt{N_{pr}} \tag{4.10}$$

where it is assumed $\eta = 1$, since CARS radiation is coherent and thus highly directional, and E is the CARS enhancement factor due to the coherence of the process. If we take $\eta = 5\%$ for the SR case and $E = 10^7$, the detection curves can be plotted for the case of SNR $= 1$. The SNR for both SR and CARS is plotted in figure 4.2 by setting SNR$= 1$, or one photon generated in the dwell time. It can be seen in figure 4.2 that there is a point at which the CARS detectability is better than SR i.e. for a certain photon budget N_p, the minimum absorbance is lower for CARS. The crossing point is determined by the enhancement factor E and collection efficiency η. It should however be noted that CARS is typically never operated in the shot noise limited regime since since the non-resonant background contributes significant intensity noise.

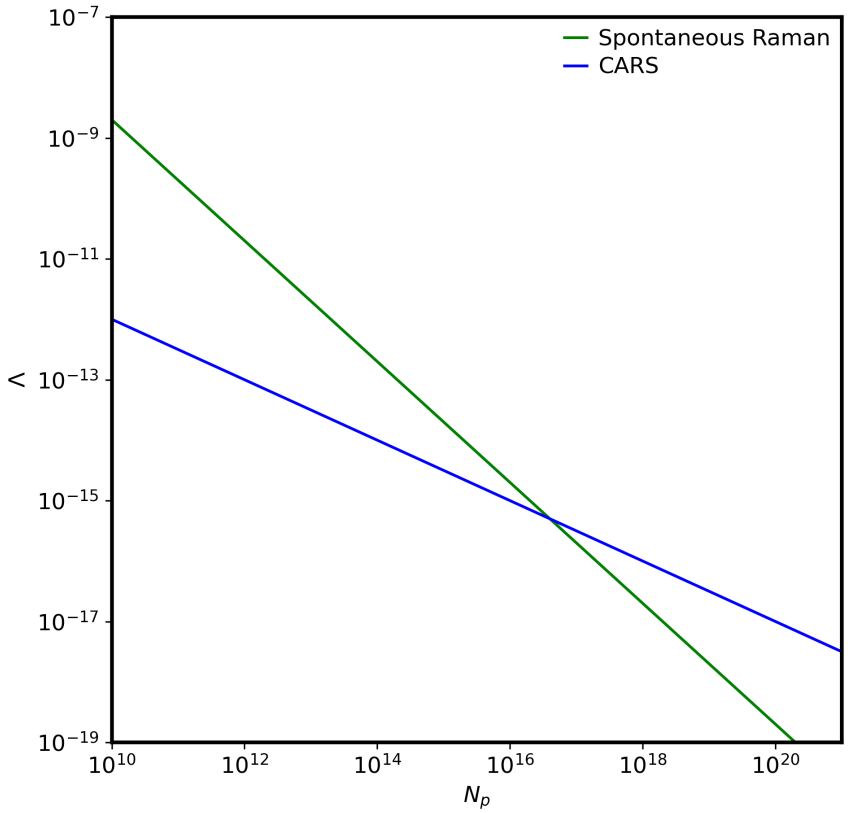

Figure 4.2: Detection curve for spontaneous Raman scattering and CARS.

4.4 Preprocessing a BCARS image for cell analysis

When analyzing a hyperspectral BCARS image, there are necessary steps required in order to remove the distortion of the NRB and other non-chemical effects. As with any spectral measurement, the spectral axis and CCD sensitivity need to be calibrated using a reference. Wavelength calibration is virtually identical to SR, however there is no requirement for intensity calibration in BCARS by virtue of the co-generated NRB, as will be discussed below.

A simple diagram of the main features of a hyperspectral image (HSI) are shown in figure 4.3. In a standard HSI, two dimensions represent space and one represents frequency. In dispersive spectroscopy measurements such as BCARS the non spatial dimension is wavelength, which may be converted to Raman shift accordingly using knowledge of the probe laser wavelength. In ideal

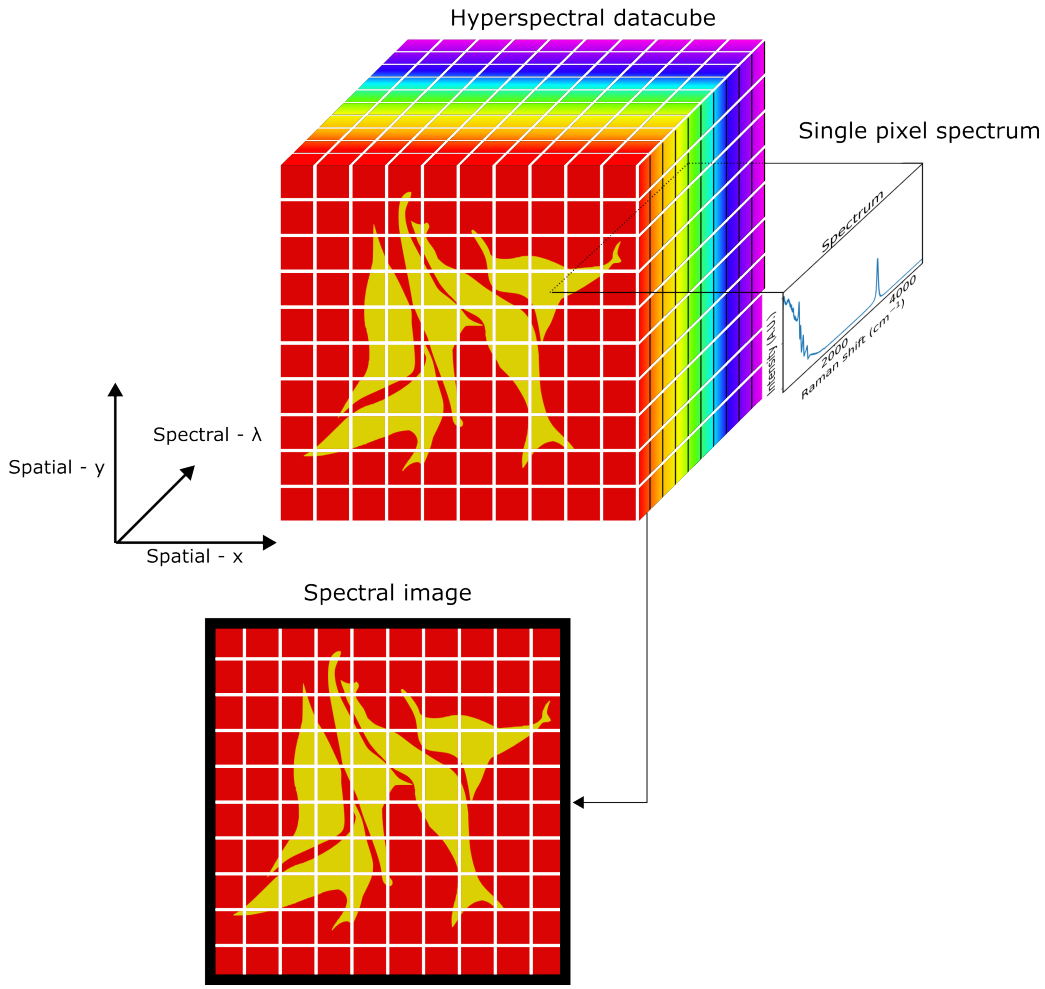

Figure 4.3: Hyperspectral datacube illustration.

circumstances, the HSI contains information about the sample only, however this may not be the case for several reasons[2]. The main sources of this spurious signal that are not due to random noise in BCARS are described below.

Common spurious effects in BCARS experiments

1. Physical contrast
   (a) Optical path length variation
   (b) Absorption coefficient variation
2. System induced contrast
   (a) Laser irradiance variation

   (b) Laser central frequency variation
   (c) Cosmic ray artefacts
3. Anomalous chemical contrast
   (a) Photochemical interaction
   (b) Photothermal interaction
   (c) Competing nonlinear interaction

Physical contrast is the most common type of spurious signal in BCARS experiments since the process is third-order in the laser intensity. Thus a variation in optical path length or the local absorption coefficient may cause a wavelength-dependent change in received flux. This change in flux may then cause downstream analyses to erroneously attribute the change to chemical contrast and thus it must be removed. In SR, typically this is performed using a scatter correction procedure. This involves regressing all data to a common reference measurement using a low-order function such as a cubic function. The function then obtained is used to detrend each spectrum.

System induced contrast from the sources and detectors can typically be mitigated such that it is negligible. In most commercial laser systems, the output irradiance and frequency are measured and stated to vary within a small percentage of the nominal value over a period of time. This requires a temperature controlled environment and stable laser which is commonplace in modern laboratories. Cosmic ray artefacts are commonly treated in SR using specific algorithms[96, 97] that can be applied to BCARS without modification.

In a well designed experiment, the choice of the source laser incident frequency and power should also prevent anomalous chemical contrast arising from photochemical and photothermal effects. However, in BCARS, since a broadband laser is required, there is often many simultaneous dissipative and parametric nonlinear effects occurring because phase matching is satisfied for a broadband pulse. In the experiments within this thesis, second-harmonic generation (SHG), two-photon fluorescence (TPF) and difference-frequency mixing (DFM) can all be detected during normal operation. SHG is the conversion of two photons in to a single photon at twice the frequency. DFM is the conversion of two photons in to a single photon at the difference frequency of the pair. Since SHG is a second-order nonlinear process, it may only occur in non-centrosymmetric

media and therefore does not typically occur in single cells[80]. Using an unlabelled sample, TPF is the simultaneous absorption of two photons to an excited state from which fluorescence ooccurs, and requires an endogenous fluorophore within the sample for the emission occur. In single mammalian cells, autofluorescence is a normal feature and occurs mostly in the mitochondria within the cytoplasm[98]. Furthermore, the intensity of emission and other spectral properties changes with cell state[99]. In this work, TPF however could only be detected in highly absorbing fluorophores from chlorophyll in plants, where the quantum efficiency can be approximately 25%[100]. In human cells, the BCARS signal is at such an intensity that the TPF is approximately equal to the noise floor. Lastly, the DFM signal although present, lies within a frequency range that is outside the biologically relevant region. Thus, DFM does not actually affect the analysis. Therefore, other than denoising and NRB removal, scatter correction and cosmic ray removal are the other two primary algorithms that are necessary to preprocess the HSI. The basic preprocessing procedure for all BCARS experiments in this thesis is shown in figure 4.4. Each step in the figure will now be described in detail in the next subsections.

4.4.1 Denoising

Denoising is an important step for obtaining good quality results from raw hyperspectral images. In such an image, there is an abundance of both signal and noise and depending on the context, the noise can be removed with little to no effect on the signal. In BCARS images, denoising is not just useful to increase the SNR, it is mandatory because of the requirement for phase retrieval. It is known that the inverse problem of phase retrieval is ill-posed, that is, it is a problem for which any one of the requirements of existence of a solution, uniqueness of a solution, and continuity dependence of the output on the input is not satisfied[101]. In phase-retrieval, uniqueness is not met since information is lost through the operation of taking the magnitude of a complex number. Continuity is more subtle and is generally described by the condition number of the problem. In attempting to solve the phase retrieval problem, it is often the case that the solution is highly sensitive

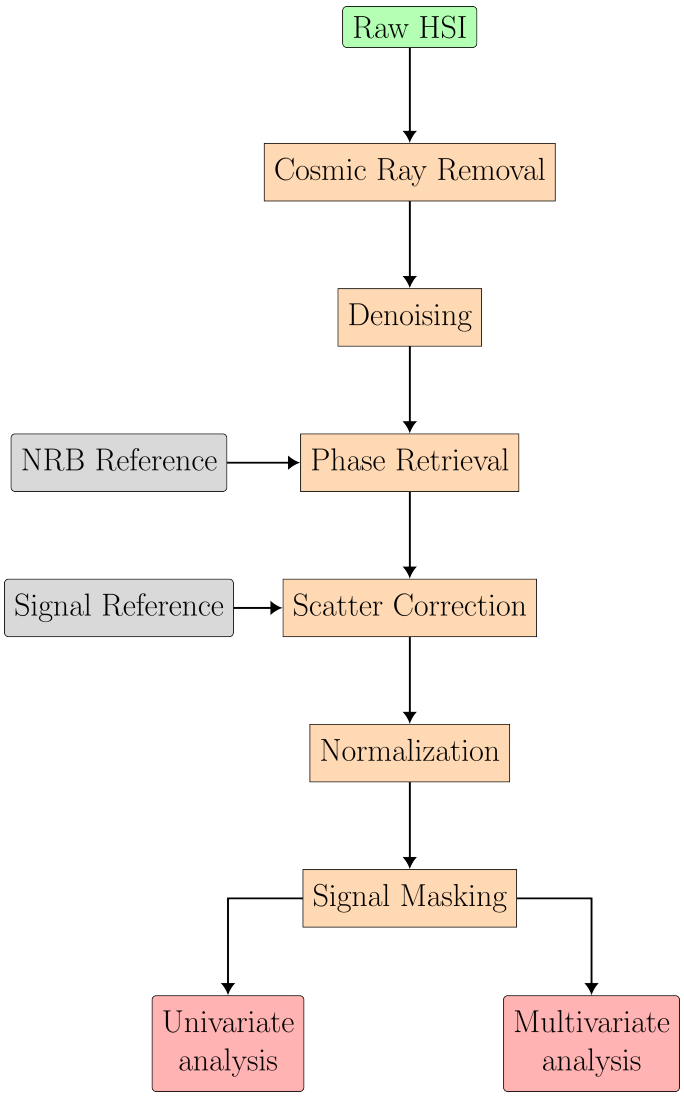

Figure 4.4: BCARS HSI preprocessing pipeline. The NRB reference is a measurement of the BCARS intensity in a non-resonant material. The signal reference is a signal on to which all spectra are regressed, and is typically obtained from the average of multiple spectra in a HSI.

to the input data. The condition number is given as

$$\kappa = \frac{\|\Delta y\|}{\|\Delta x\|} \tag{4.11}$$

where Δy and Δx represent unit changes to the output and input value respectively. In problems with a high condition number, noise, which can be viewed as random fluctuations in the input, can be amplified by the inversion operation, leading to meaningless results. A simple mathematical diagram of phase retrieval is shown in figure 4.5. We denote the set of all inputs to the operator of interest $\mathbf{A}$, as the object space, and the set of all outputs of $\mathbf{A}$ as the image space. In the figure

below, the distance between points indicates a measure of "proximity" of points in each space. $\mathbf{A}$ takes an input from the object space to the image space and in BCARS, the operation of concern is the magnitude-square $\mathbf{A} \equiv |x|^2$

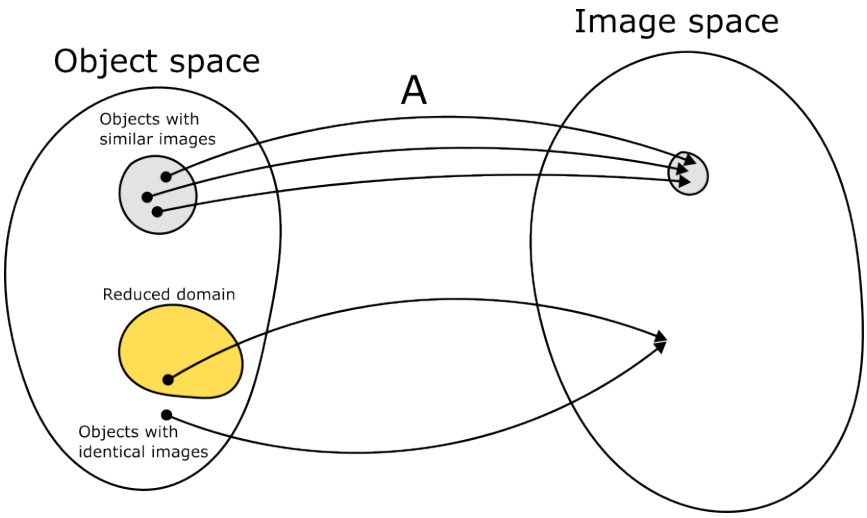

Figure 4.5: Diagrammatic representation of the object and image space in an ill-posed problem such as phase-retrieval involving the operator $\mathbf{A}$.

From figure 4.5, the inverse operation $\mathbf{A}^{-1}$ takes a point, or multiple points as for a spectrum, from the image to object space. A^{-1} may not have a unique solution for some value in the image space since there is a loss of information as A is applied. The loss of information for $\mathbf{A}$ is due to the non-negativity requirement of the range (assuming the image space is real). This can be viewed in figure 4.5 as the constriction of points to a smaller region of the image space (grey regions). In phase-retrieval algorithms, typically it is known that the domain of the operator has some properties that reduce the set of possible solutions. This reduced domain shown as a yellow subset in the above figure can therefore eliminate many potential solutions that, for example, do not satisfy some conditions imposed by the system under study. Such a condition might be that the phase is non-zero everywhere, that it has no discontinuities, or that it has a particular value within some region etc. These constraints are linked to the physical system being studied and are termed physical constraints of the problem. The combination of these physical constraints with the mathematical constraints of equivalence are used in many optimisation algorithms in order to find an approximate solution of phase-retrieval problems. The effect of denoising then should be to accurately represent the signal without the disturbances from random variables that may cause the inverse-problem to become unstable.

In order to optimally reduce noise in a HSI, the truncated singular value decomposition (SVD) is used extensively in this thesis because it allows global structure preservation of HSIs while approximating the data in a lower dimension. The SVD of a matrix D is given as[102]

$$D = U\Sigma V^* \tag{4.12}$$

where U and V are both unitary and Σ is a diagonal matrix consisting of the r singular values $(\sigma_1, \sigma_2, \cdots \sigma_r)$ of D, where r is the rank of D. The columns of U are eigenvectors of the product DD^*, and the columns of V^* are eigenvectors of D^*D. The decomposition can also be formulated as a sum of rank-1 matrices

$$D = \sum_{i=1}^{r} u_1\sigma_1 v_1^* + u_2\sigma_2 v_2^* + \cdots + u_r\sigma_r v_r^* \tag{4.13}$$

where u_i and v_i^* are the i^{th} column and row of U and V^* respectively. The rank-k truncated SVD of D is

$$M_k = \sum_{i=1}^{k<r} u_i\sigma_i v_i^* \tag{4.14}$$

The utility of truncation is due to the fact that the rank-k truncated SVD of D is the closest k matrix to D in a Frobenius norm sense. That is,

$$\inf\{||D - B||_F : \text{rank}B = k\} = ||D - D_k||_F \tag{4.15}$$

where $||\cdot||_F$ denotes the Frobenius norm, calculated as

$$||D||_F = \sqrt{\sum_{i}^{m}\sum_{j}^{n} |d_{ij}|^2} \tag{4.16}$$

where D is of size $m \times n$ and d_{ij} are the matrix elements of D. For this reason, the application of the truncated SVD to a data matrix is known as low-rank approximation. It is typically assumed that the noise in a data matrix is additive and that the rank of the noise-free signal in the matrix is much lower than the number of independent variables (columns) N. The measurement can be considered an addition of an N-dimensional signal vector with an N-dimensional noise vector.

The SVD will then partition the data in to rank-1 subspaces that are a mixture of signal and noise components. However, since the signal rank is lower than the data rank, a truncated reconstruction containing signal-dominant vectors should effectively remove noise in the matrix. In BCARS the additive noise condition is not met due to the presence of shot noise, however a variance stabilisation algorithm such as the Anscombe transform can be used to make the standard deviation of the signal approximately constant[103]. The truncated SVD is then applied to the transformed data and then the inverse-Anscombe transform is applied to recover the original signal characteristics. This procedure was used extensively throughout this thesis. In performing the truncation of singular values (SV), typically one selects the highest n values in the reconstruction, using a metric such as the reconstruction error to guide selection. In the case of high noise levels, this may not be optimal since the distribution of signal and noise may not monotonically decrease with the reconstruction rank k. In order to optimally select only the signal SVs in the reconstruction a method based on the spatial signal fraction was used[1].

This procedure begins with performing variance stabilisation. Then the SVD of the unfolded data matrix is obtained. Unfolding consists of concatenating the two orthogonal spatial dimensions together such that the matrix changes shape from size $n \times m \times l$ to $nm \times l$, where l is the length of the spectral dimension. The U vector is then of size $nm \times nm$. If U is the re-folded, one obtains m matrices of size $n \times m$, which we denote spatial eigen-maps of the data matrix. These can be considered the 2-dimensional arrangement of eigenvectors that correspond to the 1-dimensional eigenvectors in the spectral dimension. These eigen-maps are thus quasi-images that contain details on the distribution of the energy of the corresponding rank-1 sub-matrix. Visualisation of eigen-maps reveals details of the underlying data matrix whenever the SV chosen corresponds mainly to signal. Conversely, when the SV is dominated by noise, the eigen-map has the appearance of a random variable. Thus, the selection of the optimal SVs to use in the truncation can be obtained from a measure of the spatial frequencies present in U. This was done using the 2D discrete Fourier transform of U. The spatial signal fraction was then obtained using

$$\mathrm{SF}_i = \frac{M \sum U_i}{\sum U_i} \tag{4.17}$$

where M is a Boolean lowpass mask that is 1 in the region from the DC component to the cutoff spatial frequency f_{cutoff}, and zero everywhere else. The signal fraction is thus a normalized ratio of the low frequency energy in the specific eigen-map. A threshold value τ was then used to detect signal SVs based on the SF_i value. This was chosen empirically based on inspection of the U and V vectors. After determining the set of SVs that correspond to signal, they were used to generate a modified diagnonal matrix Σ_{signal}

$$\Sigma_{\text{signal}} = \text{diag}\{\sigma_i : \text{SF}_i > \tau\} \tag{4.18}$$

the denoised matrix was then obtained using the recomposition of U, V and the new Σ matrix,

$$A_{\text{denoised}} = U\Sigma_{\text{signal}}V^* \tag{4.19}$$

4.4.2 Removal of Non-resonant background

After denoising the dataset, the next step was to remove the NRB from each spectrum in the HSI. The removal of the non-resonant background is crucial in BCARS because it drastically affects the resonance lineshapes in the Raman spectrum due to the mixing of the resonant and non-resonant components of the nonlinear susceptibility. This is seen in figure 4.1 (c). The NRB is typically removed using a post-processing method which takes both a reference measurement of the NRB and the resonant CARS signal as inputs. To record the reference NRB signal, typically a reference sample of which there are no vibrational resonances in the probed spectral band is used. Glass is one example, which is non-resonant over the 500 - 3600 cm^{-1} range. The recorded NRB is ideally a smooth, slowly-varying signal over the whole frequency interval of interest that essentially captures the laser spectral variation only. However, likely due to chemical impurities and the laser excitation profile, the NRB may not be smooth. In this case its removal may prove problematic. At the start of this research, there were two established methods for removing the NRB; the Kramers-Kronig method and the maximum entropy method. As part of this thesis, a new method involving deep-learning was developed which is one of the novel contributions in this thesis. This method is described in chapter 6.

Kramers-Kronig Method

The Kramers-Kronig method is one of the most popular methods for NRB removal in BCARS due to its relatively ease of use and low computational cost. This method is based on the principle that the amplitude and phase of any driven oscillator are related through a Kramers-Kronig (KK) relation. The KK relations generally relate the real and imaginary parts of any complex quantity which describes a causal system. The KK-relations are widely-accepted tools used in acquiring knowledge of dispersive phenomena from measurements on absorptive phenomena. This has proved useful in CARS for determining the imaginary part of the electronic susceptibility when only the squared modulus $|S \cdot \chi^3|^2$ is known. Liu *et al.*[104] show that the spectral phase of the susceptibility can be retrieved from its modulus squared[104]

$$\varphi(\omega) = -\frac{P}{\pi} \int_{-\infty}^{+\infty} \frac{\ln|\chi^{(3)}(\omega')|}{\omega' - \omega} \, \mathrm{d}\omega' \tag{4.20}$$

where P is the Cauchy principal value. Since $|\chi^{(3)}| \propto \sqrt{I_{\mathrm{CARS}}}$, applying the Hilbert transform to the natural logarithm of the CARS intensity should retrieve the spectral phase of the susceptibility. Since the CARS intensity is windowed by the detector instrument range, a "windowed" Hilbert transform is used together with a phase error estimate from the non-resonant spectrum. The complex susceptibility is then given as

$$\chi^{(3)}(\omega) = \sqrt{I_{\mathrm{CARS}}} \exp(i\varphi(\omega)) \tag{4.21}$$

This method has been tailored to BCARS by Camp *et al.*[105] and where KK is used in this thesis, the CriKit2 package was used. This implementation utilises detrending of the phase and unity-scaling of the amplitude as was found to be optimal for retrieving the Raman-like spectrum from BCARS measurements.

An example retrieval of the resonant susceptibility using the KK method developed by Camp *et al.* is shown in figure 4.6. The CARS spectrum was simulated using a method developed in chapter 7 and aims to highlight the uncorrected phase-retrieval result and the importance of phase-detrending. It can be seen in figure 4.6 (a) that the initial retrieved but uncorrected estimate of $\chi_{\mathrm{R}}^{(3)}$ is highly

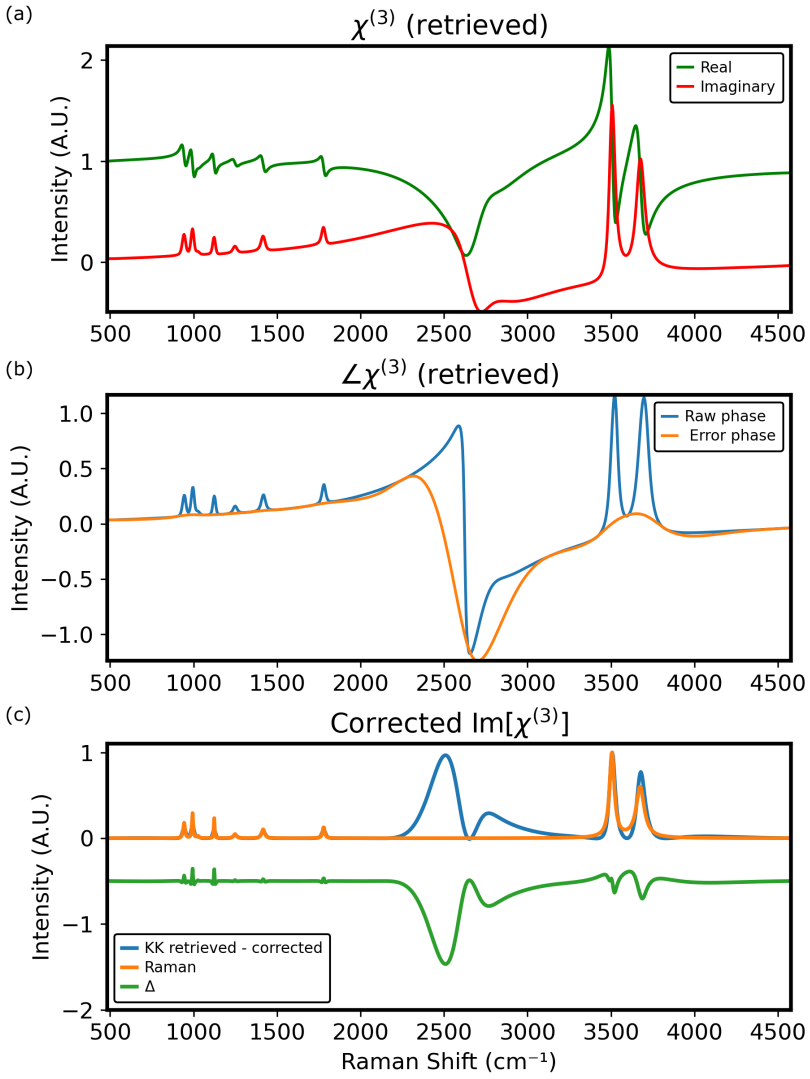

Figure 4.6: (a) Retrieved real and imaginary parts of susceptibility obtained from the Kramers-Kronig method in CriKit2[1], (b) phase and phase-error of retrieved susceptibility in (a), (c) Phase- & amplitude-corrected susceptibility, true Raman spectrum obtained from simulation and the difference of the KK-retrieved and true spectrum.

representative of an electronic susceptibility with the imaginary part having lineshapes centered approximately at the location of the resonances. There is however two notable features of the spectra in (a), the first being a background signal on both the real and imaginary parts of the susceptibility, and also a dispersive lineshape in the imaginary part around 2700 cm^{-1}. The first anomaly is mainly due to the varying NRB and the windowing error from the use of the discrete Hilbert transform (DHT) in the KK method. Secondly, the dispersive lineshape in the imaginary part is due to the two distinct excitation mechanisms in BCARS and the fact that the laser spectrum is zero in the region

between the two and three-colour regions.

In the retrieved phase of $\chi^{(3)}$, the baseline is noticeable throughout the full bandwidth of the spectrum. The phase-correction procedure in the KK method fits a smooth function to the phase to detrend this baseline (here the asymmetric least-squares algorithm was used). It can be seen that the fitting is quite good using a smoothness parameter of 1000 and asymmetry parameter of 0.001. The anomalous dispersive lineshape around 2700 cm^{-1} however results in the fitting procedure underfitting since the amplitude variation is high. The result of the phase and amplitude-corrected KK retrieval is shown in figure 4.6 (c). The corrected retrieval has no baseline and the retrieval is successful in regions where the resonances exist. The anomalous phase results in a retrieved signal around 2700 cm^{-1}, however this is in a region that is of no interest in biological systems. In (c) the difference spectrum (Raman-retrieved) is plotted. The mean absolute error (MAE) of the retrieval is 0.07. While this is reasonably good, we have shown an idealised retrieval here, using a noise-free CARS simulation with relatively few and non-overlapping resonances. This presents a simple case for phase-retrieval since an isolated resonance results in a high frequency variation in the phase due to the application of the DHT, to which a low frequency signal can be fitted to remove phase error. However as we will see in later chapters, the introduction of noise and resonance amplitudes that are similar to those in biological systems results in the phase-retrieval procedure becoming highly unstable.

Maximum Entropy Method

A phase retrieval method was proposed by Vartiainen[106] utilising the maximum entropy method (MEM). This method has an advantage over the KK retrieval method because it theoretically does not require the determination of the intensity spectrum over an infinite frequency range, but only over the actual measured range. The phase retrieval process in MEM involves fitting the measured intensity spectrum R to its maximum entropy representation given by[107]

$$R(\nu) = \frac{|\beta|^2}{|A_M(\nu)|^2} \tag{4.22}$$

where the MEM polynomial $A_M(\nu)$ is given as,

$$A_M(\nu) = 1 + \sum_{m=1}^{M} a_m \exp(-i2\pi m\nu) \tag{4.23}$$

The polynomial is constructed from M coefficients and the frequency range is normalised to the interval (0,1) by defining the new variable $\nu = (\omega - \omega_1)/(\omega_3 - \omega_1)$, where ω_1 and ω_2 are the lower and upper frequency limits of the recorded spectrum. The MEM coefficients are found by solving a Toeplitz matrix of the form

$$\begin{pmatrix} C(0) & C(-1) & \dots & C(-M) \\ C(1) & C(0) & \dots & C(1-M) \\ \vdots & \vdots & \ddots & \vdots \\ C(M) & C(M-1) & \dots & C(0) \end{pmatrix} \begin{pmatrix} 1 \\ a_1 \\ \vdots \\ a_M \end{pmatrix} = \begin{pmatrix} |\beta|^2 \\ 0 \\ \vdots \\ 0 \end{pmatrix} \tag{4.24}$$

where $C(t)$ is the autocorrelation function defined by the Fourier transform of $R(\nu)$

$$C(t) = \int_0^1 R(\nu) \exp(i2\pi t\nu)\, \mathrm{d}\nu \tag{4.25}$$

The susceptibility is then given as $\chi^{(3)} = \sqrt{R}\exp(i\theta)$, where θ is the phase of the complex susceptibility which is related to the MEM phase ψ

$$\chi^{(3)}(\nu) = \frac{|\beta|\exp(i\theta(\nu))}{|A_M(\nu)|} = \frac{|\beta|\exp(i(\theta(\nu) - \psi(\nu)))}{A_M(\nu)\exp(-i\psi(\nu))} = \frac{|\beta|\exp(i\phi(\nu))}{A_M^*(\nu)} \tag{4.26}$$

where ϕ is an error phase term, consisting of a slowly varying background. To obtain the error phase, a low order polynomial fit of the MEM phase was obtained and subtracted from it leaving the high-frequency phase response due to vibrational transitions. The constant phase φ_0 is determined by noting that far from resonance, $\mathrm{Im}[\chi^{(3)}] = 0$, therefore

$$\varphi_0 = \tan^{-1}\left(\frac{\mathrm{Im}(\beta)}{\mathrm{Re}(\beta)}\right) \tag{4.27}$$

4.4.3 Scatter correction

Scatter correction is a routinely used procedure in conventional Raman spectroscopy in order to retain only chemical information so its use for BCARS data is thus pertinent. Since the NRB removal step returns a signal that is proportional to $\mathrm{Im}[\chi_{\mathrm{R}}^{(3)}]$, which is proportional to the Raman spectrum of the material, the scatter correction when applied after NRB removal has been performed should be identical to its conventional implementation. This assumes that the NRB removal is optimal which as we will show, is often not the case in biological cells. Nevertheless, in ideal circumstances such as when studying highly resonant materials, NRB removal performs well and the resulting signal is very similar to a Raman-like signal. Scatter correction is then trivial. In this thesis, the extended multiplicative scatter correction (EMSC) algorithm was applied as needed to correct a HSI[108]. It was found that this procedure greatly improved the contrast in univariate spectral images of cells. EMSC was applied by obtaining a reference signal with a high SNR (typically through manual inspection of a spectral image in the CH-band).

4.4.4 Normalization

Normalization is required for a HSI since downstream algorithms typically perform better when data is all on a common scale. As per the processing diagram in figure 4.4, normalisation is performed subsequent to scatter correction. Typically there are two main types of normalisation performed on a HSI, area and max-min. In area normalization, each spectrum is normalised by the total area under the spectrum.

$$I^i_{\text{area}} = \frac{I^i}{\Sigma I^i \Delta S} \tag{4.28}$$

If the spectral spacing ΔS is constant, this is identical to dividing each spectrum by the total sum of its intensity. Max-min normalization involves taking

$$I^i_{\text{max-min}} = \frac{I^i - I_{\text{min}}}{I_{\text{max}} - I_{\text{min}}} \tag{4.29}$$

The importance of which type of normalization to use is lessened when multivariate algorithms are used, however it is important to note that when using max-min normalization, typically the univariate contrast at the maximum is lost, since all values will equal unity. In this work, both types of normalization were used depending on the analysis.

4.4.5 Signal masking

Signal masking by segmentation is the last preprocessing step used in the preparation of a HSI for analysis. This involves removing non-signal pixels such as the background substrate within the image in order to keep only the useful information i.e. the spectra of cells for multivariate statistical analysis. There are a variety of methods to do this such as morphological operations, intensity thresholding, semantic segmentation and clustering algorithms. The necessity is of paramount importance in classification, since a HSI will often contain regions that only relate to the background and their inclusion in statistical classifiers will greatly reduce the accuracy of the result. In this work, intensity based thresholding and deep-learning based thresholding was used. In intensity thresholding, the background is obtained by selecting the pixels that satisfy a rule, such as a minimum intensity at a specific or multiple wavenumbers. The pixels that do not satisfy the condition are set equal to zero. Deep learning based approaches are tailored to noisy images where intensity thresholding often fails. These algorithms are typically based on convolutional networks that were trained on noisy pairs of labelled and unlabelled data in order to segment the signal from the background. In this thesis, the Cellpose[109, 110] model was used for cell segmentation using the "cyto-3" pretrained model.

5. Development of opto-electronic system

5.1 Optical system

5.1.1 Laser Sources

The main component of the broadband CARS system is a mode-locked master oscillator pump amplifier (MOPA) laser (FemtoFiber Pro NIR, Toptica). During all experimental work, custom eye protection was used to prevent accidental exposure to the laser radiation. The oscillator diode emits with a fundamental wavelength of 1550 nm. This source is passively mode-locked using a semiconductor saturable absorber mirror. The seed emission is amplified using an erbium doped fiber amplifier (EDFA) and the pulse repetition rate is 40 MHz. The seed is frequency doubled using second harmonic generation in periodically-poled Lithium Niobate (PPLN). This results in a flat-top pulse at approximately 770 nm with an approximate duration of 3.4 ps. This source acts as the narrowband probe beam. The amplified seed is also split and coupled using an optical fiber in to a separate module (FemtoFiber UCP) consisting of a highly nonlinear fiber (HNF). The pulse emerging from the HNF spans from approximately 1000-1400 nm with a duration of $\approx$ 50 fs. This pulse passes through an SF10 prism compressor and then exits the module. This pulse acts as the broadband beam. Both laser arms include separate EDFA stages for additional gain.

It was determined that the internal SF10 compressor within the UCP module did not sufficiently reduce the group velocity dispersion in the broadband beam. This was based on initial tests of the four-wave mixing in glass. Thus, the internal pulse compressor was bypassed and an external 6

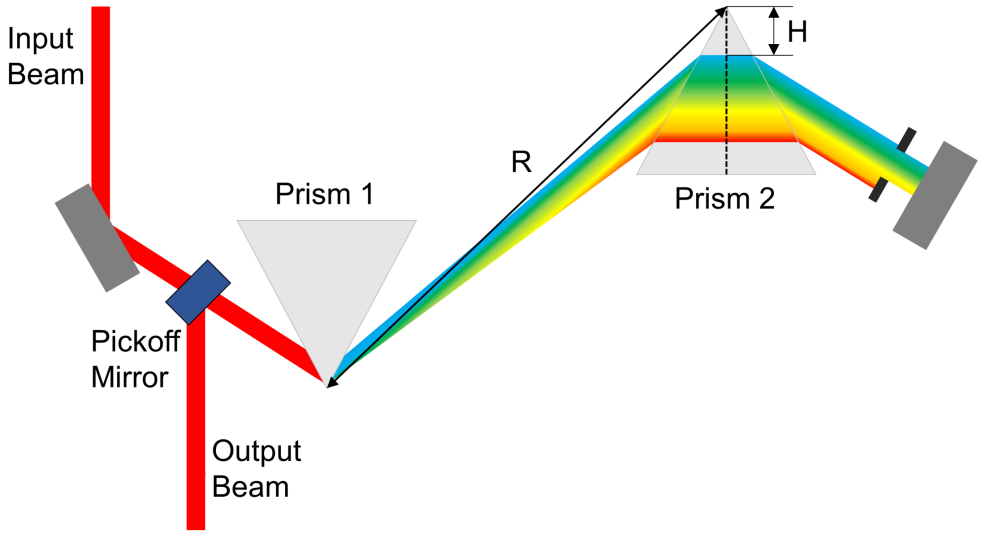

Figure 5.1: Diagram of the two-prism pulse compressor. H is the insertion of prism 2, calculated as the distance from the relevant blue side of the Stokes dispersed beam to the apex of the prism. R is the distance between apices.

cm SF10 prism pair (Laser Components (UK) Ltd) compressor was constructed with a motorized stage for fine tuning of the dispersion. These prisms were significantly larger in base height than the internal prisms, allowing for finer dispersion control. The prisms were equilateral in shape and the optimal distance (from each apex) was found to be 60 cm after several iterations. A diagram of the setup of a typical compressor is shown in figure 5.1, however the geometry used had a further optimized design including two anti-parallel mirrors for a reduced footprint. In order to find the level of prism insertion that corrected the group velocity dispersion, pulse shaping of the broadband Stokes source was performed using a non-iterative procedure described below. In order to control the spectral width of the broadband beam, a NIR spectrometer was placed after the compressor, and two knife-edge filters were placed in the Fourier plane of the compressor. These provided fine control of the spectral bandwidth of the Stokes pulse. The probe laser was filtered using a 766 band-pass filter (BPF) that acted as a long-pass filter, preventing the transmission of the fundamental 1550 nm source. A 2$\times$ beam expander was also used to overfill the microscope objective with the probe beam (2.4 mm diameter) for optimal focussing. This was not detrimental to the average laser power at the focus, since there was attenuation of the narrowband beam required in order to prevent sample photodamage. The Stokes beam was 4 mm in diameter.

The separate sources were combined using a dichroic mirror (DMSP950, Thorlabs) and then

coupled in to a light transmission microscope system (BX51, Olympus). This microscope is not a laser microscope and is typically used for material inspection in quality control environments. Thus, significant novel modifications were required to convert it into a BCARS microscope. Although the BX51 operates in transmission mode, it is designed for white light/fluorescence imaging. In order to allow enough room for a focussing objective beneath the sample, the lower condenser lens was removed and the manual positioning stage was also removed. This allowed the placement of a laser objective and two motorized stages in the focal plane for image scanning. The coarse stage was an ASI MS-2000 XYZ stage that had a range of 120 mm by 110 mm. This was a DC servo stage and thus the repeatability of movement was < 700 nm. This stage was used for targeting samples using the imaging camera. The second stage was a P-545.xR8S PInano XYZ stage that had a range of 200 by 200 μm and repeatability of 1 nm. Both stages were controlled in software using a custom script developed in MATLAB. The focussing objective was an UPlanSApo 60x/1.2 NA (Olympus) and was custom mounted to the prior sample stage. This had a coarse and fine translation wheel for vertical axis movement. The focussing lens also had a high transmission over the NIR range. The collection objective was varied depending on experiment but typically a 20x/0.46 NA UmPlanFl (Olympus) was used. It should be noted that contrary to spontaneous Raman imaging, a higher NA collection objective serves limited advantage for BCARS because the anti-Stokes beam is highly directional. Thus, typically a longer working distance can be achieved with little loss of collection efficiency. After the collection objective, light is typically directed to the eyepiece or to the CCD module of the BX51. In order to get access to the transmitted beam for spectroscopy a custom mirror was mounted within the rotating turret that directed the transmitted beam to the side of the microscope. A hole was drilled in the side to allow the light to exit the microscope. A diagram of the adapted platform is shown in figure 5.2. The output from the microscope is then coupled into an Andor Shamrock 500i (Czerny-Turner) spectrograph using an achromatic doublet lens (AC080-020-B-ML, Thorlabs). The spectrograph contains a rotating turret containing three diffraction gratings at 300 l/mm, 600, l/mm and 1000 l/mm. The specifications for each grating are shown in table 5.1.

A delay line consisting of two mirrors on a motorised stage provides fine control of the narrow-band pulse delay relative to the broadband pulse. A diagram of the optical system is shown in figure

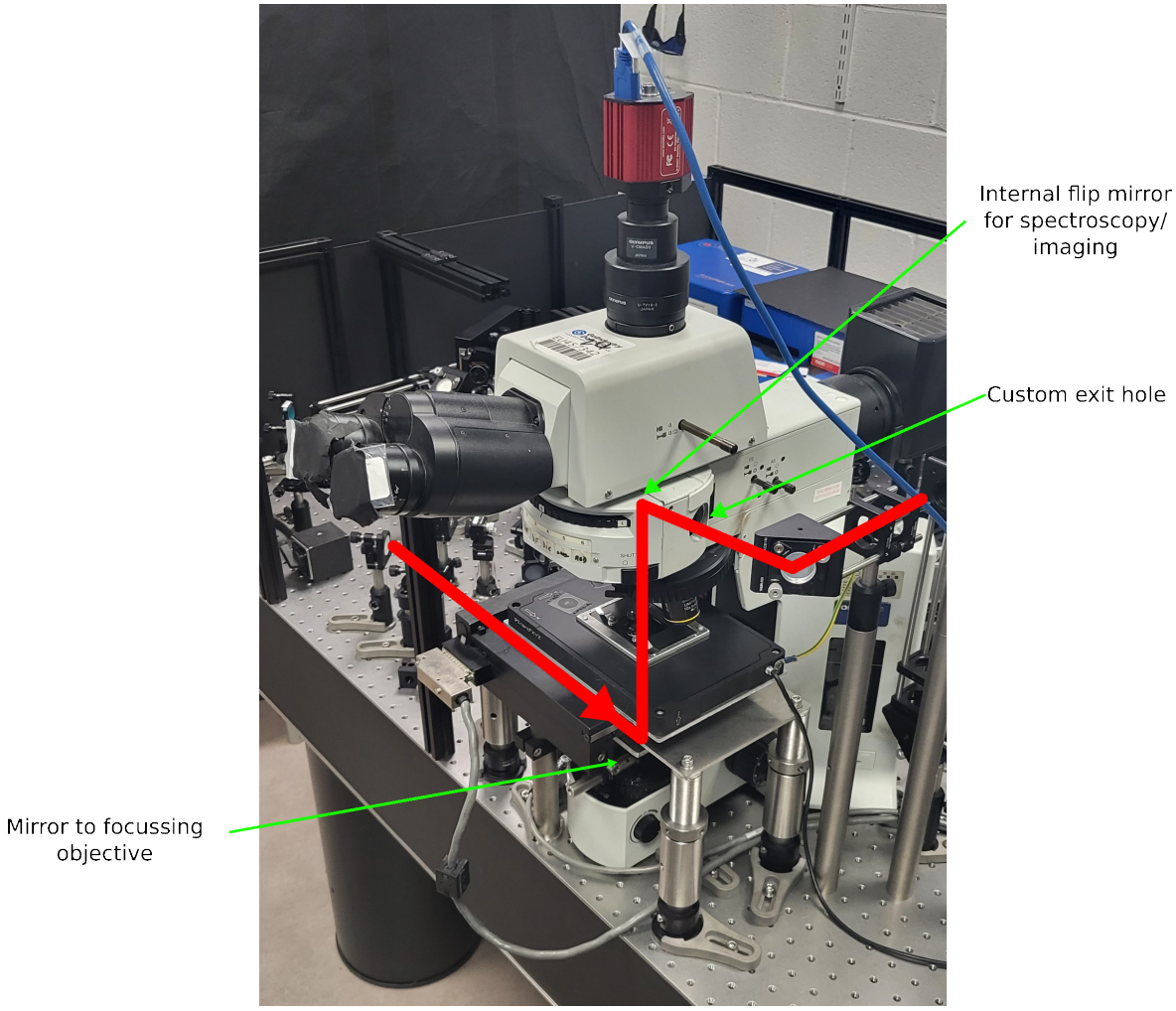

Figure 5.2: Image of the BCARS microscope platform using a modified BX 51 platform. The laser path is shown in red and enters from below.

5.3. Prior to entering the microscope there are also two additional components used to optimize the beam parameters of the collinear beams. First, there is a Cassegrain beam expander used to expand both beams by 2x[111]. This allowed optimal expansion of the broadband beam in order to match the aperture of the focussing microscope objective without introducing dispersion. The design of the expander also minimizes astigmatism at a particular tilt angle which is required for microscopy. The second element after the expander is a piezoelectric deformable mirror (DMP40/M-P01). This mirror can control the Zernike polynomials Z_1 to Z_{14} (ANSI index) using software. Thus, the mirror can correct any residual astigmatism aberration in the beam due to the Cassegrain telescope. The Cassegrain could also precompensate for spherical aberration due to varying thickness of samples.

Grating (l/mm)	Blazed optimized wavelength (nm)	Bandwidth (nm)
300	760	177.3
600	750	89.11
1000	900	52.83

Table 5.1: Diffraction gratings used in the BCARS spectrograph.

In order to measure the astigmatism in the beams, a BCARS intensity scan was measured in glass as the depth was varied. The astigmatism would result in a bimodal maximum of the integrated spectrum due to the two foci. To correct for this, the weight of the Z_5 polynomial was varied using a grid search and the intensity profile measured. A diagram of the optical system is shown in figure 5.3.

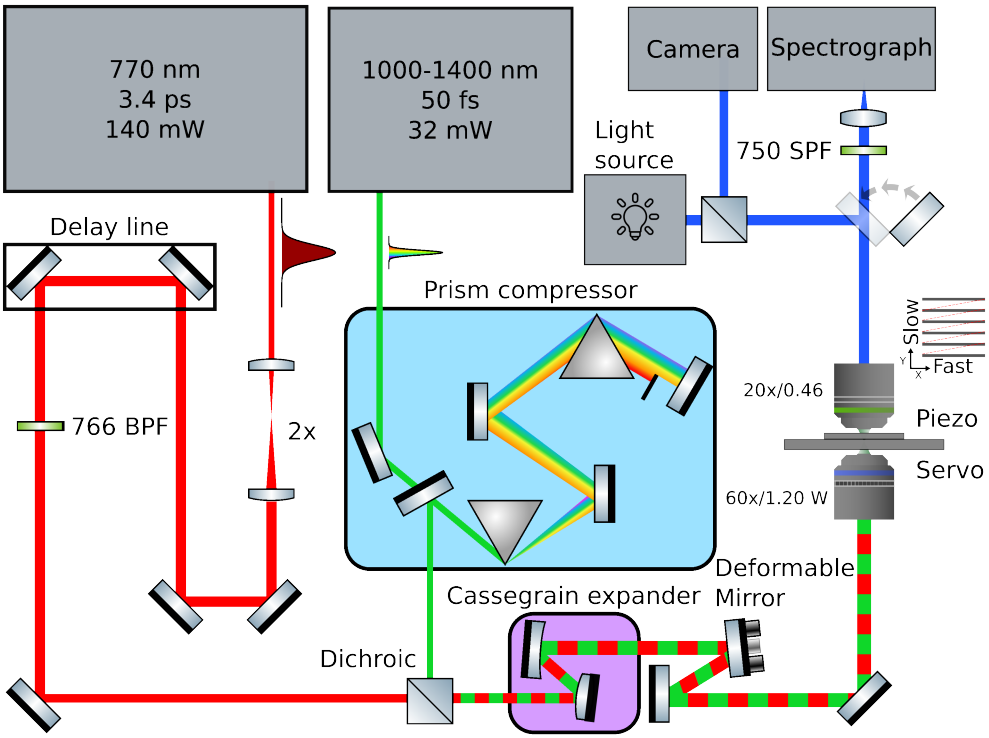

Figure 5.3: Diagram of the BCARS Spectroscopy System. The narrowband probe beam is in red and the broadband Stokes beam is in green. BPF: band-pass filter, SPF: short-pass filter.

5.1.2 Optical resolution

When performing nonlinear microspectroscopy the intensity profile in each dimension of the focal volume, referred to as the point spread function (PSF) is exponentiated to the order N of the nonlinearity[112]. Thus, using the the Rayleigh criterion, the spatial resolution is given as

$$d^{(N)} = \frac{1}{\sqrt{N}} \frac{0.61\lambda}{\text{NA}} \tag{5.1}$$

where λ is the wavelength of the focused light and NA is the numerical aperture of the focussing lens. The depth of focus is also given as

$$z^{(N)} = \frac{1}{\sqrt{N}} \frac{2n\lambda}{\text{NA}^2} \tag{5.2}$$

where n is the refractive index of the medium. At a wavelength of the probe pulse in this work (770 nm) and NA of 1.2, the CARS ($N = 3$) focal radius is 0.225 μm and the depth of focus in air is 0.617 μm. The lateral area of the focal spot is then 0.159 μm^2. Single biological cells vary in size from 5 μm for red blood cells to 1 m for neurons[113]. However in this thesis, the application is oriented towards obtaining chemical information from the primary cells studied in cytopathology; epithelial cells[114]. Across 15 different epithelial cells, Devany *et al.*[115] reported the average cell volume using measurements from over 50 cells. The mean cell volume across all cell types was 629 μm^2. Assuming a spherical shape, this results in a diameter of approximately 10.6 μm. However, the shape of many epithelial cells are squamous or cuboidal and arrange in flat sheets. This results in an actual diameter of roughly 10-20 μm. When such cells are grown on glass in culture, the size also varies according to the osmolarity of the culture medium. Nevertheless, in BCARS microscopy, the focal area as calculated above, is typically much smaller than the cell size, allowing for the imaging of sub-cellular components such as nucleoli, lipid droplets and the golgi apparatus within cells.

5.2 Optical Pulse Characterisation of the Sources

Characterisation of the input beams is crucial when optimising a four-wave mixing process such as that used in CARS scattering experiments, since the spectral output intensity (I_{CARS}) of the CARS signal is proportional to the product of the electric fields of the three input pulses. The accurate measurement of the Stokes (broadband) beam electric field $E_S(\omega)$ was the most difficult task, since this pulse is generated in the nonlinear fiber using multiple non-linear processes, which alter the time-frequency profile of the pulse greatly. Thus, the Stokes pulse is not transform limited in nature and the temporal complexity prevents simple methods such as intensity autocorrelation from being used to characterise it.

In this work, the Stokes pulse was characterised using the Cross-Correlation Frequency Resolved Optical Gating (XFROG) technique with the four-wave mixing interation used as the nonlinear process. It is thus termed FWM-XFROG. As described in section 3.4.4 XFROG uses a reference pulse to measure an ultrashort pulse and in this case, the reference pulse was the narrowband beam. Although not technically fully characterised, the narrowband pulse spectrum was assumed to be known. The spectral phase was also assumed to be flat since the pulse duration was in the picosecond range. The narrowband and broadband beams were coaxially focused on to a glass slide. Two-dimensional time-frequency spectrograms were constructed by spectrally recording the output four-wave mixing signal as a function of the time-delay between the probe and Stokes Beams by using the optical delay line on the probe beam.

In this implementation of FWM-XFROG, the probe delay, τ, is scanned over the full temporal envelope of the unknown pulse and the BCARS signal in a non-resonant sample (such as a glass coverslip) at each delay $I_{\text{XFROG}}(\omega, \tau)$ is measured. Only the 2-colour interaction was recorded since the two regions do not overlap spectrally. The recorded signal is given by[90]:

$$I_{\text{XFROG}}(\omega, \tau) = \left| \int_{-\infty}^{\infty} \tilde{E_S}(t) \cdot \tilde{E}^2_{pr}(t - \tau) e^{-i\omega t} dt \right|^2 \tag{5.3}$$

where $\tilde{E_S}$ and $\tilde{E}_{pr}$ are Fourier transform pairs of E_S and E_{pr}. According to equation 5.3, in the two-colour interaction, the time-marginal of the spectrogram is equivalent to the Stokes spectral

amplitude due to the linear relation between the recorded signal and the Stokes pulse intensity for each delay

$$I_S(\omega) = \int I_{\text{XFROG}}(\omega)\, d\tau \tag{5.4}$$

The conversion from the XFROG wavelength to the Stokes Wavelength is given by

$$[\lambda_S] = \Big(\frac{2}{\lambda_p} - \frac{1}{\lambda_{\text{CARS}}}\Big)^{-1} \tag{5.5}$$

which is given from the energy conservation law for the four-wave mixing relation.

$$\omega_{\text{CARS}} = \omega_{\text{p}} + \omega_{\text{pr}} - \omega_{\text{S}} = 2\omega_{\text{p}} - \omega_{\text{S}} \tag{5.6}$$

To obtain the spectral phase of the Stokes pulse $\varphi(\omega)$, the group delay as a function of frequency $t_{\text{gd}}(\omega)$ is first determined. A cross-correlation of each frequency in the spectrogram with a particular reference frequency yields another 2D matrix denoted $C(\tau, \omega)$, with the location of the maximum of each frequency describing the relative temporal delay of the pulse with respect to the reference frequency.

$$C(\tau, \omega) = S(\tau, \omega) \star S(\tau, \omega = \omega_{\text{ref}}) C(\tau, \omega) \tag{5.7}$$

thus, the relative group delay is given as

$$t_{\text{gd-rel}}(\omega) = \underset{\tau}{\text{argmax}}[C(\tau, \omega)] \tag{5.8}$$

The relative group delay was then shifted such that the reference frequency used ω_{ref} corresponded to zero relative delay. Once $t_{\text{gd}}(\omega)$ is known, the spectral phase can be determined, since

$$t_{\text{gd}}(\omega) = \left(\frac{d\varphi}{d\omega}\right)_{\omega} - t_{\text{gd}}(\omega_{\text{ref}}) \tag{5.9}$$

From the group delay, the relative spectral phase of the Stokes pulse is found directly

$$\varphi(\omega) = \int_{\omega_0}^{\omega} t_{\text{gd}}\, d\omega \tag{5.10}$$

The Stokes pulse is then reconstructed

$$E_S(\omega) = \sqrt{I_S(\omega)}e^{i\varphi(\omega)} \tag{5.11}$$

The probe pulse intensity can also be obtained from the spectrogram, since for each frequency, the XFROG intensity is proportional to the square of the probe intensity. The electric field of the probe can then be found as follows:

$$\tilde{E}_{pr}(t) = \sqrt[4]{I_{\text{XFROG}}(t)}e^{\omega_l t} \tag{5.12}$$

where ω_l is the probe carrier frequency obtained from a spectrometer measurement. $E_{pr}(\omega)$ can be obtained from this function via a Fourier transform. The result of the pulse characterisation procedure on the uncorrected broadband pulse is shown in figure 5.4. In (a) the spectrogram is shown. A linear chirp can be observed due to group velocity dispersion. This is the strongest phase distortion in the pulse. There is also however noticeable third-order dispersion (TOD) that causes a nonlinear variation of instantaneous chirp. In (b), the probe temporal intensity is shown, as obtianed from the frequency marginal at a wavelength of 594 nm. In (c), the retrieved Stokes electric field is shown and the quadratic phase profile across the spectrum is evident. (d) shows the Stokes pulse in time and the amplitude is seen to have a complex structure due to the chirp, TOD and possibly higher order dispersion.

In figure 5.5 (a), the spectrogram of the Stokes pulse after pulse compression optimization is shown. Here, the pulse energy is confined to a minimum duration and there is no apparent variation of the mean optical intensity over the frequency range of the pulse. It is also observed that the spectral width changed drastically. This is due to a modification of the knife-edge filter and pre-HNLF prism insertion that affects the spectral output of the Stokes pulse from the laser. During this optimization, the narrowband spectral width was also changed by varying the BPF filter incidence angle manually, this changed the duration of the probe pulse as can be seen in (b). In (c), the retrieved Stokes electric field is shown and the phase is almost flat everywhere except for the region from 900-990 nm and 1240-1350 nm. Although not ideal, the phase variation is still very low over the support of the pulse and thus these do not drastically affect the pusle length. It is likely that these are due to high order dispersion that emerges from the supercontinuum after the fiber. The

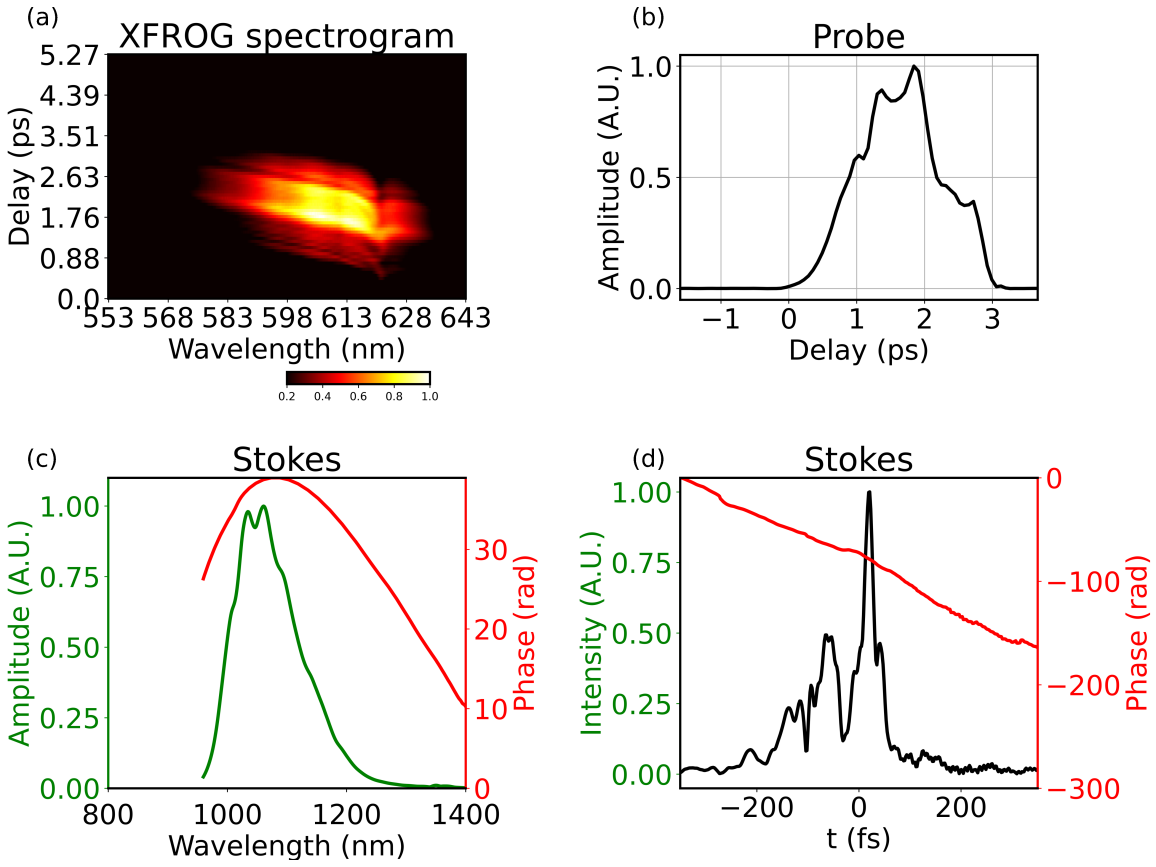

Figure 5.4: XFROG spectrogram of an uncorrected broadband pulse using an acquisition time of 50 ms.

pulse temporal amplitude and phase are shown in (d) and the achieved full width at half maximum was $\approx$ 20 fs.

5.2.1 Adjusting chirp for increased fingerprint bandwidth

The above pulse characterisation and optimization procedure describes an optimal way to obtain the shortest pulse (through minimizing GVD only) using a prism compressor. The obtained pulse does not correspond to a transform-limited pulse, since only GVD can be corrected, and cubic and higher phase variations will almost always exist. However, in this work, it was found that while the GVD-corrected pulse provided a useful stimulation profile (region over which vibrational resonances are amplified and can be measured), adding a slight insertion of the second prism provided a better bandwidth for the stimulation in the upper part of the fingerprint region ($>$ 1500

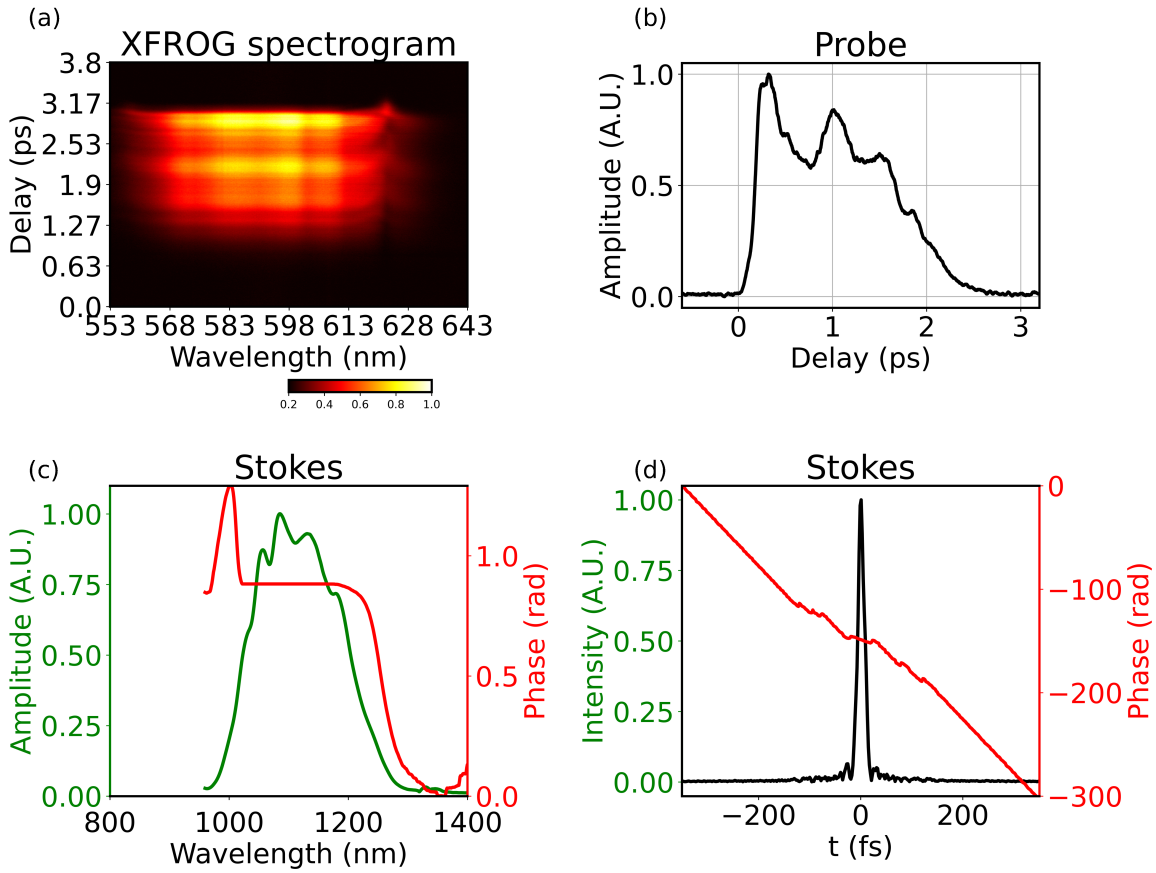

Figure 5.5: XFROG spectrogram of a corrected broadband pulse using an acquisition time of 50 ms.

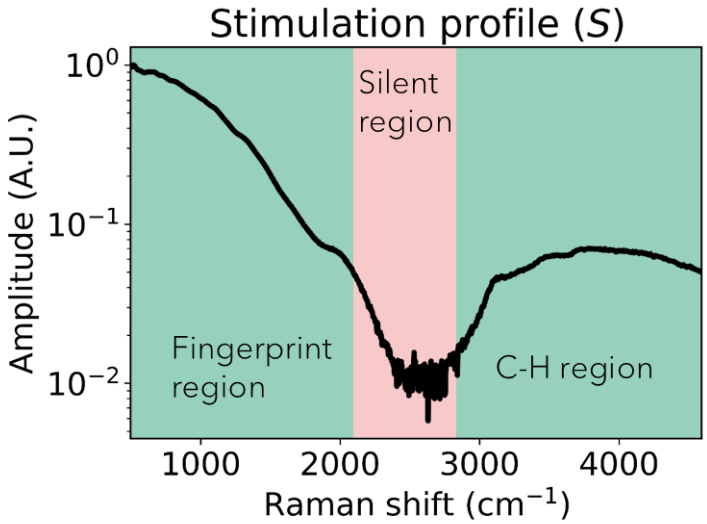

Figure 5.6: Stimulation profile obtained from a measurement of BCARS in a glass coverslip.

cm^{-1}). This insertion corresponded to a positive GVD being introduced and did reduce the intensity of the stimulation profile in the region from 0-600 cm^{-1}, but since this is already the maximum intensity of the profile (assuming a transform limited pulse), a slight loss of amplitude did not impact spectroscopic results. The reason for such an improvement in the BCARS bandwidth is likely because of both the increased TOD present from the glass that causes a skew in the Stokes spectrum and also an increase in the upper wavelength range of the Stokes pulse as it intercepted the second prism. The upper part of the fingerprint region contains several vibrational resonances in biological cells that otherwise would go undetected since the stimulation profile approached the noise floor in the GVD-corrected case. A measurement of the four-wave mixing signal in glass is shown in figure 5.6. It can be seen that there are two distinct regions of finite spectral intensity, in the fingerprint region (500-1800 cm^{-1}) and in the CH region (2800-3000 cm^{-1}) which correspond to the simulated BCARS spectra in figure 4.1. Notable is the slight increase in intensity around 2000 cm^{-1} due to the increased prism insertion.

5.3 Photodamage management in biological cells

In this thesis, all cell samples were fixed using a conventional formalin washing procedure before imaging. When imaging any material with focussed lasers, it is paramount that the potential for laser induced damage on the sample is managed in order to obtain repeatable results and prevent sample destruction. The average power of the probe beam on-sample in a typical microspectroscopy experiment was 10 mW. Thus the average irradiance is approximately 62 kW/m^2, using the focus area calculated in section 5.1.2. The peak power of the probe pulse at 40 MHz repetition rate and pulse duration of 3.4 ps was 73 W and the pulse energy was 0.25 nJ. The average power of the broadband (Stokes) pulse was 6mW on-sample. The peak power of the broadband pulse at 40 MHz repetition rate and pulse duration of 25 fs was 6 kW and the pulse energy was 0.15 nJ.

In order to prevent damage due to the lasers, it is useful to determine the most likely form of damage. There are three main types of laser induced damage, photothermal absorption, photochemical effects and photoionization. These are described in table 5.2. Photothermal absorption is the

Damage Type	Description	Relevance in Biological Media
Photothermal	Heat production	Single-photon absorption unlikely in NIR
Photochemical	Creation of new species	Can damage live cells
Photoionization	Formation of plasma	Damage can occur at 0.1-30 nJ/pulse

Table 5.2: Most common laser induced damage mechanisms in biological media.

production of heat from photon absorption. However, since biological media are weakly absorbing in the NIR, one-photon absorption is unlikely to cause damage. Multiphoton absorption is however possible in BCARS since broadband sources are used and in order to prevent this, continuous movement of the sample was used during imaging. This resulted in a very short time of laser exposure in one area of the sample. Photochemical effects can induce the production of new species in the cell due to the breaking of chemical bonds, since the laser light can supply the bond activation energy. In living cells, this can result in the creation of reactive species that can damage the cell. However, in fixed cells, the specimen does not contain active biochemical reactions that would be susceptible to such reactive species. The third kind of damage can be caused when an ultrashort pulse causes highly localised plasma formation in the material. The rapid expansion of the plasma can create a localized micro-explosion and pressure wave. This interaction can happen even at energies where the photon would not be absorbed. The threshold for biological damage due to photoionization using 100 fs pulses is 0.1-30 nJ/pulse[116]. Thus for this work, at the above used pulse powers of 10mW for the narrowband beam and 6 mW for the broadband beam on-sample, no laser-induced photodamage was expected. The optical system described in this chapter underpins all of the results presented in this thesis. The scripts developed for scanning provided a very quick turn-around time for analyzing a study. Alignment of the BCARS microscope took approximately 30 minutes, including time for the lasers to warm up and become stable. After alignment, a sample of interest was placed on the stage and a region of interest was centered over the laser using the reflection imaging capability. Hyperspectral images could be then obtained by running the necessary script. In the next chapter, the main results of the application of the BCARS opto-electronic system will be presented.

6. Convolutional Autoencoders for blind NRB removal: VECTOR

This chapter is based on the published article entitled "VECTOR: Very deep convolutional autoencoders for non-resonant background removal in broadband coherent anti-Stokes Raman scattering" published in the Journal of Raman Spectroscopy[22]. This chapter was the first project of my thesis. My contributions to the results presented in this chapter were as follows; conceptual design of the simulation of BCARS spectra for training a deep neural network, applying the theory of conventional phase retrieval for analysis of the performance of the approach taken to NRB removal and data analysis of the results of the neural network on simulated spectra.

As mentioned in section 4.4, obtaining physically meaningful data in a BCARS experiment is tantamount to solving an ill-posed problem with considerable amounts of noise present in the data. In imaging applications, it is simply not possible to increase the acquisition time to remove noise since high-speed imaging requires low pixel dwell times. Furthermore, even if noise could be entirely removed, the NRB would remain a difficult problem to overcome, since it interfered with the resonant signal in a complex manner. The coherent interference between the non-resonant background (NRB) and the vibrationally resonant response leads to asymmetric lineshapes in BCARS signal intensity, which can obscure the relative concentration of different species. This characteristic of BCARS is a well-known limitation, for which various experimental and mathematical methods have been developed to address it, and for this reason stimulated Raman scattering is often preferred to CARS for imaging because it does not have an NRB. Experimental approaches to NRB removal in BCARS

include techniques such as adjusting the excitation and detection polarization angle (P-CARS)[20], frequency-modulation CARS (FM-CARS)[117], and time-resolved CARS (T-CARS)[118]. While these methods are effective, they increase the complexity of the measurement and, in some cases, may reduce the resonant contribution during the process.

As mentioned in section 4.4, the conventional methods for recovering the resonant susceptibility involve using BCARS intensity data and the mathematical relationships between the phase and intensity of the BCARS signal. One such technique leverages the fact that susceptibility adheres to causality, allowing the Kramers–Kronig relations to be used in a BCARS measurement to determine the phase of $\chi^{(3)}$, as shown by Liu *et al.*[104]. In practice, this approach requires pre-processing the spectra, either through singular value decomposition for denoising and spectral encoding, as demonstrated by Masia *et al.*[119], or through baseline correction of the retrieved phase to account for errors arising from the finite frequency range of actual measurements and the use of surrogate NRB[1].

The other common post-processing NRB removal approach, the maximum entropy method (MEM)[120, 121] also requires prior knowledge of at least two points in the spectrum where the phase is known for accurate retrieval, as well as an NRB measurement. Since baseline correction is a supervised process and the MEM requires prior information, both the KK and MEM methods must be supervised for Raman signal extraction. Therefore, current mathematical approaches are not suitable for bulk phase retrieval of unknown BCARS spectra. Furthermore, the application of the conventional phase retrieval methods to experimental data such as single cell data requires manual tuning of algorithm hyperparameters which reduces the applicability of imaging to instances where expert knowledge of the algorithm is available. The second and possibly greater drawback of current conventional methods is the requirement for a measurement of the NRB signal, typically obtained from a microscope slide or coverslip that ideally has no vibrational resonances within the measurement window. However, these materials contain vibrational and other electronic resonances outside the window, and even far from tuning they can perturb the measurement of the NRB. The reference NRB measurement serves to remove the effect of the laser excitation profile S which may vary over the whole spectrum and in conventional methods, the effect of the convolution with the

probe pulse E_{pr} is typically ignored.

In BCARS, the two main problems that are required to be overcome are phase retrieval and mixing with an unknown excitation profile. These two tasks are suited to deep learning (DL), especially in the presence of noise. DL approaches to NRB removal using a network comprised of convolutional and fully-connected layers has been previously published and shown good promise[122]. This approach was tested on simulated and experimental measurements of different solvents. The main problem with this approach was when the resonant to non-resonant amplitude ratio approached that typical for biological samples i.e when $\chi^{(3)}_{\text{Res}}/\chi^{(3)}_{\text{NRB}} \ll 1$. In this case the retrieved spectrum significantly differed from the underlying Raman spectrum. During the time of writing this section, there were further developments in deep learning for NRB removal in BCARS data. Long short-term memory (LSTM) networks were also applied to this task[123], with their performance evaluated on real spectra. Saghi *et al.*[124] later demonstrated enhanced retrieval by training on semi-synthetic data and fine-tuning a pre-trained network. They also compared this methods performance to the MEM approach. The semi-synthetic data were generated from actual Raman spectra recordings, with the NRB simulated using sigmoid functions. The approach taken in this work was to use fully convolutional layers in a specific architecture known as an autoencoder, to perform the NRB removal using the BCARS spectrum only.

6.1 Convolutional Autoencoder Architecture

Convolutional neural networks (CNN) have shown great promise for blind deconvolution because of their ability to learn patterns in specific signal domains[125]. The accuracy of CNNs in denoising, classification, object detection and image generation is unparalleled[126]. Thus, it was hypothesized that an approximate signal that was free from the NRB could be obtained by training a deep CNN without the need for a reference NRB measurement. A CNN is comprised of convolutional layers, which are followed by fully connected layers and have been shown to be particularly useful in identifying patterns within images with spatial invariance. A convolutional layer represents a sequence of element-wise convolutions using kernels (filters) w of size $F_q \times G_q \times d_q$ applied to the

input data. The convolution operation h from the q^{th} layer to the $q+1^{\text{th}}$ layer can be stated as[127]

$$h_{ijp}^{q+1} = \sum_{r=1}^{F_q} \sum_{s=1}^{G_q} \sum_{k=1}^{d_q} w_{rsk}^{(p,q)} h_{i+r-1,j+s-1,k}^{(q)} \tag{6.1}$$

where i and j denote the spatial positions and p denotes the filter depth. It can be seen from equation 6.1 that the result of applying a convolutional layer is to dot product the input with a filter over the entire filter volume. In the application of a CNN to spectra, the spatial size of the input is governed by the spectral axis. For a spectrum with 1024 individual pixels, $F_q = 1024$ and $G_q = 1$. Thus, the filters are applied 1-dimensionally. The dimension d_q is typically referred to as the depth of a layer, and corresponds to d_q independent filters being applied. In order to train a CNN, a signal is propagated through the network, at each layer convolution and possibly other operations are applied. After each propagation, a loss is calculated, which is related to the goal of the training, and by changing the filters in a structured way so as to minimize this loss, the CNN "learns" the problem.

In this work, a specific type of CNN was used known as an autoencoder (AE), which was named VECTOR, named for Very deep convolutional autoencoders for non-resonant background removal in broadband coherent anti-Stokes Raman scattering. An AE is a neural network with three main components; (1) an encoder, (2) a bottleneck and (3) a decoder. The main goal of an autoencoder is to take an input and encode it in to an efficient representation, from which the input is then reconstructed. An efficient representation is a type of compression of the data which is as close to the original input as possible. The 1-D spectrum is propagated through n_{encoder} convolutional layers to a representation of reduced spectral dimension known as the latent space. This representation is then decoded using transposed deconvolution through n_{decoder} layers. This is the typical structure of an autoencoder. Since the output should be the same size as the input, $n_{\text{encoder}} = n_{\text{decoder}}$ and layers of equal depth are paired in size. Batch normalization[128, 129] and ReLU[130] are added to each convolutional layer and transposed convolutional layer except for the last layer in the decoder which is the same size as the output. After this layer, a sigmoid function is applied which restricts the range of the output to $[0, 1]$.

The loss function of an autoencoder is traditionally a vector p-norm of the difference between the input and output of the network. This would result in the network trying to approximate the input

using an efficient representation. However, in our application, we intended to use an autoencoder to apply a transform to the data to retrieve the NRB-free spectrum from a BCARS spectrum. Thus, the mean absolute error (MAE), also known as the L_1 norm, between CARS spectra and the Raman spectrum was used as the loss to train the network in an end-to-end manner. Equation 6.2 describes the loss function used

$$L_1 = \frac{1}{N}\sum_{i}^{N} |f(\mathbf{X}_i;\theta) - \mathbf{Y}_i|^2 \tag{6.2}$$

where $\mathbf{X}_i$ is CARS input spectrum, $\mathbf{Y}_i$ is the Raman spectrum, f is the network, and θ represents the network parameters, which have been optimized by the training process with no a priori knowledge. Skip connections were also implemented between all convolutional layers to their paired transposed-convolutional layer, where output feature maps are passed and summed to the corresponding input. Skip connections are used to mitigate the vanishing gradient descent to bottom layers[131]. The vanishing gradient problem is well known in deep learning. A brief summary of the issue is as follows. During the training stage of the network, backpropagation computes the gradient of the loss with respect to the parameters using the chain rule, which results in multiplying n small numbers to compute the gradients of early layers in an n-layer network. Skip connections allow information to bypass early layers which can reduce the effect of vanishing gradients. An example of a skip connection in a residual block from the architecture known as ResNet[132] is shown in figure 6.1.

In addition to the vanishing gradient problem, increasing the depth of the autoencoder architecture may result in the loss of crucial input information, making it unrecoverable through the

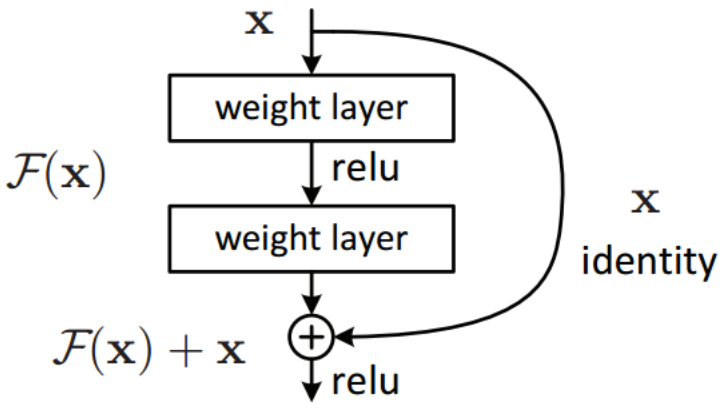

Figure 6.1: Diagram of a residual layer[132].

encoding and decoding processes. Skip connections facilitate the recovery of such information. As mentioned above, the VECTOR network was designed symmetrically, pairing each convolutional layer in the encoder with a corresponding transposed convolutional layer in the decoder. This arrangement allows for connections that bypass one convolutional layer to reach its paired transposed convolutional layer. An added advantage of this symmetrical skip connection is that it eliminates the need for padding. In this study, the number of skip connections matches the number of layers in both the encoder and decoder. The basic layout of VECTOR is shown in figure 6.2 VECTOR

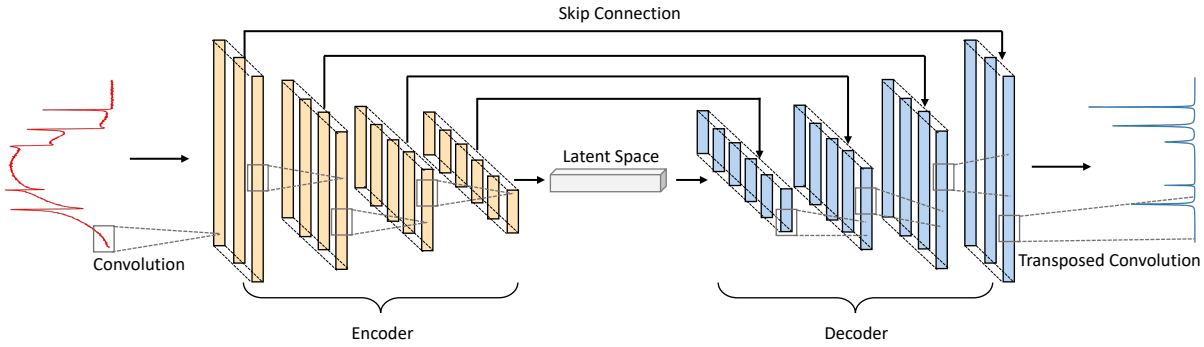

Figure 6.2: Diagram of the general architecture of the VECTOR network. Each layer in the encoder and decoder consists of multiple convolutional kernels of varying size (coloured rectangles). The network input is to the left and proceeds toward the right.

is an architecture, and in this work we built several distinct networks of varying complexity using the architecture described. The individual networks were different in the number of convolutional layers used e.g. VECTOR-16 had 16 convolutional layers. In this work, one of the main goals was to determine the optimal depth (number of layers) for NRB removal.

6.2 Generating training data

VECTOR was trained using a dataset of simulated CARS spectra, as it enabled us to generate pairs of ground truth Raman and BCARS data. The algorithm's effectiveness was evaluated by training it on several different datasets with varying complexities. These datasets differed in terms of the number of Raman peaks per spectrum and the variations in the full-width half-maximum (FWHM) of the peaks. This distinction is particularly relevant due to the diverse types of Raman spectra encountered in various applications. For instance, chemical and pharmaceutical samples

typically exhibit sharper peaks that can be clearly identified, whereas biological samples, such as cellular spectra, tend to show broader peaks that create a more complex mixture of wide and narrow features[133, 36].

The resonant susceptibility was generated according to equation 6.3 and was represented as a sum of Lorentzian functions.

$$\chi^{(3)}_{\text{Res}} = \sum_{n=0}^{N_{\text{peaks}}} \frac{A_n}{\Omega_n - \omega - i\Gamma_n} \tag{6.3}$$

where Ω_n is the vibrational frequency, A_n is the amplitude, Γ_n is the half-width and ω is the independent frequency. The axis over which the resonances were generated was defined as a linear function of wavenumber over 0.1 to 2000 cm^{-1}. For each Lorentzian function, the peak amplitude is a uniformly random value between 0 and 1, with resonant peaks located between 300 and 1700 cm^{-1} and a FWHM of 2 cm^{-1}.

Nine datasets were created, varying in peak widths and the number of peaks per spectrum, labeled (i–ix). Each spectrum consists of 1000 datapoints spanning 2000 cm^{-1}. The FWHM ranges from low (2–10 cm^{-1}) in datasets (i–iii), to moderate (2–25 cm^{-1}) in (iv–vi), and high (2–75 cm^{-1}) in (vii–ix). The datasets are further categorized by the number of spectra: datasets (i, iv, and vii) contain between 1 and 15 peaks per spectrum, (ii, v, and viii) have between 15 and 30 peaks, and (iii, vi, and ix) consist of 30 to 50 peaks. The simulation datasets are summarised in table 6.1.

Table 6.1: Spectral parameters of each dataset.

Dataset	Γ_{min} (cm^{-1})	Γ_{max} (cm^{-1})	n_{min}	n_{max}
i	2	10	1	15
ii	2	10	15	30
iii	2	10	30	50
iv	2	25	1	15
v	2	25	15	30
vi	2	25	30	50
vii	2	75	1	15
viii	2	75	15	30
ix	2	75	30	50

The non-resonant susceptibility is generally described as an arbitrary, slowly varying function. In this instance, it was modeled as the product of two randomized, opposing sigmoid functions, as stated in equation 6.4.

$$\chi_{\text{NR}}^{(3)} = S_1(\omega) \cdot S_2(\omega) \tag{6.4}$$

where $S(\omega)$ was a sigmoid function given as

$$S(\omega) = \frac{1}{1 + \exp[-b(\omega + c)]} \tag{6.5}$$

where the parameters b and c were shape parameters of the sigmoids and were generated randomly as

$$c = \mathcal{N}(a_1\omega_{\text{max}}, a_2\omega_{\text{max}}) \tag{6.6}$$

$$b = \mathcal{N}(10\omega_{\text{max}}^{-1}, 5\omega_{\text{max}}^{-1}) \tag{6.7}$$

where $\mathcal{N}(\mu, \sigma)$ denotes a normal distribution with mean μ and standard deviation σ. The parameters a_1 and a_2 are given in table 6.2.

Sigmoid	a_1	a_2
S_1	0.2	0.3
S_2	0.7	0.3

Table 6.2: NRB generation parameters.

After generating both $\chi_{\text{Res}}^{(3)}$ and $\chi_{\text{NR}}^{(3)}$, the total third-order susceptibility was then generated as

$$\chi^{(3)} = \alpha \frac{\chi_{\text{Res}}^{(3)}}{\max(|\chi_{\text{Res}}^{(3)}|)} + \chi_{\text{NR}}^{(3)} \tag{6.8}$$

where α is a scaling parameter that determined the resonant to non-resonant amplitude. The parameter α was given as

$$\alpha = \mathcal{U}(k_{\text{min}}, k_{\text{max}}) \tag{6.9}$$

where $\mathcal{U}(x, y)$ denotes a uniform distribution from $k_{\text{min}} = 0.3$ to $k_{\text{max}} = 1$. The BCARS intensity

spectrum was then calculated as the magnitude square of the total third-order susceptibility, with additive Gaussian noise ϵ.

$$I_{\text{CARS}} = \frac{|\chi^{(3)}|^2}{2} + \epsilon \tag{6.10}$$

where the factor 2 scales the maximum possible value of I_{CARS} (without noise) to 1. The noise term was generated as

$$\epsilon = \beta \mathcal{N}(0, 1) \tag{6.11}$$

$$\beta = \mathcal{N}(\rho_1, \rho_2) \tag{6.12}$$

where $\rho_1 = 0.0005$ and $\rho_2 = 0.003$. The corresponding Raman spectrum was calculated as

$$I_{\text{Raman}} = \text{Im}(\chi^{(3)}_{\text{Res}}) \tag{6.13}$$

6.3 Training

The training set consisted of 200,000 spectra and the validation set consisted of 30,000 spectra. Experiments were conducted on nine synthetic datasets using the formulation described in Section 6.2. A comparison with a previous NRB removal study was also performed in order to interpret the accuracy of the developed network. For these evaluations VECTOR-16 was chosen as the default option, balancing computation time and performance. The full architecture diagram of VECTOR-16 is shown in appendix A. The models were trained using a TITAN Xp GPU, employing stochastic gradient descent (SGD) as the optimizer with a momentum of 0.9 and weight decay. The training batch size was set to 256. The initial learning rate was 0.1, which was decreased by a factor of 10 at the 25th, 50th, and 75th epochs, with training concluding at 100 epochs. The code was implemented in the Pytorch library and is available for free on GitHub[1].

Figure 6.3 illustrates the performance of six VECTOR architectures with varying depths, highlighting those with (red) and without (blue) skip connections. The Mean Absolute Error

[1] https://github.com/villawang/VECTOR-CARS

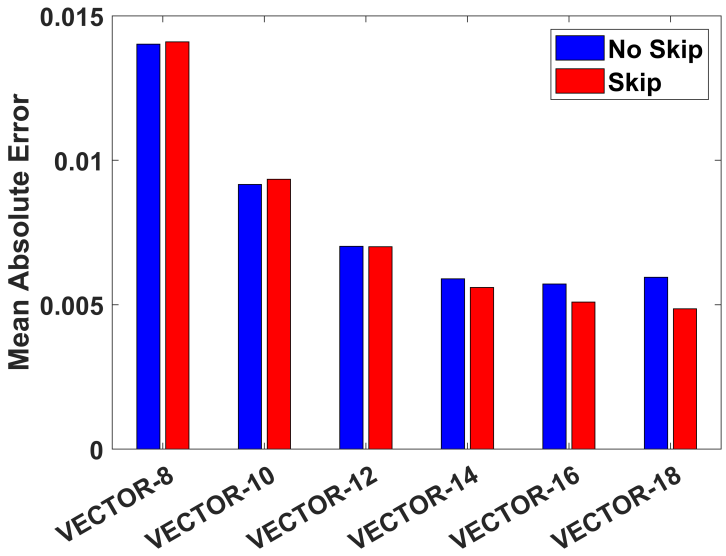

Figure 6.3: Loss for varying network depths using both skip connections and no skip connections.

(MAE) between the true Raman spectrum and the recovered Raman spectrum derived from the corresponding CARS spectrum in the validation datasets served as the performance metric for this study. Notably, architectures without skip connections demonstrate comparable performance for lower layer configurations, specifically VECTOR-8, VECTOR-10, and VECTOR-12. However, beginning with VECTOR-14, the performance of the architectures lacking skip connections levels off, suggesting that critical information from the lower layers is not effectively transmitted to the transposed convolutional layers. For VECTOR-18, the performance declines further compared to VECTOR-14 and VECTOR-16, indicating that the vanishing gradient problem may be affecting the bottom layers, resulting in minimal gradient updates for those weights and preventing full optimization.

Adding more layers to VECTOR will lengthen computation times, offering only marginal improvements in performance. Therefore, VECTOR-16 was found to be the most effective for our needs. Figure 6.4 illustrates the training loss for both VECTOR-16 and VECTOR-18, with and without skip connections. It is evident that skip connections significantly speed up the training process, particularly during the first 25 epochs. This effect is most noticeable in VECTOR-18, where the skip connection architecture consistently delivers superior performance across all training epochs.

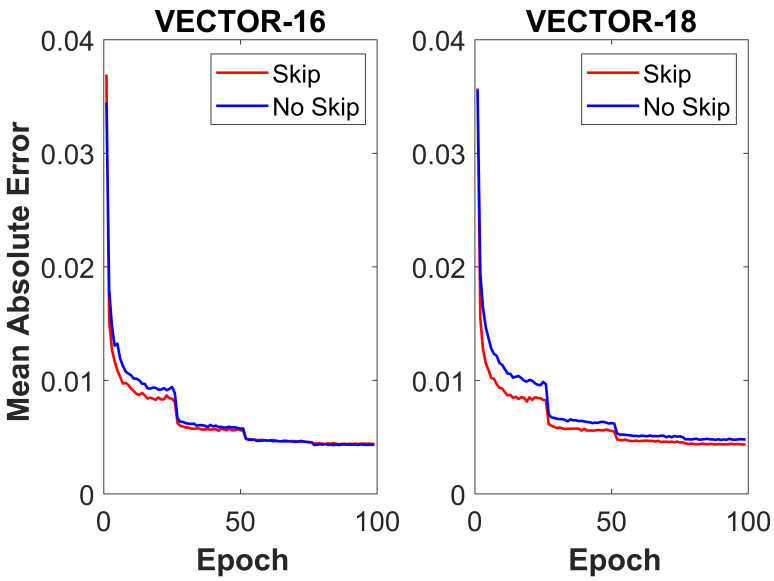

Figure 6.4: Loss curves for VECTOR-16 and VECTOR-18.

6.4 Testing

Nine distinct networks (all using VECTOR-16) were trained in total utilizing the nine different training and validation datasets outlined in section 6.2. These networks were subsequently tested with nine test datasets, each consisting of 4096 spectra. For each network, the test dataset aligned with the parameters of the corresponding training and validation datasets, specifically in terms of peak number and width. The SpecNet network was also trained and validated using the same nine datasets and was subjected to the same test datasets. Visual representations of the spectra recovered by VECTOR-16 and the SpecNet network are displayed in figure 6.5, while figure 6.6 presents the average mean absolute error (MAE) for both networks across each dataset, demonstrating that the VECTOR network significantly outperforms SpecNet in all nine cases.

For both networks, the mean absolute error (MAE) rises proportionally with the number of peaks. Datasets (i, iv, and vii) feature between 1 and 15 peaks, datasets (ii, v, and viii) contain 15 to 30 peaks, and datasets (iii, vi, and ix) range from 30 to 50 peaks per spectrum, corresponding to the left, center, and right columns in figure 6.5. Additionally, as the range of peak widths increases, so does the MAE. Datasets (i–iii) include narrow peak widths from 2 to 10, expanding to a range of 2 to 25 for datasets (iv–vi), and reaching the widest range of 2 to 75 for datasets (vii–ix), corresponding

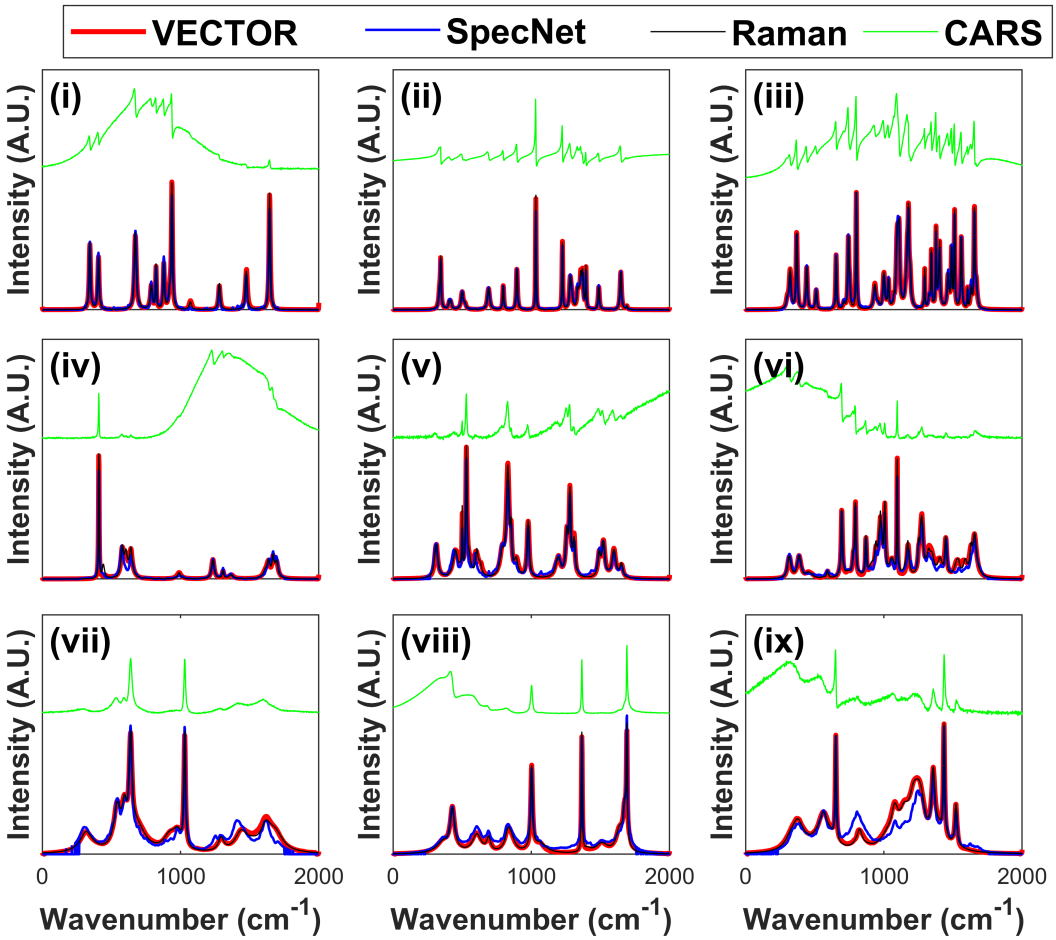

Figure 6.5: Retrieved spectra using VECTOR and SpecNet on an example BCARS spectrum from each of the nine simulation datasets. True Raman spectrum is overlaid (black) and input coherent anti-Stokes Raman scattering (CARS) spectrum (green) is plotted with offset.

to the top, middle, and bottom rows in figure 6.5. The MAE increases most significantly for the more complex datasets with the broadest peak ranges. Overall, the relative change in MAE remains consistent across datasets for both networks, with VECTOR consistently outperforming SpecNet.

Figures 6.5 and 6.6 illustrate that the VECTOR-16 network can recover high-quality spectra across all nine datasets. For datasets (i–iii), both SpecNet and our individual networks perform well in retrieving peak positions and shapes. However, a closer examination of the peak values indicates that VECTOR is more effective at recovering peak heights and reducing baseline noise. In contrast, for datasets (vii–ix), SpecNet generates incorrect values at the edges of the spectrum.

We also emphasize the VECTOR networks ability to mitigate noise in CARS intensity. Figure

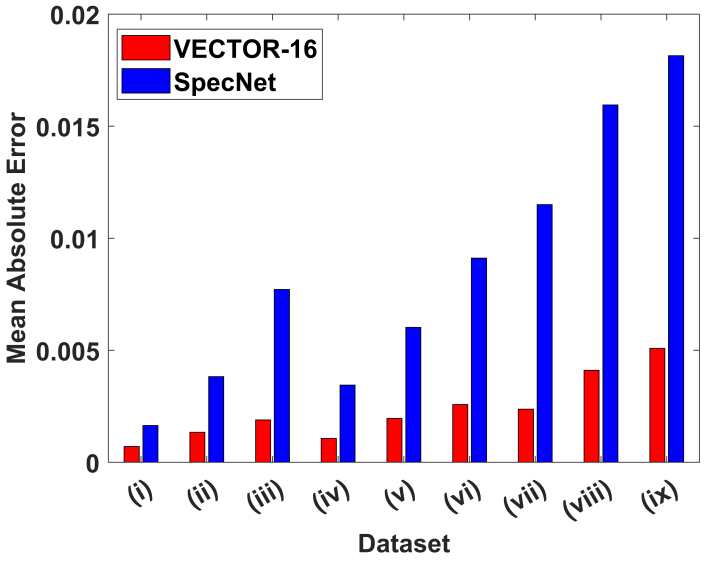

Figure 6.6: Comparison of loss between VECTOR and SpecNet across the nine simulation datasets.

6.7 illustrates the results of applying VECTOR-16 (trained on dataset ix) for two test cases from the same dataset. On the left, the outcome for a high SNR CARS spectrum is shown, which yields high-quality results as anticipated. Conversely, the right side shows the processing of a lower SNR signal, where random noise fluctuations are evident in the input spectrum. Despite this, the recovered Raman spectrum remains high quality and generally free from such noise. However, the inset in the figure indicates that small spectral features, comparable in amplitude to the noise, have been lost. These findings demonstrate that while the VECTOR network effectively handles low SNR inputs, it may lose spectral features that are close to the noise floor. Addressing very low SNR signals would necessitate additional training with datasets of similar quality.

In order to test the accuracy of VECTOR in experimental situations, a BCARS spectrum of glycerol was recorded with the microscope detailed in section 5.1. Neat glycerol was placed in a 120 μm thick imaging spacer between a microscope slide and a coverslip. A spectrum of the coverslip served as an NRB reference. The glycerol spectrum was processed using VECTOR-16, which was trained on datasets (iii), (vi), and (ix). The recovered spectrum and a corresponding spontaneous Raman (SR) measurement is presented in figure 6.8. The SR spectrum was obtained using a commercial Raman micro-spectrometer (Horiba Jobin Yvon LabRAM HR, 300 lines/mm grating, 532 nm excitation). The reference compound 4-acetamidophenol (Sigma) was used for

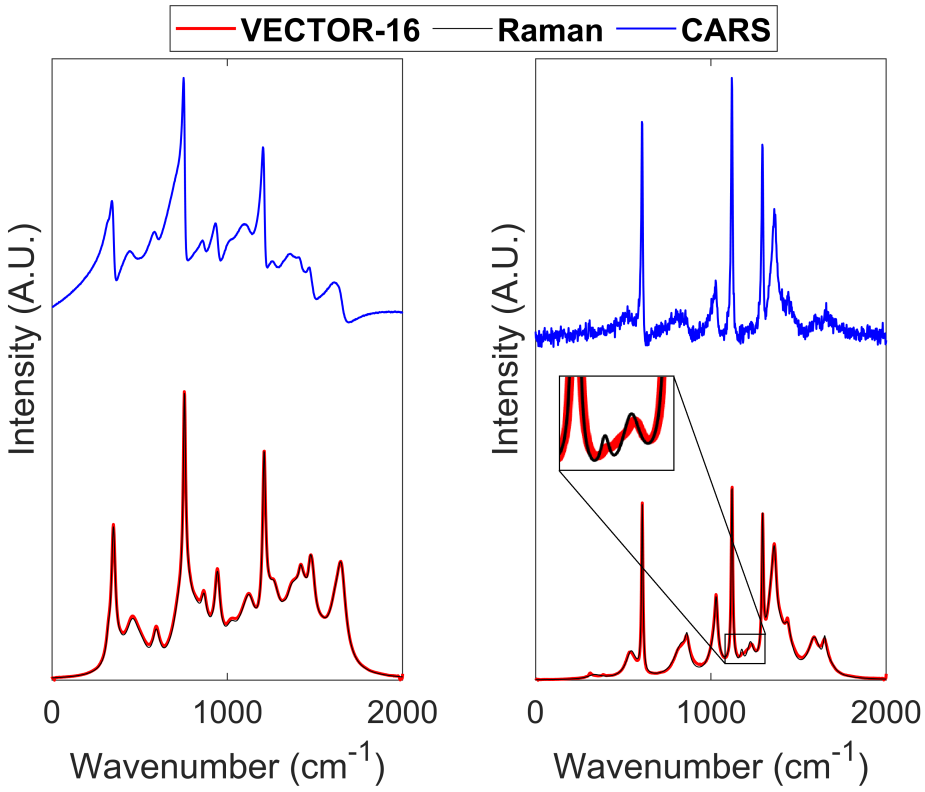

Figure 6.7: Comparison of retrieval on two spectra with different levels of Gaussian noise.

wavenumber alignment and a NIST-calibrated White-Light source (Ocean-Optics) was used for intensity calibration. The Kramers-Kronig (KK) retrieval procedure was also applied to the spectrum using the reference NRB. It can be seen that VECTOR recovers the Raman spectrum quite well in this case, with considerable qualitatively better performance than the KK method when using dataset vi. In particular the plateau region of the glycerol spectrum from 1250 cm^{-1}-1400 cm^{-1} is consistently erroneously retrieved for both VECTOR and the KK method. In the KK method, this is likely due to the unusual characteristic of this region, whereby it approximates a flat response over hundreds of wavenumbers. In such cases, the phase detrending procedure may erroneously be detrending real phase variations because they are much lower frequency than typical in this region. This may be corrected in the KK algorithm by tuning the hyperparameters of the detrending, but this is tedious and difficult to generalize to any spectrum. The results of VECTOR are quite remarkable because considerably less information was used to perform the retrieval, compared to the conventional methods. In the implementation, half the data is required (1 spectrum instead of two for the KK method) per retrieval. However, the methods are also quite different in terms of the

total resources required since VECTOR requires on the order of tens of hours to train a useful model, whereas KK is analytic in nature and requires no training. Another interesting feature of VECTORs result is the apparent lack of any residual laser excitation profile in the retrieved spectrum. As no information on the laser was given to the network in training or implementation, it is clear that the network is still somewhat invariant to multiplicative slowly-varying signals.

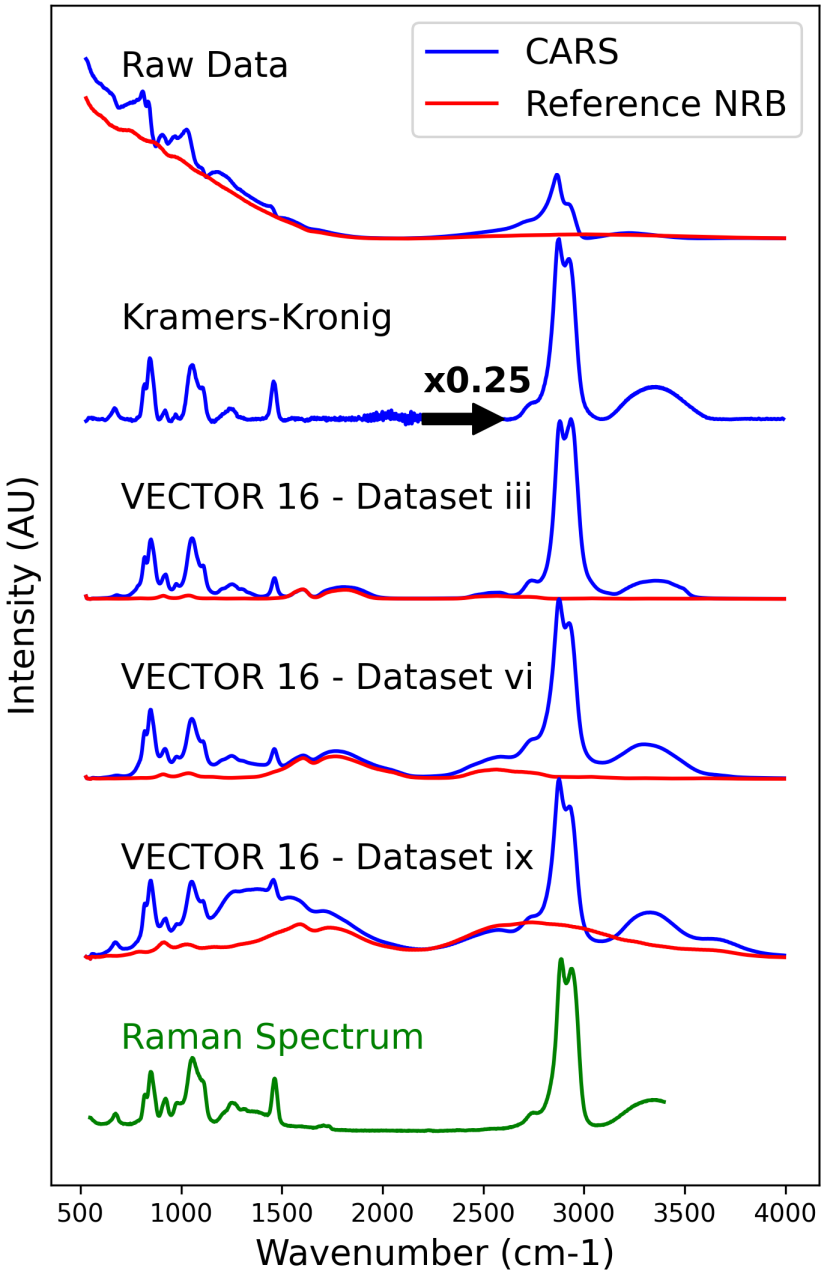

Figure 6.8: Experimental implementation of VECTOR on a BCARS spectrum of glycerol. The reference NRB measurement (top, in red) was also procesed by VECTOR. Also shown is a spontaneous Raman spectrum of glycerol in green.

The NRB observed in an Er-Fibre CARS system such as the one used here cannot be accurately represented accurately using the countervailing sigmoids used here, which are more suitable for conventional two-color B-CARS platforms. The interplay between two-color and three-color excitation leads to a complex NRB signal that is heavily influenced by laser characteristics, including the spectral envelope and phase delay. This presents challenges for an NRB-agnostic system like VECTOR, especially when compared to KK or MEM methods that integrate an NRB reference. Consequently, the significant variability in NRB intensity results in lower peak heights for the C–H band in glycerol than expected, as seen with KK. Thus, elements of the NRB profile are interpreted by the network as resonant features, leading to attempts to construct peaks, particularly evident in datasets (vi) and (ix), which are trained on broader peak width ranges. In contrast, VECTOR minimizes many artifacts associated with the KK method, especially in low-intensity regions, such as the Raman silent zone, where small value quotients can create noisy results. VECTOR also smooths the extracted Raman-like output. Interestingly, the spectrum obtained from the various VECTOR configurations shows greater consistency in the relative intensities of peaks at higher wavenumbers.

In this work, we have demonstrated that VECTOR outperforms the previous CNN approach[122] across all nine datasets. Our network was trained on various configurations of simulated spectra, highlighting the importance of tailoring the training process to the specific types of spectra it is intended to analyze. While the model developed previously by others[122] showed strong performance on datasets similar to or less complex than its training set (i–iv), its qualitative and quantitative results declined when faced with more intricate datasets. Despite VECTORs effectiveness with synthetic spectra used in training, further development is needed for application with real-world experimental data. Training on experimental spectra poses challenges due to the extensive volume of data required, necessitating enhancements to the training set to more accurately reflect the spectra obtained from the CARS platform. Additionally, it is inherently difficult to acquire a definitive ground truth Raman spectrum for a given CARS spectrum; any retrieval algorithm will only yield an approximation, which could introduce additional errors to the retrieval network. To address this, we aim to refine the peak shapes, heights, and frequencies to better align with those seen in the fingerprint and C–H stretching regions of the spectrum. This will involve a broader range

of peak amplitudes, varying signal-to-noise ratios, and generating taller, sharper peaks in the C–H region alongside smaller, denser peaks in the fingerprint region.

7. Physical modelling for improved NRB removal: VECTOR2

This section is based on the published article entitled "Removing non-resonant background from broadband CARS using a physics-informed neural network" published in Analytical Methods[23]. For this chapter, I developed the BCARS simulation generator, trained the neural network, obtained spectra from our BCARS system and a high-resolution spontaneous Raman microscope in the FOCAS institute at TU Dublin. I also analysed the result of the network on simulated and experimental data.

In the previous chapter, a deep convolutional autoencoder named VECTOR was designed and trained on paired CARS intensity data and corresponding Raman intensity, with the CARS spectra simulated under the assumption of a spectrally flat excitation. This assumption is approximately satisfied in the two-colour BCARS mechanism, because the excitation profile here is a symmetric copy of the Stokes pulse, and each vibrational resonance is located within this profile (for the specific laser wavelengths used). However, in the three colour mechanism, the excitation profile resembles the one-sided autocorrelation of the Stokes pulse, which rapidly varies across the whole band of vibrational resonances in the fingerprint region. This is exemplified in figure 4.1 of section 4.2. Thus, modelling the actual laser system to include the real laser profile S should provide VECTOR with higher fidelity training samples from which it can perform the retrieval with greater accuracy. In the updated simulation model, the effect of probe convolution was also implemented, such that the retrieved spectrum should identically match Im $\left(\chi^{(3)}_{\text{Res}}\right)$.

In order to completely model the physical process of BCARS, all variables in the definition of the intensity were required. This equation is repeated here for completeness

$$I_{as}(\omega) = \left| \left\{ \chi^{(3)} \left[E_s(\omega) \star E_p(\omega) \right] \right\} * E_{pr}(\omega) \right|^2 \tag{7.1}$$

In theory, all laser parameters E_{S}, E_{p} and E_{pr} could be measured and it was assumed that they were stationary. The Stokes electric field E_{S} was fully defined using the procedure outlined in section 5.2. The probe electric field was obtained from a measurement of the spectrum of the probe laser with the shortpass filter removed. Since this pulse was narrowband and thus assumed to have a flat spectral phase, the electric field was fully determined by the intensity spectrum. The sample specific parameter, namely $\chi^{(3)}$, was determined as before, using a sum of Lorentzian functions, however an inclusion of a discrete CH and OH band was added.

7.1 Simulating the susceptibility

Raman spectra were first produced by generating independent spectra in three distinct frequency regions: the fingerprint, the CH-stretch, and the OH-stretch regions. The fingerprint region was characterised by resonances that spanned from 600–1800 cm^{-1}. The CH-stretch region contained resonances that spanned from 2900– 3500 cm^{-1}, and had fewer peaks than the fingerprint region but each with significantly higher amplitudes, as per realistic measurements. Finally, the OH-stretch region was simulated as a single resonance that spanned from approximately 3200–3400 cm^{-1}.

The resonant susceptibility for each region was generated as a sum of individual complex Lorentzians as follows:

$$\chi^{(3)}_{\mathrm{Res}}(\omega) = \sum_{n=0}^{N_{\mathrm{peaks}}} \frac{A_n}{\Omega_n - \omega - i\Gamma_n} \tag{7.2}$$

where A_n, Ω_n and Γ_n are the amplitude, frequency and half width of the n^{th} resonance, respectively. ω is the independent frequency. In BCARS, this is the difference frequency of the pump and Stokes sources; a resonance occurs when $\omega_{\mathrm{p}} - \omega_{\mathrm{S}} = \Omega_n$. The choice of n values of a, Ω and Γ defined the Raman spectrum of each training sample. The specific parameters chosen for simulating the

susceptibility are described in table 7.1. Two different datasets were generated, relating to either a chemical sample which often contains sparse and narrow resonances or a biological sample, which is typically more complex due to the much larger number of resonances present. The networks were named sparse and dense to signify a chemical or biological spectrum respectively.

The form of equation 7.2 is the resonance approximation for the susceptibility, as mentioned in section 3.2.2. This simplifies the simulation and is often used to simulate Raman spectra. Its impact on the resulting spectra was tested by calculating the difference between the approximated susceptibility and the full form of the susceptibility[80]. It was found that the approximation resulted in a maximum error of 3 % for both the Raman and CARS intensity. The resonance approximation was chosen as valid for this approach.

In chapter 6, the NRB was modelled as a product of sigmoids, which has a characteristic ramp shape. The non-resonant susceptibility in this chapter was generated using a Gaussian function, as it was assumed that the sigmoid shape may have been unrealistic due to its flat tailedness at the edges of the curve. The NRB was assumed to vary continuously over the whole frequency range and may not be zero.

$$\chi_{\text{NR}}^{(3)} = e^{\frac{-(\omega-\omega_{\text{NRB}})^2}{2\sigma^2}}, \tag{7.3}$$

where ω_{NR} and σ denote the centre frequency and width of the Gaussian. The parameters of the Gaussian were chosen such that the NRB was a slowly-varying function of frequency over the frequency band of the susceptibility. This form more accurately resembles the NRB in reality[134].

Both $\chi_{\text{Res}}^{(3)}$ and $\chi_{\text{NR}}^{(3)}$ were normalized using the maximum of their absolute values over the measurement window. After normalization, the resonant susceptibility was scaled by a factor β and the non-resonant susceptibility by $1-\beta$. The β parameter was designed to control the relative amplitude of the two components of the susceptibility, and was randomly chosen from a uniform distribution in the range of 0.3 to 0.5. The total susceptibility was then generated according to equation 3.68. The Raman spectrum, I_{Raman} used in the loss function of the neural network was defined as the imaginary part of $\chi_{\text{Res}}^{(3)}$:

$$I_{\text{Raman}} = \text{Im}\big[\chi_{\text{Res}}^{(3)}\big] \tag{7.4}$$

Component	symbol	Name	Unit	Dataset	
				VECTOR-MU -Sparse	VECTOR-MU -Dense
NRB	ω_{NRB}	NRB centre frequency	THz	$U(600, 800)$	
	σ_{NRB}	NRB width	THz	$U(400, 500)$	
	β	NRB amplitude	-	$U(0.3, 0.5)$	
Noise	SNR	SNR (Poisson)	-	$U(200, 1000)$	
	σ_{read}	Gaussian noise	-	$U(0.00001, 0.0001)$	
Distortion	A	Ripple amplitude	-	$U(0, 0.02)$	
	T	Ripple frequency	pixels	$U(50, 1000)$	
	ϕ	Ripple phase	-	$U(0, \pi)$	
Fingerprint	a	Amplitude	-	$U(0, 0.1)$	
	N	Number of peaks	-	$U(1, 15) \in \mathbb{Z}$	$U(1, 50) \in \mathbb{Z}$
	Γ	Half-width	cm^{-1}	$U(2, 10)$	$U(2, 75)$
	Ω	Resonant frequency	cm^{-1}	$U(600, 1800)$	
CH-region	a	Amplitude	-	$U(0, 1)$	
	N	Number of peaks	-	$U(0, 3) \in \mathbb{Z}$	
	Γ	Half-width	cm^{-1}	$U(2, 30)$	
	Ω	Resonant frequency	cm^{-1}	$U(2900, 3500)$	

Table 7.1: BCARS training data parameters (The symbol $U(x, y)$ denotes a uniform distribution from x to y).

The simulation and training procedure is shown in figure 7.1.

7.2 Including the system-specific excitation profile

After the susceptibility is generated for each training sample, it is multiplied by the laser excitation profile, S, and the result is convolved with the probe pulse E_{pr} as described in equation 7.1. In order to calculate S, two methods were identified, each with its own advantages and disadvantages. The first method involves the cross-correlation frequency-resolved optical gating (XFROG), as described in section 5.2, which provides the electric fields E_{S} and E_{pr}, from which S can be calculated precisely. The second method involves approximating S using a measurement of the BCARS signal in a non-resonant material such as glass. Such a measurement results in $\chi^{(3)} \approx \chi^{(3)}_{\text{NR}}$ and is real valued. It follows that $\sqrt{I_{\text{CARS}}} \approx \chi^{(3)}_{\text{NR}}|S * E_{pr}|$. If the NRB is assumed to be approximately spectrally flat, E_S is assumed to have an approximately flat phase, and E_{pr} is sufficiently narrow,

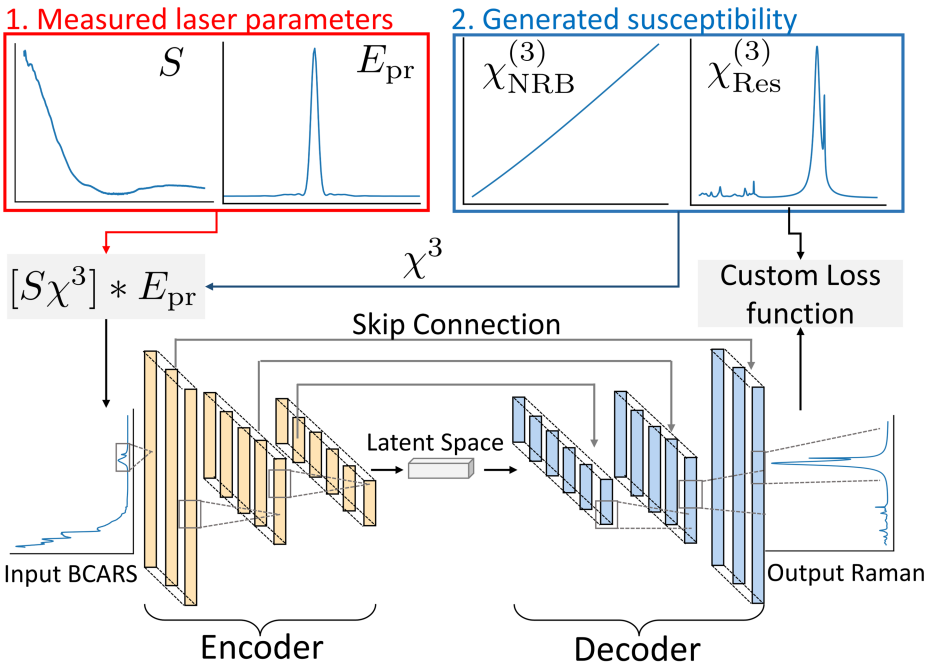

Figure 7.1: Diagram of the VECTOR2 simulation approach. The simulation process includes (1) estimation of the source laser profiles, (2) generation of a complex susceptibility, (3) modelling of a BCARS response according to the physical process.

then it follows that $S \approx \sqrt{I_{\mathrm{glass}}}$. The result of this approach is shown in Fig. 7.2 (b) in which it can be seen there is good agreement with the XFROG method. The probe pulse could also be approximated by a standard spectral profile such as a Gaussian or sinc function using known parameters. The simulated and measured probe spectrum as obtained from XFROG is shown in figure 7.2 (a).

Both of the methods described above provide values for S and E_{pr}. The XFROG method has the advantage of providing the phase of S; however, if this phase is flat then this advantage may be overlooked. The approximation method has the advantage of being much simpler, requiring only a single non-resonant spectrum. This method also has the very significant advantage of including the same sensitivity response of the spectrograph with respect to the BCARS spectra. This is not true for the XFROG method, which involves recording spectra in a different band of wavelengths centered on the two-colour region. The difference in the estimates for S between the methods could be attributed to this difference.

In this work, the use of S obtained directly from glass was preferable as this provided self-

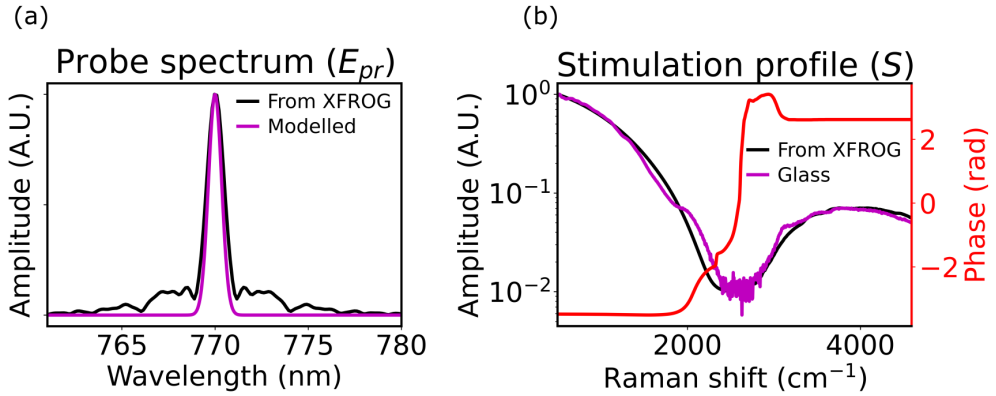

Figure 7.2: (a) probe pulse amplitude obtained from the discrete Fourier transform of the marginal plot of the XFROG. Also shown in this figure is the result of modelling the amplitude as a Gaussian function based on the laser specification – centre at 770 nm and FWHM 0.58 nm, (b) amplitude of excitation profile obtained using two methods: firstly the E_{S} and E_{pr} obtained from XFROG are used to generate $S = E_{\mathrm{S}} \times E_{\mathrm{p}}$ where E_{p} is given by E_{S} and E_{pr} for the 3- and 2-colour regions, respectively. This method also enables the phase of S to be obtained; secondly, the amplitude of S is estimated using the square root of a glass spectrum. This method does not permit measurement of the phase.

referencing for intensity calibration of BCARS spectra. This method was employed for estimating S in subsequent sections. Once the susceptibility was generated, and S and E_{pr} were obtained, the BCARS spectrum was calculated according to equation 7.1. This involves multiplication of the susceptibility with S, followed by convolution with E_{pr}. The resultant function I_{CARS} was then normalised between 0 and 1. Normalization was necessary because the subsequent processing, including noise modelling required a consistent SNR.

7.3 Simulating system-specific noise

Excluding the NRB, three separate noise sources were incorporated into the simulation to more accurately reflect the experimental conditions. These include: shot noise, arising from the quantum nature of light; additive Gaussian noise, representing sources such as camera read noise; and a weak, slowly varying distortion of the overall intensity in the form of a randomly fluctuating ripple, intended to account for experimental variability. For a given irradiance I, shot noise is due to fluctuations in the number of photons arriving over a unit time and follows a Poisson distribution, where the variance equals I. This can be directly related to the well-known signal-to-noise ratio through this relationship.

Given the linear relationship between intensity and irradiance, the SNR of a given BCARS spectrum can be approximated as proportional to the square root of the BCARS intensity. To simulate an appropriate BCARS intensity, a desired SNR value was chosen for the maximum signal intensity. This value was randomly selected from a uniform distribution ranging from 200 to 1000, reflecting observed experimental conditions. It was then multiplied by the normalized BCARS intensity. Each individual sample in the spectrum $I_{\text{CARS},m}$ was scaled by the square of the SNR, and this result was used as the mean of a Poisson distribution P. A value was then randomly sampled from this distribution, and then scaled by SNR squared to ensure normalization, as required by the VECTOR2 architecture. This process is summarised as

$$I'_{\text{CARS},m} = \text{SNR}^{-2} P(\text{SNR}^2 \cdot I_{\text{CARS},m}) \tag{7.5}$$

The shot noise can be modelled for any SNR and the output is limited to the range [0,1]. The dark current of the detector can be trivially included by increasing the mean of the Poisson distribution by a relative amount, however this was omitted due to the extremely low value observed in the setup used. The effect of read noise was also modelled using an additive zero-mean Gaussian function. This was applied to the normalised data from equation 7.5. The Gaussian noise had a standard deviation that was sampled from a uniform distribution between $1 \times 10^{-}5$-$1 \times 10^{-}4$. The resultant intensity was given by

$$I''_{\text{CARS},m} = I'_{\text{CARS},m} + \mathcal{N}(0, \mathcal{U}(0.00001, 0.0001)) \tag{7.6}$$

where $\mathcal{N}(\mu, \sigma)$ denotes a normal distribution with mean μ and standard deviation σ, and $\mathcal{U}(x, y)$ denotes a uniform distribution between x and y.

Finally, the third noise term was a multiplicative, low amplitude and low frequency variation (ripple) that was used to emulate all other signals not due to the sample chemistry. These variations appeared to be sample dependent and could be related to chromatic aberration. Inclusion of this noise term prevented over-training of the network on one possible excitation profile, which in fact varies slightly over time. If it were not included, any deviation in a test spectrum excitation profile would erroneously recover resonances where they did not exist. Early attempts to train the network

without this term resulted in poor generalisation performance using experimental spectra. The ripple was defined as a multiplicative sinusoidal signal which was added to the normalised intensity,

$$I'''_{\text{CARS}m} = I''_{\text{CARS}m}\left[1 + A\sin\left(\frac{2\pi m}{T} + \phi\right)\right] \tag{7.7}$$

where T is the period of the ripple, in units of pixels, A is the amplitude, and ϕ is the phase shift. The ripple varied in amplitude, frequency, and phase for each sample spectrum. The parameters in equation 7.7 were sampled from a uniform distribution as follows: $A = \mathcal{U}(0, 0.02)$, $T = \mathcal{U}(50, 1000)$ and $\phi = \mathcal{U}(0, \pi)$. The intensity was then normalised again to account for changes in the range due to the Gaussian and ripple terms. The Raman spectrum for each sample was obtained from equation 7.4 and normalised but no noise was added.

In order to demonstrate the result of the simulation, a simulated BCARS spectrum of the compound benzonitrile was compared with an experimental recording of the compound using the system described in section 5.1. The vibrational spectrum was simulated using the information in ASTM E1840-96(2014)[135]. From this, the resonant susceptibility wavenumbers and amplitudes were obtained. The linewidths were all set equal to 1 cm^{-1}. The imaginary part of the resonant susceptibility is shown in figure 7.3 (a). The randomly generated NRB is shown in 7.3 (b) and in (c) the simulated BCARS spectrum of benzonitrile is shown ($\beta = 0.5$). For comparison, the experimentally measured BCARS spectrum of neat benzonitrile is shown in figure 7.3 (d). It can be seen from (c) and (d) that there is very close agreement between the simulated and recorded spectra. The small differences can be accounted for by the unknown value of the true β and the true NRB shape.

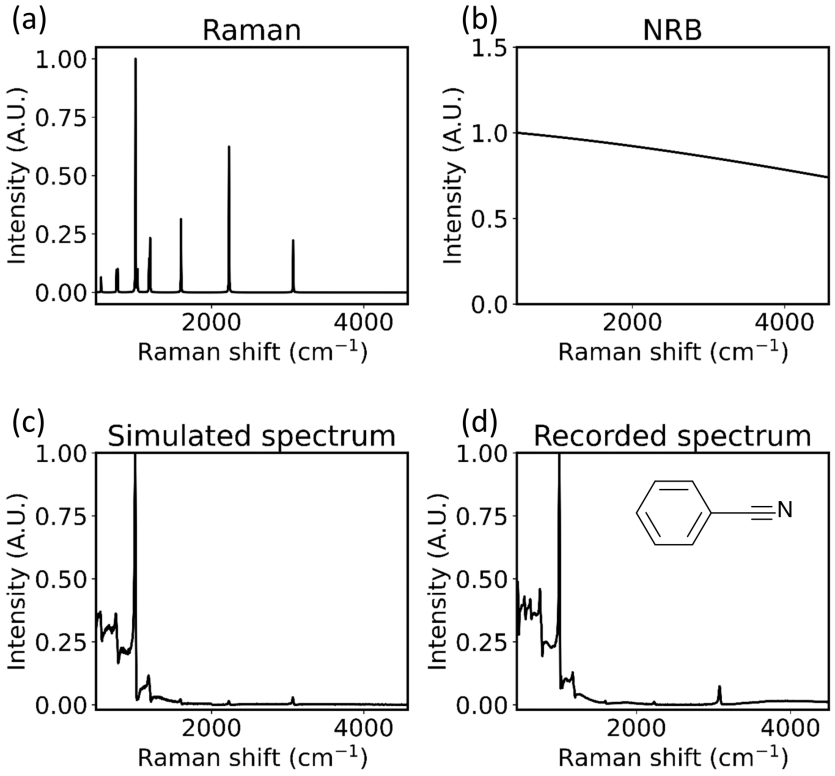

Figure 7.3: (a) Simulated Raman spectrum of benzonitrile; (b) randomly generated NRB using the developed method; (c) simulated benzonitrile BCARS spectrum with $\beta = 0.5$; (d) recorded benzonitrile spectrum using the BCARS system (inset is the chemical structure).

7.4 Training and testing the network

7.5 Custom loss function

In order to test the whole deep-learning approach, two test datasets with features corresponding to sparse and dense samples were created. The goal was to train two separate networks, each optimized for these different types of spectra. These parameters of these datasets are presented in Table 7.1. In both datasets, resonances were randomly chosen for the fingerprint CH- and OH- regions, but the amplitudes in the CH region were designed to be 10 times stronger than those in the fingerprint region in order to match spectra in reality. This necessitated the use of a custom loss function in order to balance the loss between the scaled regions. The custom loss function was given as

$$\ell = \sum \frac{\zeta |f(\mathbf{X}) - \mathbf{Y}|}{N} \tag{7.8}$$

where $f(\mathbf{X})$ is the network output for a given input BCARS spectrum $\mathbf{X}$. $\mathbf{Y}$ is the Raman spectrum of the input $\mathrm{Im}\left[\chi^{(3)}_{\mathrm{Res}}\right]$ and ζ was the normalisation factor used to ensure the fingerprint and CH loss were of similar magnitude. ζ was defined as,

$$\zeta = \begin{cases} 1, & \Omega < 2272\,\mathrm{cm}^{-1} \\ 0.1, & \Omega \geq 2272\,\mathrm{cm}^{-1} \end{cases} \tag{7.9}$$

Thus, the objective of the network is to retrieve the Raman spectrum directly from the noisy and realistic BCARS input. In contrast, the original VECTOR network was designed to recover the Raman spectrum from purely theoretical BCARS spectra that did not contain the imbalance of excitation in the two and three colour regions due to the lasers. Here, we fully account for this effect.

7.6 Training

Two networks were trained, with the only difference being the training set used (sparse or dense). The trained networks were named after the original network architecture (VECTOR), the experimental system used for modelling (Maynooth University-MU) and the specific training set used (sparse/dense). Thus, the networks were named VECTOR-MU-sparse and VECTOR-MU-dense. The two networks were trained on a single TITAN Xp GPU. The stochastic gradient descent (SGD) optimizer was used in computing the weights and the learning rate was reduced by a factor of 10 every 25 epochs. All other training parameters are shown in table 7.2. The results of training are shown in figure 7.4. As shown in figure 7.4, the training loss has sharp discontinuities where the learning rate drops by a factor of 10. The approach for varying the learning rate using discrete changes every 25 epochs was built upon the results from the previous network described in section 6.2. The lower loss values for the sparse dataset can be explained by the lower complexity in the training set.

Parameter	Value
Training set size	1,000,000
Validation set size	10,000
Testing set size	10,000
Epochs	100
Batch size	256
Weight decay	5×10^{-4}
Momentum	0.9
Initial learning rate	0.1

Table 7.2: Training parameters of the VECTOR2 network.

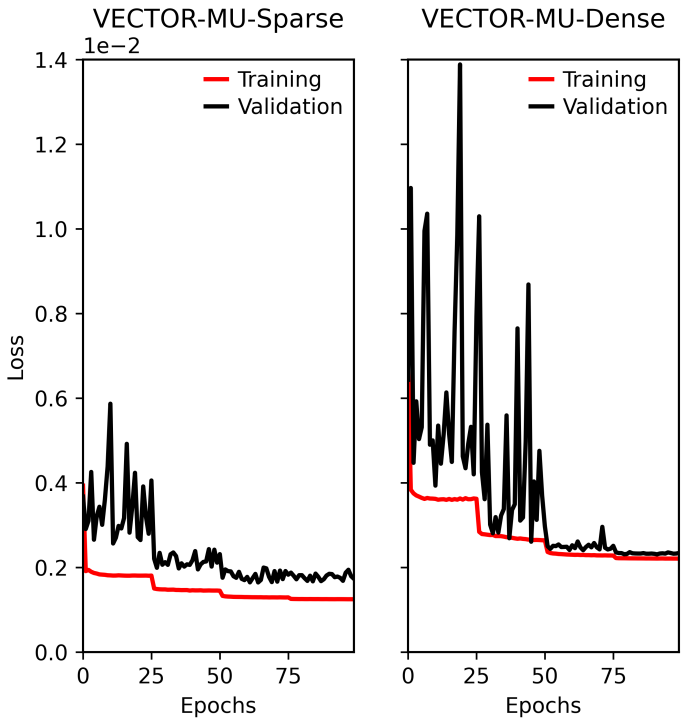

Figure 7.4: Average training and validation loss per epoch for the two different autoencoder networks (both on same ordinate scale).

7.7 Testing

The results of the network's retrieval on two simulated spectra from the sparse and dense datasets are shown in figure 7.5. 7.5 (a) illustrates a simulated BCARS spectrum from the sparse test set. The noise level is relatively low in this example, and the characteristic CARS lineshape is present

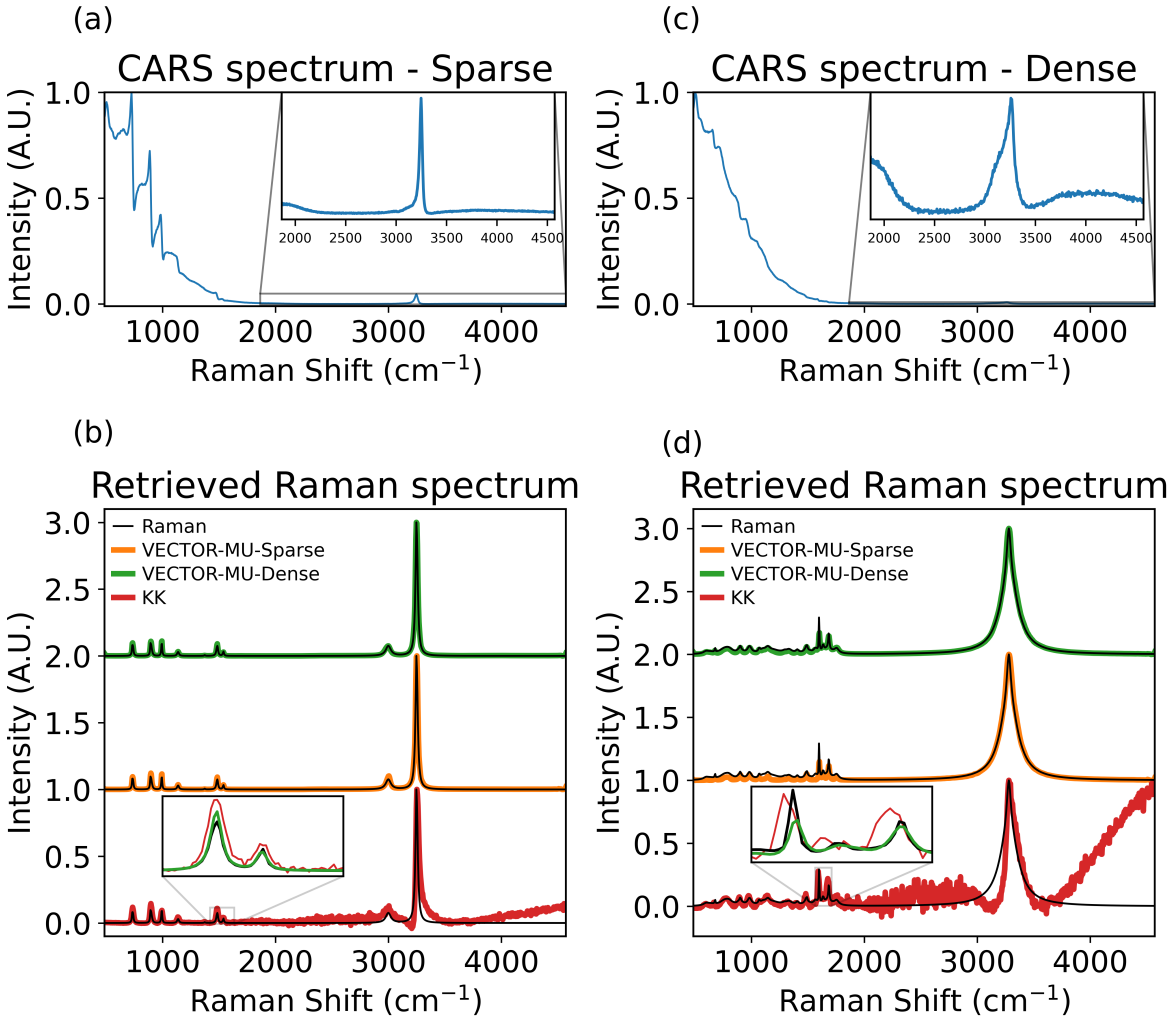

Figure 7.5: Examples of two test BCARS spectra, processed using the two trained networks; (a) simulated BCARS test spectrum of a sparse spectrum (inset zoom on 2-colour region) and (b) retrieval of Raman spectrum using the two networks; (c) and (d) the same results are shown for a simulated dense spectrum. As expected, the network VECTOR-MU-dense performs better on the more complex data but surprisingly, it performs similarly to VECTOR-MU-sparse on simulated sparse data.

where vibrational resonances exist. In regions without resonances, the BCARS intensity closely resembles the excitation profile. 7.5 (b) displays the retrieval results of the sparse Raman spectrum in (a) for both networks, which show comparable performance on sparse spectra. The equivalent performance between VECTOR2-MU-sparse and VECTOR2-MU-dense is likely because the sparse dataset is a subset of the dense dataset, and the more complex network (VECTOR2-MU-dense) may essentially subsume the less complex network. Also shown in (b) is the result of applying the phase

and amplitude corrected Kramers-Kronig method[1] using CRIKit2[1] to the BCARS spectrum in (a). Default parameters for the KK method were used, except for the phase-detrending smoothness parameter which was set to 1000. This value relates to the smoothness of the function used to detrend the phase. The level of smoothing is approximately logarithmic in this parameter. The NRB reference was also required for the KK implementation, which was obtained from the simulation by setting $\chi^{(3)}_{\text{Res}}$ to zero. Notably, the KK method retrieves the fingerprint resonances quite well in this example, but there is an apparent broadening of the retrieved lineshape, since the KK method does not deconvolve the probe laser from the spectrum. This is evident in the inset zoomed region of 7.5 (b). While in a highly resonant material such as a pure solvent, this is quite straight forward to do, as will be shown, the combined phase-retrieval and deconvolution is not trivial for complex samples such as biological cells. In the CH-region the KK method also fails to recover the true lineshape of the strongest resonance, as the dispersive lineshape persists. The windowing effect of the discrete Hilbert transform is also very evident at the highest wavenumbers with an unphysical amplitude increase here. The other major difference between the proposed method and the KK method is the perceived noise level in the retrieved spectrum. The KK result has noise that is actually greater than the noise in the input. This is due to the KK being ill-conditioned when applied to real spectra, or in this case, simulated spectra that are highly realistic.

The phase retrieval problem is simpler when the number of resonances n is small and the asymmetric lineshape features are clear in the BCARS spectrum ($\beta \gg 0$). Figure 7.5 (c) shows the BCARS spectrum from the dense test set, which looks very different from the spectrum in (a). This difference is due to the large number of vibrational resonances in the fingerprint region, resulting in a Raman spectrum that has a nonzero baseline almost everywhere in this region. The overlap of resonances causes the characteristic lineshapes to become distorted, making it harder to retrieve the resonant component accurately. This is the main reason for the difficulty in applying conventional phase-retrieval methods to biological spectra such as cells. The nonzero baseline in dense spectra, caused by the high number of resonances, is the reason for the lower efficiency in training the VECTOR-MU-dense model compared to VECTOR-MU-sparse. In (d), the resulting retrieval on the dense test spectrum is shown. The sparse network retrieves the CH region resonance accurately

[1] https://github.com/CCampJr/CRIkit2

but performs poorly for the whole fingerprint region. The simplified training data used means that such data is not encountered in minimizing the loss, and as expected the network does not provide a good result. However the dense network accurately retrieves the full broadband spectrum. The two VECTOR results are also significantly denoised compared to the input, showing the power of the approach. The KK result notably has the windowing effect and high amounts of noise present. In the inset zoom, the retrieval of the two resonances is erroneous, likely because in this region, the excitation profile approaches the noise floor as it is at the width of the Stokes autocorrelation. The dense network shown very accurate retrieval in this region.

For a quantitative comparison, two test sets were created. These were not used to train any network. Each set contained 10,000 simulated spectra using the parameters from table 7.2. Both test sets were input into both networks, and the mean absolute error (MAE) of the output spectra was calculated using the true Raman spectrum. The results are presented in Figure 7.6 as a violin plot on a logarithmic scale. VECTOR-MU-dense showed slightly better performance to VECTOR-MU-sparse when tested on sparse spectra, possibly due to the greater training complexity. The performance in the CH-region was similar for both networks, which was expected since both training sets used the same parameters for this region. For the dense test set, VECTOR-MU-dense performed significantly better, which was also expected because the VECTOR-MU-sparse network was trained on simpler spectra. Also shown is the resulting loss for the KK method, which, for both test datasets, showed significantly higher loss values in both the fingerprint and CH regions.

7.8 Experimental results on real spectra

The performance on experimental spectra obtained with the BCARS microscope described in section 5.1 was then tested. The samples used were benzonitrile, ethanol, polystyrene, PMMA, a proprietary polymer from a flow channel (μ Slide I Luer, Ibidi GmbH, Munich, Germany), and glycerol. The polymer slide, is designed with a flow channel for imaging adherent cells during flow, as well as in 3D culture. The base of the polymer slide, which was targeted for Raman spectroscopy, is made from a transparent polymer with a thickness similar to that of a coverslip. This polymer has beneficial

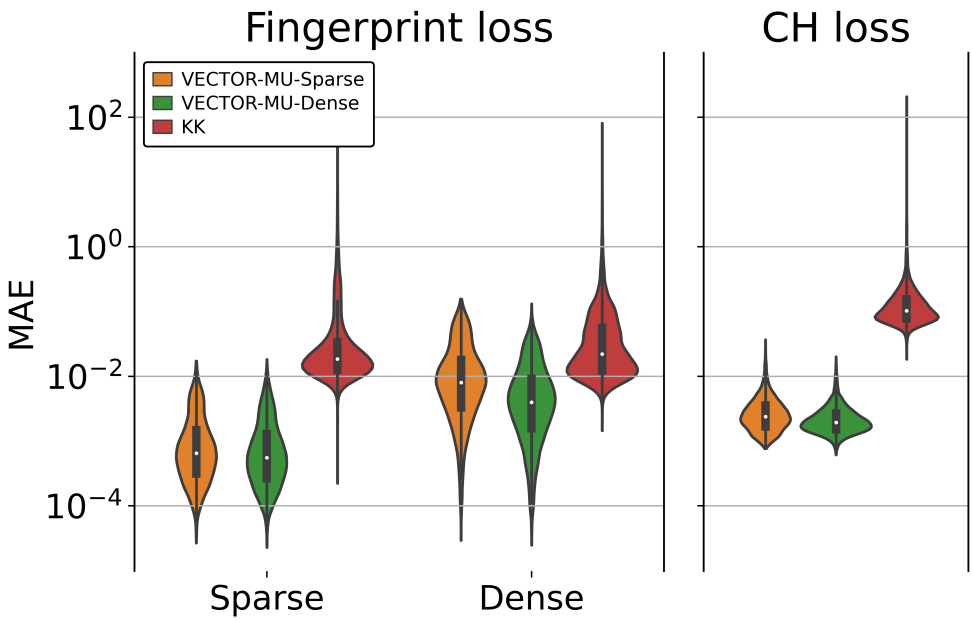

Figure 7.6: Mean absolute error (MAE) of test sets that were input to each network/KK method. Results are separated for the fingerprint and CH-regions. Inner box and bars represent descriptive statistics (boxplot), coloured areas are kernel density estimates of the loss distribution.

imaging properties, including a refractive index that matches glass. Its specific chemical structure is proprietary and not disclosed by the manufacturer. This polymer was chosen because it has a diverse spectral profile with various resonances and linewidths in the fingerprint and CH-stretching regions, resembling the spectra of complex materials like biological samples.

All chemicals, except the polymer slide, were sourced from Sigma-Aldrich in Ireland. Liquid chemicals such as benzonitrile, glycerol, and ethanol were pipetted onto a glass coverslip. The PMMA and polystyrene were in the form of 10 μm diameter beads and were mixed with distilled water, applied to the coverslip, and then air-dried. All spectra were recorded using the system described in 5.1, with a 1-second exposure time for each recording. The average of five exposures was taken and the dark current subtracted from each. Cosmic rays were eliminated using a published algorithm[96]. The resulting raw BCARS spectra are displayed in figure 7.7. The full sized spectra are also shown in appendix B. No effort was made to apply intensity calibration to the BCARS spectra shown in figure 7.7, relating to the sensitivity response of the system. This step would have been superfluous because the excitation profile that was used to train the network (obtained

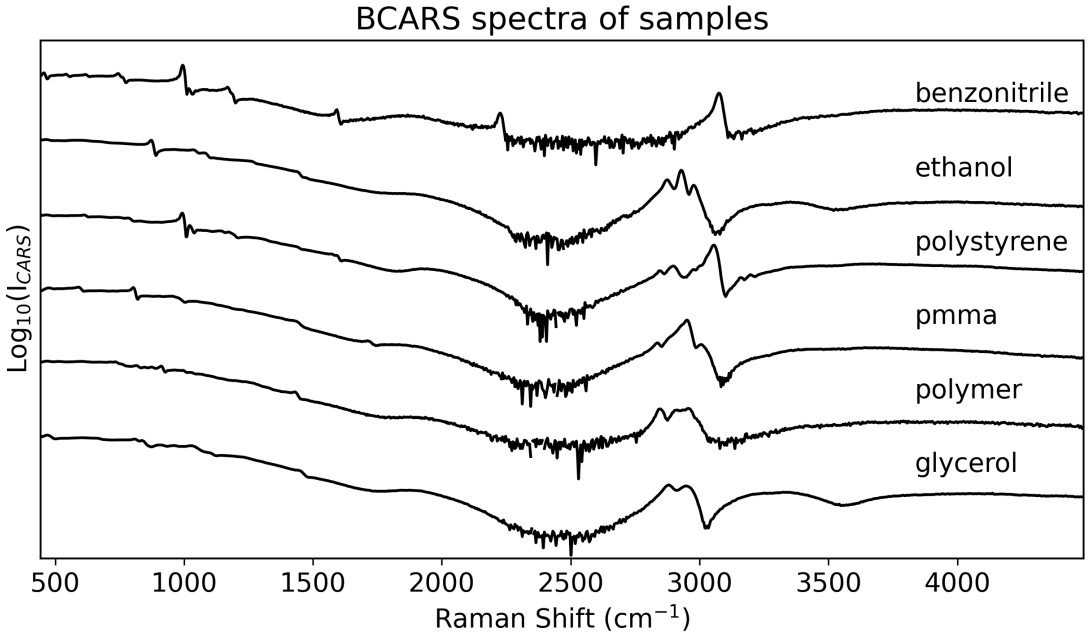

Figure 7.7: Six experimental BCARS spectra. The logarithm of the intensity is shown and the spectra were offset vertically for clarity. The retrieved Raman spectra are shown in the next figure.

from a glass spectrum) was modulated by the same sensitivity response. Therefore, all retrieved Raman spectra were inherently corrected for the system sensitivity. This point is also true for spectra retrieved using the KK method, which also makes use of a reference NRB spectrum.

To compare a Raman spectrum obtained using VECTOR-MU with a corresponding spontaneous Raman spectrum, each sample was also analyzed with a high-resolution commercial Raman spectrometer. The setup included an Horiba Jobin Yvon LabRAM HR Raman micro-spectroscopy system equipped with a 660 nm excitation laser and an 1800 L/mm grating, using an MPlan 10×/0.25 NA (Olympus) objective. The system employed an automated routine to record spectra from 400 to 4500 cm^{-1}, achieving an approximate theoretical resolution of 0.4 cm^{-1}, which resulted in 25,232 spectral pixels. The acquisition time for each spectral band was 10 seconds, and the average of five separate measurements was taken. The Raman spectra were processed by subtracting the dark current and calibrating the intensity using a NIST-calibrated white light source[136]. For benzonitrile, a 532 nm laser excitation was used to prevent a broad spectral peak at 800 cm^{-1} that appears with 660 nm excitation, likely due to fluorescence. The Raman data was filtered using a Savitzky-Golay filter with a window size of 9 and an order of 3. The Raman spectra were high-resolution and background free, allowing for a qualitative estimate of the performance of VECTOR2 on real data. The result of

the retrieval on the six chemicals is shown in figure 7.8. The KK method was also applied, using identical parameters to the simulated spectra.

In the case of glycerol, both VECTOR-MU networks aligned well with the relative peak heights and positions observed in the spontaneous Raman spectrum for both the fingerprint and CH regions. However, VECTOR-MU-sparse struggled to reconstruct the slowly varying peaks from 1200 to 1500 cm^{-1}, which was expected since no training examples of this kind were included. Both networks failed to capture the relative strength between the three- and two-color regions (hence the scaling factors applied in the fingerprint region). The reason for this may be due to a drastically different excitation profile between the one used in simulation and the one measured at the sample. Another potential reason is the choice of two separate Raman amplitudes for the two spectral regions, which may have caused ambiguity in the relative height between the regions that the network could not resolve. In each region, the relative amplitudes are well resolved and true to the spontaneous Raman spectrum, meaning that both the fingerprint and CH regions are well retrieved independently. This issue was consistent across all tested spectra and will be discussed further later. For the polymer sample, both networks performed well in the fingerprint region, but VECTOR-MU-dense excelled in retrieving relative peak heights. In the CH region, VECTOR-MU-sparse displayed a significant error in the height of the peak at 2900 cm^{-1}; this could be attributed to random sampling effects during training, as both networks shared the same CH region parameters, and therefore while the underlying probability distributions were identical, they used different training spectra. In the PMMA sample, which has a sparse Raman spectrum with only a few strong resonances, the sparse network performed better than the dense network. Both networks retrieved results in the CH-stretch region that closely matched the actual Raman spectrum. For polystyrene, the Raman spectrum features a strong resonance around 1000 cm^{-1}, which VECTOR-MU-sparse failed to retrieve accurately compared to neighboring peaks. Additionally, the dense network incorrectly generated baselines at 780 cm^{-1} and 1550 cm^{-1}, indicating it can struggle with baseline corrections when handling sparse, narrow resonances. The ethanol sample was also particularly sparse, containing about ten resonances in its Raman spectrum. In this case, VECTOR-MU-sparse outperformed VECTOR-MU-dense, which again inserted an incorrect baseline upwards of 1500 cm^{-1}. Both networks successfully identified the hydroxide bond in the CH region at approximately 3200–3400 cm^{-1}. Finally, for the benzonitrile

spectrum, both networks accurately recovered the positions and amplitudes of nearly all of the fingerprint peaks, although the ratio between the peaks at 1150 and 1600 cm^{-1}, as well as the peak at 1000 cm^{-1}, were noticeably incorrect. Once more, VECTOR-MU-sparse demonstrated superior performance.

In all samples the KK method had visibly worse results for the specific parameters used, compared to the two networks. For example, in Glycerol, the region around 1400-1500 cm^{-1} was severely distorted. The CH band in this spectrum also had the two main peak amplitudes inverted. This also occurs for ethanol and the polymer sample. It was clear that VECTOR2 outperformed KK for all the samples tested. The findings of this work show that deep learning can effectively perform phase retrieval and denoising simultaneously in one forward pass through a fully trained neural network, as demonstrated by VECTOR2. However, importantly, when combining KK with statistical denoising methods like singular value decomposition (SVD), the phase retrieval results may reach levels similar to those of VECTOR2, provided the phase-retrieval parameters are tuned to the spectrum of interest. Conversely, using single-spectrum denoisers is unlikely to greatly enhance the performance of KK-based phase-retrieval beyond what VECTOR offers. Even when applied on denoised datasets, since KK cannot be tuned per spectrum, batch error can occur in the results as a result of the NRB varying during the recording. Additionally, SVD-based statistical denoising necessitates a large dataset of similarly noisy and shaped spectra, such as those found in hyperspectral imaging, without which, statistical denoising is impossible. It should be emphasized that SVD denoising would benefit both conventional methods of phase-retrieval and VECTOR2, so it is likely to narrow the performance gap between the two methods. This paper, however, solely addresses single spectrum processing and demonstrates that VECTOR2 outperforms KK in terms of noise reduction, phase retrieval accuracy, and spectral resolution.

The current version of VECTOR2 takes longer to run, particularly during training, compared to MEM or KK. However, once trained, it can process new data very quickly (1 ms), and its speed could be improved further using more efficient coding practices. Once optimized as part of a laser alignment procedure, the laser excitation profile of a BCARS microscope typically remains relatively stable for hours to possibly days in a temperature and vibration controlled laboratory,

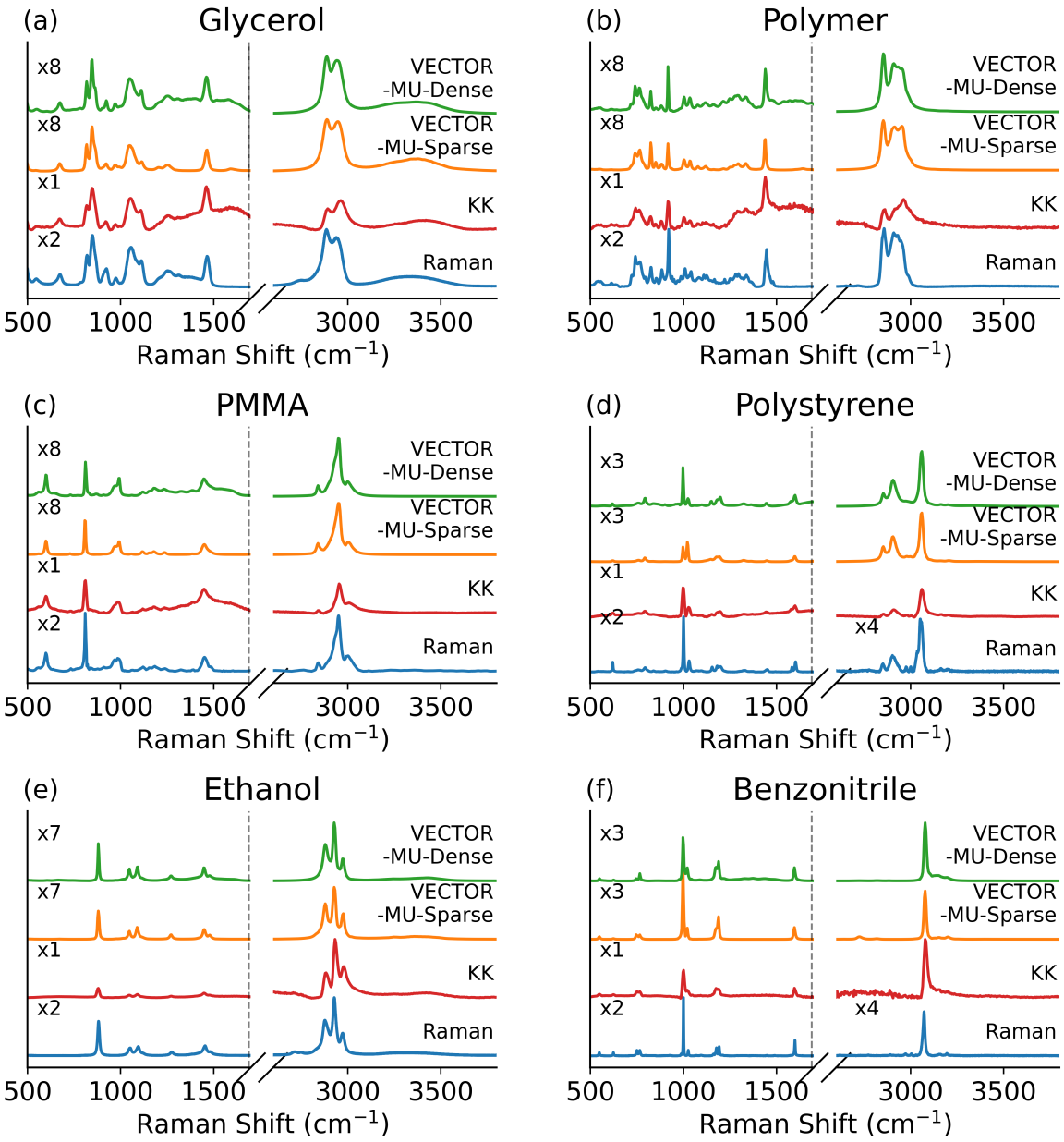

Figure 7.8: Retrieval of the six chemicals: (a) glycerol, (b) a proprietary polymer slide, (c) PMMA, (d) polystyrene, (e) ethanol, (f) benzonitrile. The spectra retrieved from both networks are shown, together with the corresponding intensity calibrated spontaneous Raman spectrum.

allowing the trained network to be reused during this period without retraining. New experimental results generated by an updated system with a new laser excitation profile could also be used to update the current network through ”transfer learning,” eliminating the need to retrain from scratch.

VECTOR2 has significant potential to enhance Raman signal extraction from raw BCARS spectra, particularly those in large batches. The KK and MEM methods can produce artifacts that

VECTOR2 can avoid due to the large heterogeneity in the samples on which it was trained. In the KK implementation, the discrete Hilbert transform (DHT), which is the main operator used, is not fully equivalent to the continuous Hilbert transform, resulting in baseline errors that the detrending procedure is required to correct. This issue is also observed in MEM methods, necessitating padding schemes for both KK and MEM, especially for peaks near the edge of the window.

Another advantage of VECTOR2 over KK is its higher accuracy in noisy environments. The approach developed here effectively removes noise from the retrieved Raman signal and extracts the signal itself more accurately from within a noisy background, as demonstrated in figure 7.7. Additionally, errors in phase-retrieval methods like MEM and KK depend on detrending methods for corrections, as shown by Camp *et al.*[1] However, these detrending methods may not accurately retrieve the baseline in low SNR spectra, or where the excitation profile amplitude approaches zero (as in the Amide I band in the system developed here). Higher-order polynomial detrending is commonly used for detrending the Raman spectrum, but it assumes the baseline is a polynomial, which lacks theoretical justification. Asymmetric least-squares (ALS) methods offer more flexibility when the signal contains dispersive peaks, yet they are constrained by two hyperparameters that may be ineffective for complex spectra. In contrast, deep learning methods like VECTOR2 can be trained using purely synthetic data or a mix of synthetic and experimental data. Moreover, VECTOR2 could be trained with data generated using KK or MEM to convert raw BCARS spectra, integrating other physics-based approaches into the deep learning model. Unlike deep learning methods, it is impossible to ”train” a polynomial detrending or ALS method to improve their performance.

VECTOR2, being a neural network, necessitates normalization for effective generation of simulated spectra. In this context, both the input spectra and the simulated Raman spectra were normalized to their minimum and maximum values. Consequently, absolute concentration information cannot be retrieved with VECTOR2 in its current form. However, it does preserve relative species concentrations, which can be obtained from the ratio of two or more detected peaks. Although we did not evaluate the capacity for concentration measurements in this study, this area may warrant exploration in future research. Additionally, KK-retrieved spectra have demonstrated a linear relationship with concentration[4]. In summary, while MEM and KK provide robust methods

for extracting Raman features, they also require supplementary tools to enhance their extraction capabilities, such as phase-error correction, scale-error correction, and denoising. Moreover, these techniques may face limitations when dealing with samples that exhibit low NRB-to-resonant ratios or low SNR. In this work, VECTOR2 is introduced, an enhancement of VECTOR that incorporates the excitation profile of a specific laser system, resulting in significantly improved accuracy for practical experiments. The training method enables a network to learn the relationship between Raman spectra and experimental BCARS spectra. No specific assumptions were imposed on the form of the non-resonant background, except that it should be a slowly varying function of frequency.

It is crucial to note that this training approach is highly tailored to the specific laser system used in the BCARS setup and this specificity allows any BCARS system to simply record a glass spectrum and incorporate it into the training process, creating a network customized for that system. Additionally, including this information during training provides an inherent intensity calibration to adjust for the system's sensitivity response. However, a significant drawback is the extensive time required to train VECTOR2, necessitating retraining if the excitation profile changes. In our study, the network required over 48 hours to train, with a per-spectrum runtime of approximately 1 ms. That said, it may be possible to significantly reduce the retraining time as described in the previous section. VECTOR2 could be improved upon in two primary ways: by improving the network architecture and by expanding the physical model underlying the training sets. For the first improvement, experimenting with deeper and higher-dimensional layers could enhance VECTOR2's performance on more complex spectra. Other architectures could also be explored, such as generative adversarial networks, transformers, or diffusion networks. For the second improvement, the physical model could be broadened to include electronic resonances for relevant samples, by appropriately modelling one-photon absorption.

Two networks were trained using distinct Raman datasets. VECTOR-MU-sparse was designed to represent pure chemical spectra (for example, simple compounds like benzonitrile), while VECTOR-MU-dense dealt with more complex spectra, such as biological samples. The sparse dataset was a subset of the dense dataset, leading to the argument that the sparse network may be redundant. However, utilizing the sparse network on sparse data offers two key advantages: (i) it requires

less training time, as shown by the quicker convergence of the loss functions in figure 7.4, and (ii) it achieves higher accuracy than the dense network when applied to sparse data, as indicated in figure 7.8 (c). It was observed that both VECTOR-MU networks struggled to recover the relative strengths between the 3-color and 2-color regions for all chemical spectra. This issue may have arisen from the low intensity of the 2-color region, resulting from the weak excitation profile of the specific system. This in turn leads to a limited dynamic range for BCARS intensity in that region, causing a wide range of values for the resonant susceptibility in the 2-color regions to be mapped to a narrow range of values in the BCARS spectrum. Consequently, this could have made it difficult for VECTOR2 to accurately determine the correct scale in the retrieved spectrum. As mentioned previously, this could have also been due to the simulation parameters used in the underlying Raman spectrum, such as the choice of amplification coefficient for the two-colour region, although this value was consistent with reality. Nevertheless, the retrieval in each independent spectral region was superb compared to the current state of the art. While both networks performed well on sparse test sets, VECTOR-MU-sparse underperformed on dense test sets, which was anticipated. It was demonstrated that both networks excelled at retrieving Raman spectra from experimental chemical measurements taken with the BCARS microscope developed, showing good agreement with the corresponding spontaneous Raman spectra. Another important feature of the network is its potential for deconvolution concerning the probe laser, as illustrated in figure 7.5. Since the simulated data used for training includes convolution with the probe, the network learns to deconvolve, potentially yielding higher-resolution retrieved spectra compared to those obtained using the KK and MEM methods. This could be further improved by incorporating a second convolution to model the spectrometer impulse response function, although this was not explored in this study.

8. Immune cell phenotyping using BCARS hyperspectral imaging

In the previous chapters we have introduced BCARS both in terms of its experimental implementation, and also in terms of the NRB removal methods that must be applied in order to render a recorded spectrum useful for subsequent analysis. In this chapter we begin to apply BCARS to cellular classification of eukaryotic cells. This work was a collaboration with the Maynooth University Department of Biology, who provided samples for imaging. My contribution was in the acquisition of the BCARS hyperspectral images of cells, development of a novel classification procedure, and application of the classifier on a mixture dataset. At the time of writing a paper based on the results in this chapter has been accepted for publication pending major revisions in the Journal of Biophotonics.

At the time of writing, BCARS had not been applied to single-cell label-free classification. There have been some applications of multiplex CARS to single cell imaging[119, 9], however, the retrieved Raman spectra were not used for any cell classification. In this chapter, the first demonstration of a two-species cell classification is described, using the custom microscope and methods developed in chapter 4.4. The substantially higher signal intensity of BCARS compared to spontaneous Raman (SR) scattering allows the recording of Raman hyperspectral images (HSI). Since BCARS is free from fluorescence, the application toward adherent cells on glass is attractive. Furthermore, the excellent depth selectivity, due to the nonlinear nature of the effect, provides axial resolution comparable to that of a confocal Raman spectroscopy system. In a confocal setup, pinholes at the

illumination and detection plane filter out-of-focus light from reaching the detector[137]. However confocal Raman scattering is slow, with pixel acquisition rates on the order of tens of seconds[138]. Since BCARS gives access to the Raman spectrum, with a nonlinear dependence on the input intensity, it should, in theory, provide HSIs comparable to confocal Raman imaging, at faster rates.

It is well established that SR alone can differentiate between various cellular pathologies[15, 139, 140]. Advancements in automating SR point measurements and implementing statistical denoising[11, 10] has also reduced acquisition times to around 1 second per cell in cytology, although the throughput and complexity of these systems is still too low for widespread use. In confocal Raman, it is mainly a throughput issue, since data rates are limited by the laser damage threshold and spontaneous Raman cross-section. A practical enhancement for any Raman cytology experiment would be to increase the data acquisition rate, as this would enable higher throughput analysis and offer numerous other advantages, such as the potential for live feedback in surgical environments. Consequently, due to the benefits described above, BCARS has the potential to achieve the acquisition speeds that have previously limited the use of spontaneous Raman spectroscopy as a high-throughput technique for cytology.

BCARS spectroscopy of single cells has faced several challenges, preventing it from achieving the same success as SR has had in this area. The key issue is that, despite BCARS being confocal by nature due to its nonlinear electric field dependence, the amplitude of the anti-Stokes signal is influenced by the ratio of resonant to non-resonant susceptibility at each given frequency[6]. In the fingerprint region, the resonant susceptibility $\chi^{(3)}_{\text{Res}}$ is much smaller than the non-resonant susceptibility $\chi^{(3)}_{\text{NR}}$ due to low molecular concentrations and small scattering cross-sections. This results in a weak resonant signal. Theoretically, the minimum concentration needed in order for the CARS signal to surpass that of spontaneous Raman was reported to be in the millimolar range[141]. Therefore, research has focused on samples with either a high localized density of scattering species or a high Raman cross-section, both of which increase the resonant susceptibility. Lipids are a prime example, as they meet these criteria and can be effectively imaged using CARS[78, 142, 61, 143, 144].

BCARS has been more commonly applied to tissue imaging than to single cells, as the diverse

chemical content of biological tissue provides sufficient contrast among various structures, such as collagen, myosin, and nucleic acids, which can be analyzed using univariate methods. In contrast, single-cell imaging is more challenging due to the cells' thin morphology and high spectral similarity within and between species, as many cells contain similar organelles and biomolecules. Nevertheless, CARS hyperspectral imaging has shown the potential to distinguish cellular organelles like the nucleus, nucleolus, endoplasmic reticulum, and lipid droplets using the high-wavenumber region[145].

This study aimed to use BCARS to produce high-speed chemical images of multiple cells with as little sample preparation as possible, ultimately for automated high-speed classification of microscope slides. The cells chosen for this study were two distinct immune cells. These cells were chosen due to the relatively thick morphology of immune cells and because the main clinical diagnostic method used for blood analysis is high-throughput flow cytometry. The cell types used were plasmacytoid dendritic cells (PDC) and Jurkat cells. The PDC is a type of dendritic cell that resembles a plasma B cell in morphology. Jurkat cells are a type of T lymphocyte which is mononuclear and has a large nucleus to cytoplasm ratio. Both PDCs and Jurkat cells are peripheral blood mononuclear cells (PBMC) originating from haematopoietic stem cells. These cell types can become cancerous and diagnostic tests typically involve cytochemical staining for confirming the presence of cell neoplasia and immunophenotyping or cytogenetic testing for confirmation of specific cancer subtype. Thus, the classification of these cells in a label-free measurement could provide another approach for cancer screening or phenotyping in the clinical environment. In this thesis, the cells used were obtained from isolated culture and ethical approval was not required for their use.

Chemical images offer both molecular and morphological information at each sample point, which can improve diagnostic accuracy but was not used here. A pre-trained cell segmentation algorithm was employed to identify the cell area and integrate all retrieved Raman spectra within the cell boundary. This generated a single representative spectrum for each cell with higher signal-to-noise ratio (SNR). This approach provides a robust measurement of the cell's chemical profile and avoids biases inherent to point measurements due to the differing molecular composition of

cellular organelles[146].

8.1 Sample preparation and BCARS imaging

Suspended blood cells of each type (Jurkat T and Cal-1 PDC) were resuspended in 5 mL of cRPMI. Cell counting was performed by diluting 50 μL in 200 μL of cRPMI. Next, a total volume of 1 mL containing 10^5 cells was prepared in phosphate-buffered saline (PBS) in centrifuge tubes. The samples were centrifuged at 500$\times$g for 5 minutes at 4°C, and the supernatant was decanted. The resulting pellet was then resuspended in 1 mL of PBS. From each cell suspension, 500 μL was transferred to a new tube to create a 1:1 mixture. Both the mixture and the individual samples were again centrifuged as before, followed by decantation. The individual samples were resuspended in 500 μL of 10% formalin (filtered through 0.2 μm) and incubated for 10 minutes at room temperature. The mixture was resuspended in 1 mL of formalin and fixed and incubated as the individual samples. The three samples were then centrifuged under the same above conditions, after which the supernatant was decanted, and the samples were resuspended in 1 mL of PBS. The individual samples were again centrifuged, and the supernatant was discarded before being resuspended in 150 μL of molecular grade water. The mixture underwent centrifugation, the supernatant was removed, and it was then added to 300 μL of molecular grade water. From each cell suspension (both individual and mixed), 50 μL was pipetted on to separate glass coverslips and allowed to dry at room temperature for two days.

BCARS hyperspectral images (HSI) of each blood cell type were captured (10 images each) using the system described in chapter 5.1. The pixel acquisition time was set to 5 ms with constant velocity raster scanning. During the slow axis movement, the full vertical binning (FVB) data was collected from the detector. The probe's temporal delay was approximately 0.5 ps relative to the SC. Astigmatism compensation of the deformable mirror was optimized by measuring the resonant CARS signal in the cytoplasm of a cell. The hyperspectral images measured 200 $\times$ 200 μm with a 1 μm step size, covering the biological vibrational spectrum from 500 to 4554 cm^{-1}. A dark current spectrum was also recorded. This entire procedure was repeated for the mixture samples, capturing

12 images each.

8.2 Spectral processing

All HSIs were processed individually using the steps mentioned in 4.4. Specifically, cosmic rays were identified by thresholding the mean spectral intensity of the raw hyperspectral images (HSI). Under the experimental conditions, a cosmic ray event resulted in an average of less than one corrupted pixel per image. The corrupted pixels consistently exhibited a mean count exceeding ten times the average signal intensity, leading to the selection of this value as the detection threshold for each pixel. Any remaining cosmic rays would have been captured by the denoising process, which did not reveal any additional detections. The de-spiking was conducted using mean replacement based on the four nearest pixels, with no edge pixels showing corruption. The average replacement method was chosen since it operates on a single-pixel basis, whereas other techniques, like PCA, may introduce spectral bias in pixels that remain unaffected. Denoising was performed using truncated singular value decomposition (SVD), with the specific singular values retained in the reconstruction being guided by the custom algorithm that utilized the 2D Fourier transform of the right singular vectors, as detailed in section 4.4.1. The effect of the denoising method used is shown in figure 8.1 (a).

All hyperspectral images presented in this section were processed using the phase and amplitude-corrected Kramers-Kronig (KK) method[1]. The choice of method for NRB removal was based on the fact that the study was completely novel, and the various aspects that could aid in any classification, including all preprocessing and statistical methods should be based on standard methods as a first attempt. This would allow a determination of the quality of the underlying spectra, and whether the results are generally applicable to wider sample types using BCARS.

The average signal from the segmented background region of each image served as the reference non-resonant background measurement. The segmented image could be obtained using the raw BCARS image or the Raman-retrieved image. The smoothing parameter for phase retrieval was set to 100, while the asymmetry parameter was configured to 0.0001 for the high-wavenumber region

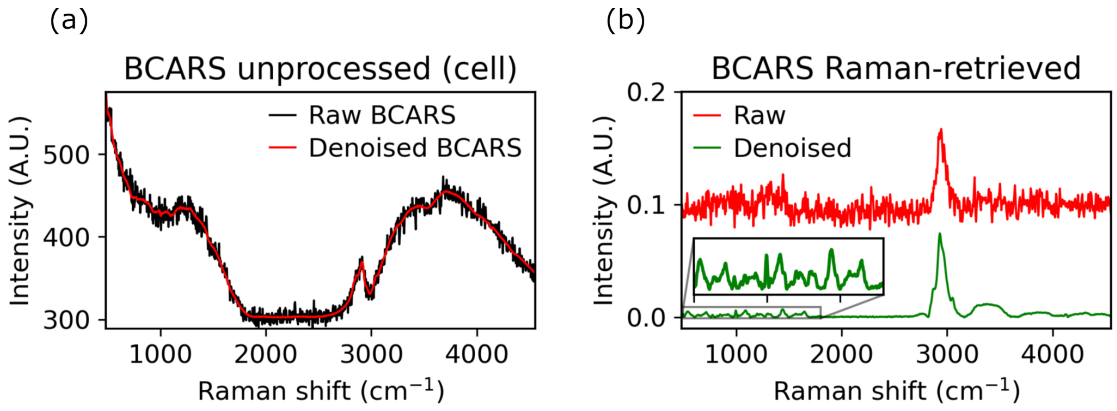

Figure 8.1: (a) Raw and denoised single cell BCARS spectrum prior to any further preprocessing, (b) Raman-like spectrum obtained using KK using both the raw and SVD denoised signals shown in (a). The raw spectrum was scaled vertically for clarity.

(2745 cm^{-1} - 4554 cm^{-1}), 0.001 for the fingerprint region (500 cm^{-1} - 1708 cm^{-1}), and 0.01 for the silent region (1708 cm^{-1} - 2745 cm^{-1}). Each cell's spectrum was then averaged to produce a single cell spectrum. To eliminate residual inter-sample variance caused by scatter, the EMSC algorithm was applied using a 5th-order polynomial and a mean reference BCARS spectrum. Finally, each spectrum was cropped to a range of 500 cm^{-1} - 3142 cm^{-1} and normalized to its minimum and maximum values. In figure 8.1 (b), the effect of the NRB removal is shown for an undenoised cell spectrum and denoised spectrum.

8.3 Methodology for BCARS hyperspectral single-cell classification (HSCC)

Hyperspectral BCARS images of two distinct isolated leukemic blood cell types—Jurkat T-lymphocytes and Cal-1 plasmacytoid dendritic cells (PDCs)—were obtained as described earlier. These hyperspectral images capture the full spatial extent of the cells, eliminating the need for cell targeting, as is typically required in Raman spectroscopy. In brief, preprocessing involved SVD denoising and KK-based NRB removal. Additionally, a pre-trained deep learning method was used to segment the cell regions from the total BCARS intensity image. The spectra within each segmented region were integrated to generate a single spectrum representing each individual cell. This process provided labeled single-cell spectral datasets, which were then used to train a Random Forest classification

model to identify distinguishing features between the two cell types. Finally, hyperspectral images of a mixed sample containing both cell lines at a 1:1 concentration were obtained to simulate a clinically relevant scenario with multiple unknown cell types in a single specimen. The processing workflow for this experiment is detailed in figure 8.2. Further details on the steps are provided below.

8.3.1 Step 1: Preprocessing

BCARS HSIs were preprocessed using SVD denoising as per section 4.4.1 followed by NRB removal using the KK method using the parameters described in 8.2. The next step involved integrating the resulting 3D dataset over the wavenumber dimension to generate a 2D image of the cells. This total intensity image was then processed using the Cellpose 3 segmentation algorithm[109, 110] to isolate individual cell regions. To obtain the NRB reference for KK, the raw denoised BCARS intensity image was integrated, and the largest area mask was averaged to extract the spectrum of the coverslip. Cellpose is a deep-learning, cell-agnostic segmentation algorithm that does not require any retraining or parameter adjustments. Traditional segmentation methods like the watershed algorithm often fail to separate closely positioned cells due to overlapping regions, which was also observed in this experiment. However, the Cellpose model accurately identified cell boundaries, even when cells were in contact. The Cellpose ”cyto-3” model was used, which includes an image restoration step aimed at improving segmentation accuracy. After identifying cell boundaries, the spectra for each cell were averaged based on the mean spectrum within the boundaries.

Noisy cell spectra from the labeled dataset were detected using Pearson correlation analysis, comparing each cell sample with a high-SNR reference that was obtained empirically. Samples with a Pearson correlation coefficient $\rho < 0.995$ were excluded from the dataset, leaving 346 cells in total, with a 1:1.7 split between Jurkat and Cal-1 cells. EMSC normalization was then applied, and the data was normalized to the minimum and maximum values for each cell.

For an initial evaluation of the single-cell spectra, principal components analysis (PCA) was conducted on the labelled dataset to visualize spectral variance. PCA revealed the differences

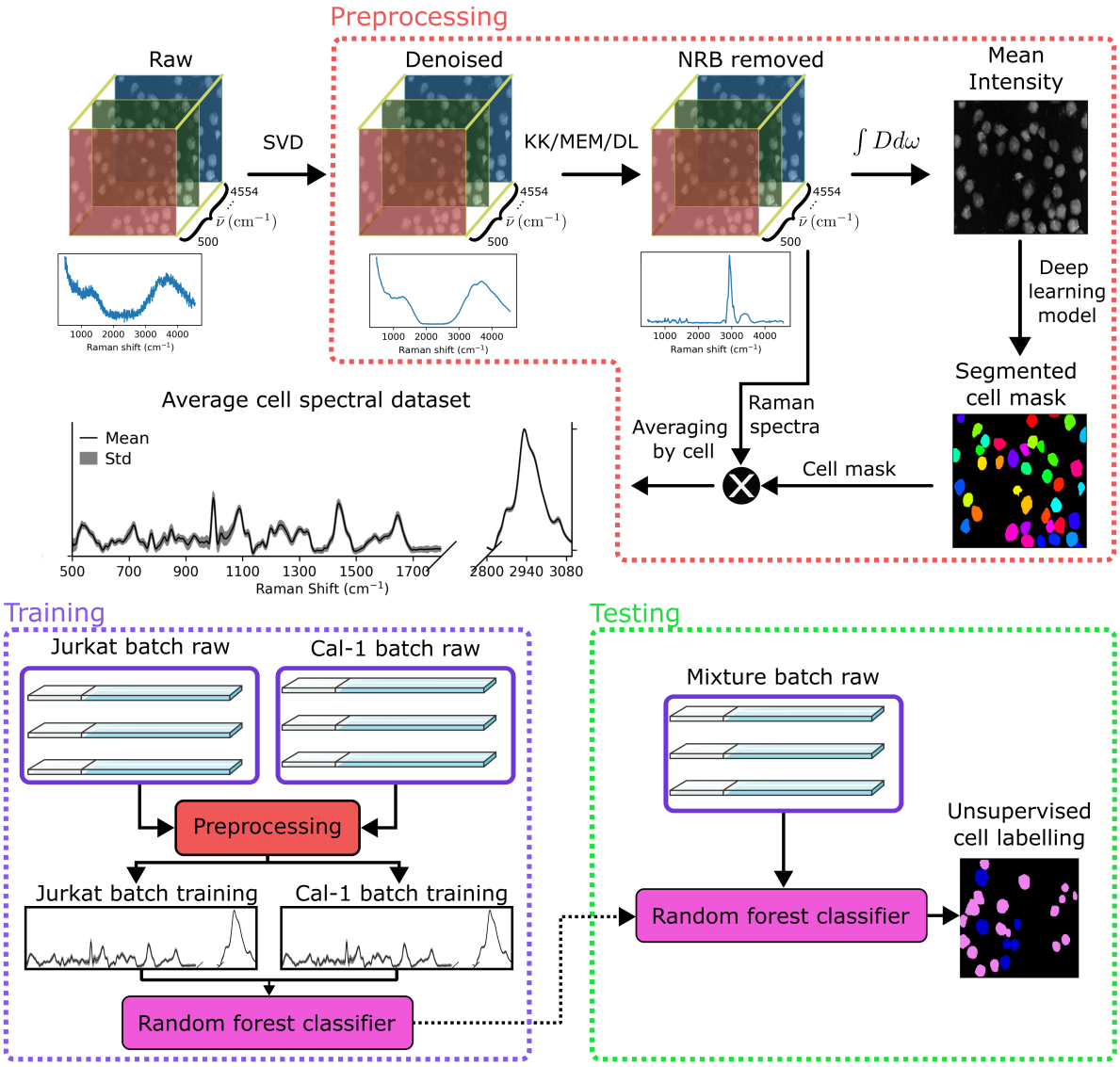

Figure 8.2: Flow-chart of the experimental and data analysis pipeline.

between the spectra of the different cell types. It is important to note that PCA was used solely for data evaluation and not for the multivariate classification model in Step 2.

8.3.2 Step 2: Training a multivariate classifier

The dataset of independently prepared cell samples is termed the labelled dataset, since any cell in each batch was known. A random forest (RF) classifier was trained on the full labelled dataset using 40 decision trees and balanced class weights to address the bias from the uneven sample

distributions. An RF is an ensemble method for supervised classification. It uses bootstrapping to create a training set, which is then split through a series of binary decision trees. At each node, a sample is classified based on a randomly selected feature, with the model learning by maximizing the impurity decrease as it moves from one node to the next. This same method was used in Reference 11 to classify leukocytes. Hyperparameter tuning was applied only to optimize the number of trees, using 10-fold cross-validation. The RF model was built with the SciKit-learn package in Python, using default settings except for those specified. The out-of-bag training score for the RF model was 97%. The importance of each spectral feature was determined by calculating the mean decrease in Gini impurity within each tree.

8.3.3 Step 3: Testing on a mixture

The mixed HSIs were preprocessed using the method described in Step 1. The resultant dataset was input to the trained RF model in order to predict the class probability of each detected cell in the mixed dataset. The class probabilities were then used to classify each cell using a threshold of 0.5. Separately, as a form of validation, the predicted cell spectra were projected on to the principal components obtained from the labelled dataset in Step 1. Labels were applied based on the RF prediction. The resultant scatter plot of the PC scores was investigated for similarities to the corresponding result for the labelled dataset.

8.4 Experimental Results

8.4.1 Labelled cell analysis

In figure 8.3, the mean BCARS image and the corresponding cell segmentation mask are displayed for two example HSIs of each labeled cell species. Each color in the mask represents the boundaries of an individual cell. The segmented mask images demonstrate that the segmentation was precise even when cells were close in proximity, which typically causes errors in the watershed algorithm. No misclassified cell boundaries were observed across the entire dataset. Additionally, the average

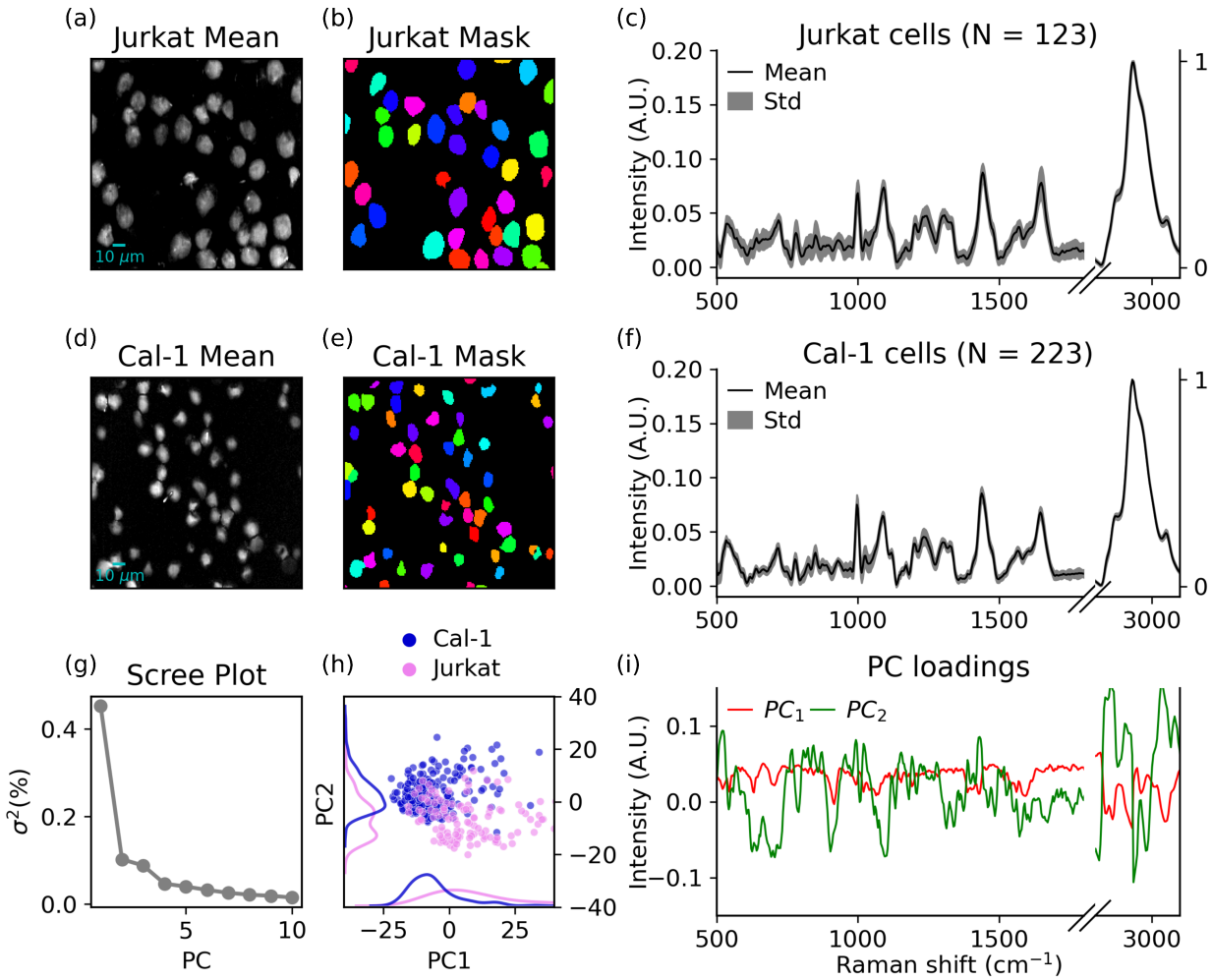

Figure 8.3: Supervised analysis of each cell species using PCA. (a) mean intensity image of BCARS hSI for a Jurkat sample, (b) Jurkat cell mask obtained from segmentation model applied to (a), (c) mean and standard deviation of spectral data for the whole Jurkat dataset, (d) mean intensity image of BCARS hSI for a Cal-1 sample, (e) Cal-1 cell mask obtained from segmentation model applied to (d), (f) mean and standard deviation of spectral data for the whole Cal-1 dataset, (g), scree plot of explained variance proportion versus the principal components, (h) PCA score plot of each cell species on the first two principal components (also showing kernel density estimate), (i), first two loadings of the PCA data.

spectrum retrieved for each cell species was consistent with a spontaneous Raman spectrum of a blood cell[147]. The relative intensity between the high-wavenumber and fingerprint regions also matched the expected ratio, reflecting the relative abundance and cross-sections of the vibrational modes in each region. As expected, the signal-to-noise ratio was visibly higher in the high-wavenumber region due to the greater signal intensity and lower relative NRB strength in this region. A PCA scree plot is also provided, showing the percentage of variance explained by each principal component. The first two principal components accounted for 55.4% of the variance in the data.

The PC scores for each cell are also shown, with moderate overlap between the two species on the first two PCs.

The supervised analysis of the labeled data revealed distinct features in the Raman spectra, which are commonly associated with known vibrational modes in eukaryotic cells. As illustrated in figure 8.3 (h), the two species show moderate separation along the first two principal components (PCs). However, no distinct clusters were observed on these PCs. Examination of the first PC indicates that most of the variation originated from the high wavenumber region at 2934 cm^{-1} and 3054 cm^{-1}. On PC2, several peaks within the fingerprint region contributed to the data's variability, including the CH_2 scissoring mode at 1440 cm^{-1}, the phenylalanine ring breathing mode at 1003 cm^{-1}, markers for adenine and guanine at 1575 cm^{-1}, vibrational modes from uracil, cytosine, and thymine ring breathing, the O-P-O symmetric stretch at 784 cm^{-1}, and the PO_2 stretching mode at 1095 cm^{-1}.

8.4.2 Supervised classifier performance

A representative broadband CARS spectrum obtained from a Cal-1 cell is displayed in figure 8.4. The spectrum closely resembles a spontaneous Raman spectrum from a blood cell, featuring distinct peaks and characteristics in both the fingerprint region (nucleic acids, lipids, proteins) and the high-wavenumber region (symmetric and asymmetric stretching of CH_2 and CH_3). The major bands in the cell measurement are labelled in the figure. Given that the high-wavenumber region of a cell's vibrational spectrum contains only a limited number of broadly overlapping features (primarily from alkyl groups), it is likely to provide less diagnostic information compared to the fingerprint region. The feature importance analysis from the supervised RF classifier highlights the specific wavenumbers contributing to the classification. A built-in algorithm was used to calculate the feature importance (FI) based on the normalized decrease in impurity, which measures the randomness of a node when a specific feature is applied. FI is a non-negative value, with higher numbers indicating greater importance. Since the full BCARS spectrum was employed to train the RF model, examining the FI after training is a valuable way to analyse spectral features that are relevant in the classification. The spectral FI of the trained model is displayed in 8.4. High FI values

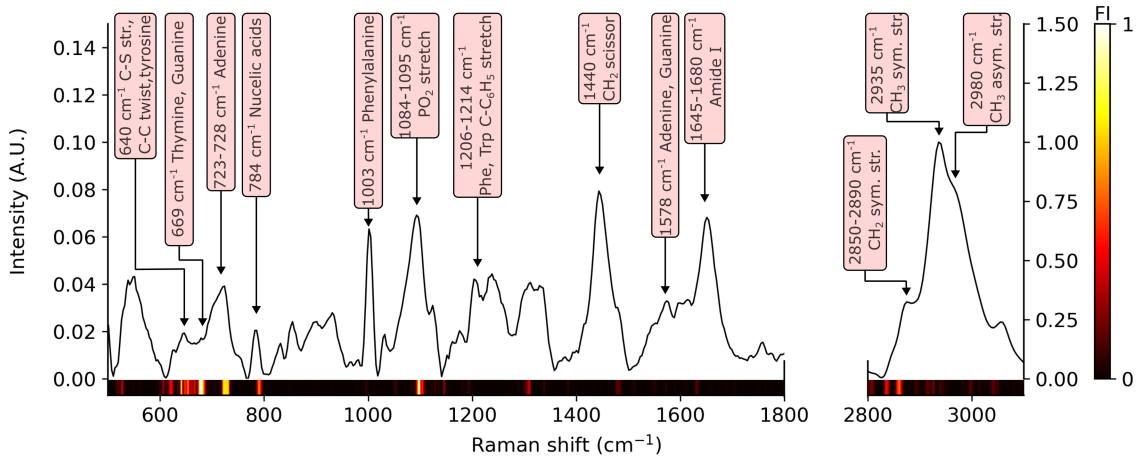

Figure 8.4: Single cell retrieved BCARS spectrum from a Cal-1 sample. Vibrational peaks were assigned based on references [148] & [149]. Also shown is the normalised feature importance from the RF classifier.

aligning with vibrational resonances suggest their likely contribution to classification. The highest FI was observed in the fingerprint region, corresponding to the 669 cm^{-1} band, which is associated with the nucleobases thymine and guanine. Another prominent feature was the 723-728 cm^{-1} band, linked to adenine. Relatively high FI values were additionally noted in the high-wavenumber region, spread across multiple wavenumbers rather than concentrated in a single band. The specific bands with high FI in this experiment give an indication of systematic differences in molecular concentration of each band in the two cell types studied. As the mean cell spectrum over the entire cell area was used, these molecular differences are likely due to variations in the concentrations and types of expressed proteins and micro-molecules within the cytoplasm and could also be due to differences in nuclear organelles. The supervised classification accuracy was assessed using 10-fold cross-validation, yielding a mean balanced accuracy of 99.4% for the test set and 100% for the training set. The RF model, trained on the full dataset, had an out-of-bag error of 3%. Cross-validation results are shown in figure 8.5

8.4.3 Unlabelled sample testing

The classification results using the RF model on the unlabelled dataset are presented for nine different hyperspectral images in figure 8.6 (a). The color of each detected cell region represents the class probability for one specific class (Cal-1). Cells with a probability greater than 0.5 were

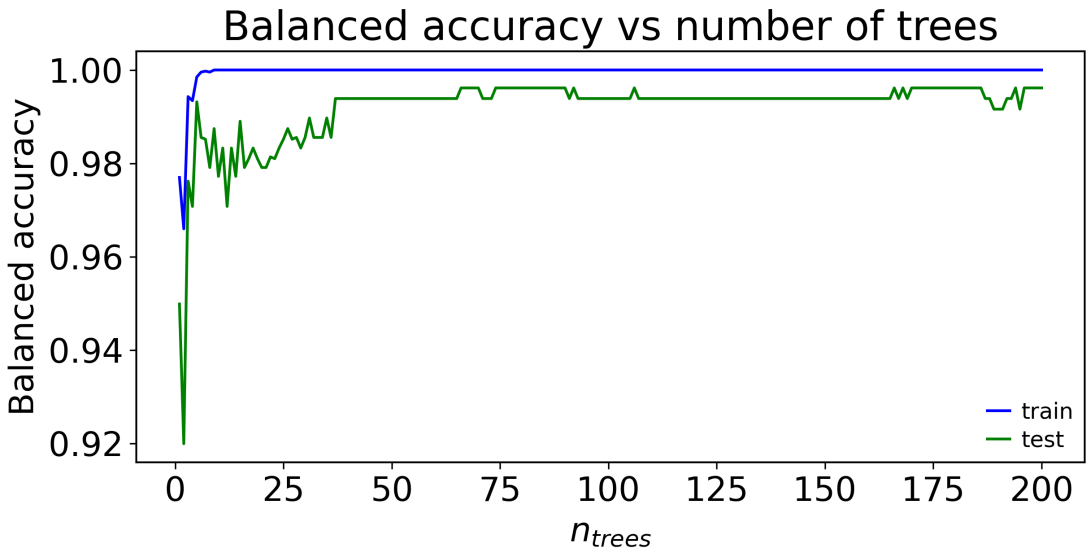

Figure 8.5: Results of cross-validation to determine the optimum number of trees in the Random Forest model.

classified as Cal-1, and those with lower probabilities were classified as jurkat cells. The class probability essentially reflects the likelihood, based on the data and model, that the cell belongs to that class. Some regions exhibit a class probability around 0.5, indicating low confidence in assigning the cell to either class, likely due to a low signal-to-noise ratio (SNR). This issue is further discussed later.

Figure 8.6 (b) shows the projection of the classified mixed samples onto the principal components from the labelled study, along with a kernel density estimate of the distribution. The separation of data is notably similar to the PCA score plot in figure 8.3 (h). The centroids of each species distribution are nearly identical between the labelled and unlabelled data, indicating that the spectra have similar weightings along the first two principal components. While this PCA analysis does not validate the classification of unlabelled cells, it suggests that the classified unlabelled spectra share similar spectral characteristics with the labelled datasets of the same species. To further evaluate the classification results, the expected proportion of cells classified was compared with the actual proportion observed in the mixture. Using a Chi-square test, a null hypothesis was formed; there was no difference between the expected and observed cell frequencies. The test produced a p-value of 0.979, meaning the null hypothesis was not rejected using this test. Additionally, the relative size distribution could be obtained from the segmentation process for both labelled and

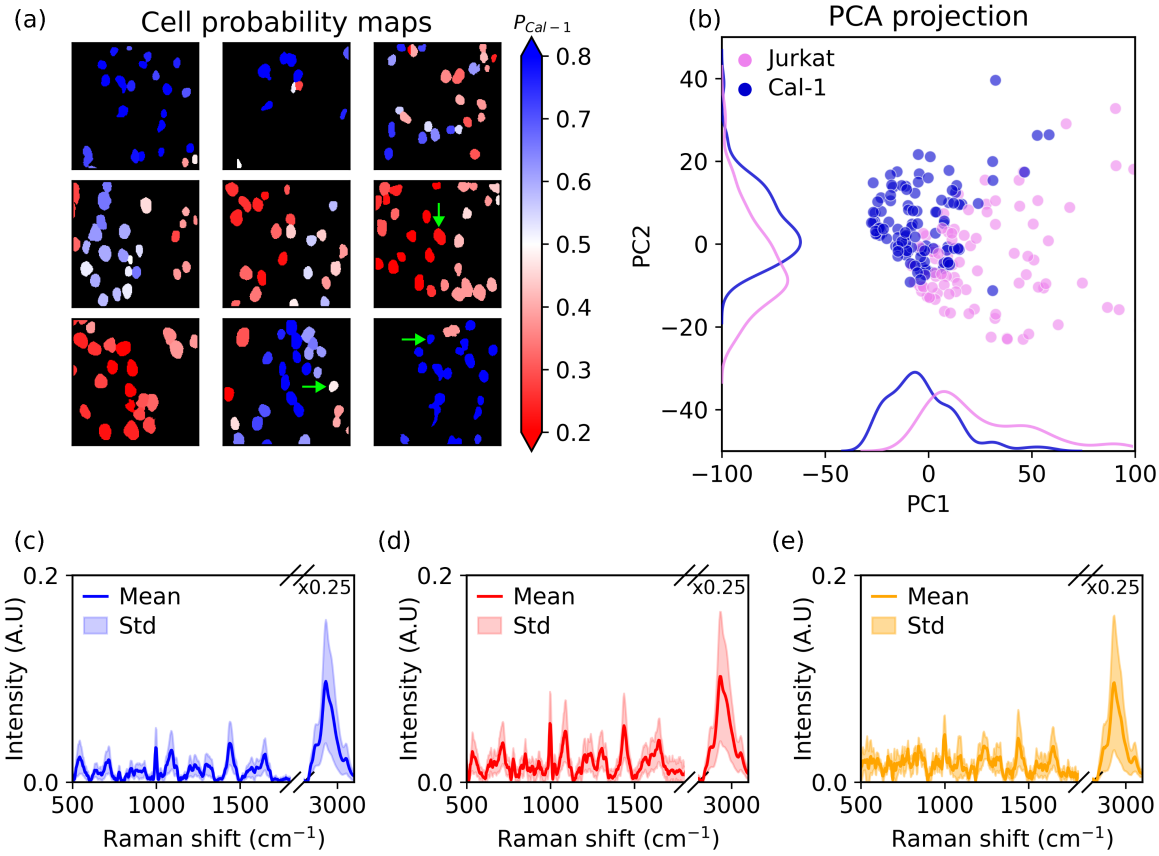

Figure 8.6: (a) Cell probability maps using the RF classifier trained using the labelled cell species data, (b) PCA scores and kernel density estimates of each segmented cell on the principal component vectors obtained from the labelled data, (c) Single cell Raman spectrum and variability of a Cal-1 high probability sample, (d) Single cell Raman spectrum and variability of a Jurkat high probability sample, Single cell Raman spectrum and variability of a low probability sample. Green arrows indicate cells shown in (c), (d) and (e).

unlabelled data and this was used to confirm whether the expected cell size distributions matched the known distribution. Assuming a circular cell area, the distribution of the diameters for each cell type and both experiments (labelled and unlabelled) is shown in Fig. 8.7 for cells that had a prediction probability of being a Cal-1 of $0.7 < p < 0.3$. Thus, only cells with a high confidence of classification were used in this analysis. It was observed that the labelled data had a significant difference in average cell diameter between cell types. Jurkat cells had a median diameter of 17.3 μm, while Cal-1 cells had a median diameter of 11.9 μm. Across experiments, the cell diameter was not statistically different between the Jurkat cells, however it was for the Cal-1 cells. This may be due to some actual Cal-1 cells being classified as Jurkat cells.

To better clarify why certain cells were not classified with high probability, the individual “pixel”

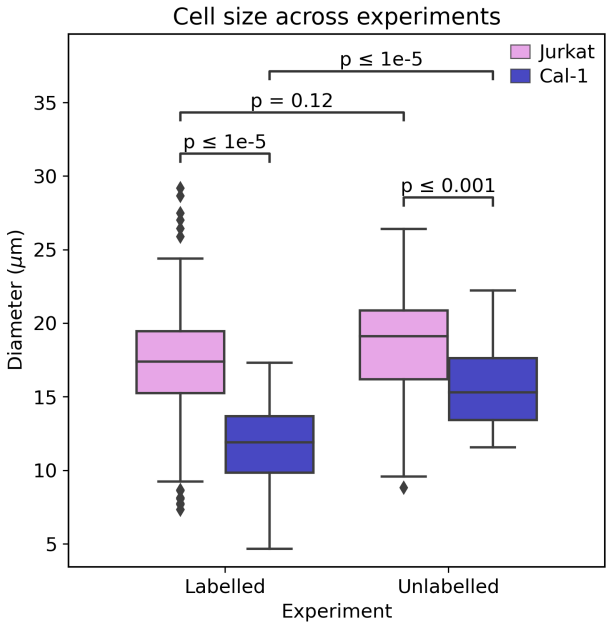

Figure 8.7: Boxplot of the cell diameter across species and experiments. An independent sample t-test was used to determine if the difference between mean diameters was statistically significant.

spectra within a specific cell area for three distinct cases was examined: a cell exhibiting a high prediction score for each cell line, and a cell showing a low prediction score. The locations of each cell are indicated with a green arrow in figure 8.6 (a). For all three scenarios, the mean and standard deviation spectra of the intra-cell data is plotted. The results for the high-probability Cal-1 and Jurkat cells are displayed in figure 8.6 (c) and (d), while the low-probability cell is represented in (e). These spectra revealed substantial intra-cell variability, even among the high-probability samples. This variability may stem from the natural macromolecular distribution of Raman scatterers within the cells, underscoring one advantage of HSI classification: the ability to identify sub-cellular features that might significantly differentiate species. Notably, the CH-stretching signals exhibited considerable variation across all cases, likely due to scattering effects from the varying thickness of the cells (since these data were not scatter-corrected). It is important to highlight the difference between the mean spectrum of the low-probability cell in (e) and those of the two high-probability cells. The fingerprint region in this spectrum showed a significantly lower signal-to-noise ratio (SNR), potentially attributable to an incorrect focal depth due to an abnormal cell morphology on the coverslip. Additionally, there was greater variability in the spectrum below 1000 cm^{-1} and in the

PO_2-stretching band. Increased variability within a cell may indicate the presence of a single outlier pixel or more systematic differences in noise levels within that cell.

8.5 Discussion

The results above demonstrate a fully automated high-speed cell classification method for label-free analysis. The Raman spectra obtained in this study were comparable in signal content to spontaneous Raman spectra of leukocytes. Achieving a high signal-to-noise ratio (SNR) for BCARS cell spectra used in classification is challenging and denoising was found to be critical in achieving the result. While the nonlinear BCARS process can yield high signal intensity, the single-pixel SNR in the fingerprint region still remains quite low due to the scan times required for imaging, making singular value decomposition (SVD) crucial for enhancing the signal-to-noise ratio to a practical level. The combination of SVD and cell averaging yielded relatively high-quality Raman spectra with clearly identifiable vibrational features within the biologically relevant range of 600 cm^{-1} to 3200 cm^{-1}. Using SVD for signal denoising effectively increases the exposure time during experiments since the optimal low-rank truncation is learned from the data itself. Essentially, the strength of SVD lies in the extensive distribution of similar signals within the input data. While this data is abundant in hyperspectral imaging (HSI), classification of individual cells without HSI would require alternative denoising methods unless extensive datasets were collected.

In the mixed sample, notable clustering of similarly labelled cells was observed on the coverslip. Although the data was pseudo-labelled based on prediction scores, and no ground truth was available, such clustering was unexpected in a homogenous mixture. It was suspected that this clustering resulted from differing transport properties of each cell species, potentially creating a spatial gradient of cell types from the center (where the drop was pipetted) to the edge of the coverslip. This is supported by the visible difference in average cell diameter from the center to the edge as shown in figure 8.8. In figure 8.8 (a) and (b), a brightfield image is shown for each independent cell species, while in (c), an image of the mixture is shown. Upon inspection, there was a clear grouping of cells by size and thus, since there was a significant difference observed between cell sizes, the cells may

have separated based on their size.

Effectively removing the non-resonant background (NRB) is critically important in any BCARS bio-classification experiment. Laser characteristics, including spectrum, power, and pulse duration, significantly influence NRB generation; however, fiber lasers such as the one used here offer remarkable stability over time. To minimize potential confounding from the laser system, all imaging measurements were conducted on the same day with minimal time between acquisitions. Nevertheless, the NRB can vary from one point to another. In the context of full automation, the NRB removal step was the only supervised aspect of preprocessing, as the phase detrending parameters must correspond to NRB strength to avoid overfitting or underfitting to the resonant susceptibility phase. It was noted that once optimization was performed on a representative spectrum for either cell class, the Kramers-Kronig (KK) procedure yielded consistent results throughout the experiment.

In a classification study, it is also essential to ensure that spectral classification results stem from resonant differences in the spectra rather than variations introduced by the experiment itself. Differences in spectral datasets, as quantified by principal component analysis (PCA), appear at characteristic Raman shifts corresponding to prevalent biomolecules, which is typically used to confirm that chemical features can discriminate the cells. The results here indicate that BCARS can extract high-content chemical information from cells at approximately 5 ms per pixel. At the imaging resolution of 1 μm, this leads to a total scan time of about 300 seconds (with an additional 0.5 seconds of dwell time between each fast-axis scan). This performance is promising for single-cell analysis, as an area of 1 mm^2 could be scanned in about 1.38 hours, provided data can be transferred post-scan. The primary advantage of this method over spontaneous Raman (SR) imaging is its ability to rapidly record hyperspectral images of microscopic areas. It is expected that the pixel exposure time could be reduced to around 1 ms, with approximately equal quality results. In addition to yielding a better average spectrum compared to SR, which typically uses point scanning, this method also avoids fluorescence interference and allows for the use of low numerical aperture (NA) collection optics. This is particularly beneficial for imaging glass slides or through flow apparatus.

Our approach to cell classification can also be compared with stimulated Raman scattering (SRS) imaging for similar information acquisition. SRS studies have been restricted to narrow bandwidths like the high-wavenumber region, as broadband detection is impractical. Nevertheless, this information allows for label-free cell imaging. While the chemical information might be less comprehensive than full fingerprint analyses, the absence of interfering NRB in SRS means it typically requires less processing to achieve sub-cellular imaging. To obtain the full biological frequency band for a cell using SRS would necessitate wavelength tuning across 3500 cm^{-1}, which can be time-consuming. Although SRS benefits from lacking an NRB, instantaneous SRS methods require complex systems with parallelized lock-in amplifiers and are generally limited to higher wavenumbers. It has yet to be demonstrated that this band can provide for cellular classification studies similarly to the Raman fingerprint region.

A central aspect of this study was the confidence in classifying unlabelled data. While supervised testing showed high balanced accuracy on a test set, quantifying accuracy on unlabelled data was challenging. Two semi-quantitative methods, PCA and size analysis, were employed to assess the likelihood of successful implementation on unlabelled data. The projection of unlabelled data onto the principal components derived from labelled data showed strong agreement between cell types, suggesting that the pseudo-labelled data varied similarly to known labels. To further understand the results, size analysis revealed a statistically significant difference in cell diameter between the two labelled cell types. The average cell diameter was compared between labelled and unlabelled data, showing no significant difference for Jurkat cells, but a significant difference for Cal-1 cells across experiments. This may be attributed to some misclassifications. However, both labelled and unlabelled data exhibited the same signed significant difference in cell diameters, providing further evidence for successful classification.

A key feature of this work is the spectral averaging of the entire BCARS spectrum for each cell. Since chemical information is generally more informative than morphological information, chemical averaging was deemed appropriate. However, morphological information, which is always present in hyperspectral images, could also enhance the classification accuracy. Some features could be computed from the image and appended to the spectrum as additional variables, such as cell

diameter, ellipticity, or convexity. A higher resolution could enable a deeper model that utilizes the full cell hypercube for classification rather than relying on a single spectrum; this would, however, necessitate a custom deep-learning architecture. The single-cell spectrum was derived using the mean over the entire cell extent, which is the most common method for obtaining a representative spectrum. However, several potential improvements could be explored in future iterations of this work. For example, removing outliers before calculating the average using statistical metrics could prevent atypical pixels from skewing the results. Such outliers may arise from abnormal cell morphologies or errors in segmentation or NRB removal. Another approach could involve using the median Raman spectrum as the representative spectrum to further mitigate the impact of outliers. Nonetheless, the single-cell classification method demonstrated here has its limitations, and there remain experimental improvements to be made. First, manual intervention may be needed for NRB when the resonant-to-non-resonant susceptibility ratio changes, as previously discussed. This issue could potentially be addressed through deep learning methods. Additionally, certain cells may pose challenges, particularly those with thin morphologies (e.g. epithelial cells), resulting in low SNR even with denoising and cell averaging. One possible improvement in this regard might involve implementing dynamic focusing techniques using real-time deformable mirrors. Finally, a flow cytometry approach could outperform the HSI method for spectral classification; however, this would necessitate careful consideration of how to achieve sufficient SNR for subsequent classification from a single high-speed spectral recording, possibly achieved through optical averaging over a line scan of the passing cell. While SVD could be applied to the total dataset if many thousands of cells are analysed, the advantage of spectral averaging across the cell area would be compromised.

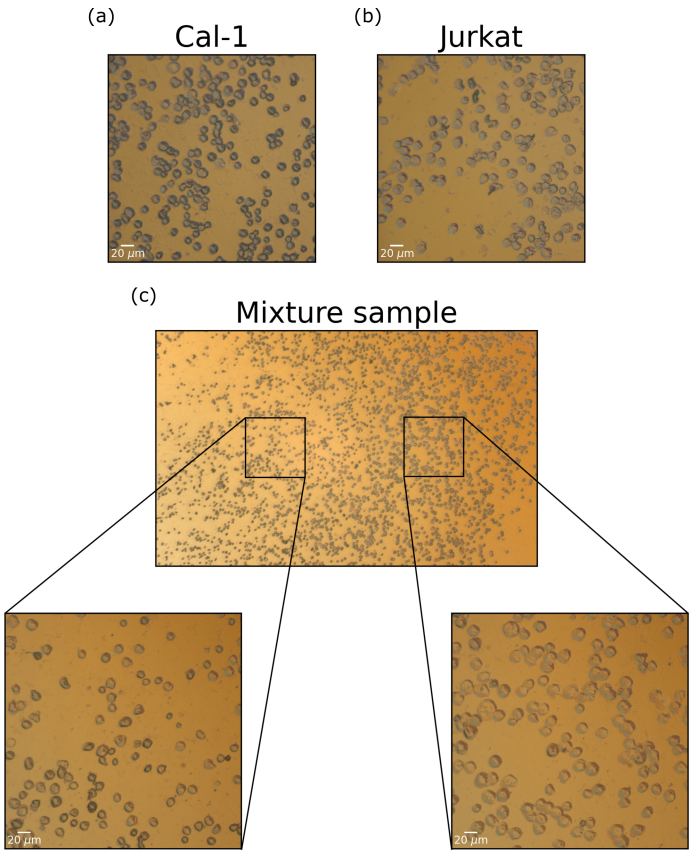

Figure 8.8: (a) Brightfield image of the independent Cal-1 cell, (b) Jurkat cell and (c) mixture.

9. Fungal pathogen identification using BCARS hyperspectral imaging

In this chapter, the development of BCARS toward unsupervised label-free epithelial cell imaging is explicated. This work is the culmination of several iterations to the BCARS acquisition procedure described in 8.1. A bespoke analysis pipeline was also developed, without which, efficient identification was not possible. The factors in obtaining label-free epithelial cell images will be discussed and the importance of enhancements will be qualified. The Maynooth University Department of Chemistry generously supported this work by providing valuable expertise on the nature of the samples used and for preparing samples for imaging. The Department of Biology provided expertise on the clinical aspect of the pathogen used. In this chapter, I was responsible for designing the experiment, acquiring the BCARS images and analysing the results. At the time of writing we are considering submitting the results of this chapter to a journal, pending improved experimental results.

9.1 Introduction - BCARS as an alternative to diagnostic cytology

Fungal infections are already a global threat causing approximately 1.7 million deaths per year[150]. This is mainly due to the higher load of immunocompromised patients suffering from diseases which reduce the immune systems efficacy of infection mitigation. The increasing prevalence of anti-fungal resistant strains is also of concern, such as *Candida Auris*, which is now listed

as an urgent antimicrobial resistant (AMR) threat by the CDC[151]. Optical microscopy is the cornerstone analysis technique still used in cytology for the diagnosis of disease at the cellular level[152]. The diagnosis is thus based on morphological changes present within cells that may be due to an infection, cancer or immune response. The diagnosis of invasive pathogen is typically confirmed by specimen collection from the suspected site by swab, sterile sample, venipuncture or other method, and subsequent staining to improve visual contrast. Calcofluor white is a stain that can aid in the identification of all fungi through highlighting the chitin within the cell wall[153]. Such methods however, are cumbersome as they require a wet laboratory for sample preparation and interpretation is always performed by an expert pathologist. As a consequence of this, diagnosing fungal infections is time and resource intensive, with the possibility for false-negatives due to background fluorescence.

Other common methods for fungal detection are immunologic methods which focus on the detection of pathogen-specific antibodies, antigens or other biochemical markers. Methods incorporating these markers are peptide nucleic acid (PNA)–fluorescence in situ hybridization (FISH) and matrix-assisted laser desorption ionization–time of flight (MALDI-TOF) mass spectrometry (MS) [154]. These methods are highly specific, allowing positive fungal species detection, however they require correct selection of the marker prior to analysis (PNA-FISH) and are only suitable for confirmation of species, not initial screening. MALDI-TOF also requires a pure culture and so cannot be performed on clinical samples. The field of mycology has seen recent advances in molecular diagnostic techniques for fungal detection[155], such as polymerase chain reaction (PCR)[156], T2 magnetic resonance (T2MR) analysis[157] and genetic sequencing[158]. The advantage of molecular methods over traditional detection using immunofluorescence and direct examination are the high specificity to the pathogen and ability for automation, since an expert analyst is not required. These methods also have their drawbacks however, such as extensive sample preparation and analysis times, and *a priori* molecular target selection requirements.

Optical spectroscopy is another method that has become popular for cytology studies due to its high sensitivity. The Raman spectrum of a cell encodes information on the biochemicals present within the focal volume, which results in a specific cell fingerprint that can be used to distinguish

cell types and states of the cell cycle[159]. The benefits of Raman spectroscopy for cytology are the high spatial resolution ($\sim$ 300 nm) and ability to acquire molecular information without introducing exogenous fluorophores to the sample[160]. One of the major drawbacks to Raman spectroscopy is the time required for a single measurement, which is largely the reason precluding its use in chemical imaging studies or flow analyses in the clinical context. Due to its aforementioned enhancements, as highlighted in previous chapters, BCARS is a highly attractive modality for the detection of invasive pathogens, since it allows for rapid chemical imaging of a sample without the need for labelling. Furthermore, being a spectroscopic technique, BCARS is also non-destructive, allowing for samples to be re-analysed using the same or even a different technique. In the context of cytology specimens, this is a significant benefit, since sample volumes can be extremely low, especially from immunocompromised patients. In light of this, BCARS imaging could be used as the first diagnostic test, performed on an unprocessed sample, with confirmatory analysis being done by an expert. In this way, label-free high-throughput analysis of infectious pathogen could be realized.

In this chapter, the ability for BCARS hyperspectral imaging to perform an unsupervised classification of a fungal pathogen (*Candida albicans*), an opportunistic fungal pathogen, within human buccal epithelial cells (BEC) is demonstrated. The classification is performed using the information within each pixels Raman spectrum. This approach does not require sample labelling or sample ground truth spectra and in theory can be used in a flow cytometry setup. The spatial dimension in the HSI provides spatially relevant information for subsequent analysis e.g. membrane binding, pseudohyphae formation and fungal cluster size. The classification performance is verified using common clustering metrics and a comparison between detected spectra from the pathogen and known spectra of the pure pathogen is performed. For completeness, a comparison between the BCARS spectra with the spontaneous Raman spectra obtained with a conventional Raman microspectroscopy system is also shown.

9.2 Conventional cytology of invasive fungal pathogen

Yeast of the genus *Candida* forms part of the normal flora of humans, where it can be found in the alimentary tract, female genitalia and skin[161]. Candidiasis is an infection caused by *Candida spp.* that may occur in healthy people, but in other people is typically due to an immunologic impairment[162]. Mucosal infections from *candida* are the most common form of fungal infection encountered clinically. Clinical signs and symptoms are not specific for fungal infections and diagnosis of the disease combines clinical suspicion combined with physical examination and procurement of an appropriate specimen for laboratory analysis[153]. The principal diagnostic technique used for identifying the presence of the pathogen within clinical specimen is direct examination using brightfield microscopy with complementary fluorescent staining. Fungal pathogen are distinguished in to two groups, those that infect the skin, nails and hair, so called dermatophytes, and those that infect the mucosa[162]. Direct examination of a wet mounted (unstained) sample can provide characteristic morphological information for preliminary identification or definitive identification in some cases, provided the sampling is adequate. Increased detection speeds and higher specificity of identification can be obtained by fluorescent staining using Calcofluor white[153]. Another common method of detection, more sensitive than direct examination is culturing a clinical sample and observation of the growth of colonies using microscopy. Isolation of *candida* from a normally sterile site is indicative of candidiasis. The positive detection can be aided using a germ-tube test, whereby a small volume of the colony is placed into a tube with human serum and incubated for 2.5-3 hours. Microscopic examination and germ tube production in the form of hyphal structures emerging from cells confirms the presence of *C. albicans*. The quantity of germ tube production may vary between different strains of *C. albicans*. It should be clear that due to the necessity for incubation, culturing cannot provide rapid diagnostic information.

9.3 Raman spectroscopic fungal detection

The information provided by Raman spectroscopic measurements are indicative of the biomolecular constituents of the sample in the form of vibrational frequencies, and each spectrum could be

analyzed based on the presence of known vibrational frequencies (mode assignment) or used in a spectral matching procedure that provides an indication of the similarity between the unknown spectrum and a known spectrum from a material database. It was previously shown that eleven different species of *Candida* could be classified based on the spontaneous Raman spectrum (using point measurements) of the cells with an average accuracy of 80 %[163]. Therefore, there is strong evidence that BCARS can potentially provide a label-free imaging capability for candida identification. The use of Broadband CARS imaging for fungal pathogen detection would require the same sample preparation as direct examination using transmission microscopy, since it is a label-free technique. BCARS can provide either a full chemical image of the sample, sub-sampled measurements over a spatial grid or single point measurements. Prior to analysis, the ideal clinical sample would be either filtered or centrifuged depending on the specimen collection method, in order to increase the concentration of the solute, however, if time or resource constraints prevent this, analysis of a raw specimen would also be possible, however, at risk of a potential decrease in detection sensitivity. Due to these properties, BCARS imaging is highly compatible with cytological diagnostics using virtually any sample preparation technique, such as slide smears, liquid-based cytology or scrapings. In the next section, the sample preparation of a clinically relevant specimen is described, with the ultimate goal of performing a label-free identification of candidiasis.

9.4 Sample preparation

9.4.1 Fungal strain

C. albicans was maintained on sabouraud dextrose agar and cultures were grown to the stationary phase (1-2 x 10^8/ml) overnight in yeast extract peptone dextrose (YEPD) broth (1% (w/v) yeast extract, 2% (w/v) bacteriological peptone, 2% (w/v) glucose) at 30 °C and 200 rpm. Stationary phase yeast cells were harvested, washed with PBS, and resuspended at a density of 1.5 x 10^8/mL in PBS.

9.4.2 Buccal Epithelial Cells

Buccal epithelial cells (BECs) were harvested from healthy volunteers by gently scraping the inside of the cheek with a sterile tongue depressor. Cells were then washed in phosphate-buffered saline (PBS) and resuspended at a density of 2.5 x 10^5 /ml.

9.4.3 Adherence assay

The yeast cells were suspended in the desired concentration of compound solutions and PBS, then left to pre-label for 1 hour. Yeast cells were mixed with BECs in a ratio of 50:1 and PBS to give a final volume of 2 mL and incubated at 37 °C and 200 rpm for 1.5 hours. The BEC/pre-labelled yeast cell mixture was harvested by passing through a poly-carbonate membrane containing 30 mm pores which allowed yeast cells to pass through whilst retaining the BECs on the membrane surface. The membrane was washed twice with 5 mL of water to remove the excess unbound yeast. The remaining cells on the membrane were collected in water and placed on glass coverslips (2 slides per compound) which were left to air dry overnight. The cells were heat fixed and the coverslips were rinsed using cold water to remove any impurities, and then left to air dry for 30 minutes.

9.5 Procedure

The identification of the presence of a specific species of a cell in a HSI requires a significant spectral difference between the pathogen of interest and the “normal” cells for univariate or multivariate methods to be successful. In particular, univariate methods require at least one spectral band to be significantly different in intensity between the species, which may be obscured due to noise or overlapping vibrational modes. In biological samples, while the number of Raman modes can be high (> 40)[164], the resultant spectral fingerprint can be similar even among different cells. There are also variations in the molecular constituents depending on the spatial location, due to the heterogeneity of a cells structure, resulting in biologically-induced noise within the results. These variations are exacerbated when only a single measurement per cell is obtained. In genetically

identical cells, there are also Raman-relevant biochemical differences due to cell-maturity[165] and random biological noise[166]. A whole cell averaging approach as performed in the previous experiment on blood would mitigate the location dependence of spectra. However, in the particular case of a diagnostic test where the presence of a small invasive pathogen is to be determined, the cell averaging procedure is not appropriate. This is because such a method requires highly robust segmentation of individual cells, which can be difficult to achieve for pathogen that are invasive to a larger cell. In this experiment, the buccal epithelial cells were artificially infected with a pathogen that naturally adhered to the membrane during incubation, as is typical for the species. In fact, the ability for *candida* to adhere to tissues and other material is suspected to contribute to its pathogenicity[153]. The adherence of the pathogen is due to ligand-receptor and Van der Waals interactions and is considered one of its most important virulence factors[167]. In a typical clinical sample from a patient positive for candidiasis, it is foreseen that the pathogen would be adhered to the host cell membrane. In these samples, the close proximity and potential for apical adherence would preclude segmentation as a processing step, since it would merge the overlapping cell boundaries. This problem is depicted in figure 9.1. It can be seen that due to the size of the smaller pathogen, cell boundaries could erroneously be merged in to one region. This is likely to happen regardless of the segmentation algorithm chosen, as current deep-learning models assume a single species is present. Regardless, as can be seen in the figure, when the pathogen is bound to the apical surface of the membrane of the normal cell, a two dimensional mask will inevitably merge the two overlapping cell boundaries. The effect of merging will be to generate a single cell spectrum containing an average of the mixture of the two cell species, and this will not be an informative sample for classification, whether supervised or unsupervised. Thus, a single pixel classification is the preferred approach to this type of problem, and this was explored in this thesis.

The acquisition of a hyperspectral image of the BECs was non-trivial, as the sample is extremely thin and has a relatively low number density of molecules, especially in the cytoplasm. This required an explorative approach to determine the optimal vertical position of the sample stage for imaging. At the exposure time and laser power used for high-speed imaging, the indication of on-sample resonance was barely noticeable in the spectrum. Thus, the initial step for acquisition was to increase the exposure time or laser power to a level that allowed visual feedback of the state of resonances

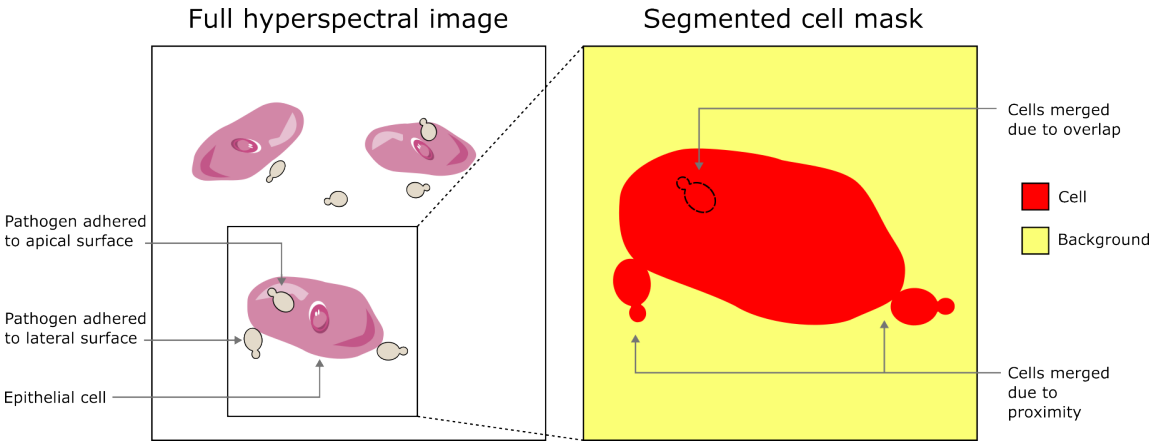

Figure 9.1: Depiction of single cell segmentation when one species is significantly smaller and can adhere to the surface of the other cell.

in the two-colour region. In the fingerprint region, even at greatly increased exposure times, the presence of vibrational resonances were not noticeable in the raw spectrum. Thus, the CH-region provided the only indication of correct sample height positioning. Once the sample height was found, a hyperspectral image scan could be performed.

Hyperspectral images (HSI) of the prepared samples were obtained using the system described in Section 5.1. Deionized water was used as the objective immersion medium. For optimal spectral resolution, the probe pulse was positively delayed with respect to the Stokes pulse such that the maximum coherence was obtained (maximum intensity at 0 cm^{-1}). Images of size 200 by 200 μm were obtained at a pixel exposure time of 5 ms. The lateral pixel resolution was 0.5 μm. One HSI was acquired in 16 mins. The confluence of buccal cells on the coverslip was approximately 50 %, and it was observed that cell flattening had occurred since the epithelial cells were on average larger than expected. This is typical of dry mounted epithelial cells and it caused two unintentional consequences; (1), it made 2D imaging using high NA objectives more difficult to obtain, since there was a possibility of missing the sample plane as the sample is scanned over the focus, due to tilt. (2) The flattened cells rendered more detail in the 2D chemical image because structures are spread over a larger area and are not obscured by other features in the foreground.

9.6 Spontaneous Raman measurements

Since BCARS measurements are always obscured by the NRB, the spontaneous Raman spectrum of the pure fungal pathogen and pure host (BEC) were obtained. This would give an indication of the quality of the NRB removal process through comparison between the retrieved Raman spectrum from BCARS and an independent spontaneous Raman spectrum. Raman spectra from the samples were recorded at 10 s exposure time using a custom built Raman micro-spectroscopy system. This system employs a 150 mW laser with a wavelength of 532 nm and a coherence length of $\geq$100 m (Torus, Laser Quantum), which is driven by a computer-controlled power supply unit (mpc3000, Laser Quantum). The system also employs a spectrograph (Kaiser, Holospec f/1.8i), operating with a 25 μ m slit and a holographic grating (HSG-532 LF). The spectrum is recorded using a low-noise CCD camera (DU920P BEX2-DD, Andor, Belfast, Northern Ireland) with 1024 $\times$ 256 pixels, of size 26 $\times$ 26 μ m cooled to -80°C and operating in full vertical binning mode. The camera was controlled using the Micro-Manager Andor device adapter. The spectrograph and CCD provided a bandwidth of -34-2517 cm^{-1} and an average resolution of 5.48 cm^{-1}. Included in the spectrograph housing was a holographic notch filter (Kaiser; HSPF 532.0), providing an optical density of 6 at the laser wavelength and a spectral bandwidth of 350 cm^{-1}. The laser and spectrograph were coupled into a fully automated inverted microscope (IX81, Olympus, Tokyo, Japan). The microscope included a closed-loop high precision stepper motor translation stage (XY, 96S108-O3-LE, Ludl, Hawthorne, NY, USA) with a linear encoder, which provides repeatability of 0.25 μ m and a resolution of 100 nm. The stage was driven by a control system (MAC 5000, Ludl), which could be controlled using an RS-232 cable, using the Micro-Manager Ludl device adapter. A 40x microscope objective, with numerical aperture of 0.75 (UMPlanFl, Olympus), was used to image the spectral irradiance to a 100 μm confocal aperture (CA, P100D, Thorlabs, Newton, NJ, USA). A long pass filter (F, LP03-532RU-25, Semrock) and a dichroic beamsplitter (DB1, LPD-01-532RS, Semrock, NY, USA) were also used to filter the laser wavelength from reaching the spectrograph, while transmitting the Raman scattered light. A dichroic short pass filter (DB1, 69-202, Edmund Optic, Barrington, NJ, USA) permitted imaging of the sample to a digital camera (CMOS, MU300, AmScope, Irvine, CA, USA). All spectra were recorded using the Andor Solis software plugin for Micro-Manager. The system was wave-number calibrated, using benzonitrile. Intensity calibration was performed using a

NIST calibrated white light lamp.

9.7 Data analysis

In this study, HSIs of dimension 400 by 400 by 1024 were denoised using the truncated singular value decomposition (SVD) as described in section 4.4.1. The data was then scatter corrected using EMSC with a reference spectrum based on the glass spectrum used to train the VECTOR2 autoencoder. This approach was critical to removing the effect of laser and NRB variations in the retrieved spectrum. The resulting data was then processed using the pre-trained neural network VECTOR2-MU-Dense[23] in order to remove the NRB. VECTOR2 processed each spectrum of the hyperspectral image independently. After NRB removal data was area normalized per pixel and then processed in order to remove the background pixels by using principal component (PC) thresholding. PC thresholding is a common method for hyperspectral segmentation based on dimensionality reduction to a more informative basis[168]. Use of the deep-learning based cell segmentation method used in the blood analysis experiment of section 8.3 was not possible in this experiment because that method assumes a single cell species is present. This assumption is utilized because the network estimates the mean cell diameter prior to feed-forward propagation of an image sample. Since the *candida* cells were much smaller in size compared to the buccal cells, this causes erroneous segmentation results. In the principal components thresholding method, the weight of the first PC (W_1) of each pixel x_i was calculated using the full dataset and the decision to assign each pixel to a class $\mathcal{C}$ was given as

$$x_i = \begin{cases} \mathcal{C}_{\text{bg}} & \text{if} \quad (-1)^n W_{1,i} < t \\ \mathcal{C}_{\text{signal}} & \text{if} \quad (-1)^n W_{1,i} \geq t \end{cases} \tag{9.1}$$

where $\mathcal{C}_{\text{bg}}$ and $\mathcal{C}_{\text{signal}}$ are the background and signal classes respectively, and n and t are directionality and threshold parameters respectively, which were determined empirically. n can be either 0 or 1 and simply inverts the signs of the inequalities, while t is usually 0 but may vary due to noise present in the image. Other methods such as k-means clustering could also prove efficient for segmentation of cells, however use of the first PC proves reliable when applied to the BCARS raw

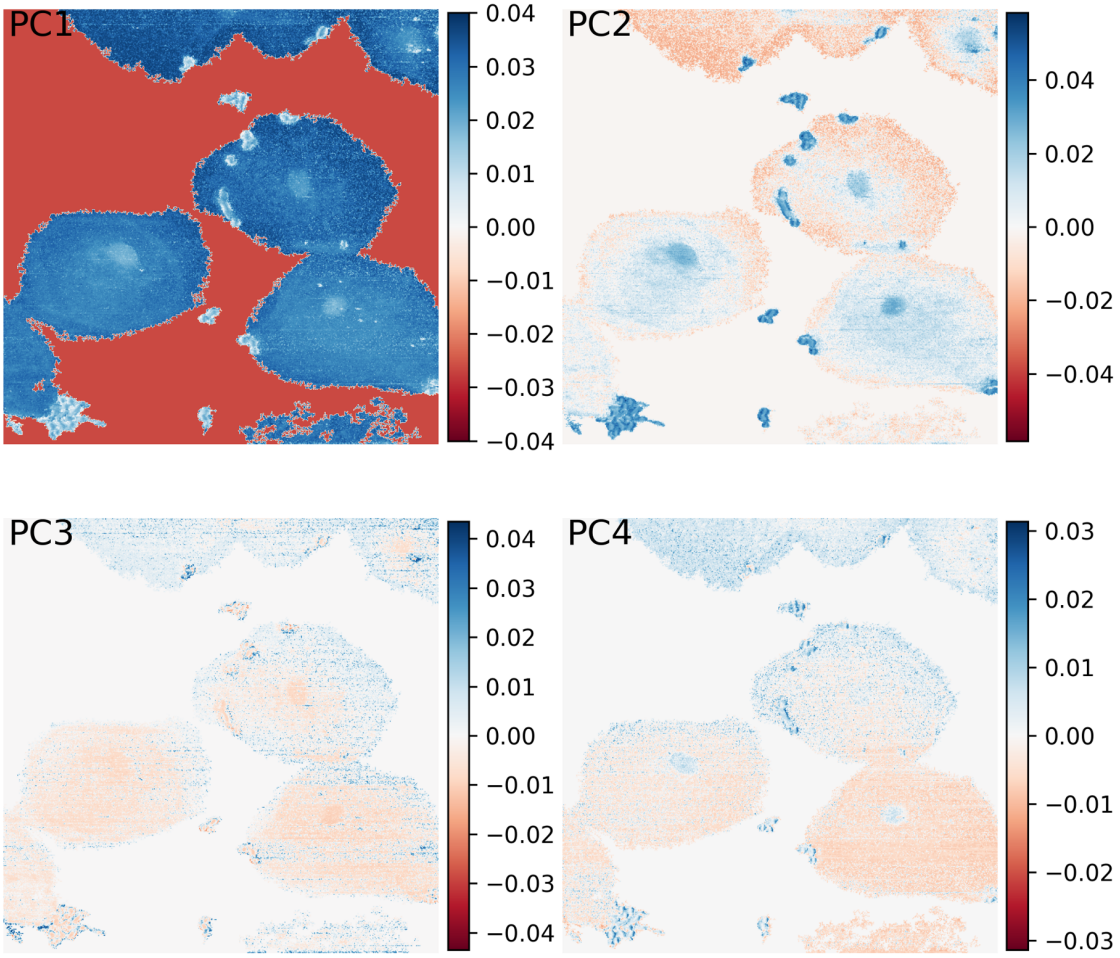

Figure 9.2: PCA score images of the first four PCs of the mixed candida/BEC sample.

or NRB-removed intensity, due to variations in the NRB and high-wavenumber regions in cell and non-cell regions. The PCA score for each pixel in the image for the first four PCs is shown in figure 9.2. The subsequent analysis was then performed on pixels in the $\mathcal{C}_{\text{signal}}$ class.

Once the background pixels were removed from the image, the potential for using PCA as a tool for identification of the pathogen was investigated. In HSIs, PCA can be used for blind unmixing and has been applied to cell images obtained from stimulated Raman scattering (SRS)[169]. The applicability however is dependent on the separability of the underlying data. In this experiment, the first two PCs appeared to account for variations due to the cell and background, and the BEC nucleus and pathogen respectively as seen in figure 9.2. The next two PCs corresponded mainly to noise, with some minor variance due to the pathogen and BEC. The use of PCA as a species clustering

method would require a consistent variation in the PC score between the species of interest, which was not the case for the data. Therefore, a more advanced approach to label-free identification was explored and the PCA based approach was abandoned.

It was decided to perform clustering analysis based on a low-dimensional projection of the data. Each cell extent was first cropped manually and was reduced in dimension using the uniform manifold approximation and projection (UMAP). UMAP is a stochastic algorithm that seeks to approximate input data as a Riemannian manifold while preserving its topology in a low-dimensional representation[170]. Since UMAP and clustering are generally intensive algorithms, each spatial image dimension was downsampled by $70\,\%$ using linear spline interpolation prior to further analysis, resulting in an image area approximately half the size of the original. Using UMAP, the data of size $n_{\text{pixels}} \times 1024$ was reduced to $n_{\text{pixels}} \times 2$ (i.e. 2 channels), where n_{pixels} is the number of image pixels in the HSI. Projection of this data in two dimensions provides a visualisation of the whole hyperspectral image, where points closer together in the low dimensional embedding space are ideally similar in the full dimensional data space. Since there was no ground truth data available within each HSI experiment, the UMAP projection requires interpretation and further analysis to understand its output. The UMAP projection was used to classify groups within the data with the aim of identifying pixels containing the pathogen and buccal cells. The spectral clustering algorithm was used to perform unsupervised clustering on the results of the dimensionality reduction[171]. Spectral clustering first calculates an affinity matrix characterising the similarity between all n^2 pairs of datapoints. Then, given an input number of clusters k, the algorithm calculates the first k eigenvectors of the un-normalized graph Laplacian L and constructs a matrix $U \in \mathbb{R}^{n \times k}$ from the set of eigenvectors of L. Finally, k-means clustering is performed on the n rows of U. The choice of k was initially based on visual inspection of the UMAP projection in 2D. k was then refined using cluster validation based on the average silhouette coefficient for each HSI. The silhouette coefficient is typically used in k-means clustering and is a measure of the ratio of within-group similarity and between group similarity for each sample, and therefore the average value for all samples is an indication of the overall clustering quality. It should be noted that clustering only assigns samples to classes, but does not identify the classes. Therefore, the output of clustering should enable an inference that samples in different classes are distinct. The experimental workflow is shown in

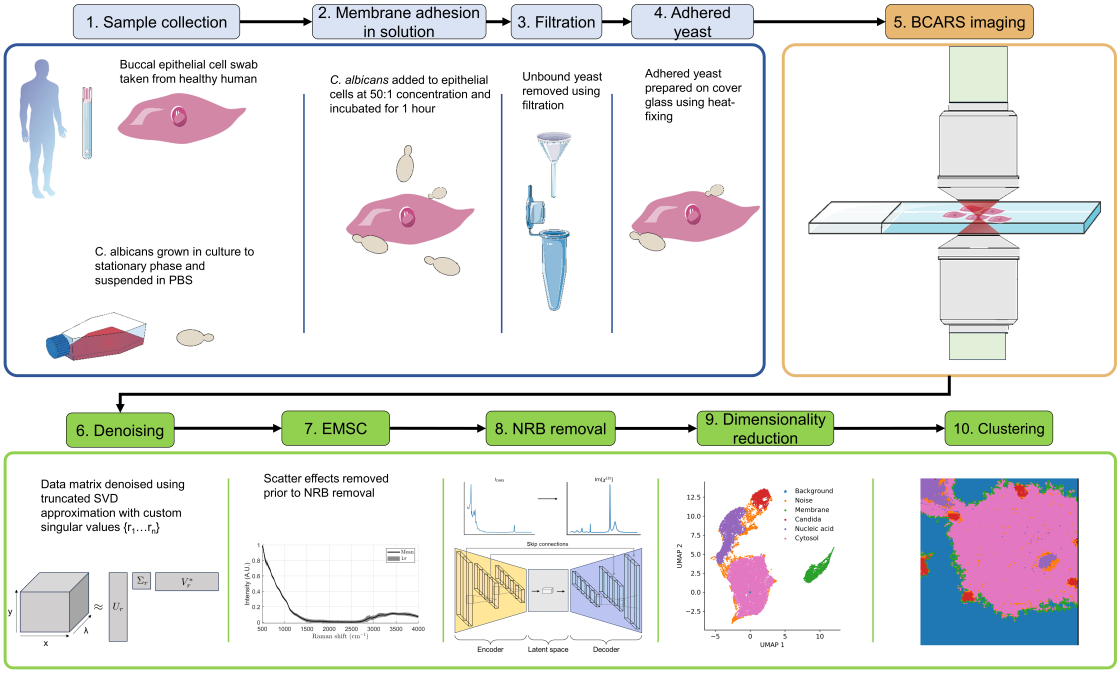

Figure 9.3: Flow chart of the experimental fungal classification procedure.

figure 9.3.

9.8 Results of unsupervised clustering

The results of the clustering procedure on five cells from the mixture sample are shown in Figure 9.4. The mean intensity of the Raman shift corresponding to 1003 cm^{-1} is shown in the first column and gives an indication of the relative concentration of phenylalanine in the image. The intensity image is over all pixels, both from $\mathcal{C}_{bg}$ and $\mathcal{C}_{signal}$. It was observed that subcellular features were resolved such as the nucleus in the BECs and small features that resembled the candida. At the Raman shift of 1000 cm^{-1}, the regions suspected of containing candida had a larger intensity relative to any other region in the cell. These images also showed that there was still a noticeable amount of noise present throughout the images. The UMAP projection is also shown with the results of the spectral clustering displayed as coloured points for each distinct cluster, where the optimal number of clusters k varied from 3-4, depending on the image. The cluster labels were assigned to groups using visual inspection of the BCARS mean intensity image. The pixel class labels were

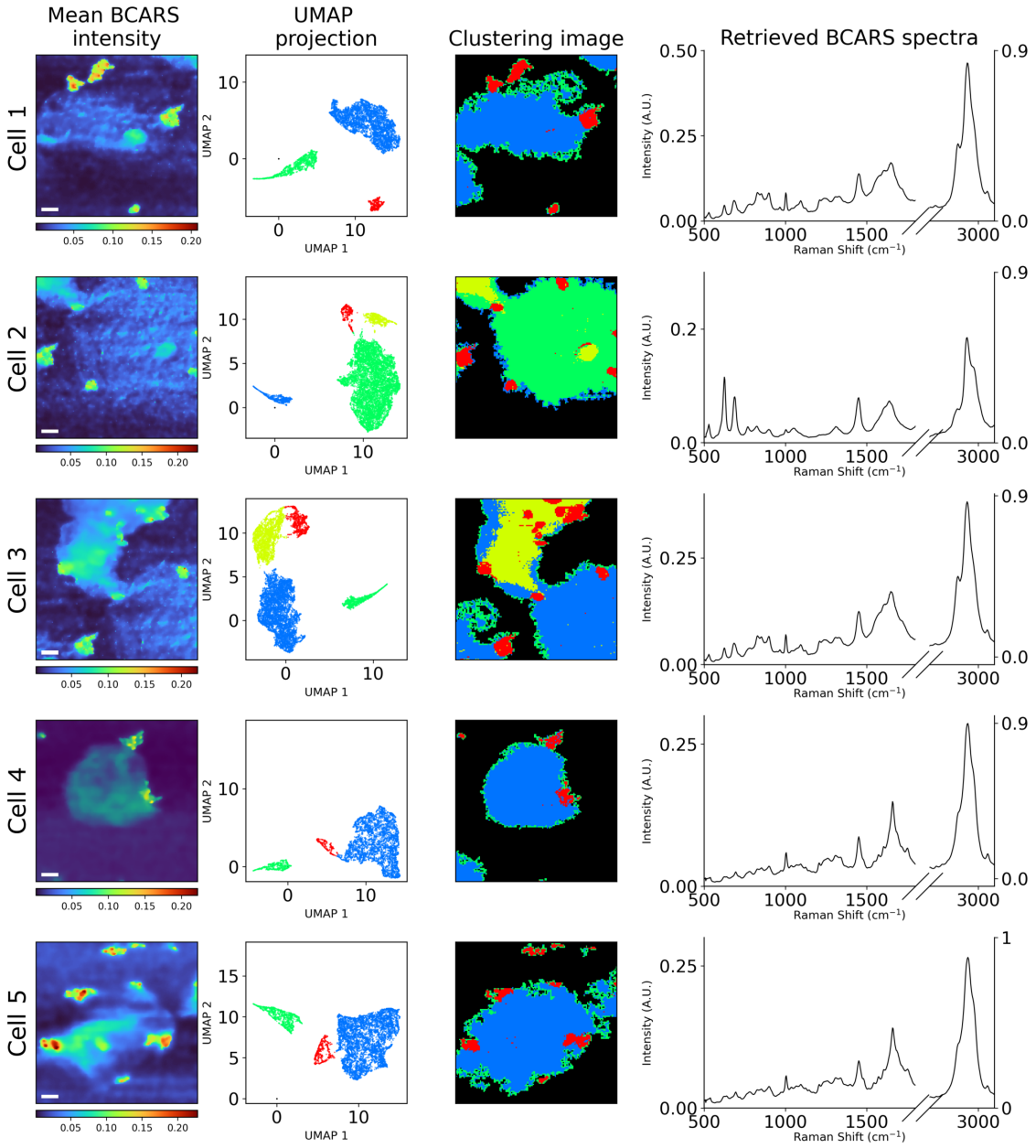

Figure 9.4: The results of unsupervised segmentation of five epithelial cells infected with *C. albicans*. The UMAP projection was clustered using spectral clustering. The mean BCARS spectrum of the pathogen which was extracted using the cluster model is also shown. Scale bar 10 μm.

also reshaped to the original image dimensions to give a labeled "clustering image" of the cells. Finally the average BCARS spectrum for the identified candida class is shown for each image. In the UMAP projection, for all cells there was distinct clustering that corresponded generally to the BEC cytoplasm, BEC nucleus, whole *candida* pathogen, and BEC membrane. It was suspected that the BEC membrane cluster was distinct because the pixels here were a mixture of sub-pixels

containing both pure substrate and cell-specific Raman features from the edge of a cell. It can be seen in the UMAP image that the suspected candida pixels (coloured in red) were all contained within a convex cluster that was highly separated from any other class. This was clear evidence for the distinct fingerprint spectrum of the pathogen, compared to the BEC. It can be seen in the clustering image of cell 3 that there was two distinctly classed clustered that both corresponded to BEC cytoplasm. It was suspected that this occurred because the two cells in the image were at different depths relative to the laser focus. This may have caused some vibrational bands in one of the cells to possibly fall below the noise floor and cause enough variation in the spectra in this region to separate from the in-focus pixels in the UMAP projection. It is still apparent however that candida pixels were positively identified in the two regions within cell 3.

The spectral quality of the retrieved Raman spectra obtained from VECTOR2 was also high as can be seen in the last column of figure 9.4. The CH-band was consistently greater in intensity as expected, and the fingerprint spectrum was approximately similar across the cell images. One exception was in cell 3, where there was an unusually high intensity for two peaks in the 620-700 cm^{-1} region. These peaks were not present in independent measurements of a pure *candida* sample, however they do correspond to previously reported bands due to the steroid ergostane at 624 and 657 cm^{-1} in the *candida* species[172].

In Figure 9.5 single pixel fingerprint spectra of the epithelial cell and candida class are shown together with Raman spectra obtained from the system described in Section 9.6. The Raman measurements represent single point spectra of the known species, from a pure sample. For the BEC, the nucleus was targeted, and the centre of the yeast body was targetted for the *candida* sample. The BCARS spectrum of the BEC in blue shows very close agreement with the spontaneous Raman measurement in red. Notable peaks corresponding to the Amide I, phenylalanine and lipids are present at Raman shifts of 1560 cm^{-1}, 1002 cm^{-1} and 1440 cm^{-1} respectively. Similarly, for the BCARS and SR measurements of the yeast, the spectra were similar in their general features. Notably, a peak at approximately 1120 cm^{-1} from glycosidic bonds[173] is present in the SR spectrum and has a high intensity, while it is very low in intensity in the BCARS spectrum. These bonds may be from the presence of β-glucans, the most abundant polysaccharide in the *candida*

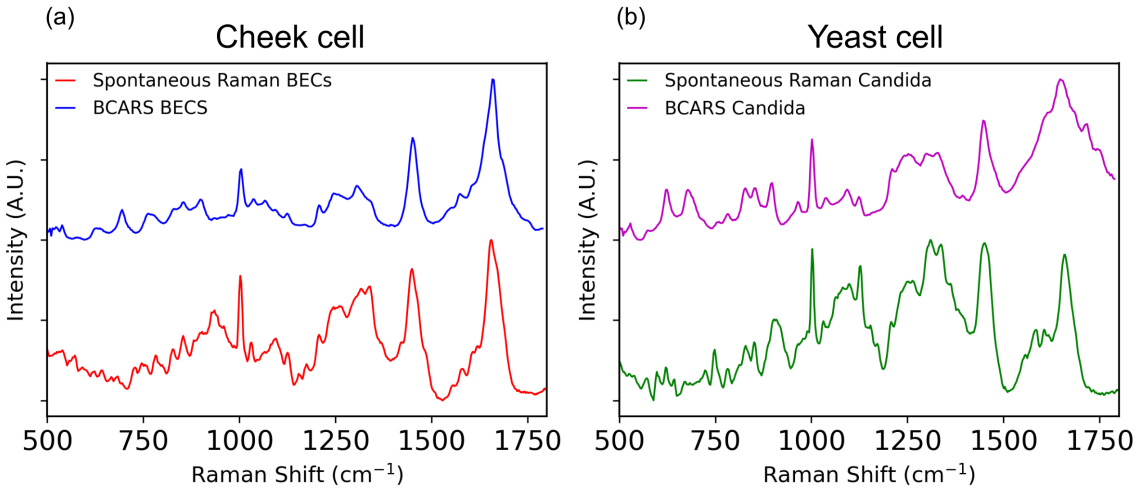

Figure 9.5: (a) Single pixel fingerprint BCARS spectra from the clustered classes of BEC and independent measurement from spontaneous Raman using a pure sample. (b) Single pixel fingerprint BCARS spectra from the clustered classes of candida and independent measurement from spontaneous Raman using a pure sample. All spectra were shifted vertically for clarity.

species[174]. Although this is a highly characteristic peak of the pathogen, the difference in the two measurements could be due to the cell heterogeneity resulting in a high intra-cell variance of this peak as has been previously observed[163].

The quality of the clustering was analysed using the silhouette coefficient as described in Section 9.7. The coefficient was calculated for each sample, and the mean value is shown in Figure 9.6 (a) for each cell image. The value of the silhouette coefficient varies from -1 to 1 and is higher for more dense and well-separated clusters. The approach taken here was to classify individual pixels in a hyperspectral image into distinct clusters based on the retrieved BCARS spectrum with the goal of an unlabelled screening for a pathogen. Other methods of single-cell clustering typically perform an initial cell masking step whereby each cell entity is identified using image analysis techniques such as watershed segmentation, topological methods, or as shown in this work, using a pre-trained deep learning model. Cell masking was not applicable here however since the pathogen can bind to the apical surface of the epithelial cell membrane resulting in overlapping species in the HSI. These single-cell analysis methods are thus only applicable when the cell sample is moderately confluent and each cell is not overlapping within the image. It was demonstrated that clustering processed BCARS spectra resulted in distinct groups of pixels being identified. The BCARS intensity image in Figure 9.4 shows contrast with respect to the background in areas where the cell and fungus were

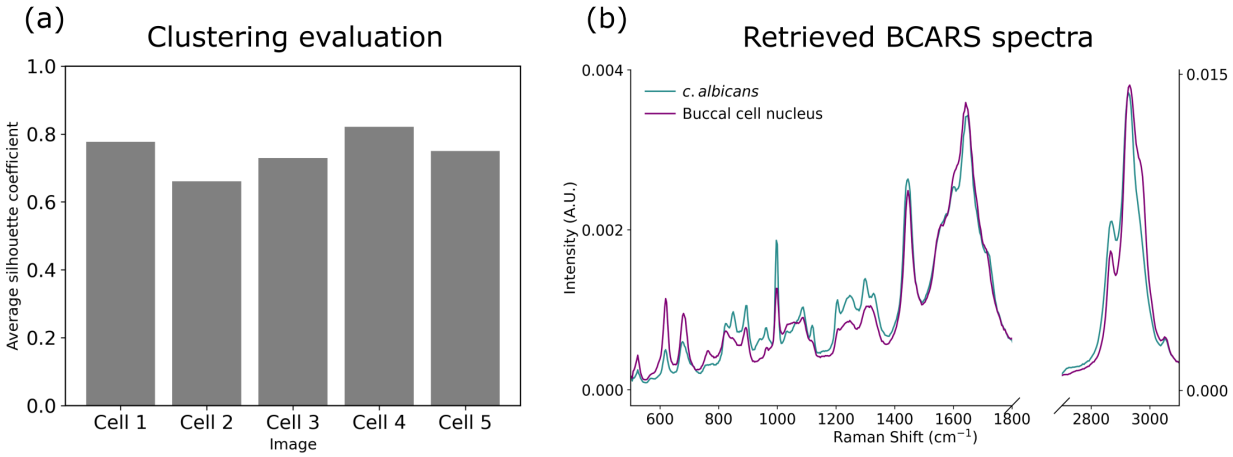

Figure 9.6: (a) Cluster validation analysis using the average silhouette coefficient of each image, (b) single pixel retrieved BCARS spectra of candida cell and buccal epithelial cell nucleus.

present, likely due to the high abundance of nucleic acids in the buccal cell nucleus and within the whole yeast body. The dimensionality reduction using UMAP produced visually distinct clusters that corresponded to the cell extent, cytoplasm/nucleus, and pathogen. Each cluster was labeled based on analysis of the mean and single pixel spectra of the known samples. The cell extent was spectrally distinct from the cell cytosol most likely because the high lateral sampling resolution resulted in cell edge pixels being a mixture of the BCARS response from both the cell and the coverslip. The segmented clusters were either fully separated in their feature space or connected only by sparse points which resulted in a good overall clustering quality as measured by the validation approach. The mean silhouette coefficient for all but one image (cell 2) was greater than 0.7, representing a high quality of clustering.

9.9 Conclusions

In this chapter, we have shown promising results for a label-free identification of a pathogen in a mixture of buccal epithelial cells. This work contrasts with a hyperspectral imaging segmentation approach, where it can be assumed that multiple species are distributed in a sample and have approximately equal size such that their boundaries can be distinguished prior to multivariate analysis. In this work, instead of segmenting each cell, a simple approach to foreground and background detection was implemented using PCA. This then allowed the processing of all sample

pixels and their dimensionality reduction using UMAP. It was assumed that the spectra of each pixel in the UMAP projection would be separated based on spectral differences due to the composition of the sample. Inspection of the mean cluster spectra and corresponding chemical images showed that the candida could be positively identified within the samples. This work contributes to the application of BCARS in the field of cytology, with the potential for rapid pathogen detection in a clinical sample. In future work, it would be fruitful to test a wider array of pathogen common to cytologic examination, such as other fungal species, parasites and bacteria.

In this work, while we have shown that clustering based on the BCARS single pixel spectrum alone is providing an indication of contrast for the candida pathogen among BECs, the accuracy was not quantitatively measured. An expected next step in this work that could aid in such a quantitation would be to perform a concurrent fluorescence imaging study on multiple samples. This would consist of a mixed sample including the target cell and pathogen first being imaged using BCARS. The sample would then be labelled using a pathogen specific stain such as calcofluor white. A fluorescence image of the sample would then be obtained. Evidence of chitin binding by observed fluorescence in areas of the BCARS HSI that were segmented and or further classified as the pathogen using a pattern recognition algorithm, would strongly suggest predictive accuracy. A numerical estimate of accuracy could be obtained using an image based algorithm to detect the approximate number of pathogenic cells in the fluorescence and clustered BCARS images, thus assuming the fluorescence image provides a ground truth for positive identification.

As the method proposed here is an unsupervised approach, and clusters points based on the spectrum, not using any spatial information, the possibility of using the identified clusters as training samples for a multivariate classifier could be explored. In effect, the whole imaging and processing procedure could in theory be used to pseudo-label a dataset of multiple unknown or known species. The ability of the classifier to then distinguish and classify single observations with high accuracy would remove the burden of having to acquire images of independent labelled datasets for training, which can be cumbersome. Ultimately, to better validate the clustering approach, more samples within the should be studied. A logical next step would be to prepare a sample with other species of candida, and investigate the identification quality. This would require a more specific approach to

obtain the ground truth species data, since many of the species appear identical in morphology. It is envisaged that genetic techniques such as immunolabelling of species-specific surface proteins or spontaneous Raman acquisitions of detected points in the image be recorded in order to acquire this information, which would require further experimental consideration.

10. Spectral interferometric polarization imaging using broadband CARS

This chapter is based on a conference paper submitted to SPIE Optics in Health Care and Biomedical Optics XIII, entitled: Spectral interferometric polarization imaging using broadband CARS[175]. This work was a collaboration between the Maynooth University department of Biology, who provided the samples, and my group. In this chapter, I conducted all imaging experiments, including measurements of spontaneous Raman spectra and conducted data analysis of all results.

BCARS has been shown to be capable of producing high-speed images of biological cells using the vibrational contrast present in the molecular bonds. As shown in previous chapters, the NRB must be removed in order for a meaningful analysis of the contrast to be performed. While all approaches thus far have used post-processing techniques such as the conventional KK or novel DL methods, there have also been several published experimental techniques that can suppress the NRB signal generation at the source, or which filter the signal before detection such as time-resolved CARS (T-CARS)[118], polarization CARS (P-CARS)[20] and frequency-modulated CARS (FM-CARS)[117]. These methods have shown the ability to provide NRB suppression, removing the presence of the off-resonant signal. Experimental suppression however usually reduces the measured CARS signal intensity, due to the reduced coherence in T-CARS and the rejection of non-depolarized bands in P-CARS. In FM-CARS, this is not the case, however amplitude modulation and lock-in detection is required, which is not suited to simultaneous broadband detection.

In this chapter, a form of Broadband CARS is performed using an interferometric detection of different components of the material response $\chi^{(3)}$, using two separate measurements of the BCARS signal. It was shown by Littleton *et al.*[67], that this detection scheme, named spectral interferometric polarization CARS (SIP-CARS) permits full recovery of the NRB-free BCARS spectrum from isotropic media. Furthermore, there is the benefit of the preservation of the NRB heterodyne amplification in this detection scheme, which is often suppressed in conventional P-CARS. This method is effectively a hybrid NRB removal approach, as it requires experimental modification to the optical setup, as well as post-processing of the spectra. In this work, the SIP-CARS theory and method was extended to the hyperspectral imaging of single cells, namely fungal spores. The application of SIP-CARS to biological cells is the primary novel aspect of this work.

10.1 Theory of SIP

SIP-CARS is an interferometric detection applied to CARS measurements. The theory of BCARS was described in section 3.2.3. Again, the measured BCARS intensity in the frequency domain is given as

$$I_{\mathrm{CARS}}(\omega) \propto \left| \left\{ \left[E_{\mathrm{p}}(\omega) \star E_{\mathrm{S}}(\omega) \right] \chi^{(3)}(\omega) \right\} * E_{\mathrm{pr}}(\omega) \right|^2 \tag{10.1}$$

where E_{p}, E_{S} and E_{pr} are the pump, Stokes and probe electric fields, and $\star$ and $*$ are the cross-correlation and convolution operators respectively. The correlation $E_{\mathrm{p}} \star E_{\mathrm{S}}$ is typically called the stimulation or excitation profile and serves to generate the vibrational coherence within the frequency range given by $\omega_{\mathrm{p}} - \omega_{\mathrm{S}}$. When the pump photon is provided by a narrowband source, it is termed two-colour CARS. The broadband Stokes beam itself can provide the pump photon at a range of different frequencies, thus also generating a coherence within the frequency range $\omega_{\mathrm{S}} - \omega_{\mathrm{S}}$, known as the 3-colour mechanism. If a vibrational resonance exists at $\omega_{\mathrm{p}} - \omega_{\mathrm{S}}$, then the coherence is amplified. A probe photon at a frequency ω_{pr} may scatter from the coherence, generating light at the anti-Stokes frequency $\omega_{\mathrm{as}} = \omega_{\mathrm{p}} - \omega_{\mathrm{S}} + \omega_{\mathrm{pr}}$. The anti-Stokes field thus provides information on $\chi^{(3)}$.

It is typically assumed that the lasers used are far below the electronic resonant frequencies

of the sample, and thus the non-resonant susceptibility is essentially lossless (purely real). The NRB contributes an additional phase on the resonant signal which results in interference effects in the overall signal intensity; notably, the dispersive lineshapes. However, considering a lossless response, for elliptically polarized input fields, it was shown[67, 68] that the NRB interference signal is common when measured along two orthogonal anti-Stokes orientations. This result, coupled with the fact that Raman modes can depolarize the input fields, allows for the subtraction of two orthogonal BCARS intensities with the effect of removing the NRB contribution. The remaining signal then consists of the resonant contribution only.

10.1.1 Removing the NRB using spectral interferometric polarization

Spectral interferometric polarization CARS (SIP-CARS) is based on the premise that the non-resonant tensor components of the third-order susceptibility are equal regardless of field permutation and that all components are lossless. This is due to the Kleinman condition being satisfied for the non-resonant susceptibility[80]. Assuming a right-hand elliptically polarized narrowband beam and linearly polarized broadband beam along the x-axis, a description of their Jones vectors is given. The Jones vector for an arbitrary elliptical field of unit intensity is given as[176]

$$|\mathbf{E}_{\phi,\psi}\rangle \triangleq \begin{pmatrix} \cos(\psi) & -\sin(\psi) \\ \sin(\psi) & \cos(\psi) \end{pmatrix} \begin{pmatrix} \cos(\phi) \\ i\sin(\phi) \end{pmatrix} \tag{10.2}$$

where ϕ is the ellipticity angle ($-\frac{\pi}{4} \leq \phi \leq \frac{\pi}{4}$), being negative for right-handed elliptical states, and ψ is the azimuth of the ellipse ($0 \leq \psi \leq \pi$) describing the angle between the semi-major axis and the positive x-axis. The ellipticity angle is related to the eccentricity e through $e = \sqrt{1 - \tan^2(\phi)}$. The right-hand matrix of equation. 10.2 describes an elliptically polarized field with $\psi = 0$, whereas the left-hand matrix describes a clockwise rotation by the angle ψ. The Jones vector for a linear horizontally polarized field is

$$|\mathbf{E}_{\text{LHP}}\rangle \triangleq \begin{pmatrix} 1 \\ 0 \end{pmatrix} \tag{10.3}$$

Thus, for $\psi = 0$, the polarisation along the two Cartesian axes is given as,

$$P_x = \cos(\phi)\chi^{(3)}_{1111}E_{\mathrm{p}}E_{\mathrm{pr}}E^*_{\mathrm{S}} \tag{10.4}$$

$$P_y = i\sin(\phi)\chi^{(3)}_{2121}E_{\mathrm{p}}E_{\mathrm{pr}}E^*_{\mathrm{S}} \tag{10.5}$$

It is also known that for an isotropic medium $\chi^{(3)}_{2121} = \chi^{(3)}_{1212} = \chi^{(3)}_{1122}$. Therefore, equation 10.4 can be stated as

$$P_x = \cos(\phi)\chi^{(3)}_{1111}E_{\mathrm{p}}E_{\mathrm{pr}}E^*_{\mathrm{S}} \tag{10.6}$$

$$P_y = i\sin(\phi)\chi^{(3)}_{1122}E_{\mathrm{p}}E_{\mathrm{pr}}E^*_{\mathrm{S}} \tag{10.7}$$

where $\chi^{(3)}_{ijkl}$ describes the susceptibility tensor component with indices describing the direction of the anti-Stokes, pump, probe and Stokes pulse wavevectors respectively. For clarity, the superscript denoting the order of the nonlinearity will be dropped. The SIP-CARS signal, defined as the difference between the polarization components at +45°(S_+) and -45°(S_-) relative to the Stokes polarization ΔS is then given as

$$\Delta S = (S_+ - S_-) \tag{10.8}$$

$$\Delta S = P_x P_y^* + P_x^* P_y \tag{10.9}$$

$$\Delta S = i\cos(\phi)\sin(\phi)\left(\chi^*_{1111}\chi_{1122} - \chi_{1111}\chi^*_{1122}\right) \tag{10.10}$$

If the substitution is made $\chi^*_{1111}\chi_{1122} = z = a + ib$, then,

$$i\cos(\phi)\sin(\phi)(z - z^*) = i\cos(\phi)\sin(\phi)((a + ib) - (a - ib)) \tag{10.11}$$

$$= i\cos(\phi)\sin(\phi)(2ib) \tag{10.12}$$

$$= \cos(\phi)\sin(\phi)(2i^2 b) \tag{10.13}$$

$$= -\cos(\phi)\sin(\phi)(2b) \tag{10.14}$$

Using the relations $\chi_{1111} = \chi_{1212} + \chi_{1122} + \chi_{1221}$ and $\chi_{1212} = \chi_{1122}$, the SIP-CARS intensity can be restated as

$$\Delta S \propto -2\cos(\phi)\sin(\phi)\,\mathrm{Im}\{\chi^{*}_{1111}\chi_{1221}\} \tag{10.15}$$

Expanding,

$$\Delta S \propto A\,\mathrm{Im}\Big\{\chi^{\mathrm{R}}_{1111}{\chi^{\mathrm{R}}_{1221}}^{*} + \chi^{\mathrm{R}}_{1111}{\chi^{\mathrm{NR}}_{1221}}^{*} + \chi^{\mathrm{NR}}_{1111}{\chi^{\mathrm{R}}_{1221}}^{*} + \chi^{\mathrm{NR}}_{1111}{\chi^{\mathrm{NR}}_{1221}}^{*}\Big\} \tag{10.16}$$

where $A \triangleq 2\cos(\phi)\sin(\phi) = \sin(2\phi)$. The last term is zero since it is purely real. This also results in $\chi^{\mathrm{NR}}\chi^{\mathrm{R}*} = -(\chi^{\mathrm{NR}}\chi^{\mathrm{R}*})^{*}$, therefore

$$\Delta S \propto A\,\mathrm{Im}\Big\{\chi^{\mathrm{R}}_{1111}{\chi^{\mathrm{R}}_{1221}}^{*} + \chi^{\mathrm{R}}_{1111}{\chi^{\mathrm{NR}}_{1221}}^{*} - \chi^{\mathrm{NR}}_{1111}\chi^{\mathrm{R}}_{1221}\Big\} \tag{10.17}$$

The first term is purely real since it is a product of two complex numbers with opposite magnitudes of their imaginary parts (other than their real amplitudes), therefore

$$\Delta S \propto A\,\mathrm{Im}\big\{\chi^{\mathrm{R}}_{1111}\chi^{\mathrm{NR}}_{1221} - \chi^{\mathrm{NR}}_{1111}\chi^{\mathrm{R}}_{1221}\big\} \tag{10.18}$$

making use of the Kleinman relation $\chi^{\mathrm{NR}} = \chi^{\mathrm{NR}}_{1111}$,

$$\Delta S \propto \sin(2\phi)(1-3\rho)\chi^{\mathrm{NR}}\,\mathrm{Im}\big\{\chi^{\mathrm{R}}_{1111}\big\} \tag{10.19}$$

where $\rho = \frac{\chi^{\mathrm{R}}_{1221}}{\chi^{\mathrm{R}}_{1111}}$ is the Raman depolarisation ratio. The difference signal in SIP-CARS is proportional to the imaginary part, $\mathrm{Im}\big\{\chi^{\mathrm{R}}_{1111}\big\}$, which correlates with the conventional linear Raman signal [51]. Ideally, χ^{NR} would be a real, constant value that amplifies the signal. However, it is known to vary spectrally due to its finite coherence time, and the local intensity of the NRB is also influenced by the local oscillator number density. In conventional BCARS measurements, χ^{NR} acts as a noise signal that degrades the signal. In SIP-CARS, when applied to isotropic materials, χ^{NR} simply scales the resulting intensity, allowing any local variations in the NRB to be corrected through standard scatter correction procedures.

Since the SIP-CARS signal is also scaled by $1-3\rho$, the resulting spectrum carries the imprint of

the Raman depolarization spectrum. Therefore, careful analysis of the SIP-CARS signal is essential, as assumptions like signal non-negativity and linear proportionality to sample concentration are not applicable. The SIP-CARS signal is best approached as a distinct type of signal, using general methods that extract contrast (e.g., PCA). Alternatively, when ρ is known, the imaginary part of χ_{1111} can be determined exactly.

10.2 Procedure

10.2.1 BCARS system modifications

Hyperspectral BCARS images of *Glomeromycotina* - Arbuscular Mycorrhizal Fungi (AMF) were acquired using the custom BCARS microscope and broadband laser system described in section 5.1, with some modifications. A diagram of the microscope is shown in figure 10.1. In this experiment, the Stokes and Pump photons are derived from a broadband source, while the probe photon comes from a narrowband source. The pump beam, initially linearly polarized in the horizontal direction, was transformed into circular polarization using a half-wave plate with its fast axis set at 22.5° and a quarter-wave plate with its fast axis aligned at 0° to the horizontal. The circular polarization was confirmed with a linear polariser. Just before the anti-Stokes shortpass filter, a linear polariser was positioned at 45° to the horizontal to collect the first polarization signal (n_+). A BCARS hyperspectral image of the sample was then recorded, denoted as S_+. The acquisition time for each pixel in the BCARS image was 1 ms. A second hyperspectral image was captured with the polariser rotated to -45° relative to the horizontal (n_-), and this image was labelled as S_-.

10.2.2 NRB acquisition

An estimate of the non-resonant background signal was required in this experiment to remove the influence of the lasers in the SIP-CARS result. This signal was obtained using a single acquisition from the glass coverslip at both polarizer orientations n_+ and n_-, designated B_+ and B_-. The experimental parameters were identical to the sample images.

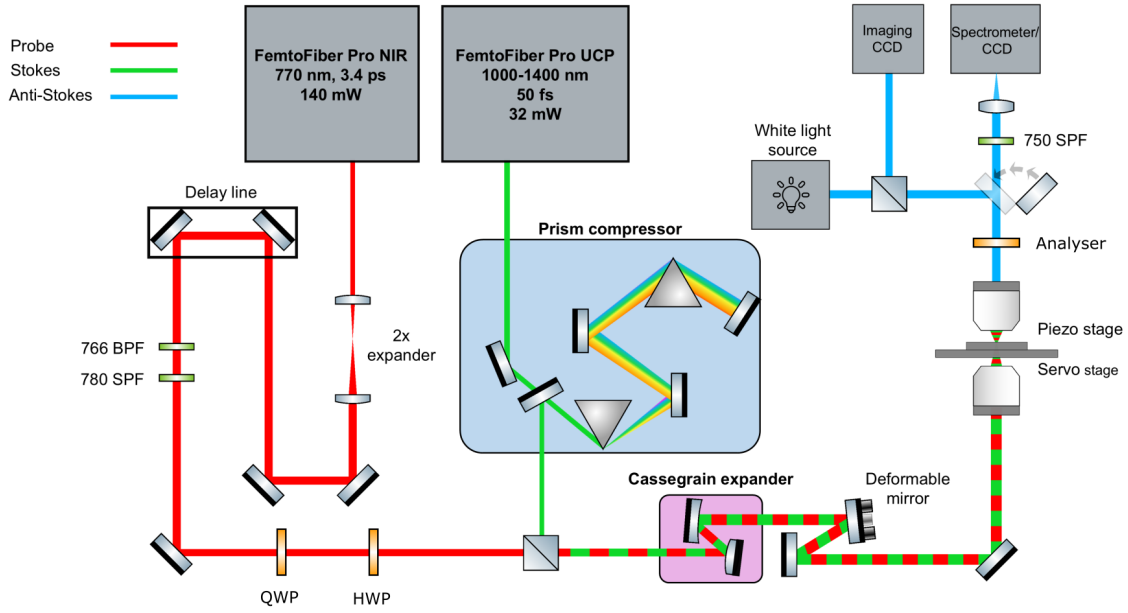

Figure 10.1: Diagram of the SIP-CARS experimental setup. QWP: quarter-wave plate, HWP: half-wave plate.

10.2.3 Signal processing

Both hyperspectral images were denoised using the truncated singular value decomposition and the method presented in section 4.4.1. After denoising, the images were then corrected for scatter using a multiplicative scatter correction (MSC) procedure. After MSC, each spectrum was detrended using the NRB as a reference spectrum, and a Butterworth filter. Each spectrum was then divided by the NRB to remove the effect of the lasers. The filtering procedure effectively removed a slowly varying baseline from each pixel due to local differences in the NRB.

The normalised SIP-CARS signal S_{norm} was calculated by

$$S_{\text{norm}} = \frac{S_{\text{corrected}}}{B} \tag{10.20}$$

where the corrected spectrum is given as

$$S_{\text{corrected}} = S - H\{S - B\} \tag{10.21}$$

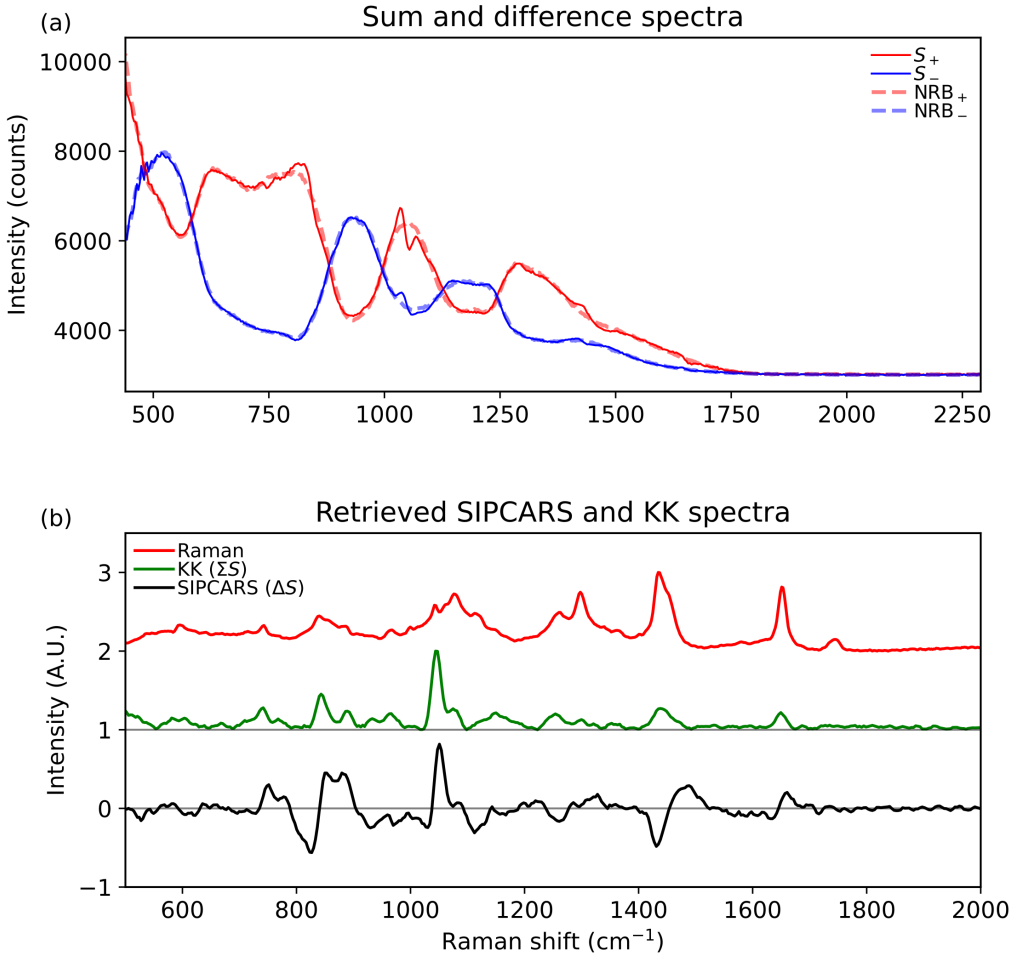

Figure 10.2: (a) Raw BCARS spectrum of S_+ and S_- (both corrected) and the NRB references of each, (b) SIPCARS signal, KK-retrieved spectrum and spontaneous Raman spectrum from the fungal spore body.

where H is a lowpass Butterworth filter operation using a cutoff frequency of 0.08 nm^{-1}, which was chosen by visual inspection of the residual $S - B$. In figure. 10.2 (a), the SIP-CARS spectra (corrected) are shown along with the NRB signal obtained from the coverslip, for both polarization orientations. It is apparent that after the filtering procedure both the signal and NRB spectra are highly similar, other than where vibrational resonances exist. Shown in figure. 10.2 (b) is the resulting NRB corrected difference signal $\frac{S_+}{B_+} - \frac{S_-}{B_-}$. The signal obtained from the Kramers-Kronig method applied to the sum signal $\Sigma S = S_+ + S_-$ is also shown, since for isotropic samples ΣS is equivalent to the conventional BCARS signal. Finally, a Raman measurement of the same region of the sample is shown, taken using the system described in section 9.6.

The flowchart describing the process of obtaining the SIPCARS difference image is shown in figure 10.3.

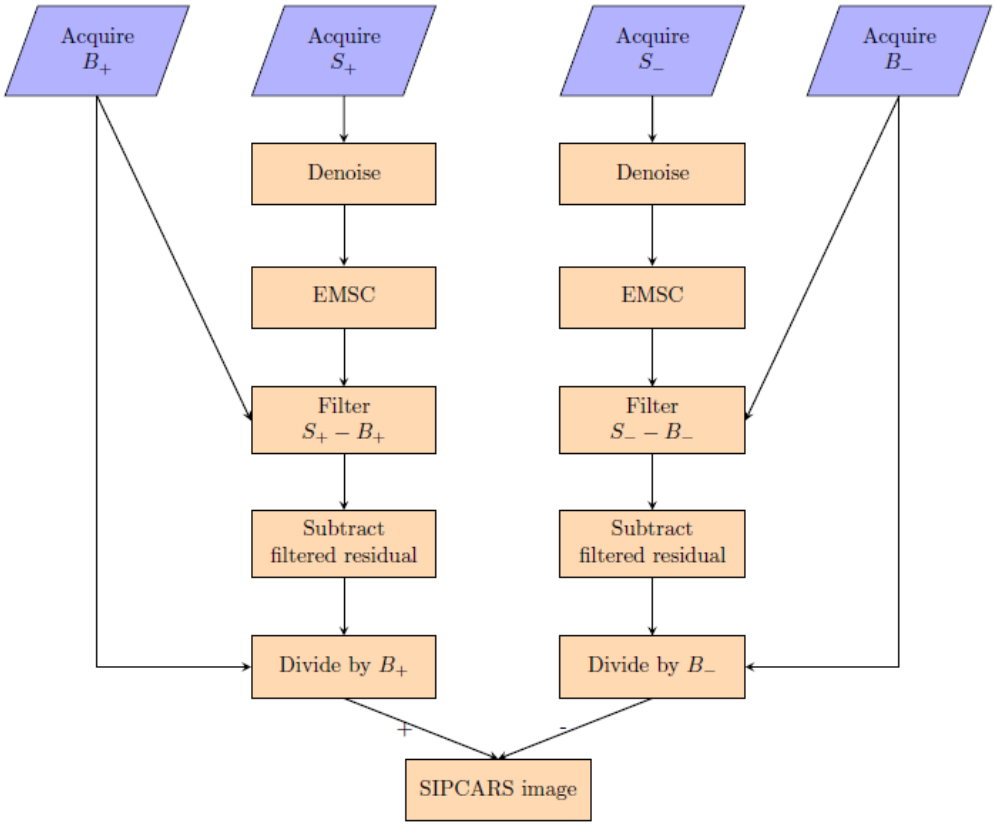

Figure 10.3: Flowchart for processing of the SIPCARS image

10.3 Results

In figure 10.2 (b), the KK and Raman spectra show similar resonances at 1020 cm^{-1}, 1415 cm^{-1}, 1625 cm^{-1}, 820 cm^{-1}, 831 cm^{-1}. There is some discrepancies however between the two spectra, notably the broad band from 1000-1100 cm^{-1} in the Raman spectrum that is not in the KK spectrum. This appears to be fluorescence, however experimentally, it was not indicative of such a signal as it largely correlated with Raman mode intensity. The SIPCARS signal has a very different structure, as it is centered on zero and has fluctuations corresponding to $(1 - 3\rho)$. Therefore, for an intensity of

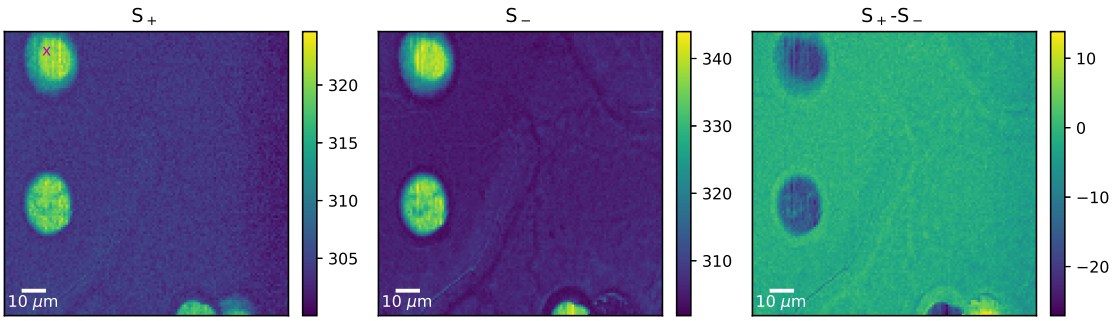

Figure 10.4: Spectral mean images of the two polarization orientations and the difference image. The magenta 'x' marks the location of the spectra shown in figure 10.2

zero, $\rho = 1/3$, or is non-resonant. It can be concluded that there is significant resonant structure in the SIPCARS specctrum corresponding to depolarization in the Raman spectrum. Several bands in both the KK and Raman spectra are present, although sign inversions accompany many of the peaks. Strong associated bands were observed at 1020 cm^{-1}, 1415 cm^{-1} and 1625 cm^{-1}. Mode assignment was not performed here, as this study was focussed on the information similarity between the SIPCARS image and the conventional KK-retrieved image.

The SIP-CARS spectral average image for both polarization orientations is shown in figure 10.4. Also shown is the average difference image, the "SIP-CARS image". It can be seen from the figures that the independent acquisitions are both coincident on the same region of the sample, with two spore bodies fully visible as high contrast circular features.

The next step in the analysis was to obtain an estimate of the uncoupled depolarization ratio image based on the SIPCARS image and knowledge of $\mathrm{Im}\{\chi^{\mathrm{R}}_{1111}\}$ from the sum image $S_+ + S_-$. Using KK, the imaginary susceptibility was retrieved using the sum image, and then the SIPCARS image was divided by this image. This provided a hyperspectral image of $1 - 3\rho$. Principal components analysis was then performed to reduce the dimensionality of the resulting image. The results of PCA are shown in figure 10.5. It can be seen in the figure that the principal component score images drastically increase the contrast present in the SIPCARS difference image, compared to

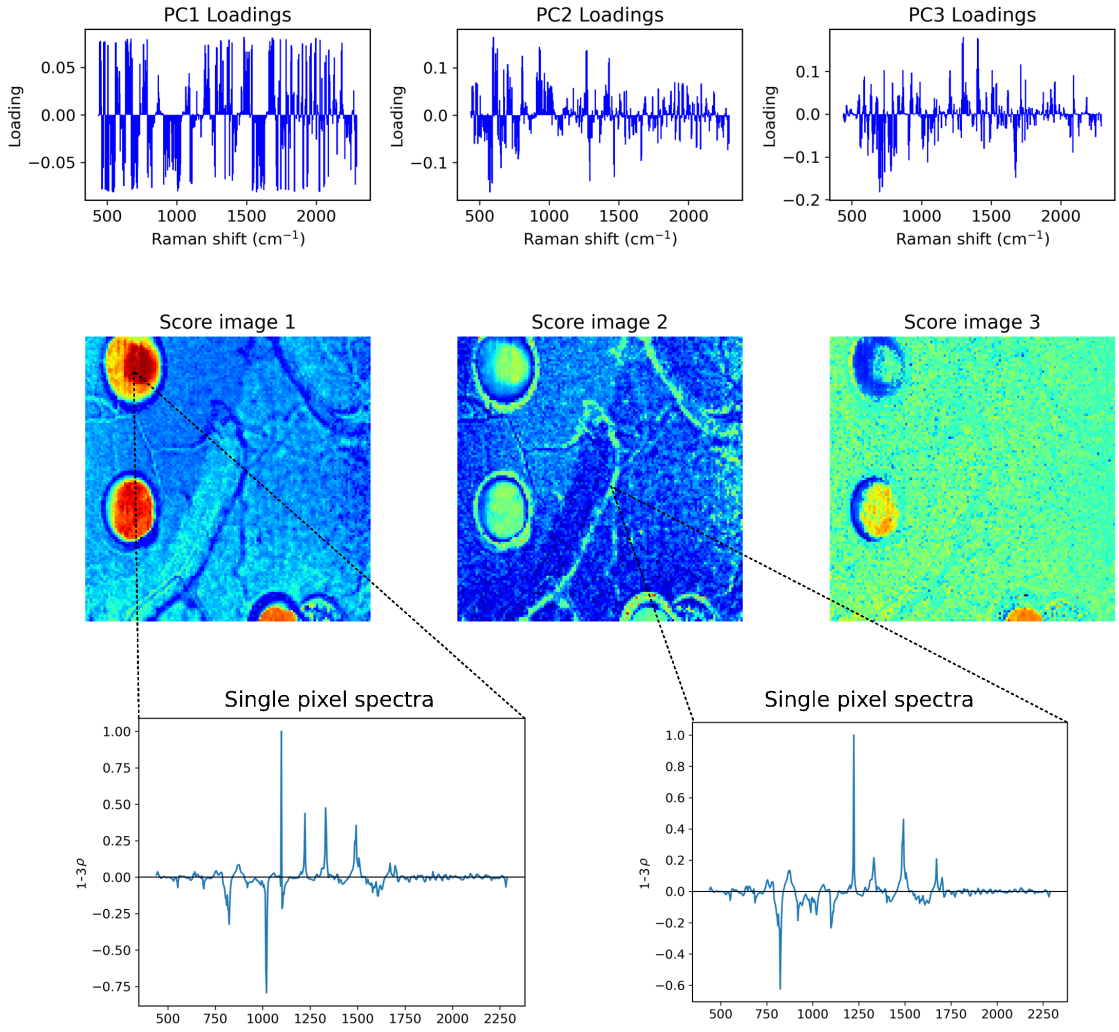

Figure 10.5: Results of principal components analysis performed on the depolarization hyperspectral image.

that which is still coupled to the resonant Raman intensity in figure 10.4. Uncoupling also presents a way to analyse only the depolarization properties of the sample, given that the image depends only on ρ. In particular, specific values of rho were seen for the fungal body and the hyphae across the image, and which varied spectrally. This may be due to the structural differences in these two features of the spore. In the single picel spectra, it can also be seen that the uncoupled depolarization ratio no longer resembles a spectrum with the typical Voigtian lineshapes. This is expected, as the depolarization ratio only exists where a resonance exists, and such more closely resembles Dirac functions of Raman shift.

10.4 Discussion

The ability for SIP-CARS to resolve a broadband Raman spectrum and the depolarization spectrum is apparent in Fig. 10.2 (b). The SIP-CARS difference spectrum shows characteristic vibrational resonances as narrow lineshapes with a signal mean of zero. The presence of negative signal results from vibrational resonances where $\rho > \frac{1}{3}$. The Kramers-Kronig (KK) retrieved signal based on the SIP-CARS sum signal shows resonances in locations where the difference signal is rapidly varying such as at 1020 cm^{-1} and 1415 cm^{-1}. Due to the depolarization spectrum being mixed with the Raman spectrum, the SIP-CARS difference peak heights vary rapidly when the sample has a large number of vibrational resonances (e.g. biological tissues). The proximity of two or more resonances with different values of ρ will result in an averaging of ρ when their separation is closer than the probe laser linewidth or spectrograph resolution. This causes SIP-CARS spectra to have a highly complex structure even when the Raman spectrum may not.

It is apparent from equation 10.19 that if $\rho = \frac{1}{3}$, the contrast in SIP-CARS vanishes since the phase shift induced by a resonance is identical to that introduced by the NRB. Therefore, SIP-CARS is expected to have higher contrast for materials with depolarized vibrations ($\rho \geq 0.75$). SIP-CARS is therefore highly useful for analysis of ordered materials such as crystals. In this case, the Raman information and polarization information could easily be decoupled using known Raman spectra or a separate measurement using conventional BCARS. When applied to biological materials that have a combination of isotropic and anisotropic contents, the SIP-CARS signal should be analysed using a data mining procedure such as ICA for example.

In this chapter, it was shown that using a novel approach, namely two sequentially acquired orthogonal BCARS measurements, the 3-colour SIP-CARS method can obtain both Raman information and polarization-sensitive information simultaneously. The efficacy and utility of this approach is largely based on the sample. When isotropic samples with a low number density are studied, e.g. pure liquids or crystals, the Raman and depolarization-based contrast could be fully decoupled for use in material analysis using the approach shown in figure 10.5, or jointly used for identification of an unknown substance using pattern recognition. This approach has the benefit of including more

information than the Raman spectrum, which should enable a higher specificity in identification of samples. When applied to complex biological samples, the mixing of the Raman and depolarization ratio in the signal results in a rich contrast that is most easily analysed using feature extraction methods such as PCA. In this work, the method was applied to hyperspectral imaging of fungal spores and their associated hyphae.

11. Conclusions

In this thesis we have explored Broadband CARS for imaging single eukaryotic cells, with a view to demonstrating its clinical potential. The speed increase in imaging compared to spontaneous Raman (SR) spectroscopy was known from the outset, but fast scan speeds are not the only important factor for use in a clinical scenario. Other important factors are the specificity and sensitivity of the measurement with respect to the problem. While it is commonly cited that the sensitivity of BCARS is greater than SR due to the nonlinear response, this is only true for the most abundant resonant species in biomolecules. In the fingerprint region, BCARS spectra are extremely weak, and the added non-resonant background obscures the signal to the extent that it is virtually indistinguishable from noise. Using methods based on deep-learning described in chapters 6 and 7, we believe this issue has been largely surmounted in the non-biological case, based on our published works[22, 23]. These methods perform drastically better than the conventional methods such as the Kramers-Kronig (KK) method in retrieving the Raman-like spectrum from a raw BCARS spectrum. In the case of biological spectra, we have demonstrated, to the best of our knowledge, the first successful classification of two eukaryotic cells using hyperspectral BCARS imaging in chapter 8. This work utilised the KK method and a customised pre-processing step that was tailored to the problem. In particular, cell-based spatial masking and scatter correction significantly reduced the level of noise and scatter effects in training samples, and we noted that these likely contributed to the high perceived quality of the Raman-like spectra obtained. The spectral quality in the form of the resolution, SNR and bandwidth we obtained from single cells has not previously been achieved with conventional or deep-learning NRB removal approaches. Further work related to this chapter should focus on applying the deep-learning methods we have developed to this use-case in order to test the ultimate limit of pixel dwell time in BCARS imaging for classification. Also, it is

expected that testing the accuracy of the classification on more cell lines would be highly beneficial, and if successful could open the possibility for high-throughput Raman cell mapping. Molecular phenotyping of specific cells based on the Raman spectrum is likely to have the most impact for low-dimensional problems, such as classifying a cell sample as cancerous or not. These problems can be optimized to have a low false negative rate and could help in identifying diseases in the early stages of progression. We suspect that as the number of classes in a multivariate statistical model becomes larger, the accuracy of correctly identifying the cell type decreases. However, when the problem is framed in an unsupervised context, distinct benefits arise, as described in chapter 9. In this chapter, we demonstrated the applicability of BCARS for high-speed identification of different species in a cell sample. We did not classify each species, but rather segmented spectra based on the retrieved Raman spectrum and then produced a pseudo-labelled image. This method used a novel approach of a dimensionality reduction technique and a robust clustering algorithm to reduce the image to a user-defined number of clusters. Using this method in a purely automated approach, an oral cytology sample was then screened for the presence of an invasive pathogen. Further quantitative variables that could help to identify the presence of the pathogen could be based on a clustering metric such as the silhouette coefficient, or use a more advanced approach that aims to classify the overall average cluster spectra. In a semi-automated manner, the approach we have developed could be used to detect the number of identified species in a cytology sample, and if this was greater than some threshold, it could notify a clinical expert for further investigation. Further work related to this chapter should focus on verifying the diagnostic accuracy of the approach using a gold standard method such as microscopic staining or immunofluorescence. After this validation, a species with more than one pathogen species should enable the testing of scalability to more complex disease presentations. A more in-depth analysis of the cluster vibrational spectra obtained using a statistical classifier and feature importance analysis should enable targeting of the spectral features that are contributing to the identification. This could aid in improving the imaging speed, where a sub-region of the detector could be used, rather than the full spectral window. These further tests should provide the necessary evidence for broader utility within the clinical context, and would likely meet the standard for a journal publication.

During the experimental phase of completing chapter 9, our group also focussed on utilising

BCARS in a flow cytometry modality. Early results of this work prompted a consideration for duplicating the results of chapters 8 and 9 using suspended blood and oral samples. While the lack of the spatial dimension in a flow setup might be seen as a disadvantage, it opens the possibility of much higher throughput, since there is no mechanical motion involved. Loss of spatial information would however preclude the possibility of image-based studies to verify the accuracy at the single sample level(i.e. cell by cell), but other methods such as conventional flow cytometry could be used subsequently, and the accuracy based on whole-sample statistical measures such as relative cell frequencies. In our opinion, BCARS is highly suited to label-free flow cytometry, but the ability to denoise and pre-process the signal is of paramount importance, as was shown throughout the results chapters in this thesis. Also, for the phenotyping problem, consideration would need to be given to the spatial heterogeneity of the Raman response in cells, which can easily be mitigated in a hyperspectral image as shown in chapter 8 but in flow conditions requires focal volume averaging, whether in real-time using an optical approach or afterwards using knowledge of each cell size.

In chapter 10, we demonstrated the first application of the hybrid NRB removal approach on single fungal cells. This method, known as SIP-CARS was previously demonstrated to remove the NRB and provide a coupled Raman and polarization spectrum of a sample. In our work, we devised a novel acquisition and processing pipeline for SIP-CARS, whereby two sequential hyperspectral images were obtained and processed to obtain the NRB-free signal. This contrasts with a previous approach that used a simultaneous acquisition that was resolved into orthogonal polarization components prior to imaging on the sensor. While much more experimentally stable, this approach requires multi-track sensor acquisitions, preventing full use of the binning mode on the sensor, which increases noise in the result. Our approach obtains two images, both using full vertical binning, but does require two scans. We hypothesised that this drawback could be mitigated using a second CCD after the dispersive element of the spectrograph, that resolved the two polarization components simultaneously. Furthermore, in our application of SIP-CARS to imaging fungal cells, a novel variance reduction procedure was developed that removed intra-acquisition variance between polarization components that would have induced erroneous baselines in the final measurement. This issue is highly specific to the dual acquisition approach, and thus had not been overcome previously. Conventional scatter correction approaches also failed to preserve the extremely weak

resonant features in each image when applied separately, thus requiring the new approach. In using the orthogonal polarization components, the conventional BCARS image can also be computed. This enabled decoupling of the depolarization spectrum from the Raman spectrum, which also has not previously been demonstrated. The applications of this approach are in two main areas, (1) in high-speed polarization imaging of complex microscopic structures such as biological tissues and crystalline compounds, and (2) spectral classification using the coupled Raman-polarization information that should complement the information present in a Raman spectrum with the bulk polarization properties of samples. We suspect a definitive application which demonstrates an improvement in contrast for imaging or detection specificity would provide enough data for a journal article publication of this work.

A. VECTOR-16 architecture

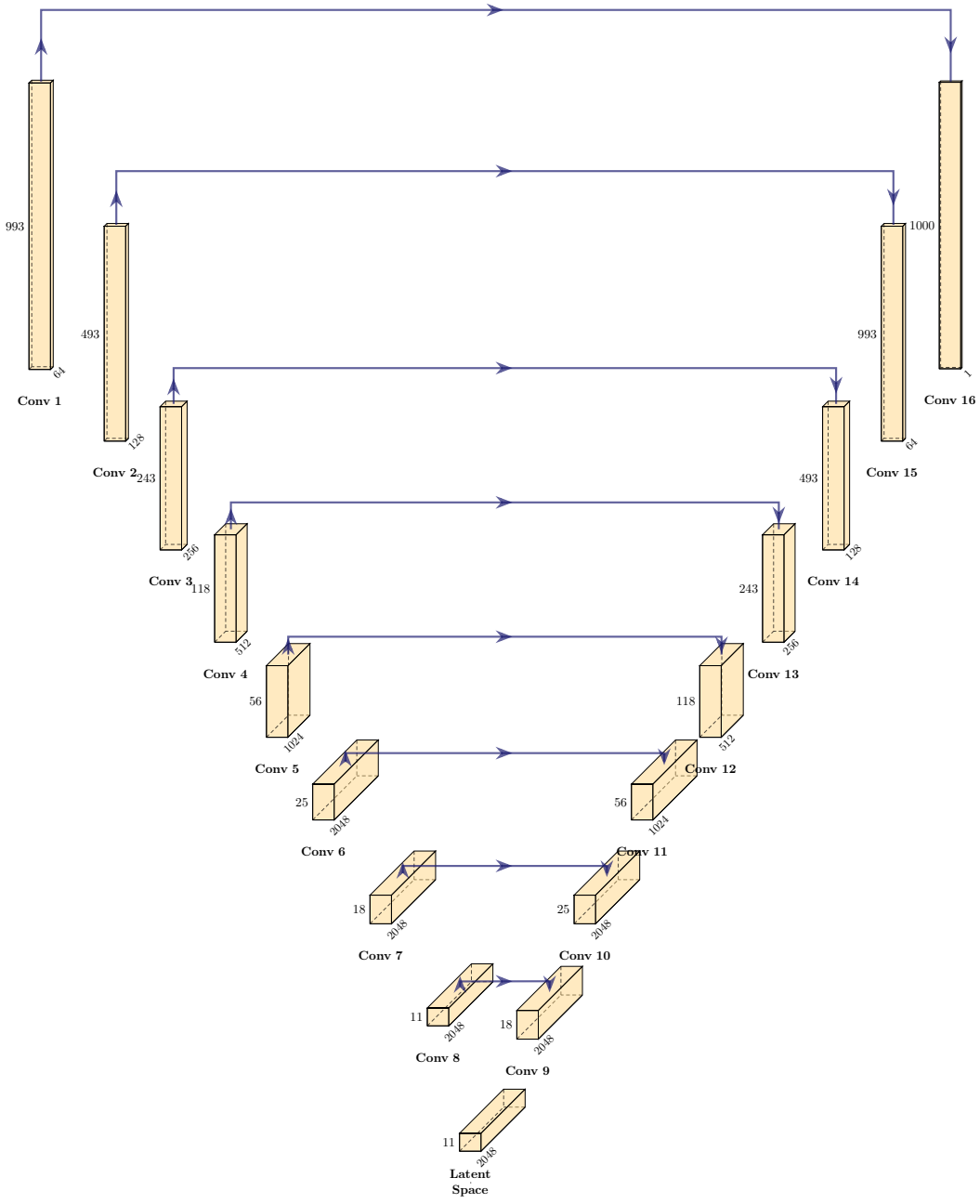

Figure A.1: Architecture of VECTOR-16. Each block shows the output dimension at the edge. Skip connections are shown as arrows paired between encoder convolutional outputs to decoder convolutional inputs. Layers proceed from left to right and depth from top to bottom.

B. VECTOR2 broadband spectra

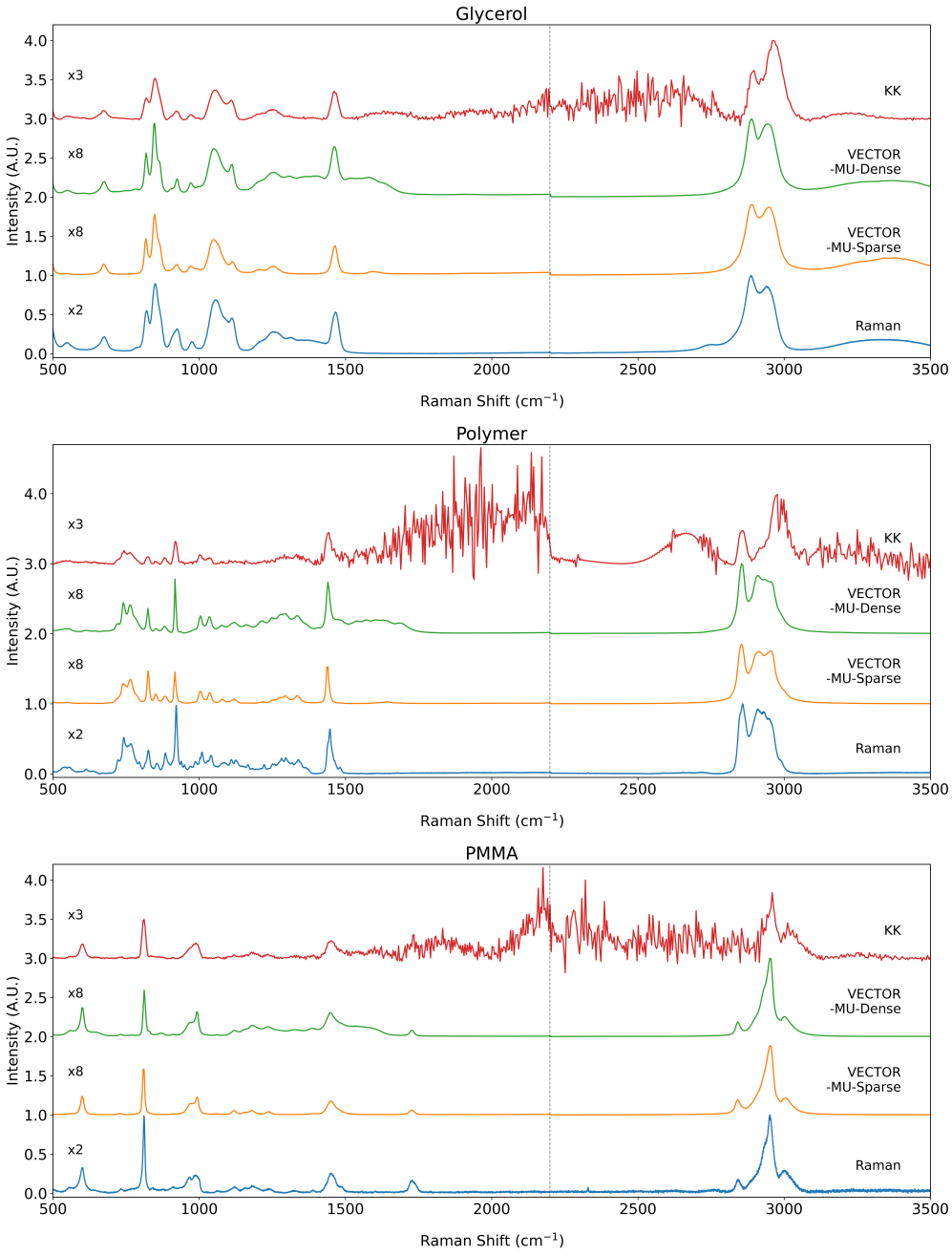

Figure B.1: Retrieved Raman spectrum of glycerol, polymer and PMMA using the Kramers-Kronig method[1] and VECTOR2. Also shown is the spontaneous Raman spectrum for each analyte. Spectra were initially normalised using data >2500 cm^{-1}, following which data to the left of the dashed vertical line were scaled for clarity with scale values shown. No post-processing or denoising was performed after phase retrieval in any case.

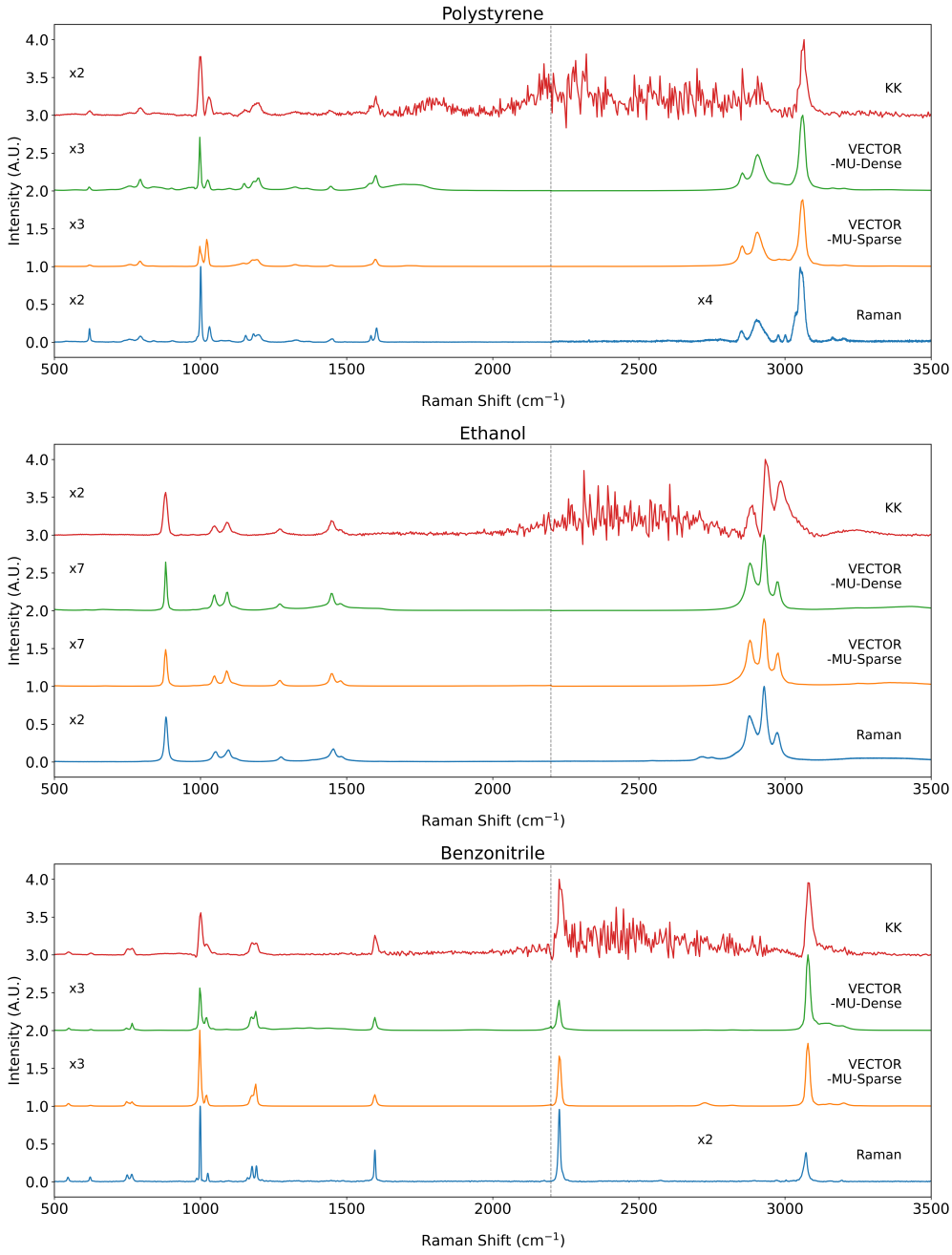

Figure B.2: Retrieved Raman spectrum of polystyrene, ethanol and benzonitrile using the Kramers-Kronig method and VECTOR2. Also shown is the spontaneous Raman spectrum for each analyte. Spectra were initially normalised using data >2500 cm^{-1}, following which data to the left of the dashed vertical line were scaled for clarity with scale values shown. No post-processing or denoising was performed after phase retrieval in any case.

Bibliography

[1] C. H. Camp, Y. J. Lee, and M. T. Cicerone, "Quantitative, comparable coherent anti-Stokes Raman scattering (CARS) spectroscopy: Correcting errors in phase retrieval," *Journal of Raman Spectroscopy*, vol. 47, no. 4, pp. 408–415, 2016.

[2] A. Zoubir, ed., *Raman Imaging Techniques and Applications*, vol. 140. Springer, 2009.

[3] K. Chen, T. Wu, T. Zhou, H. Wei, and Y. Li, "Cascaded Dual-Soliton Pulse Stokes for Broadband Coherent Anti-Stokes Raman Spectroscopy," *IEEE Photonics Journal*, vol. 8, no. 6, 2016.

[4] C. H. Camp, Y. J. Lee, J. M. Heddleston, C. M. Hartshorn, A. R. Walker, J. N. Rich, J. D. Lathia, and M. T. Cicerone, "High-speed coherent Raman fingerprint imaging of biological tissues," *Nature Photonics*, vol. 8, no. 8, pp. 627–634, 2014.

[5] F. Vernuccio, R. Vanna, C. Ceconello, A. Bresci, F. Manetti, S. Sorrentino, S. Ghislanzoni, F. Lambertucci, O. Motin, I. Martins, G. Kroemer, I. Bongarzone, G. Cerullo, and D. Polli, "Full-Spectrum CARS Microscopy of Cells and Tissues with Ultrashort White-Light Continuum Pulses," *The Journal of Physical Chemistry B*, 2023.

[6] M. T. Cicerone and C. H. Camp, "Histological coherent Raman imaging: A prognostic review," *Analyst*, vol. 143, no. 1, pp. 33–59, 2018.

[7] J. G. Porquez and A. D. Slepkov, "Application of spectral-focusing-CARS microscopy to pharmaceutical sample analysis," *AIP Advances*, vol. 8, no. 9, 2018.

[8] C. M. Hartshorn, Y. J. Lee, C. H. Camp, Z. Liu, J. Heddleston, N. Canfield, T. A. Rhodes, A. R. Hight Walker, P. J. Marsac, and M. T. Cicerone, "Multicomponent chemical imaging of pharmaceutical solid dosage forms with broadband CARS microscopy," *Analytical Chemistry*, vol. 85, no. 17, pp. 8102–8111, 2013.

[9] S. H. Parekh, Y. J. Lee, K. A. Aamer, and M. T. Cicerone, "Label-free cellular imaging by Broadband coherent anti-stokes raman scattering microscopy," *Biophysical Journal*, vol. 99, no. 8, pp. 2695–2704, 2010.

[10] K. O'dwyer, K. Domijan, A. Dignam, M. Butler, and B. M. Hennelly, "Automated raman micro-spectroscopy of epithelial cell nuclei for high-throughput classification," *Cancers*, vol. 13, no. 19, pp. 1–21, 2021.

[11] I. W. Schie, J. Rüger, A. S. Mondol, A. Ramoji, U. Neugebauer, C. Krafft, and J. Popp, "High-Throughput Screening Raman Spectroscopy Platform for Label-Free Cellomics," *Analytical Chemistry*, vol. 90, no. 3, pp. 2023–2030, 2018.

[12] D. Traynor, I. Behl, D. O'Dea, F. Bonnier, S. Nicholson, F. O'Connell, A. Maguire, S. Flint, S. Galvin, C. M. Healy, C. M. Martin, J. J. O'Leary, A. Malkin, H. J. Byrne, and F. M. Lyng, "Raman spectral cytopathology for cancer diagnostic applications," *Nature Protocols*, vol. 16, no. 7, pp. 3716–3735, 2021.

[13] J. Wen, T. Tang, S. Kanwal, Y. Lu, C. Tao, L. Zheng, D. Zhang, and Z. Gu, "Detection and Classification of Multi-Type Cells by Using Confocal Raman Spectroscopy," *Frontiers in Chemistry*, vol. 9, no. April, pp. 1–8, 2021.

[14] G. Moore, G. Knight, and A. D. Blann, *Haematology*. Fundamentals of biomedical science, Oxford University Press, 2016.

[15] K. Kong, C. Kendall, N. Stone, and I. Notingher, "Raman spectroscopy for medical diagnostics - From in-vitro biofluid assays to in-vivo cancer detection," *Advanced Drug Delivery Reviews*, vol. 89, pp. 121–134, 2015.

[16] Y. J. Lee and M. T. Cicerone, "Vibrational dephasing time imaging by time-resolved broadband coherent anti-Stokes Raman scattering microscopy," *Applied Physics Letters*, vol. 92, no. 4, 2008.

[17] P. V. Kolesnichenko, J. O. Tollerud, and J. A. Davis, "Background-free time-resolved coherent Raman spectroscopy (CSRS and CARS): Heterodyne detection of low-energy vibrations and identification of excited-state contributions," *APL Photonics*, vol. 4, no. 5, 2019.

[18] S.-H. Lim, A. G. Caster, and S. R. Leone, "Fourier transform spectral interferometric coherent anti-Stokes Raman scattering (FTSI-CARS) spectroscopy," *Optics Letters*, vol. 32, no. 10, p. 1332, 2007.

[19] C. L. Evans, E. O. Potma, and X. S. Xie, "Coherent anti-Stokes Raman scattering spectral interferometry: determination of the real and imaginary components of nonlinear susceptibility $\chi\hat{}(3)$ for vibrational microscopy," *Optics Letters*, vol. 29, no. 24, p. 2923, 2004.

[20] J.-X. Cheng, L. D. Book, and X. S. Xie, "Polarization coherent anti-Stokes Raman scattering microscopy," *Optics Letters*, vol. 26, no. 17, pp. 1341–1343, 2001.

[21] C. W. Freudiger, W. Min, B. G. Saar, S. Lu, G. R. Holtom, C. He, J. C. Tsai, J. X. Kang, and X. S. Xie, "Label-Free Biomedical Imaging with High Sensitivity by Stimulated Raman Scattering Microscopy," *Science*, vol. 322, no. 5909, pp. 1857–1861, 2008.

[22] Z. Wang, K. O'Dwyer, R. Muddiman, T. Ward, B. Hennelly, and C. H. Camp Jr., "VECTOR: Very deep convolutional autoencoders for non-resonant background removal in broadband coherent anti-Stokes Raman scattering," *Journal of Raman Spectroscopy*, vol. 53, no. 6, pp. 1081–1093, 2022.

[23] R. Muddiman, K. O' Dwyer, C. H. Camp, and B. Hennelly, "Removing non-resonant background from broadband CARS using a physics-informed neural network," *Analytical methods : advancing methods and applications*, vol. 15, no. 32, pp. 4032–4043, 2023.

[24] A. Smekal, "Zur Quantentheorie der Streuung und Dispersion," *Die Naturwissenschaften*, vol. 16, no. 31, pp. 612–613, 1928.

[25] C. V. Raman and K. S. Krishnan, "A New Type of Secondary Radiation," *Nature*, vol. 121, no. 3048, pp. 501–502, 1928.

[26] M. Harrand and R. Lennuier, "Exaltation of the intensity of certain bands in the Raman spectra emitted from solids with an absorption band near the excitation wavelength," *C. R. Hebd. Acad. Sci*, vol. 223, pp. 356–357, 1946.

[27] E. V. Efremov, F. Ariese, and C. Gooijer, "Achievements in resonance Raman spectroscopy.

Review of a technique with a distinct analytical chemistry potential," *Analytica Chimica Acta*, vol. 606, no. 2, pp. 119–134, 2008.

[28] A. L. Schawlow and C. H. Townes, "Infrared and optical masers," *Physical Review*, vol. 112, no. 6, pp. 1940–1949, 1958.

[29] T. H. Maiman, "Stimulated Optical Radiation in Ruby," *Nature*, vol. 187, no. 4736, pp. 493–494, 1960.

[30] A. Javan, W. R. Bennett, and D. R. Herriott, "Population inversion and continuous optical maser oscillation in a gas discharge containing a He-Ne mixture," *Physical Review Letters*, vol. 6, no. 3, pp. 106–110, 1961.

[31] S. P. S. Porto and D. L. Wood, "Ruby Optical Maser as a Raman Source," *Journal of the Optical Society of America*, vol. 52, no. 3, p. 251, 1962.

[32] P. A. Franken, A. E. Hill, C. W. Peters, and G. Weinreich, "Generation of optical harmonics," *Physical Review Letters*, vol. 7, no. 4, pp. 118–119, 1961.

[33] R. W. Terhune, P. D. Maker, and C. M. Savage, "Optical harmonic generation in calcite," *Physical Review Letters*, vol. 8, no. 10, pp. 404–406, 1962.

[34] W. Ng and E. Woodbury, "Ruby Laser Operation in Near IR," *Proceedings of the Institution of Electronic and Radio Engineers*, vol. 50, 1962.

[35] J. L. Koenig, "Raman spectroscopy of biological molecules: A review," *Journal of Polymer Science: Macromolecular Reviews*, vol. 6, no. 1, pp. 59–177, 1972.

[36] Z. Movasaghi, S. Rehman, and I. U. Rehman, "Raman spectroscopy of biological tissues," *Applied Spectroscopy Reviews*, vol. 42, no. 5, pp. 493–541, 2007.

[37] M. Fleischmann, P. J. Hendra, and A. J. McQuillan, "Raman spectra of pyridine adsorbed at a silver electrode," *Chemical Physics Letters*, vol. 26, no. 2, pp. 163–166, 1974.

[38] D. L. Jeanmaire and R. P. Van Duyne, "Surface raman spectroelectrochemistry: Part I. Heterocyclic, aromatic, and aliphatic amines adsorbed on the anodized silver electrode,"

Journal of Electroanalytical Chemistry and Interfacial Electrochemistry, vol. 84, no. 1, pp. 1–20, 1977.

[39] P. L. Stiles, J. A. Dieringer, N. C. Shah, and R. P. Van Duyne, "Surface-enhanced Raman spectroscopy," *Annual Review of Analytical Chemistry*, vol. 1, no. 1, pp. 601–626, 2008.

[40] J. R. Lombardi, R. L. Birke, T. Lu, and J. Xu, "Charge-transfer theory of surface enhanced Raman spectroscopy: Herzberg-Teller contributions," *The Journal of Chemical Physics*, vol. 84, no. 8, pp. 4174–4180, 1986.

[41] E. C. Le Ru, E. Blackie, M. Meyer, and P. G. Etchegoint, "Surface enhanced raman scattering enhancement factors: A comprehensive study," *Journal of Physical Chemistry C*, vol. 111, no. 37, pp. 13794–13803, 2007.

[42] L. Vázquez-Iglesias, G. M. Stanfoca Casagrande, D. García-Lojo, L. Ferro Leal, T. A. Ngo, J. Pérez-Juste, R. M. Reis, K. Kant, and I. Pastoriza-Santos, "SERS sensing for cancer biomarker: Approaches and directions," *Bioactive Materials*, vol. 34, no. September 2023, pp. 248–268, 2024.

[43] A. P. Holman and D. Kurouski, "Surface-enhanced Raman spectroscopy in forensic analysis," *Reviews in Analytical Chemistry*, vol. 43, no. 1, 2024.

[44] P. Maker and W. Terhune, "Study of Optical Effects Due to an Induced Polarization Third Order in the Electric Field Strength," *Phys. Rev.*, vol. 137, no. 3, 1965.

[45] J. X. Cheng and X. S. Xie, "Coherent anti-Stokes Raman scattering microscopy: Instrumentation, theory, and applications," *Journal of Physical Chemistry B*, vol. 108, no. 3, pp. 827–840, 2004.

[46] P. R. Régnier and J. P. Taran, "On the possibility of measuring gas concentrations by stimulated anti-Stokes scattering," *Applied Physics Letters*, vol. 23, no. 5, pp. 240–242, 1973.

[47] G. C. Bjorklund, "Effects of Focusing on Third-Order Nonlinear Processes in Isotropic Media," *IEEE Journal of Quantum Electronics*, vol. 11, no. 6, pp. 287–296, 1975.

[48] R. Begley, A. Harvey, and R. Byer, "Coherent anti-Stokes Raman spectroscopy," *Applied Physics Letters*, vol. 25, no. 7, 1974.

[49] W. M. Tolles, J. W. Nibler, J. R. McDonald, and A. B. Harvey, "Review of the Theory and Application of Coherent Anti-Stokes Raman Spectroscopy (Cars).," *Applied Spectroscopy*, vol. 31, no. 4, pp. 253–272, 1977.

[50] M. D. Levenson and S. S. Kano, *Introduction to Nonlinear Laser Spectroscopy*. Academic Press, 1988.

[51] G. Eesley, *Coherent Raman Specttroscopy*. Warren: Pergamon Press, 1981.

[52] M. D. Duncan, J. Reintjes, and T. J. Manuccia, "Scanning coherent anti-Stokes Raman microscope," *Optics Letters*, vol. 7, no. 8, p. 350, 1982.

[53] N. Bloembergen, "A Quarter Century Of Stimulated Raman Scattering," *Pure and Applied Chemistry*, vol. 59, no. 10, pp. 1229–1236, 1987.

[54] G. J. Puppels, F. F. de Mul, C. Otto, J. Greve, M. Robert-Nicoud, D. J. Arndt-Jovin, and T. M. Jovin, "Studying single living cells and chromosomes by confocal Raman microspectroscopy," *Nature*, vol. 347, pp. 301–303, 9 1990.

[55] A. Zumbusch, G. R. Holtom, and X. S. Xie, "Three-dimensional vibrational imaging by coherent anti-stokes raman scattering," *Physical Review Letters*, vol. 82, no. 20, pp. 4142–4145, 1999.

[56] A. Volkmer, J. X. Cheng, and X. S. Xie, "Vibrational imaging with high sensitivity via epidetected coherent anti-stokes raman scattering microscopy," *Physical Review Letters*, vol. 87, no. 2, pp. 2–5, 2001.

[57] J. X. Cheng, A. Volkmer, L. D. Book, and X. Sunney Xie, "An Epi-Detected Coherent Anti-Stokes Raman Scattering (E-CARS) Microscope with High Spectral Resolution and High Sensitivity," *Journal of Physical Chemistry B*, vol. 105, no. 7, pp. 2712–2717, 2001.

[58] J.-X. Cheng, A. Volkmer, and X. S. Xie, "Theoretical and experimental characterization of coherent anti-Stokes Raman scattering microscopy," *Journal of the Optical Society of America B*, vol. 19, no. 6, p. 1363, 2002.

[59] C. L. Evans, E. O. Potma, M. Puoris'haag, D. Côté, C. P. Lin, and X. S. Xie, "Chemical imaging of tissue in vivo with video-rate coherent anti-Strokes Raman scattering microscopy," *Proceedings of the National Academy of Sciences of the United States of America*, vol. 102, no. 46, pp. 16807–16812, 2005.

[60] J. X. Cheng, A. Volkmer, L. D. Book, and X. S. Xie, "Multiplex coherent anti-stokes Raman scattering microspectroscopy and study of lipid vesicles," *Journal of Physical Chemistry B*, vol. 106, no. 34, pp. 8493–8498, 2002.

[61] J. X. Cheng, Y. K. Jia, G. Zheng, and X. S. Xie, "Laser-scanning coherent anti-Stokes Raman scattering microscopy and applications to cell biology," *Biophysical Journal*, vol. 83, no. 1, pp. 502–509, 2002.

[62] D. Pestov, R. K. Murawski, G. O. Ariunbold, X. Wang, M. Zhi, A. V. Sokolov, V. A. Sautenkov, Y. V. Rostovtsev, A. Dogariu, Y. Huang, and M. O. Scully, "Optimizing the laser-pulse configuration for coherent Raman spectroscopy," *Science*, vol. 316, no. 5822, pp. 265–268, 2007.

[63] C. Krafft, B. Dietzek, and J. Popp, "Raman and CARS microspectroscopy of cells and tissues," *Analyst*, vol. 134, no. 6, pp. 1046–1057, 2009.

[64] D. V. Voronine, Z. Zhang, A. V. Sokolov, and M. O. Scully, "Surface-enhanced FAST CARS: En route to quantum nano-biophotonics," *Nanophotonics*, vol. 7, no. 3, pp. 523–548, 2018.

[65] I. W. Schie, C. Krafft, and J. Popp, "Applications of coherent Raman scattering microscopies to clinical and biological studies," *Analyst*, vol. 140, no. 12, pp. 3897–3909, 2015.

[66] D. Polli, V. Kumar, C. M. Valensise, M. Marangoni, and G. Cerullo, "Broadband Coherent Raman Scattering Microscopy," *Laser and Photonics Reviews*, vol. 12, no. 9, pp. 1–36, 2018.

[67] B. Littleton, T. Kavanagh, F. Festy, and D. Richards, "Spectral interferometric implementation with passive polarization optics of coherent anti-stokes raman scattering," *Physical Review Letters*, vol. 111, no. 10, pp. 2–6, 2013.

[68] B. Littleton, P. Shah, T. Kavanagh, and D. Richards, "Three-color coherent anti-Stokes Raman

scattering with optical nonresonant background removal," *Journal of Raman Spectroscopy*, vol. 50, no. 9, 2019.

[69] W. Demtröder, *Molecular Physics: Theoretical Principles and Experimental Methods*. Wiley-VCH, 2007.

[70] H. G. M. Edwards and G. Dent, *Modern Raman spectroscopy—a practical approach*. Wiley, 2005.

[71] D. A. Long, *The Raman effect: a unified treatment of the theory of Raman scattering by molecules*. Wiley, 2002.

[72] G. Keresztury, *Raman Spectroscopy: Theory*. Chichester, UK: John Wiley & Sons, Ltd, 2006.

[73] D. J. Griffiths, *Introduction to Electrodynamics*. Cambridge: Cambridge University Press, 2023.

[74] H. Rigneault and P. Berto, "Tutorial: Coherent Raman light matter interaction processes," *APL Photonics*, vol. 3, no. 9, 2018.

[75] S. H. Ashworth, "Molecular Quantum Mechanics, 5th edn, by Peter Atkins and Ronald Friedman," *Contemporary Physics*, vol. 53, no. 4, pp. 372–373, 2012.

[76] J. L. McHale, *Molecular Spectroscopy, Second Edition*. CRC Press, 2017.

[77] H. W. Schrötter and H. W. Klöckner, "Raman Scattering Cross Sections in Gases and Liquids," in *Raman Spectroscopy of Gases and Liquids* (A. Weber, ed.), pp. 123–166, Berlin, Heidelberg: Springer Berlin Heidelberg, 1979.

[78] H. A. Rinia, K. N. Burger, M. Bonn, and M. Müller, "Quantitative label-free imaging of lipid composition and packing of individual cellular lipid droplets using multiplex CARS microscopy," *Biophysical Journal*, vol. 95, no. 10, pp. 4908–4914, 2008.

[79] J. X. Cheng and X. S. Xie, *Coherent Raman scattering microscopy*. CRC Press, 2016.

[80] R. Boyd, *Nonlinear Optics*. Academic Press, 3 ed., 2008.

[81] M. D. Levenson and J. J. Song, "Coherent Raman Spectroscopy," in *Coherent Nonlinear Optics: Recent Advances* (M. S. Feld and V. S. Letokhov, eds.), pp. 293–371, Berlin, Heidelberg: Springer Berlin Heidelberg, 1980.

[82] J.-C. D. o. P. Diels, N. Astronomy University of New Mexico Albuquerque, W. D. o. P. Rudolph, and N. Astronomy University of New Mexico Albuquerque, *Ultrashort Laser Pulse Phenomena, Fundamentals, Techniques, and Applications on a Femtosecond Time Scale*. Elsevier, 2 ed., 2006.

[83] R. L. Fork, O. E. Martinez, and J. P. Gordon, "Negative dispersion using pairs of prisms," *Optics Letters*, vol. 9, no. 5, p. 150, 1984.

[84] Y. Shaked, S. Yefet, and A. Pe'er, "The Prism-Pair: Simple Dispersion Compensation and Spectral Shaping of Ultrashort Pulses," *International Journal of Experimental Spectroscopic Techniques*, vol. 1, no. 2, pp. 1–4, 2016.

[85] R. Trebino, R. Jafari, S. A. Akturk, P. Bowlan, Z. Guang, P. Zhu, E. Escoto, and G. Steinmeyer, "Highly reliable measurement of ultrashort laser pulses," *Journal of Applied Physics*, vol. 128, no. 17, 2020.

[86] I. A. Walmsley and C. Dorrer, "Characterization of ultrashort electromagnetic pulses," *Advances in Optics and Photonics*, vol. 1, no. 2, p. 308, 2009.

[87] R. Trebino, P. Bowlan, P. Gabolde, X. Gu, S. Akturk, and M. Kimmel, "Simple devices for measuring complex ultrashort pulses," *Laser and Photonics Reviews*, vol. 3, no. 3, pp. 314–342, 2009.

[88] R. Jafari, T. Jones, and R. Trebino, "100% Reliable Algorithm for Second-Harmonic-Generation Frequency-Resolved Optical Gating," *arXiv*, 2018.

[89] R. Trebino, *Frequency resolved optical gating: The measurement of ultrashort optical pulses*. Kluwer Academic Publishers, 2002.

[90] R. Selm, G. Krauss, A. Leitenstorfer, and A. Zumbusch, "Non-iterative characterization of few-cycle laser pulses using flat-top gates," *Optics Express*, vol. 20, no. 6, p. 5955, 2012.

[91] V. Kumar, M. Casella, E. Molotokaite, D. Polli, G. Cerullo, and M. Marangoni, "Coherent Raman spectroscopy with a fiber-format femtosecond oscillator," *Journal of Raman Spectroscopy*, vol. 43, no. 5, pp. 662–667, 2012.

[92] W. Liu, S. L. Liu, D. N. Chen, and H. B. Niu, "Analysis of detection limit to time-resolved coherent anti-Stokes Raman scattering nanoscopy," *Chinese Physics B*, vol. 23, no. 10, 2014.

[93] R. L. McCreery, *Raman Spectroscopy for Chemical Analysis*. Wiley, 2000.

[94] W. Min, C. W. Freudiger, S. Lu, and X. S. Xie, "Coherent nonlinear optical imaging: Beyond fluorescence microscopy," *Annual Review of Physical Chemistry*, vol. 62, pp. 507–530, 2011.

[95] W. Min and X. Gao, "The Duality of Raman Scattering," *Accounts of Chemical Research*, vol. 57, no. 14, pp. 1896–1905, 2024.

[96] H. Takeuchi, S. Hashimoto, and I. Harada, "Simple and Efficient Method to Eliminate Spike Noise from Spectra Recorded on Charge-Coupled Device Detectors," *Appl. Spectrosc.*, vol. 47, pp. 129–131, 1 1993.

[97] S. M. Anthony and J. A. Timlin, "Removing cosmic spikes using a hyperspectral upper-bound spectrum method," *Applied Spectroscopy*, vol. 71, no. 3, pp. 507–519, 2017.

[98] J. E. Aubin, "Autofluorescence," *The Journal of Histochemistry and Cytochemistry*, pp. 36–43, 1979.

[99] A. C. Croce and G. Bottiroli, "Autofluorescence spectroscopy and imaging: A tool for biomedical research and diagnosis," *European Journal of Histochemistry*, vol. 58, no. 4, pp. 320–337, 2014.

[100] L. Donaldson, "Autofluorescence in plants," *Molecules*, vol. 25, no. 10, 2020.

[101] M. Bertero and P. Boccacci, *Introduction to Inverse Problems in Imaging*. CRC Press, 2020.

[102] G. Strang, *Linear Algebra and Its Applications*. Thomas Learning, 1988.

[103] A. F. J. Anscombe and F. J. Anscombe, "The Transformation of Poisson, Binomial and Negative-Binomial Data," *Biometrika*, vol. 35, pp. 246–254, 5 1948.

[104] Y. Liu, Y. J. Lee, and M. T. Cicerone, "Broadband CARS spectral phase retrieval using a time-domain Kramers–Kronig transform," *Optics Letters*, vol. 34, no. 9, pp. 1363–1365, 2009.

[105] C. H. Camp, Y. J. Lee, and M. T. Cicerone, "Quantitative, comparable coherent anti-Stokes Raman scattering (CARS) spectroscopy: Correcting errors in phase retrieval," *Journal of Raman Spectroscopy*, vol. 47, no. 4, pp. 408–415, 2016.

[106] E. M. Vartiainen, "Phase retrieval approach for coherent anti-Stokes Raman scattering spectrum analysis," *Journal of the Optical Society of America B*, vol. 9, no. 8, p. 1209, 1992.

[107] T. Kamiya, F. Krausz, B. Monemar, H. Venghaus, H. Weber, and H. Weinfurter, *Kramers-Kronig Relations and Sum Rules in Nonlinear Optics*. Springer, 2005.

[108] H. Martens and E. Stark, "Extended multiplicative signal correction and spectral interference subtraction: New preprocessing methods for near infrared spectroscopy," *Journal of Pharmaceutical and Biomedical Analysis*, vol. 9, no. 8, pp. 625–635, 1991.

[109] C. Stringer, T. Wang, M. Michaelos, and M. Pachitariu, "Cellpose: a generalist algorithm for cellular segmentation," *Nature Methods*, vol. 18, no. 1, pp. 100–106, 2021.

[110] C. Stringer and M. Pachitariu, "Cellpose3: one-click image restoration for improved cellular segmentation," *bioRxiv*, p. 2024.02.10.579780, 2024.

[111] P. Hello and C. N. Man, "Design of a low-loss off-axis beam expander," *Applied Optics*, vol. 35, no. 15, pp. 2534–2536, 1996.

[112] M. D. Young, J. J. Field, K. E. Sheetz, R. A. Bartels, and J. Squier, "A pragmatic guide to multiphoton microscope design," *Advances in Optics and Photonics*, vol. 7, p. 276, 6 2015.

[113] R. Phillips, J. Kondev, J. Theriot, and H. Garcia, *Physical Biology of the Cell*. CRC Press, 2012.

[114] B. Shambayati, *Cytopathology*. Fundamentals of biomedical science, Oxford University Press, 2018.

[115] J. Devany, M. J. Falk, L. J. Holt, A. Murugan, and M. L. Gardel, "Epithelial tissue confinement inhibits cell growth and leads to volume-reducing divisions," *Developmental Cell*, vol. 58, no. 16, pp. 1462–1476, 2023.

[116] J. A. Squier, M. Müller, G. J. Brakenhoff, and K. R. Wilson, "Third harmonic generation microscopy," *Optics Express*, vol. 3, no. 9, p. 315, 1998.

[117] F. Ganikhanov, C. L. Evans, B. G. Saar, and X. S. Xie, "High-sensitivity vibrational imaging with frequency modulation coherent anti-Stokes Raman scattering (FM CARS) microscopy," *Optics Letters*, vol. 31, no. 12, p. 1872, 2006.

[118] A. Volkmer, L. D. Book, and X. S. Xie, "Time-resolved coherent anti-Stokes Raman scattering microscopy: Imaging based on Raman free induction decay," *Applied Physics Letters*, vol. 80, no. 9, pp. 1505–1507, 2002.

[119] F. Masia, A. Glen, P. Stephens, P. Borri, and W. Langbein, "Quantitative chemical imaging and unsupervised analysis using hyperspectral coherent anti-stokes Raman scattering microscopy," *Analytical Chemistry*, vol. 85, no. 22, pp. 10820–10828, 2013.

[120] E. M. Vartiainen, K.-E. Peiponen, H. Kishida, and T. Koda, "Phase retrieval in nonlinear optical spectroscopy by the maximum-entropy method: an application to the —χˆ(3)— spectra of polysilane," *Journal of the Optical Society of America B*, vol. 13, no. 10, p. 2106, 1996.

[121] E. M. Vartiainen, H. A. Rinia, M. Müller, and M. Bonn, "Direct extraction of Raman line-shapes from congested CARS spectra," *Optics Express*, vol. 14, no. 8, p. 3622, 2006.

[122] C. M. Valensise, A. Giuseppi, F. Vernuccio, A. De La Cadena, G. Cerullo, and D. Polli, "Removing non-resonant background from CARS spectra via deep learning," *APL Photonics*, vol. 5, no. 6, pp. 1–8, 2020.

[123] R. Houhou, P. Barman, M. Schmitt, T. Meyer, J. Popp, and T. Bocklitz, "Deep learning as phase retrieval tool for CARS spectra," *Optics Express*, vol. 28, no. 14, p. 21002, 2020.

[124] A. Saghi, R. Junjuri, L. Lensu, and E. Vartiainen, "Semi-synthetic data generation to fine-tune

a convolutional neural network for retrieving Raman signals from CARS spectra," *Optics Continuum*, vol. 1, no. 11, pp. 2360–2373, 2022.

[125] M. Makarkin and D. Bratashov, "State-of-the-art approaches for image deconvolution problems, including modern deep learning architectures," *Micromachines*, vol. 12, no. 12, 2021.

[126] J. Dong, L. Valzania, A. Maillard, T. A. Pham, S. Gigan, and M. Unser, "Phase Retrieval: From Computational Imaging to Machine Learning: A tutorial," *IEEE Signal Processing Magazine*, vol. 40, no. 1, pp. 45–57, 2023.

[127] C. C. Aggarwal, *Neural Networks and Deep Learning*. Springer, 2018.

[128] S. Ioffe and C. Szegedy, "Batch normalization: Accelerating deep network training by reducing internal covariate shift," *32nd International Conference on Machine Learning, ICML 2015*, vol. 1, pp. 448–456, 2015.

[129] S. Santurkar, D. Tsipras, A. Ilyas, and A. Madry, "How does batch normalization help optimization?," *Advances in Neural Information Processing Systems*, vol. 2018-Decem, no. NeurIPS, pp. 2483–2493, 2018.

[130] V. Nair and G. E. Hinton, "Rectified linear units improve Restricted Boltzmann machines," *ICML 2010 - Proceedings, 27th International Conference on Machine Learning*, no. 3, pp. 807–814, 2010.

[131] S. Hochreiter, "The Vanishing Gradient Problem During Learning Recurrent Neural Nets and Problem Solutions," *International Journal of Uncertainty, Fuzziness and Knowledge-Based Systems*, vol. 06, pp. 107–116, 4 1998.

[132] K. He, X. Zhang, S. Ren, and J. Sun, "Deep Residual Learning for Image Recognition," in *Proceedings of the IEEE Conference on Computer Vision and Pattern Recognition (CVPR)*, 6 2016.

[133] C. Krafft, I. W. Schie, T. Meyer, M. Schmitt, and J. Popp, "Developments in spontaneous and coherent Raman scattering microscopic imaging for biomedical applications," *Chemical Society Reviews*, vol. 45, no. 7, pp. 1819–1849, 2016.

[134] N. Dudovich, D. Oron, and Y. Silberberg, "Single-pulse coherent anti-Stokes Raman spectroscopy in the fingerprint spectral region," *Journal of Chemical Physics*, vol. 118, no. 20, pp. 9208–9215, 2003.

[135] "ASTM E1840-96(2014)," tech. rep.

[136] D. Hutsebaut, P. Vandenabeele, and L. Moens, "Evaluation of an accurate calibration and spectral standardization procedure for Raman spectroscopy," *Analyst*, vol. 130, pp. 1204–1214, 2005.

[137] T. S. Tkaczyk, *Field Guide to Microscopy*. SPIE Press, 2010.

[138] J. M. Surmacki, B. J. Woodhams, A. Haslehurst, B. A. Ponder, and S. E. Bohndiek, "Raman micro-spectroscopy for accurate identification of primary human bronchial epithelial cells," *Scientific Reports*, vol. 8, no. 1, pp. 1–11, 2018.

[139] J. Hutchings, C. Kendall, B. Smith, N. Shepherd, H. Ban, and N. Stone, "The potential for histological screening using a combination of rapid Raman mapping and principal component analysis," *Journal of Biophotonics*, vol. 2, no. 1-2, pp. 91–103, 2009.

[140] L. T. Kerr and B. M. Hennelly, "A multivariate statistical investigation of background subtraction algorithms for Raman spectra of cytology samples recorded on glass slides," *Chemometrics and Intelligent Laboratory Systems*, vol. 158, pp. 61–68, 2016.

[141] M. Cui, B. R. Bachler, and J. P. Ogilvie, "Scattering Under Biological Imaging Conditions," *Optics Letters*, vol. 34, no. 6, pp. 773–775, 2009.

[142] M. C. Potcoava, G. L. Futia, J. Aughenbaugh, I. R. Schlaepfer, and E. A. Gibson, "Raman and coherent anti-Stokes Raman scattering microscopy studies of changes in lipid content and composition in hormone-treated breast and prostate cancer cells," *Journal of Biomedical Optics*, vol. 19, no. 11, p. 111605, 2014.

[143] C. L. Evans and X. S. Xie, "Coherent anti-Stokes Raman scattering microscopy: Chemical imaging for biology and medicine," *Annual Review of Analytical Chemistry*, vol. 1, no. 1, pp. 883–909, 2008.

[144] X. Nan, E. O. Potma, and X. S. Xie, "Nonperturbative chemical imaging of organelle transport in living cells with coherent anti-Stokes Raman scattering microscopy," *Biophysical Journal*, vol. 91, no. 2, pp. 728–735, 2006.

[145] S. F. El-Mashtoly, D. Niedieker, D. Petersen, S. D. Krauss, E. Freier, A. Maghnouj, A. Mosig, S. Hahn, C. Kötting, and K. Gerwert, "Automated identification of subcellular organelles by coherent anti-stokes raman scattering," *Biophysical Journal*, vol. 106, no. 9, pp. 1910–1920, 2014.

[146] I. W. Schie, R. Kiselev, C. Krafft, and J. Popp, "Rapid acquisition of mean Raman spectra of eukaryotic cells for a robust single cell classification," *Analyst*, vol. 141, no. 23, pp. 6387–6395, 2016.

[147] I. W. Schie and J. W. Chan, "Estimation of spectra sample size for characterizing single cells using micro-Raman spectroscopy," *Journal of Raman Spectroscopy*, vol. 47, no. 4, pp. 384–390, 2016.

[148] D. W. Shipp, F. Sinjab, and I. Notingher, "Raman spectroscopy: techniques and applications in the life sciences," *Advances in Optics and Photonics*, vol. 9, no. 2, p. 315, 2017.

[149] A. C. S. Talari, Z. Movasaghi, S. Rehman, and I. U. Rehman, "Raman spectroscopy of biological tissues," *Applied Spectroscopy Reviews*, vol. 50, no. 1, pp. 46–111, 2015.

[150] K. Kainz, M. A. Bauer, F. Madeo, and D. Carmona-Gutierrez, "Fungal infections in humans: The silent crisis," *Microbial Cell*, vol. 7, no. 6, pp. 143–145, 2020.

[151] CDC, "Antibiotic Resistance Threats in The United States 2019," *Cdc*, vol. 10, no. 1, 2019.

[152] B. Shambayati, *Cytopathology - Fundamentals of Biomedical Science*. Oxford University Press, 2018.

[153] K. L. Watson and M. A. P. Patrick R. Murray, Ken Rosenthal, *Medical Microbiology E-Book*. Elsevier Health Sciences, 2020.

[154] B. L. Wickes and N. P. Wiederhold, "Molecular diagnostics in medical mycology," *Nature Communications*, vol. 9, no. 1, 2018.

[155] W. Fang, J. Wu, M. Cheng, X. Zhu, M. Du, C. Chen, W. Liao, K. Zhi, and W. Pan, "Diagnosis of invasive fungal infections: challenges and recent developments," *Journal of Biomedical Science*, vol. 30, no. 1, pp. 1–35, 2023.

[156] P. D. Khot and D. N. Fredricks, "PCR-based diagnosis of human fungal infections.," *Expert review of anti-infective therapy*, vol. 7, pp. 1201–1221, 12 2009.

[157] I. M. Zacharioudakis, F. N. Zervou, and E. Mylonakis, "T2 magnetic resonance assay: Overview of available data and clinical implications," *Journal of Fungi*, vol. 4, no. 2, 2018.

[158] D. S. Perlin and N. P. Wiederhold, "Culture-independent molecular methods for detection of antifungal resistance mechanisms and fungal identification," *Journal of Infectious Diseases*, vol. 216, no. Suppl 3, pp. S458–S465, 2017.

[159] R. J. Swain, G. Jell, and M. M. Stevens, "Non-invasive analysis of cell cycle dynamics in single living cells with Raman micro-spectroscopy," *Journal of Cellular Biochemistry*, vol. 104, no. 4, pp. 1427–1438, 2008.

[160] I. Notingher and L. L. Hench, "Raman microspectroscopy: A noninvasive tool for studies of individual living cells in vitro," *Expert Review of Medical Devices*, vol. 3, no. 2, pp. 215–234, 2006.

[161] J. Talapko, M. Juzbašić, T. Matijević, E. Pustijanac, S. Bekić, I. Kotris, and I. Škrlec, "Candida albicans-the virulence factors and clinical manifestations of infection," *Journal of Fungi*, vol. 7, no. 2, pp. 1–19, 2021.

[162] M. Ford, *Medical Microbiology*. Fundamentals of Biomedical Science, Oxford University Press, 2019.

[163] M. G. Fernández-Manteca, A. A. Ocampo-Sosa, C. Ruiz de Alegría-Puig, M. Pía Roiz, J. Rodríguez-Grande, F. Madrazo, J. Calvo, L. Rodríguez-Cobo, J. M. López-Higuera, M. C. Fariñas, and A. Cobo, "Automatic classification of Candida species using Raman spectroscopy and machine learning," *Spectrochimica Acta - Part A: Molecular and Biomolecular Spectroscopy*, vol. 290, no. October 2022, 2023.

[164] I. Notingher, S. Verrier, S. Haque, J. M. Polak, and L. L. Hench, "Spectroscopic study of human lung epithelial cells (A549) in culture: Living cells versus dead cells," *Biopolymers - Biospectroscopy Section*, vol. 72, no. 4, pp. 230–240, 2003.

[165] Q. Matthews, A. Jirasek, J. Lum, X. Duan, and A. G. Brolo, "Variability in Raman spectra of single human tumor cells cultured in vitro: Correlation with cell cycle and culture confluency," *Applied Spectroscopy*, vol. 64, no. 8, pp. 871–887, 2010.

[166] M. Thattai and A. Van Oudenaarden, "Intrinsic noise in gene regulatory networks," *Proceedings of the National Academy of Sciences of the United States of America*, vol. 98, no. 15, pp. 8614–8619, 2001.

[167] G. Cotter and K. Kavanagh, "Adherence mechanisms of Candida albicans," *British Journal of Biomedical Science*, vol. 57, no. 3, pp. 241–249, 2000.

[168] U. A. E. Ali, P. Maniamfu, and K. Kameyama, "Efficient band reduction for hyperspectral imaging with dependency-based segmented principal component analysis," *International Journal of Remote Sensing*, vol. 00, no. 00, pp. 1–27, 2024.

[169] Y. Otsuka, K. Makara, S. Satoh, H. Hashimoto, and Y. Ozeki, "On-line visualization of multicolor chemical images with stimulated Raman scattering spectral microscopy," *Analyst*, vol. 140, no. 9, pp. 2984–2987, 2015.

[170] L. McInnes, J. Healy, and J. Melville, "UMAP: Uniform Manifold Approximation and Projection for Dimension Reduction," 2018.

[171] S. X. Yu and J. Shi, "Multiclass spectral clustering," *Proceedings of the IEEE International Conference on Computer Vision*, vol. 1, pp. 313–319, 2003.

[172] G. Pezzotti, M. Kobara, T. Nakaya, H. Imamura, N. Miyamoto, T. Adachi, T. Yamamoto, N. Kanamura, E. Ohgitani, E. Marin, W. Zhu, I. Nishimura, O. Mazda, T. Nakata, and K. Makimura, "Raman Spectroscopy of Oral Candida Species: Molecular-Scale Analyses, Chemometrics, and Barcode Identification," *International Journal of Molecular Sciences*, vol. 23, no. 10, pp. 1–26, 2022.

[173] D. S. Radić, V. P. Pavlović, M. M. Lazović, J. P. Jovičić-Petrović, V. M. Karličić, B. T. Lalević, and V. B. Raičević, "Copper-tolerant yeasts: Raman spectroscopy in determination of bioaccumulation mechanism," *Environmental Science and Pollution Research*, vol. 24, no. 27, pp. 21885–21893, 2017.

[174] J. Ruiz-Herrera, M. Victoria Elorza, E. Valentín, and R. Sentandreu, "Molecular organization of the cell wall of Candida albicans and its relation to pathogenicity," *FEMS Yeast Research*, vol. 6, no. 1, pp. 14–29, 2006.

[175] R. Muddiman, S. Baryalay, M. McCartney, G. A. Hoysted, and B. Hennelly, "Spectral interferometric polarization imaging using broadband CARS," in *Proc.SPIE*, vol. 12996, p. 129960P, 6 2024.

[176] J. J. Gil and R. Ossikovski, *Polarized Light and the Mueller Matrix Approach*. CRC Press, 2 ed., 2022.